

Analysis of Mistuned Blisk Vibrations Using a Surrogate Lumped Mass Model with Aerodynamic Influences

Von der Fakultät für Maschinenbau, Elektrotechnik und Wirtschaftsingenieurwesen der
Brandenburgischen Technischen Universität Cottbus zur Erlangung des akademischen
Grades eines Doktor-Ingenieurs genehmigte Dissertation

vorgelegt von

**Diplom-Ingenieur
Jens Nipkau**

geboren am 6.1.1982 in Herzberg/Elster

Vorsitzender:	Prof. Dr.-Ing. habil. Dieter Bestle
Gutachter:	Prof. Dr.-Ing. Arnold Kühhorn
Gutachter:	Prof. Dr.-Ing. Christoph Egbers

Tag der mündlichen Prüfung: 15.03.2011

If we knew what it was we were doing, it would not be called research, would it?
Albert Einstein (1879 - 1955)

Acknowledgements

The present work contains the results of my activities as post-graduate in the International Graduate School (IGS) in the class of "Compressor Technology & Materials" at the BTU Cottbus.

Special thanks go to Prof. Dr.-Ing. Arnold Kühhorn for giving me the chance to work at his chair, for his constant support of myself and my work and for reviewing the work. Moreover, I thank Prof. Dr.-Ing. Christoph Egbers for showing interest in my work, all the valuable advices and for his expertise as well as Prof. Dr.-Ing. habil. Dieter Bestle for being the chairman of the examination committee.

Many thanks go to PD Dr.-Ing. habil. Bernd Beirow for his persistent support of my work with the EBM and his numerous comments on this thesis.

Furthermore I'm very grateful to Dr.-Ing. Bernhard Mück from Rolls-Royce Deutschland for the inspiring discussions about aeroelastic finesses and the precious hints that helped completing the thesis. Gratitude goes also to Dipl.-Ing. Sven Schrape for his comments to my work and the stimulating discussions.

Special thanks go also to Dipl.-Ing. Ulrik Strehlau for providing me with the experimental data I needed and Dipl.-Ing. Thomas Giersch for his effort in adapting the aeroelastic methods for the use in Au3D.

I also must not forget Dipl.-Ing. Mark Golze for his technical support and all colleagues from the Chair of Structural Mechanics and Vehicle Vibration Technology for the relaxed atmosphere and the friendly collaboration.

Last but not least warm thanks go to my family for their patience and steady support.

Cottbus, March 2011

Jens Nipkau

Summary

The present work presents the aeroelastic analyses of mistuned blisk forced response employing a surrogate lumped mass model with aerodynamic influence coefficients. Prior to these, the state of the art in mistuning analysis is summarised and the theoretical background of the structural as well as the aerodynamical model employed in this work is illustrated. Consequently, the validation of the aeroelastic methods is presented at the example of the compressor like Standard Configuration 10, a standardised test case of an aerofoil vibrating in a cascade, and the aerodynamical model is validated against bidirectionally coupled fluid structure interaction simulations of a 2D compressor rotor model. Finally, the aeroelastic behaviour of a mistuned blisk is analysed featuring measured mistuning patterns and extensive probabilistic analyses of mistuned blisk forced response.

Zusammenfassung

Die vorliegende Arbeit beschäftigt sich mit der Analyse erzwungener Schwingungen von verstimmtten Verdichterlaufrädern unter Verwendung eines diskreten Ersatzmodells und aerodynamischen Einflusskoeffizienten. Zunächst werden der Stand der Technik bezogen auf die Untersuchung verstimmtter Systeme zusammengefasst und die theoretischen Hintergründe des verwendeten Struktur- sowie aerodynamischen Modells dargestellt. Im Anschluss daran werden die aeroelastischen Methoden anhand der Standard Konfiguration 10, einem standardisierten Testfall schwingender Schaufeln in einer Kaskade, überprüft und das aerodynamische Modell mit Hilfe bidirektional gekoppelter Fluid-Struktur-Interaktions-Simulationen eines 2D Modells eines Verdichterrrotors validiert. Schließlich wird das aeroelastische Verhalten einer verstimmtten Verdichter-Blisk untersucht, wobei neben der Analyse experimentell ermittelter Verstimmungsverteilungen auch ausführliche, probabilistische Simulationen durchgeführt wurden.

Contents

1	Introduction	1
1.1	Motivation	1
1.2	State of the Art	2
1.3	Results of Mistuning Research	7
1.4	Scope of the Work	9
2	Blisk Vibration Behaviour	11
2.1	Rotor Vibrations	11
2.2	Mistuning	15
2.3	Aeroelasticity in Compressors	20
2.3.1	Blade Flutter	20
2.3.2	Forced Response	23
3	Aeroelastic Methods	27
3.1	Dynamic Model of Blade Vibrations	27
3.2	Aerodynamic Model for Aerodynamically Coupled Blade Vibrations	29
3.3	Kinematic Formulation for Tuned Systems	32
3.4	Determination of Force and Moment Coefficients	35
3.4.1	Coefficients for Rigid Blade Motion	35
3.4.2	Coefficients for General Motion	36
3.5	Determination of Aeroelastic Eigenvalues	37
4	Equivalent Blisk Model	39
4.1	Overview about Lumped Mass Models	39

4.2	EBM Fundamentals	41
4.2.1	Structural Parameter Identification	42
4.2.2	Equivalent Aerodynamic Elements	46
4.2.3	Aerodynamic Influence Coefficients	49
4.3	Time Marching for Flutter and Forced Response Analysis	51
4.4	Forced Response in the Frequency Domain	56
5	Standard Configuration 10	57
5.1	Model	57
5.1.1	Parameters and Flow Conditions	58
5.1.2	Reference Results	59
5.1.3	Details about the Numerical Simulations	60
5.2	2D Model	61
5.2.1	Inviscid Steady State Simulations	61
5.2.2	Inviscid Unsteady Simulations	62
5.2.3	Viscous Steady State Simulations	69
5.2.4	Viscous Unsteady Simulations	70
5.3	3D Model	72
5.3.1	Steady State Simulations	73
5.3.2	Unsteady Simulations	75
6	E3E - Rotor 6	79
6.1	The E3E High Pressure Compressor	80
6.2	2D Linear Cascade of Rotor 6	80
6.2.1	Tuned Cascade Results	83
6.2.2	Mistuned Cascade Results	88
7	E3E - Rotor 1	95
7.1	Steady State Numerical Flow Solution	95
7.2	Modal Analysis	102

7.2.1	Tuned System	102
7.2.2	Mistuned System	104
7.3	Identification of Aeroelastic Parameters	106
7.4	Rotor 1 EBM Model	107
7.4.1	Identification of EBM Parameters	109
7.4.2	Eigenvalues of Tuned EBM	110
7.4.3	Eigenvalues of Mistuned EBM	114
7.4.4	Forced Response of Tuned and Mistuned EBM	116
8	Summary	137
A	Richardson Extrapolation	141
B	Mistuning Patterns of Rotor 1	143
C	Eigenvalues of Mistuned Rotor 1 EBM Model	145
C.1	Mode 1 - 1st flap	145
C.2	Mode 2 - 2nd flap	147
C.3	Mode 3 - 1st torsion	148
C.4	Mode 6 - tram line	149
D	Forced Response of Measured Patterns	151
E	Probability Density of Positive Nodal Diameters - Mode 1	155

Nomenclature

Latin Symbols

symbol	unit	meaning
A	m^2	area
c	m	chord length
c_L	–	lift coefficient
c_M	–	moment coefficient
\hat{C}	$N/(m\ kg)$	travelling wave mode coefficient
e	–	unity vector
f	Hz	frequency
h	m	blade height
DFT_{\max}	–	maximum Fourier coefficient
E	N/m^2	Young's Modulus
E_{kin}	J	kinetic energy
$\hat{\mathbf{E}}$	–	complex transformation matrix
f	N/\sqrt{kg}	mass normalised modal force
F	N	force
j	–	imaginary unit
\mathbf{I}	–	identity matrix
J	$kg\ m^2$	mass moment of inertia
k	N/m	stiffness
\mathbf{K}	N/m	stiffness matrix
\hat{L}	$N/(m\ kg)$	influence coefficient
m	kg	mass
\mathbf{M}	kg	mass matrix
Ma	–	mach number
\mathbf{n}	–	surface normal vector
N	–	number of blades

symbol	unit	meaning
nd	—	number of nodal diameters
NH	$1/s$	rotational speed
p	Pa	static pressure
p_t	Pa	total pressure
q	$m\sqrt{kg}$	modal displacement
\mathbf{r}	m	direction vector
r_g	—	grid refinement ratio
Re	—	Reynolds number
s	—	blade surface line segment
t	s	time
u	m/s	flow velocity
u_{ax}	m/s	axial velocity
u_τ	m/s	shear velocity
W	J	work
x	m	displacement
y	m	DOF of heaving motion
y^+	—	dimensionless wall distance

Greek Symbols

symbol	unit	meaning
α	$^\circ$	angle
β	$^\circ$	flow angle
δ	$1/s$	decay rate
ζ	—	damping ratio
θ	$^\circ$	angular position
κ	—	heat capacity ratio
λ	$1/s$	eigenvalue
Λ	—	logarithmic decrement
μ	—	blade mass ratio
ν	—	amplification factor
ν_{visc}	m^2/s	kinematic viscosity
Ξ	—	aerodynamic damping parameter
π	—	Ludolph's number
Π	—	pressure ratio
ρ	kg/m^3	density

symbol	unit	meaning
σ	$^{\circ}$	interblade phase angle
σ_{STD}	%	standard deviation
τ	N/m^2	wall shear stress
ϕ	$^{\circ}$	angular displacement
Φ	—	mode shape vector
χ	—	displacement ratio
ψ	—	localisation parameter
Ψ	$1/\sqrt{kg}$	mass normalised mode shape vector
ω	rad/s	angular frequency
ω^*	—	reduced frequency
Ω	rad/s	angular excitation frequency

Subscripts

abbreviation	meaning
1	conditions at the inlet
a	aerodynamic values
b	blade values
cos	value belonging to the cosine part
CSM	values of a particular cyclic symmetry mode
d	disk values
eff	effective
f	forcing
Im	imaginary part
is	isentropic
i, k, n	counting variables
max	maximum
min	minimum
mistuned	mistuned values
Re	real part
rel	relative frame of reference
sec	sector variables of EBM
sin	value belonging to the sine part
tan	tangential
tuned	tuned values

Symbols

symbol	meaning
\hat{x}	amplitude
\bar{x}	average
\underline{x}	complex number
$\hat{\underline{x}}$	complex amplitude
\dot{x}	first time derivative
\ddot{x}	second time derivative

Acronyms

Abbreviation	Meaning
ACARE	Advisory Council for Aeronautics Research in Europe
AIC	Aerodynamic Influence Coefficients
AMM	Asymptotic Mistuning Model
Au3D	Rolls-Royce Aeroelasticity Code
BTW	Backward Travelling Wave
CFD	Computational Fluid Dynamics
CMS	Component Mode Based Synthesis
CSM	Cyclic Symmetry Mode
DOF	Degree Of Freedom
E3E	Engine 3E
EBM	Equivalent Blisk Model
EO	Engine Order
FE	Finite Element
FEM	Finite Element Method
FMM	Fundamental Mistuning Model
FRF	Frequency Response Function
FSI	Fluid Structure Interaction
FTW	Forward Travelling Wave
HCF	High Cycle Fatigue
IBPA	Interblade Phase Angle
IGV	Inlet Guide Vane
LDV	Laser Doppler Vibrometry
LEO	Low Engine Order
LPT	Low Pressure Turbine
MCSM	Modified Cyclic Symmetry Mode
MpCCI	Mesh based Parallel Code Coupling Interface
MTO	Maximum Take-Off
NACA	National Advisory Committee for Aeronautics
NRBC	Non-Reflecting Boundary Conditions

Abbreviation	Meaning
ODS	Operating Deflection Shape
PMAC	Partial Modal Assurance Criterion
RMS	Root Mean Square
ROM	Reduced Order Model
SC10	Standard Configuration 10
SDOF	Single Degree of Freedom
SMF	Chair of Structural Mechanics and Vehicle Vibration Technology
SNM	Subset of Nominal Modes
UDF	User Defined Function
VSV	Variable Stator Vanes

Chapter 1

Introduction

1.1 Motivation

The constantly growing global air traffic poses huge challenges to current and future aircraft and jet engine developments. A predicted growth of the annual traffic of about 4.9% together with an increase of the global aircraft fleet from 18800 planes in 2008 to 35600 planes till 2028 [14] in conjunction with the ambitious objectives of the ACARE Vision 2020 [1] requires considerable progress in the development of modern technology. According to the Vision 2020 the aims are a reduction of the NO_x emissions by 80% and a reduction of the emitted CO_2 by 50% with an engine contribution concerning the specific fuel consumption of 15 to 20%. Simultaneously the time to market of aircrafts and their jet engines is desired to be shortened by half. Consequently this means that engine concepts have to become more efficient. One focus can be put on the compressor of a jet engine, as an increase of its efficiency subsequently leads to a reduction of the power needed to drive the compressor and in turn of the power that needs to be supplied of the turbine and hence of the specific fuel consumption. The reduction of the specific fuel consumption involves an immense potential of saving resources which can be seen, apart from the climate protection, as an additional stimulus for the development processes.

Concerning the high pressure compressor (HPC) of a jet engine, these developments led to numerous technologic innovations. For example, a significant effort is made with passive and active methods to be able to control the aerodynamics of a modern high pressure compressor, to reduce losses and to increase the aerodynamic efficiency. Three dimensional blade geometries with sweep and lean have already become standard in modern jet engines, [42]. Furthermore, intensive research is done to make active methods such as boundary layer suction or transition control applicable, see Gad-el-Hak [37] and [38] for details about this topic.

Concerning the structural mechanics the challenge is to guarantee the structural integrity and endurance for all kinds of components with the parts getting thinner and lighter and

being made of modern materials. In this context the design of the rotor stages has remarkably changed. Even in civil applications modern rotors are more and more designed as blisks¹ (Blade Integrated Disks.). On the contrary to the differential design, here the blades are no longer connected with the disk through slots but are an integral feature of it. Despite the advantages like lower weight, higher pressure ratios, less part numbers or minimised secondary flow, ensuring the structural integrity of blisks poses big challenges to engineers.

In comparison with the differential design, the blisk design lacks a fundamental mechanism of energy dissipation. As the blade vibrates, friction at the contact faces of blade root and disk slot dissipates vibration energy which damps the blade. Since there is no such contact with blisks, the only structural damping that remains is the material one which is some magnitudes of order smaller.

In addition, manufacturing tolerances and material inhomogeneities along with blade deterioration lead to so-called mistuning. Mistuning reveals itself by varying blade natural frequencies around the rotor's circumference. During engine operation forced and self excited high frequency blade vibrations may occur. On the contrary to a perfectly tuned system where all the blades exhibit the same vibration amplitudes, mistuned systems may respond in strong localised mode shapes. That is to say, only some of the blades in the assembly respond to the excitation or the response can even be restricted to a single blade in the worst case. In combination with the low mechanical damping in blisk structures, the amplitudes of those vibrations may well exceed the sustainable limit or reduce the high cycle fatigue (HCF) life.

Logically, such situations are undesirable and a lot of work is done to mitigate the effects of mistuning. The demand of practical working engineers for a thorough understanding of the influences coming from mistuning are the major stimulus for the research done on mistuning to ensure safe and robust engine designs.

1.2 State of the Art

The nature and consequences of mistuning have been in the focus of research for more than 40 years now. One of the pioneers in the field of mistuning have been Whitehead [119] and Ewins [28] who initiated a long tradition of research. The quest for answers to the questions what the reasons for mistuning are, which effects result from it and how to deal with the impact of mistuning on engine operation have given rise to numerous publications.

As a matter of fact, the answers to these questions can only be as good as the tools used to find them. Consequently, three major disciplines have emerged from the vast field of mistuning analysis, namely

¹For example the stages 1 to 4 of EPI's TP400 HPC, stages 2 to 6 of Rolls-Royce's BR725 HPC or 2 stages of PowerJet's SaM146 HPC

- the development of measurement techniques to offer the opportunity of quantifying mistuning in real turbomachinery structures,
- the development and enhancement of structural models to evaluate the effects on the vibration behaviour and
- the formation of aerodynamic models to allow for the consideration of the significant aerodynamic influences on mistuning.

Unquestionably, none of these disciplines can be treated separately, as in some sort, data exchange forms the basis for a holistic analysis of the mistuning problem. Within each discipline a lot of work has been done during the past decades which makes it hard to give a complete summary.

A detailed literature debate was given by Nikolic in 2006 [86]. The focus of this review is mainly on the structural modeling with some aspects of mistuning measurement. Other publications that deal with the vibration characteristics of turbomachinery bladings are the work from Srinivasan in 1997 [108], Slater et al. in 1999 [106] and Castanier and Pierre in 2006 [19]. The aeroelastic methods used in mistuning analyses and in the analyses of blade vibrations in general are the topic of a number of summaries as well. As the most important ones have to be named the work of Verdon in 1993 [114], the review of Reddy et al. in 1993 [97], Foersching's overview about aeroelastic methods in turbomachinery cascades from 1994 [36] and the review of Marshall et al. from 1996 [77].

In the following, the state of the art methods are summarised briefly, without seeking for completeness, to give an insight in the variety of problems that have been addressed so far.

Reduced Order Models

Since finite-element (FE) models of bladed disks feature great numbers of degrees of freedom (DOF) one objective has always been to reduce the effective number of DOF to allow for faster and more efficient analyses of mistuned bladed disks. A popular method is to model bladed disks with the help of lumped mass models as done by Wagner in 1967 for example [116]. The different models employing lumped masses which have evolved since then are summarised in Chapter 4 in more detail.

More sophisticated models are the so called reduced order models (ROM) which base on FE models whose numbers of DOF are reduced remarkably. One of the first to address this topic was Hurty in 1965 [57] who used a component mode based approach where components of a structure (e.g. disk and blades) are considered separately. For each of these components the modes are calculated independently and the behaviour of the global structure is reconstructed by compatibility constraints at the interconnections. Several techniques of this so

called component mode based synthesis (CMS) exist today, so for example the method developed by Craig and Bampton [21] or Castanier et al. [20]. The different techniques mainly differ in the number of modes required to obtain satisfactory compliance with finite-element results and therefore the degree of reduction and the benefit in computation. A thorough overview about CMS models has been given by Bladh et al. in 2001 [12] with some applications of the different techniques to free and forced response analyses of tuned and mistuned bladed disks [13]. Further extensions have been made by Seinturier et al. in 2002 [103] and in 2004 [104] addressing the problem of a CMS model with CFD. The work of Seinturier et al. in 2004 comprises the analyses of tuned and mistuned forced response of a high pressure compressor bladed disk including aerodynamic damping estimations from aeroelastic computations. However, the aerodynamic damping employed was constant for all blades of the tuned and mistuned system.

Another type of reduced order model is the so called SNM model (subset of nominal modes) introduced by Yang and Griffin in 2001 [124] which takes advantage of the fact that every mistuned mode can be obtained by linear superposition of a certain number of nominal/tuned modes. On the contrary to CMS models the SNM model treats disk and blade as a single structure. The methodology bases on the work of Yang and Griffin from 1997 [123] in which the close frequency spacing of the system's natural modes of the tuned system is used to make up the mistuned modes. That is why, the SNM model gives best results when one family of modes is well separated from the others and all tuned modes are summed up to obtain the mistuned modes.

The SNM model has been further extended by Feiner and Griffin in 2002 [31] taking advantage of the simplification which arises when the SNM model considerations are restricted to a single family of modes with closely spaced natural frequencies and for which the strain energy is primarily in the blades. Since this new model focuses on the fundamental parameters controlling mistuning it is termed fundamental mistuning model (FMM). A lot of attention has been paid to the FMM which lead to further adaption and improvement. In 2006 Ayers et al. [4] extended the FMM to enable transient simulations of bladed disk vibrations in the time domain. Further modifications involved the derivation of an inverse approach for the determination of mistuning and the inclusion of aerodynamic forces, both are addressed in the following paragraphs. A further reduction of the FMM method has been presented by Martel et al. in 2008 [78] termed asymptotic mistuning model (AMM), making the model applicable to families of modes whose natural frequencies are not closely spaced for all nodal diameters by regarding clustered and isolated modes separately.

Another methodology has been presented by Petrov et al. in 2002 [96] which bases on an exact relationship between the tuned and mistuned response of bladed disks. In other words the mistuned response is expressed through modification of the tuned response depending on the frequency response function (FRF) of the tuned system and a matrix representing the blade mistuning. Since the FRF matrix of the tuned system is derived using tuned mode shapes of cyclic symmetric FE models, the accuracy of the method only depends on the

number of tuned modes involved in the FRF matrix calculation.

Aerodynamic Modeling

The aerodynamics in turbomachines are one of the major influences on the responses of mistuned bladed disks. In the previous paragraph the development process of effective structural models in the absence of aerodynamic forces has been stressed. However, the evolution of simplified models has not only been restricted to structural systems but has also been an issue of aerodynamics aiming at efficient methodologies allowing for faster aeroelastic computations and simulation of mistuned forced responses considering aerodynamic coupling between the blades.

Although full scale, non-linear aeroelastic CFD computations are desirable and have already become very efficient, see Sayma et al. [99] and [112] for example, and computing power has increased dramatically over the past 20 years, the methods available today are still very time consuming limiting their usage to special interests and prohibiting their application in every day engine development processes. Consequently, enormous effort has been made to reduce the costs of full scale, non-linear computations for the determination of aeroelastic eigenvalues and forced response computations. Early analyses dealt with that problem by using incompressible and/or inviscid computations. However, the aerodynamics in today's turbomachinery are characterised by considerable, compressible and viscous flow effects. Therefore extensive research has been conducted to develop efficient CFD methods and to search for techniques allowing for a reduction of computational domains.

One of the first to address these problems were Erdos et al. in 1977 [27]. Their proposed method allows to calculate forced response of blade rows, whose pitches in the rotor and stator row are unequal, with only a few blade passages by storing the information at the periodic boundaries needed to overcome the phase lag and prescribing it on the opposite boundary time shifted. These so called phase lagged boundary conditions can also be used to determine the aerodynamic damping of any possible interblade phase angle of a blade row with a single blade passage. However, the biggest disadvantage of this technique is the memory consumption for the data storage. Consequently Giles has improved the idea of phase lagged boundary conditions in 1991 [41] employing a space-time transformation which needs no additional data storage and requires only about 15% more effort than the basic computational algorithm. Another very effective technique is the shape-correction method developed by He in 1992 [50]. The method assumes the flow variables at the periodic boundaries to be decomposable into a sum of a time averaged part and a sum of disturbances. Therefore only the coefficients obtained from Fourier decomposition need to be stored which are then used to update the flow variables at the periodic boundaries at each time step. This method has been successfully applied by Li and He to aerodynamic damping computations of vibrating blades using a single passage [74] and for rotor stator interaction computations [75].

A rather new approach has just recently been presented by Mata et al. [79] who developed a method for fast forced response computations extending the method of Erdos et al. to multi blade row computations and employing sliding planes for the data exchange between the blade rows.

The method introduced by Hanamura et al. in 1980 [48], called aerodynamic influence coefficients (AIC) technique, can be used to make aerodynamic forces available for the determination of aeroelastic eigenvalues or for structural models for flutter and forced response computations. The method considers the vibration induced aerodynamic forces on one blade coming from the other blades of the assembly separately, superposing them to the resulting aerodynamic influence seen by the blade under consideration. Details about the method are given in Chapter 3. The influence coefficient technique can be efficiently used in lumped mass models as realised by Kahl in 2002 [61] for example.

Similar approaches have been used representing aerodynamic damping by dashpots and aerodynamic stiffening and softening by springs. Such modelling has been used by Lin and Mignolet [76], Kenyon et al. [65] or Beirow [7] in conjunction with lumped mass models.

An aerodynamic reduced order model has been proposed by Willcox and Peraire [122] basing on the two-dimensional Euler equations which can be coupled with a structural model to obtain an aeroelastic model. The results of aeroelastic eigenvalues and forced response computations have been compared to those of classical influence coefficients technique which showed significant differences. However, the computations are restricted to time domain computations and the transonic test case that has been used is actually beyond the field of application of influence coefficients. Details about the comparability of results obtained with influence coefficients and bidirectionally coupled fluid structure interaction (FSI) computations are given in Chapter 6 of the present work.

Concerning the consideration of aerodynamic forces within the reduced order models summarised in the previous paragraph, different approaches have evolved. The CMS model has been extended with an aerodynamic model by He et al. [52] basing on quasi 3D, inviscid, potential flow equations allowing for an algebraic calculation of the modal blade forces. In 2004 Kielb et al. [66] incorporated aerodynamic forces obtained with the tuned mode shapes as a function of the interblade phase angle formulating the equation of motion of a mistuned bladed disk in travelling wave mode coordinates. In a similar manner Martel et al. [78] considered the aerodynamic forces in their AMM, calculating the aerodynamic force coefficients with a linearised Navier-Stokes solver employing phase lagged boundary conditions. Petrov also introduced aerodynamic coupling in his ROM [93] by calculating the FRF matrix with aerodynamic effects included from the modal forces experienced by a blade vibrating in travelling wave modes without costly matrix inversion but rather through employing aeroelastic eigenvalues and blade mode shapes.

Measurement and Model Updating

The different models presented in the preceding paragraphs can be used for any type of mistuning pattern. However, if one particular test piece is going to be analysed the determination of the actual existing mistuning pattern is desirable. For that purpose, blades from bladed disks are generally clamped individually on a supporting device and their natural frequencies are measured, see Seinturier et al. [103] for example. However, since the blades mounted on the disk may show significantly different frequencies and due to the method not being applicable to blisks, techniques have been developed to allow for a holistic determination of mistuning patterns. A lot of different methods are distributed in the literature which are summarised in the survey given by Castanier and Pierre [19]. Some of these methods are derived from the reduced order models presented in the foregoing paragraphs.

One of these is the FMM-ID presented by Feiner and Griffin in 2004 [32] basing on an inversion of the FMM equations. Two different methods have been presented, one more basic approach uses the tuned natural frequencies from finite element (FE) computations and the mistuned mode shapes determined from experimental modal analyses. A second, more enhanced version, employs only the mistuned modes and frequencies for the determination of all relevant FMM parameters including those needed to model the tuned system.

An effective method has recently been presented by Beirow [7] using additional intentional mistuning to decouple the blade of interest from the rest of the assembly. The intentional mistuning is realised via additional, small masses attached to the blades, shifting their natural frequencies outside the interesting frequency range. After the blade natural frequencies have been determined, the entire measurement campaign is repeated numerically with an iterative adjustment of the blades' mechanical properties adapting the frequency response function to the measured one.

1.3 Results of Mistuning Research

The impact of mistuning on the aeroelastic stability and the forced response of bladed disks has been scrutinised with a lot of different models with and without consideration of the aerodynamic effects. Concerning aeroelastic stability analyses the consensus is that mistuning is beneficial with respect to flutter susceptibility. In 1982 Kielb and Kaza [62] demonstrated the stabilising effect of mistuning on self excited vibrations which has been approved by numerous researches, see Kahl [61] for example. Apart from analytical results the positive effect of mistuning has also been demonstrated experimentally. In 2000 Nowinski and Panovsky [88] were able to increase the aeroelastic stability of a LPT blade cascade by introducing alternate mistuning. However, the beneficial effect may be inhibited by structural coupling as shown by Kielb et al. in 2004 [66]. Their analyses showed that mistuning with a standard deviation of $\sigma_{STD} = 1\%$ has a large stabilising effect while it changes the

tuned eigenvalues only slightly when structural coupling is considered. Moreover, they analysed the impact of the standard deviation on the flutter stability which could be shown to increase with growing standard deviation with the effect being more pronounced without structural coupling.

Another effect of mistuning is the so called mode localisation where the strain energy is located in only a few blades occurring for free and forced vibrations of mistuned bladed disks. In 1988 Wei and Pierre analysed mode localisation of free [117] and forced [118] vibrations employing a lumped mass model. They found that for comparatively small mistuning of realistic dimension mode localisation is more likely to occur for systems with weak structural coupling and that structures with closely spaced eigenvalues are more susceptible to mode localisation in case of free vibrations. Concerning forced vibrations, they concluded that blade amplitude increase due to mode localisation is rather a problem of moderately coupled systems while in case of no structural coupling the blades behave like single degree of freedom (SDOF) oscillators exhibiting almost tuned responses. However, if structural coupling is further increased and strong interblade coupling is reached the confinement of vibration energy to single blades is prohibited leading to responses close to the tuned one. In order to verify these observations Kruse and Pierre conducted experiments in 1997 [71], [72] comparing the results of free and forced vibrations with FE and ROM computations.

The aforementioned increase of blade amplitudes in case of mistuned forced response is concerned with the major question how big the amplitudes may actually get. This question has been first addressed by Whitehead in 1966 [119] who found the limit of amplification that can occur to be $\frac{1}{2}(1 + \sqrt{N})$ for which no structural coupling, no mechanical damping and only low, constant aerodynamic damping for all travelling waves is required. However he also stated that this limit is reached only under unusual circumstances when one blade is mistuned and its vibration can couple with the vibrations of all other blades in the assembly which may occur when the vibration couples with an acoustic resonance in the gas flow or a mechanical resonance in the disc. He also stated that blades should be manufactured as identical as possible and that if mistuning is unavoidable then the blades should be divided into two groups with different frequencies. This type of mistuning is commonly referred to as alternate mistuning for which, according to Whitehead, the limit of maximum amplification is $\frac{1}{2}(1 + \sqrt{2})$ which means an increase of roughly 20 per cent in blade amplitude.

In 1976 Whitehead added some aspects to his analysis concerning the maximum amplification of mistuned bladed disks [120]. In the absence of aerodynamic forces he only considered mechanical coupling. He concluded that the detuning of a single blade may lead to a maximum amplification of $\frac{1}{2}(1 + \sqrt{\frac{N}{2}})$ in cases of engine order excitation different from $EO = 0$ or $EO = N/2$. For the rest of the excitation orders, the earlier factor should apply. However, in 1998 Whitehead [121] amended this finding showing that the maximum amplification with equal damping of forward and backward travelling waves may exceed the lower factor and corrected it to the earlier one. In summary, the analyses of Whitehead yielded a maximum attainable amplification in case of mistuned forced response of $\frac{1}{2}(1 + \sqrt{N})$ under the early

mentioned conditions.

The question of maximum forced response amplification has also been addressed by Kenyon et al. in 2003 [65] who studied the maximum forced response of a lumped mass model with constant blade damping and variable damping as well. Their results agreed with those from Whitehead in 1976 in case of constant blade damping while it disagreed when variable damping was introduced showing that the variable one may lead to either lower or higher amplification factors than those given by Whitehead in 1976.

In 2010 Petrov [94] also studied the maximum forced response amplification with the reduced order model considering variable aerodynamic damping presented in [93]. His analyses also comprised an optimisation process for the determination of the worst mistuning pattern for which the maximum amplification was computed to exceed the limit given by Whitehead in 1966. Another interesting finding of his work is the possibility of maximum mistuned blade responses to drop below the tuned response which has also been observed by Kahl in 2002 [61] in case of alternate mistuning with rather large frequency deviation of 5%.

Lastly the effect coming from the rotational speed of a bladed disk rotor also influences the mistuning analyses. The centrifugal forces which are inevitably present at operation may well influence mistuning of bladed rotor disks which is especially important when mistuning measured in a laboratory at rest shall be used in a reduced order model for the comparison with engine tests. In 2002 Moyroud et al. [84] showed that the stiffening effect coming from the rotation of a fan stage tends to average out the frequency perturbations of the 2nd blade mode shape. The same observations have been made by Feiner in 2003 [30] showing alleviation of frequency deviations.

1.4 Scope of the Work

The previous activities at the chair of "Structural Mechanics and Vehicle Vibration Technology" (SMF) so far constitute the basis of the present work. In the preceding work Klauke [68] addressed the topic of mistuning measurement and numerical simulation using standard FE-software and the reduced order model developed by Petrov [96]. All his analyses have been carried out in the absence of aerodynamic influences. The following work of Beirow [7] dealt with additional aspects of mistuning measurement and the development of a lumped mass model, the equivalent blisk model (EBM), to enable fundamental analysis of mistuned bladed disks. In order to take care of the aerodynamic effects in mistuning analyses Schrape et al. [102] studied the capability of using commercial CFD software in aeroelastic investigations. These results provided input data for Beirow to conduct an enhanced analysis of mistuned blisk vibrations with an extended EBM employing equivalent aerodynamic elements [7].

The aim of the following work is to incorporate a different treatment of the aerodynamic

influences into the EBM. With the use of aerodynamic influence coefficients, the aerodynamic forces are considered in blade individual coordinates rather than being calculated in dependency of the interblade phase angle² as previously done with the equivalent aerodynamic elements. Additionally, a frequency dependency is integrated to take account of the variable aerodynamic influences of mistuned bladed disks vibrating in gas flow.

Hence standard aeroelastic analysis procedures are used in combination with commercial CFD software and the Rolls-Royce in-house aeroelasticity code Au3D. The results of those computations are validated against reference data of a compressor like standard configuration with 2D and 3D simulations. Consequently, the integration of the aerodynamic influence coefficients into the EBM is validated with bidirectional aeroelastic simulations of a tuned and a mistuned compressor geometry.

The computations of the forced response of a mistuned blisk comprise real mistuning patterns and four different mode shapes to extend the understanding of the vibration behaviour beyond the fundamental modes. Furthermore comparative results are presented employing constant aerodynamic damping showing significantly different vibration behaviour. Additionally, mechanical parameters such as the degree of mechanical coupling are varied to put the mechanical characteristics in contrast to the aerodynamic influences which may be the major perpetrators in the mitigation of blade vibration amplification of mistuned bladed disks. All these computations for real mistuning patterns are compared to extensive probability simulations taking account of the sensitivity of mistuning analyses.

One of the major objectives is to show that results obtained with lumped mass models cover the essential effects of finite-element reduced order models which makes them a valuable tool for fundamental mistuning analyses.

Consecutively the work is substructured as follows

- The second chapter gives an overview about the description of mistuning and it contains a discussion about the influences on mistuned blisk vibrations,
- the following chapter number 3 addresses the theory of aerodynamic influence coefficients together with the details of aeroelastic eigenvalue calculation,
- Chapter 4 gives the fundamentals of the EBM and elucidates the scaling of aerodynamic influences as needed when integrated into the EBM,
- the validation of the aeroelastic methods is presented in Chapter 5, presenting results of inviscid and viscous, 2D and 3D simulations of the Standard Configuration 10,
- the last two chapters deal with flutter and forced response analyses of two stages of the E3E's high pressure compressor, including the simulation of a 2D model of tuned and mistuned stage 6 rotor and the 3D computations of stage 1 rotor.

²Details about the equivalent aerodynamic elements are presented in Chapter 4.

Chapter 2

Blisk Vibration Behaviour

The vibration behaviour of tuned blisks in the absence of aerodynamics, or any non-linear effects like blade root friction, is well understood today. Nevertheless, as soon as the symmetry of the mode shapes is split up due to mistuning or the influences of aerodynamic forces are desired to be considered, things become more challenging. The following chapter is going to present the basics of tuned axial-blisk vibrations, the effects arising from mistuning and the influences of aerodynamics on mistuned blade vibrations.

2.1 Rotor Vibrations

For a description of the vibration behaviour of a tuned blisk a distinction between disk, blade and coupled vibrations is an appropriate approach as already presented by Imregun [58], Irretier [59] and Klauke [68]. In the following, a brief description of the various vibration types and influences is given.

Considering the vibrations of blisks, neither pure blade nor pure disk vibrations occur but the mode shapes can be rather characterised by the amount of which blades and disk take part in the vibration of the assembly. A common quantity used to distinguish between blade dominated and disk dominated modes is the strain energy. According to Klauke et al. [69], in case of disk dominated modes the blades feature less than 65% of the total strain energy¹, for coupled modes the blades' percentage increases to values between 65% and 90% and for values greater than 90% the blisk vibrations can be regarded as blade dominated. That is to say that to some extent coupled blisk vibrations are the normal case with blisks, it is only the amount of mechanical coupling which defines the dominating component.

¹The values given here are appropriate for axial compressor blisks as considered by Klauke et al. [69].

Disk Dominated Vibrations (percentage of blade strain energy < 65%)

When disk dominated modes are regarded the blisk can be described as a quasi-axisymmetric component. Since the bigger part of the strain energy is in the disk, the blades can be considered as point masses fixed at the outer rim following the deflection of the disk mode shape. According to Ewins [29] such 'disk-like' structures have mode shapes which can be described by

$$\phi(\theta) = \cos(nd\theta + \alpha_{nd}) \quad (2.1)$$

commonly termed *nd-nodal diameter* modes where a nodal diameter is a line of zero displacement on the diameter of the disk.

Blade Dominated Vibrations (percentage of blade strain energy > 90%)

The description of pure blade vibrations focuses on the inspection of isolated blade vibration. According to Cumpsty [25] the analysis of blade vibrations in the early years involved a consideration of axial blades as beam-like structures from which the characterisation of blade mode shapes is adopted. The mode shapes presented in Figure 2.1 are denoted as flap, flexural or bending mode (a), torsion mode (b) and edgewise mode (c). A lot of influences exist which determine the actual mode shape such as the mounting situation, shrouds, blade twist and many more. According to Srinivasan [108] the latter one for example is responsible for adding torsional components to bending components which is the reason that highly three dimensional blades exhibit no pure bending or torsion modes but rather more complicated ones.

Concerning the frequency of the blade vibrations considerable effort is done to avoid that blade natural frequencies coincide with frequencies of excitations coming from the flow, the so called forced response which is highlighted in Section 2.3.2 of this chapter. When talking about the natural frequencies of free blade vibrations various effects like the sort of material, damping, aerodynamics, centrifugal forces, blade aspect ratio etc. have to be taken into consideration. In general, the material damping of blisks is negligible and due to turbomachinery blades commonly featuring high mass densities the impact of the aerodynamic forces is low if the blade mass ratio² is sufficiently high so that most analyses are carried out employing the in-vacuo natural frequencies and mode shapes of the blades. On the contrary, the centrifugal forces coming from rotation impact on the blade natural frequencies shifting them to higher values. This may also change the order in which blade modes appear or bring different blade modes closer in terms of their natural frequencies which may lead to coupled blade vibrations.

²Details about the blade mass ratio are given in Section 2.3.

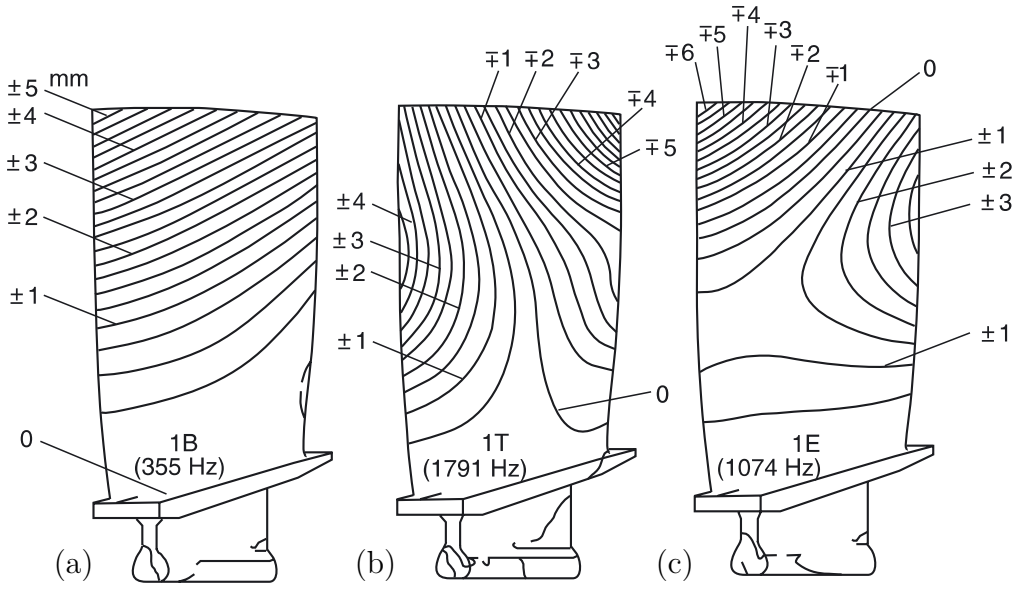


Figure 2.1: Fundamental blade mode shapes with displacement contours shown for (a) first flap, (b) first torsion and (c) first edgewise modes, taken from Grieb [44]

However, as described earlier in this section the blades of a tuned blisk are not isolated but coupled through the disk. Hence, the entire system must be considered for the description of the vibratory modes. The blisk, being a cyclic-symmetric structure, features similar mode shapes as a disk but on the contrary to the disk, the number of nodal lines is limited. These modes are also known as cyclic symmetry modes (CSM) which are differentiated by the number of nodal diameters³. The maximum CSM, or the maximum number of nodal diameters, of a blisk depends on the number of blades which can be described by

$$0 \leq nd \leq \frac{N}{2} \quad \text{if } N \text{ is even or} \quad (2.2)$$

$$0 \leq nd \leq \frac{N-1}{2} \quad \text{if } N \text{ is odd.} \quad (2.3)$$

The natural frequencies of these mode shapes occur, except for $nd=0$ and $nd=N/2$, in pairs, the so called double modes. These double modes feature identical natural frequencies and differ only in the angular orientation of the nodal lines. Hence the mode shapes are commonly referred to as cosine and sine-like modes. When modes of a system are combined, the result is also a mode shape of the system which leads to a description of the blade displacement in the form of

$$\phi(\theta) = \left\{ \hat{\phi} e^{j(\omega t + nd \cdot \theta)} \right\}_{Re} = \hat{\phi} \{ \cos(nd \cdot \theta) \cos(\omega t) - \sin(nd \cdot \theta) \sin(\omega t) \} \quad (2.4)$$

³Within this work *CSM* and *nd* are both used as equivalent descriptions of the vibrational behaviour.

with $\phi(\theta)$ being the circumferential blade displacement as function of the angular position θ . The result is a cosine mode shape with nd nodal diameters travelling around the circumference. In other words, each blade of the assembly has its own phase and will reach its maximum at a different instant in time compared to the adjacent blades. In case of $nd=0$ (in-phase motion of adjacent blades) or $nd=N/2$ (out-of-phase motion of adjacent blades) the resulting mode shape is real which means that all blades reach their maxima at the same time. Analogously, all blades go through zero displacement simultaneously which is the reason that there are two moments in a vibration cycle when the entire blisk is completely undeformed.

Coupled Vibrations ($65\% < \text{percentage of blade strain energy} < 90\%$)

In the context of coupled blade vibrations a general distinction between the frequency veering of blade modes and frequency crossing of blade and disk modes can be made. In case of frequency veering the natural frequencies of different families of modes may be closely spaced for a limited number of CSM, see Figure 2.2, which may lead to coupled blade vibrations in both modes. When frequency crossing is considered both components, blades and disks, may considerably contribute to the overall deflection of a blisk. Such vibrations are characterised by the blade vibrating in a particular mode shape with significant rigid body displacement due to the deflection of the disk. Such coupled vibrations can occur when natural frequencies of blades and disk are closely spaced as shown in Figure 2.2.

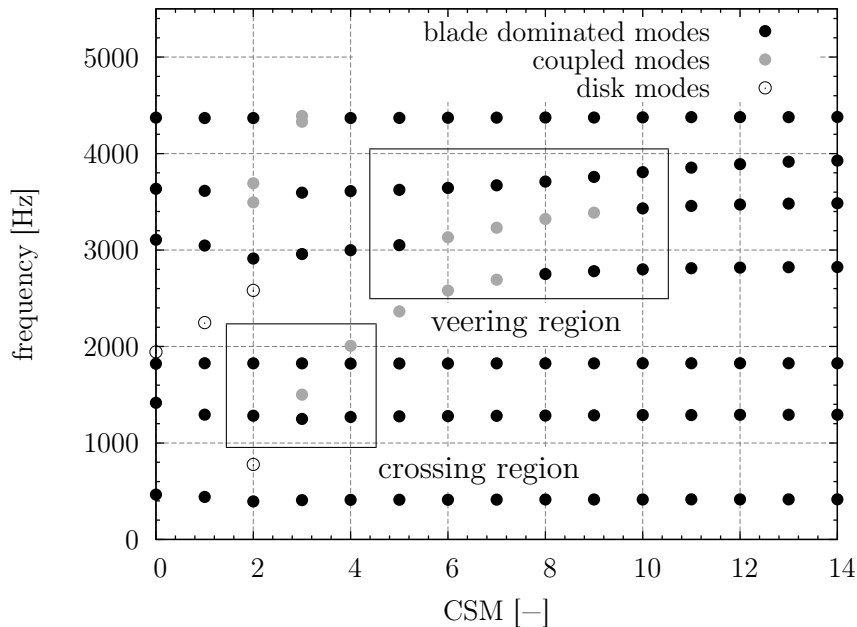


Figure 2.2: Frequency versus CSM of HPC front stage with veering and crossing regions, with courtesy of Klauke et al. [69]

2.2 Mistuning

When mistuning is present, meaning the non-uniform distribution of the blades mechanical properties due to manufacturing tolerances, material inhomogeneities, wear during operation etc., the two identical natural frequencies of the system split up into two closely spaced but different frequencies. As a result, the cyclic symmetry of the system gets lost and the nodal lines will be fixed on the blisk instead of travelling around the circumference. This means, additional diametral content is added to the modes which reveals itself by additional coefficients in the Fourier decomposition of the circumferential displacement as exemplarily shown in Figure 2.3 for a tuned and a mistuned mode. The perturbed mode shapes of a mistuned system also known as modified cyclic symmetry modes (MCSM) are identified by the maximum coefficient of the Fourier decomposition representing the dominating diametral component, also shown in Figure 2.3. In case of forced vibrations, where normally only those CSM respond which correlate to the shape of the excitation, (also known as the engine order) all modes containing a diametral component corresponding to the one of the excitation respond and complicated vibratory responses result. In other words the MCSM combine to give the resultant deflection of the blisk at the excitation frequency which is commonly referred to as the operating deflection shape (ODS).

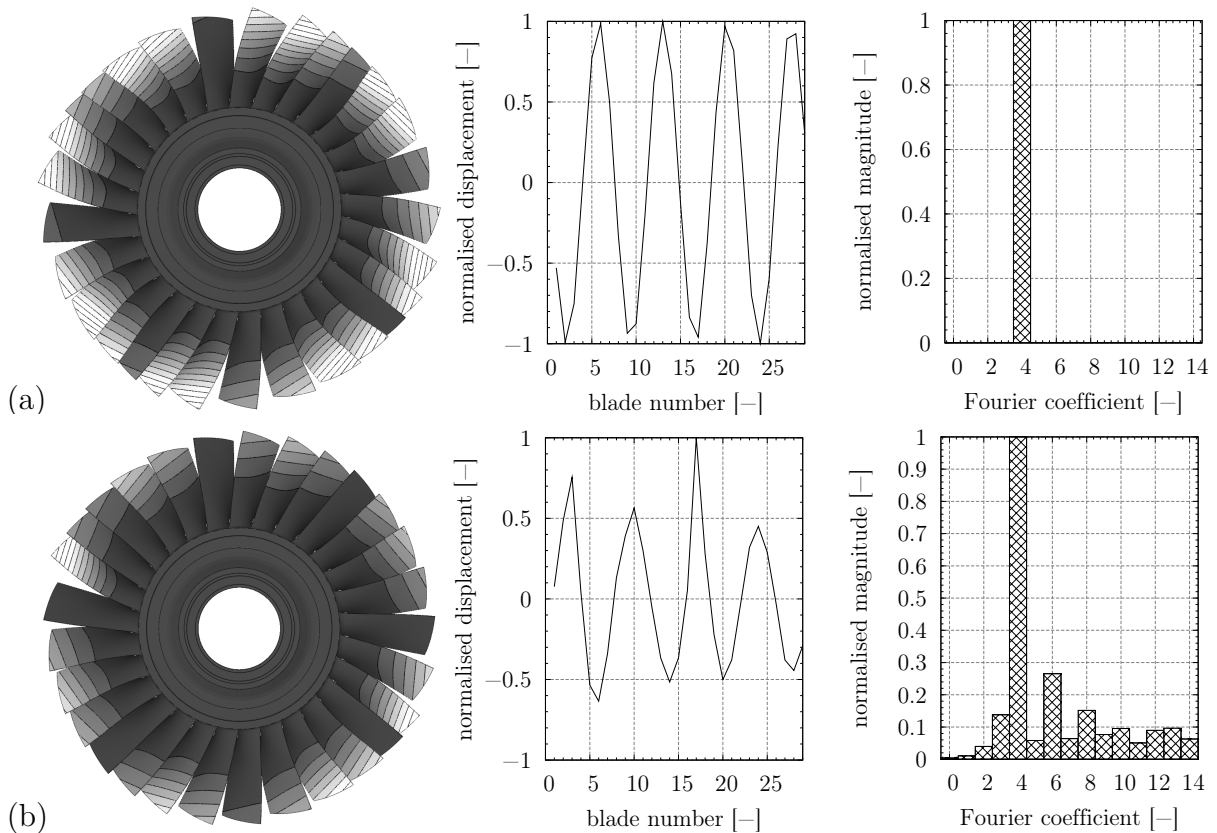


Figure 2.3: Mode shape of 1st flap family of modes of a (a) tuned and (b) mistuned HPC rotor

In case of forced vibrations either two resonances can be observed or the system may well appear as a tuned one depending on the amount of damping. Ewins [29] stated that if the frequency split quantified as percentage of the mean frequency is greater than the modal damping, then two distinct resonances should be observable otherwise the system will be effectively tuned. When the mistuning is great enough multiple resonances can occur in the frequency response function. The mode shapes corresponding to these resonances may exhibit considerably different behaviour.

Localisation Parameter

Compared to the tuned case where the strain energy is uniformly distributed over all blades the exact opposite is the vibration of a single mistuned blade in which all the strain energy localises which is the worst case and may lead to reduced blade life. This so called mode localisation has been the subject matter of several researches e.g. Wei and Pierre [117],[118] or Judge et al. [60]. In order to quantify the strength of the localisation Kahl [61] and Klauke [68] suggested the so called localisation parameters. Within this work the latter has been used which is described here shortly, for details the reader is referred to the work of Klauke. The localisation parameter relates the maximum blade displacement of a mode shape to the root mean square (RMS) of all blade displacements and correlates this displacement ratio $\chi = \hat{u}_{i,\max}/RMS$ with the value of a tuned system and the maximum achievable value of a mistuned system with only one blade vibrating.

The value of the tuned system depends on the number of blades and can be given as

$$\chi_{\text{tuned}} = \frac{\hat{x}_{i,\max}}{RMS_{\text{tuned}}} = \sqrt{2} \quad (2.5)$$

which is valid for $1 \leq CSM \leq CSM_{\max}$ if N is odd and for $1 \leq CSM < CSM_{\max}$ if N is even. For the rest of the modes ($CSM = 0$ and $CSM = CSM_{\max}$ if N is even) the ratio is determined to

$$\chi_{\text{tuned}} = \frac{\hat{x}_{i,\max}}{RMS_{\text{tuned}}} = 1. \quad (2.6)$$

In the extreme case that only a single blade vibrates the RMS only depends on the displacement of this blade, hence the displacement ratio gives

$$\chi_{\text{mistuned,max}} = \frac{\hat{x}_{i,\max}}{RMS_{\text{mistuned,min}}} = \sqrt{N} \quad (2.7)$$

which apparently only depends on the number of blades. These displacement ratios are used to define the localisation parameter $\psi_{(M)CSM}$ for a particular CSM or MCSM by

$$\psi_{(M)CSM} = \frac{100\%}{\chi_{mistuned,min} - \chi_{tuned}} \left(\chi_{(M)CSM} - \chi_{tuned} \right). \quad (2.8)$$

The localisation parameter is defined in such a way that a tuned CSM has a localisation parameter of $\psi = 0\%$ while the extreme case of only one blade vibrating yields a localisation parameter of $\psi = 100\%$.

Amplification Factor

Another measure of the impact of mistuning on the response of mistuned bladed disks is the amplification factor which correlates the maximum blade displacement of an ODS to the displacement amplitude of the tuned response, it is defined as

$$\nu = \frac{\hat{x}_{mistuned,max}}{\hat{x}_{tuned}}. \quad (2.9)$$

In case of forced responses of mistuned bladed disks, displacement amplifications of more than 100% ($\nu = 2$) can be achieved. The determination of the maximum achievable amplification factor has been the subject matter of a number of studies for which the most significant results have been summarised in Section 1.3.

Mistuning Modeling

In reality, mistuning is a result of several effects such as manufacturing tolerances, material inhomogeneities etc. The implications of these effects are changes in a blade's mass distribution and/or stiffness. The best possibility for the quantification of mistuning is measuring the geometry and using the data to build up high resolution FE-models. However, the disadvantages are the great effort of the measurement campaign and the entailing large number of finite elements. Analyses including extensively numerical computations are not feasible with such models although they give the best physical approximation to real hardware to date. Nevertheless, for studying the global effects of mistuning, mass and stiffness of a blade can also be directly varied which is the common practice in mistuning analysis today. Different approaches have evolved comprising single point masses to detune blades, changing the material density or perturbation of the mass and stiffness matrix respectively. Within this work the stiffness of the blades is changed by adapting the Young's Modulus of the blades in FE-models and by adjusting the blade stiffness parameters of the lumped mass model. Detailed description of the latter one is given in Chapter 4. Concerning the adaption process of the FE-models to measured mistuning patterns employed in this work, detailed information can be found in the work of Klauke [68], Beirow [7] and Beirow and Kuehhorn [8]. For sake of completeness, the entire method is summarised briefly.

Once a mistuning pattern has been obtained from blade by blade measurements, the experimental procedure is repeated numerically. During the simulations the Young's Modulus and the blade damping of each blade are adapted iteratively to match the measured blade frequency and the amplitude of the frequency response function. With the frequency f_i^n of the i -th blade obtained from a previous iteration step n , the adapted Young's Modulus E_i^{n+1} is calculated by

$$E_i^{n+1} = E_i^n \left(\frac{f_{i,\text{measured}}}{f_i^n} \right)^2 \quad (2.10)$$

with E_i^n representing the Young's Modulus of the previous iteration and $f_{i,\text{measured}}$ being the measured blade frequency. Similarly, the blade damping is adjusted linearly through

$$\zeta_i^{n+1} = \zeta_i^n \left(\frac{\hat{x}_{i,\text{measured}}}{\hat{x}_i^n} \right). \quad (2.11)$$

Using such an updated model, Hoenisch [55] simulated the forced response of a radial turbine rotor with one blade being excited and recording the response of all blades of the assembly. The comparison with laboratory measurements showed satisfactory correlation.

Mistuning at Rotation

Due to the influences of centrifugal forces, coming from rotation, the blade natural frequencies and hence the mistuning pattern will be different from the measured ones. When mistuning is modeled via stiffness variations, the rotational influence and the consecutive frequency change can be determined by an SDOF approximation. The following section presents a method how to derive a mistuning pattern of a rotor undergoing rotation from a mistuning pattern measured at rest. These equations are only valid for mistuning being modeled by changes of the blade stiffness, the blade mass remains constant. The method presented here is similar to the one given by Feiner [30] who achieved reasonable results with his approach.

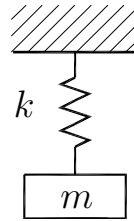


Figure 2.4: SDOF blade model

The idea of the following method is to determine the impact of rotation from the differences of the natural frequencies of the maximum CSM of a tuned FE model of a compressor blisk. The basis are the natural angular frequencies of the maximum CSM of the tuned rotor

at rest $\omega_{\text{CSM}_{\text{max}}}(0)$ and at rotation $\omega_{\text{CSM}_{\text{max}}}(\Omega)$ from FE computations. Assuming a single degree of freedom model as shown in Figure 2.4, the natural frequency at rotation can be written as

$$\omega_{\text{CSM}_{\text{max}}}(\Omega) = \sqrt{\frac{k(0) + \Delta k(\Omega)}{m}}. \quad (2.12)$$

Here, $\Delta k(\Omega)$ is the increase of the blade stiffness due to rotation. We may rewrite Equation 2.12 as

$$\Delta k(\Omega) = \omega_{\text{CSM}_{\text{max}}}^2(\Omega) \cdot m - k(0). \quad (2.13)$$

The result is an equation for the additional stiffness coming from the centrifugal forces which can be further simplified by replacing the blade stiffness at rest with $k(0) = \omega_{\text{CSM}_{\text{max}}}^2(0) \cdot m$ which leads to

$$\Delta k(\Omega) = \underbrace{(\omega_{\text{CSM}_{\text{max}}}^2(\Omega) - \omega_{\text{CSM}_{\text{max}}}^2(0))}_{\Delta \omega^2(\Omega)} \cdot m. \quad (2.14)$$

We can now consider a single mistuned blade i whose natural angular frequency is defined analogously to Equation 2.12 as

$$\omega_i(\Omega) = \sqrt{\frac{k_i(0) + \Delta k(\Omega)}{m}}. \quad (2.15)$$

Substituting the additional stiffness due to rotation $\Delta k(\Omega)$ with Equation 2.14 we finally obtain an equation for the determination of the natural angular frequency of the i -th blade of a mistuned rotor undergoing rotation with

$$\omega_i(\Omega) = \sqrt{\omega_i^2(0) + \omega_{\text{CSM}_{\text{max}}}^2(\Omega) - \omega_{\text{CSM}_{\text{max}}}^2(0)}. \quad (2.16)$$

The above equation bases on the natural angular frequency of a mistuned blade at rest $\omega_i(0)$ which is known from blade-by-blade measurements. Exemplarily, Figure 2.5 presents the comparison of FE-results in terms of relative frequency deviation defined through

$$\Delta \omega_{i,\text{mistuned}} = \frac{\omega_{i,\text{mistuned}} - \omega_{\text{tuned}}}{\omega_{\text{tuned}}} \quad (2.17)$$

of a mistuned blisk at rest and undergoing rotation with the results obtained from Equation 2.16. The mistuned blisk is the same front stage HPC blisk which is analysed in Chapter 6

and the blade mode displayed is the first flap mode (mode 1). The frequencies shown in the chart represent blade alone frequencies ($\omega_i(0)$ and $\omega_i(\Omega)$). For the example of a first flap mode, the results correlate very well. Furthermore, a considerable mitigation of the frequency deviations is observed for this first flap mode when centrifugal loading due to rotation is considered. The results of the application of this approximation to the rest of the considered blade modes is presented in Appendix B.

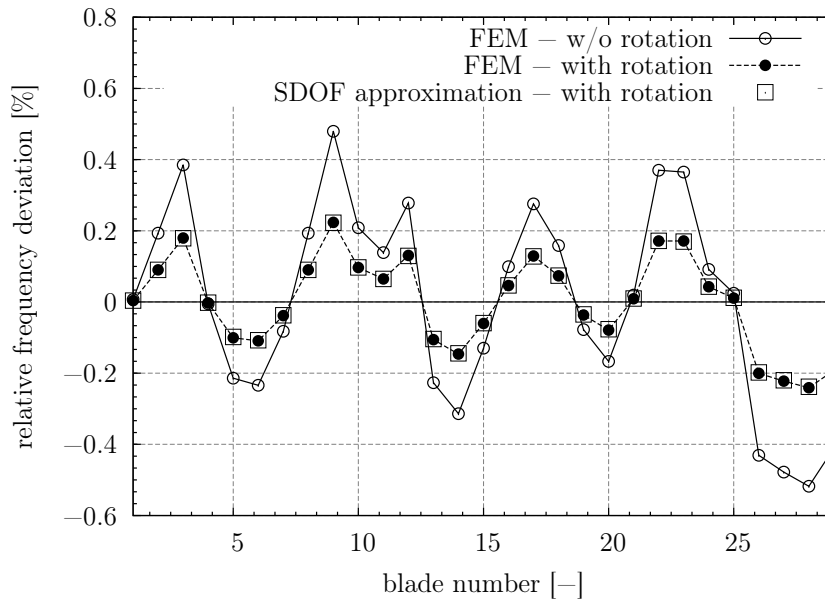


Figure 2.5: Comparison of mistuning patterns at rest and at rotation - E3E R1 / mode 1

2.3 Aeroelasticity in Compressors

The topic of aeroelasticity is a subsection of fluid structure interaction (FSI) which focuses on the interaction of aerodynamic, elastic and inertial forces. The scope of this section is not an extensive presentation of aeroelasticity in large but rather a brief introduction of selected topics touching the present work. However, there are a lot of comprehensive publications in the open literature such as the books of Foersching [35] and Dowell [24] or the article of He [51] and many others which give an insight into the basics of aeroelasticity.

In principle the causes of aeroelastic blade vibrations can be divided into self-excited (blade flutter) and forced vibrations which are going to be highlighted shortly.

2.3.1 Blade Flutter

Flutter is a self-excited aeroelastic instability arising due to aerodynamic or mechanical disturbances. The reasons for flutter to occur may be due to aerodynamic instabilities such as

vortex shedding, flow separation, shock movement etc. or the result of mechanical vibrations. Concerning the aerodynamic instabilities, periodically varying aerodynamic forces coming from the aforementioned aerodynamic phenomena may induce mechanical vibrations in the natural frequencies of the blades at small amplitudes. In turn, these small amplitudes may lead to worsening of the aerodynamic effects and hence to an increase of the unsteady aerodynamic forces. Depending on the phasing of these forces with regard to the mechanical vibration and the amount of mechanical damping an amplification of the blade vibration amplitudes may be initiated leading to blade loading far from sustainable endurance levels.

The prediction of flutter in numerical simulations requires the determination of the aeroelastic parameters, meaning the aerodynamic damping ζ_a and the aeroelastic frequency ω_a . Naturally these aeroelastic parameters are depending on the aerodynamic conditions, the geometry of the blades, the blade mode shape and the CSM which is considered. In this respect, according to He [51] one of the most important parameters for aeroelastic problems is the reduced frequency

$$\omega^* = \frac{\omega \cdot c}{|\mathbf{u}_1|}. \quad (2.18)$$

Here ω is the structural angular frequency, c is the chord length and $|\mathbf{u}_1|$ is the magnitude of the inlet velocity. According to Vogt [115] the reduced frequency can be interpreted as the relation of the time a fluid particle needs to be convected along one chord length to the time scale of the unsteadiness. In practice it has been observed that the susceptibility to blade flutter increases with decreasing reduced frequency. In other words, every blade cascade features a specific value of reduced frequency below which it will run into flutter problems. In order to find the flutter boundary the inlet flow velocity can be increased for a given structural angular frequency or the vibration frequency can be reduced at constant flow conditions, as has been done by Hennings [53] or Belz and Hennings [10]. However, the values of critical reduced frequency reported in the literature have to be handled with care since they are of purely empirical nature.

Concerning the determination of the aeroelastic parameters, three principle methods are available:

1. Bidirectionally Coupled Simulations

The numerical solution of the equations of motion of a bladed assembly with simultaneous consideration of the aerodynamic forces computed by CFD in the time domain is termed bidirectionally coupled FSI simulation. Concerning the coupling algorithms a differentiation can be made between the weak or explicit coupling where the data exchange is performed only once per time step, and the strong or implicit coupling where the data exchange is performed iteratively until an equilibrium state is achieved in each time step. However, the computations can be performed for each mode shape of

the assembly separately giving the blades appropriate initial boundary conditions and the aeroelastic parameters can be directly determined from the free blade response in the flow. The aerodynamic damping can be obtained from the logarithmic decrement Λ of the blade displacement

$$\Lambda = \frac{1}{n_{\text{cycles}}} \ln \frac{x(t)}{x(t + n_{\text{cycles}}T)} = \frac{2\pi\zeta_a}{\sqrt{1 - \zeta_a^2}}. \quad (2.19)$$

For moderate values of aerodynamic damping ($\zeta_a < 0.3$) the above equation may be linearised to obtain the aerodynamic damping

$$\zeta_a \approx \frac{\Lambda}{2\pi}. \quad (2.20)$$

Furthermore, the aeroelastic frequency can be determined by curve fitting methods for example. Another possibility is to give all blades initial boundary conditions which excite all modes equally. As a result, only the unstable modes will remain in the simulation allowing for a determination of the unstable modes, see Carstens and Belz [17] for an example.

Bidirectionally coupled FSI simulations advantage a complete consideration of all nonlinearities in the flow field while its main disadvantage is the immense demand for computational resources. This brief introduction can not cover all details about bidirectionally coupled FSI simulations, for further information refer to Kemme [63], Schrape et al. [102] or Belz [11].

2. Energy Method

The energy method presented by Carta [18] features a simplification of the bidirectional coupling method. If the mass ratio

$$\mu = \frac{2m_{\text{blade}}}{\rho hc^2} \quad (2.21)$$

which relates the blade mass to a representative fluid volume that is influenced by the blade oscillation, is high enough, the impact of the aerodynamics on the natural frequencies and blade mode shape can be neglected. Hence, in simulations the coupling of the fluid forces with the motion of the blades can be disregarded. The result is an unidirectional coupling which only considers the influence of the blade displacement on the unsteady aerodynamics. Consequently, for a given blade displacement amplitude the logarithmic decrement can be determined from

$$\Lambda = -\frac{W_{\text{a,cycle}}}{2E_{\text{kin,max}}}. \quad (2.22)$$

Here $W_{a,cycle}$ is the work done by the fluid forces on the blade surface during one vibration cycle and $E_{kin,max}$ is the maximum kinetic energy of the blade. The appendant aerodynamic damping can be calculated from Equation 2.20. By definition, a positive value of the aerodynamic work results in negative damping therefore flutter and increasing blade amplitudes while negative work yields damped blade vibrations.

3. Determination of Aeroelastic Eigenvalues

The prediction of flutter with aeroelastic eigenvalues involves a suitable determination of aerodynamic force coefficients and the solution of the aeroelastic eigenvalue problem. Detailed information about this topic is given in Chapter 3.

Impact of Mistuning

As already described in Section 2.2 when mistuning is introduced, the cyclic symmetry of the system gets lost and the eigenvalues of the double modes split up. Concerning the flutter behaviour of bladed disks and blisks, mistuning is agreed to increase the aeroelastic stability by increasing the least aerodynamic damping values as could be shown by Srinivasan [109], Campobasso and Giles [16], Kahl [61] and others. With probabilistic analyses Kielb et al. [67] were able to show a consequent increase of the damping of the least stable mode with enlarging standard deviation of frequency mistuning. Furthermore, Kahl investigated the so called alternate mistuning where all odd numbered blades feature identical frequencies different from the ones exhibited by all even blades which brought the biggest gain in aeroelastic stability.

2.3.2 Forced Response

On the contrary to the self-induced vibrations connected with the flutter phenomenon, forced vibrations can occur due to potential interaction with downstream blade rows or wakes of upstream blades. Especially the wakes may force the blades of the downstream blade row into vibrations with significant amplitudes potentially leading to HCF fatigue if the frequency of the excitation coincides with a natural frequency of a blade mode. Additionally, the wakes coming from blade rows further upstream may combine to yield excitation orders different from the actual blade numbers. In order to check potential areas of excitation the so called Spokes- or Campbell Diagram is usually constructed for a considered blade row as exemplarily shown in Figure 2.6⁴. The lines radiating out from the origin are the so called engine orders (EO) of the excitation, meaning the number of blades in the upstream blade rows or combinations of potential excitations. To these potential excitation mechanisms also

⁴The influences of temperature and rotation on the blade frequencies as well as the dependency on CSM are neglected.

belong to the so called low engine order excitations (LEO). These are excitations of orders up to 3 which may arise from compressor inlet distortions, gust winds etc. As already mentioned, forced response occurs if the angular frequency of the excitation coincides with a natural frequency of a blade which is the case if

$$\omega_{\text{blade}} = \Omega_{\text{EO}} = EO \cdot NH \quad (2.23)$$

with Ω_{EO} being the angular frequency of the excitation.

Furthermore, the blade assembly will not only respond in the frequency of the excitation but also in the CSM corresponding to the spatial pattern of the excitation. As intimated in the preceding section, the aerodynamic damping depends on the CSM which results in different blade amplitudes depending on the engine order of the excitation even if the forcing amplitude is the same. Since the maximum number of CSM depends on the number of blades an excitation with $EO > CSM_{\text{max}}$ seems not feasible. However, in case of engine orders greater than the maximum CSM the excitation will be aliased and the system will respond in a lower CSM travelling in the opposite direction. The entire problem can be best demonstrated with the help of a little example.

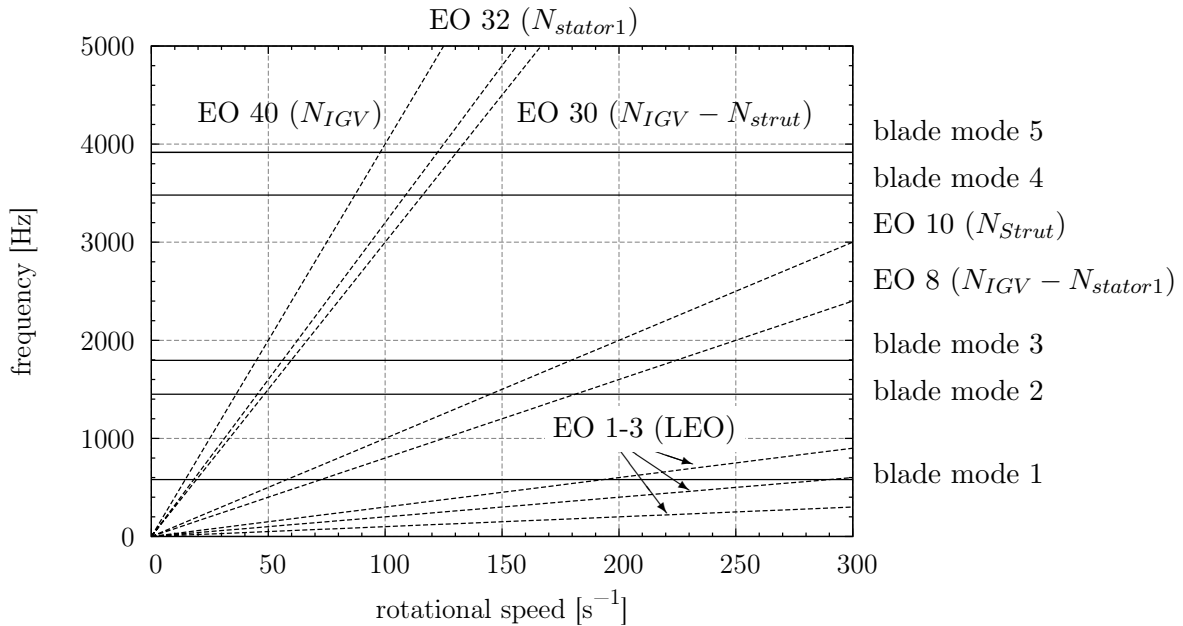


Figure 2.6: Campbell diagram with potential engine order excitations - E3E rotor 1 stage

Consider a rotor with N_{rotor} blades and an upstream stator row with variable number of vanes N_{stator} which acts as the source of excitation, hence $EO = N_{\text{stator}}$. The maximum CSM can be calculated from Equations 2.2 and 2.3. Under the assumption that the frequency of the forcing coincides with a natural frequency of the blade the excited CSM can be summarised for even and odd blade numbers as given in table 2.1.

Table 2.1: Effect of engine order aliasing

even blade number - $N_{\text{rotor},1}=16$										odd blade number - $N_{\text{rotor},2}=17$								
32	31	30	29	28	27	26	25		FTW	34	33	32	31	30	29	28	27	26
	17	18	19	20	21	22	23	24	BTW		18	19	20	21	22	23	24	25
16	15	14	13	12	11	10	9		FTW	17	16	15	14	13	12	11	10	9
0	1	2	3	4	5	6	7	8	BTW	0	1	2	3	4	5	6	7	8

As example $N_{\text{stator},1} = EO_1 = 7$ and $N_{\text{stator},2} = EO_2 = 9$ are chosen and two different rotor blade numbers are considered, $N_{\text{rotor},1} = 16$ and $N_{\text{rotor},2} = 17$. In case of $N_{\text{stator},1} = EO_1 = 7$, which is smaller than CSM_{max} for both blade numbers, the bladed disk will respond in a 7 nodal diameter shape travelling in the opposite direction to the direction of rotation. When $N_{\text{stator},2} = EO_2 = 9$ is regarded the response will be in a 7 nodal diameter shape travelling into the direction of rotation in case of even blade numbers, while the system will exhibit a 8 nodal diameter pattern in case of odd blade numbers. The aliasing effect is different for odd and even blade numbers which is due to the single standing mode in case of even blade numbers.

Impact of Mistuning

It has previously been explained in Section 2.2 that mistuning introduces additional diametral content to the CSM. As a consequence not only one MCSM will respond to a particular engine order excitation but all those MCSM will be excited which have modal content corresponding to the EO of the excitation. The loss of symmetry also leads to different phase angles between adjacent blades and hence different amounts of aerodynamic damping. As a result, the maximum blade response due to external forcing observed in a mistuned case may be significantly higher than in the tuned case which can be quantified with the amplification factor, Equation 2.9. However when aerodynamic forces are considered, significant mitigation of blade displacement amplification and localisation can be observed, see Kaza and Kielb [62] or Petrov [93] for example.

At this, the manner in which the aerodynamic forces are considered determines the quality of the results. In practical applications or due to lack of appropriate methods it has been and still is a common practice to use the tuned values of aerodynamic damping in combination with safety factors for the assessment of mistuned bladed disk and blisk vibrations. This practice is not only unable to capture some essential effects of mistuned blade vibrations in gas flows but it is also over-conservative obstructing enhanced compressor design. A more precise consideration has shown that the aerodynamic forces have the potential to mitigate the maximum blade response well below the tuned one. On the other hand, amplification factors significantly higher than those obtained with constant aerodynamic damping can also occur. In this respect Kahl [61] has been the first who gained an attenuation below

the tuned response which he achieved with alternate mistuning and comparatively large frequency deviations. Just recently Petrov [92] has obtained similar results with random mistuning patterns employing a reduced order model. For a detailed discussion of the effects on free and forced vibrations arising from mistuning see also Section 1.3.

Chapter 3

Aeroelastic Methods

The following chapter presents a method for the solution of aeroelastic problems in turbomachinery applications. For a complete description of the aeroelastic problem a structural dynamic model, a kinematic description of the blade motion and an aerodynamic model representing the fluid forces are needed. As a result, an aeroelastic equation of motion is obtained which allows for the determination of the aeroelastic eigenvalues. Furthermore the aerodynamic model presented in this chapter founds the basis for the inclusion of aerodynamic forces in the equivalent blisk model presented in Chapter 4.

3.1 Dynamic Model of Blade Vibrations

The starting point is the most general equation of motion for the i -th blade of a bladed disk which is mechanically uncoupled from the rest of the blades. At this point an infinitely stiff disk has been assumed which restricts the considerations to the blade vibrations only, neglecting potential contributions from disk vibrations.

$$\mathbf{M}_i \ddot{\mathbf{x}}_i(t) + \mathbf{K}_i \mathbf{x}_i(t) = \mathbf{F}_i^A(t) = \mathbf{F}_i^V(t) + \mathbf{F}_i^F(t). \quad (3.1)$$

Because of the low material damping of blisks and its low impact on the blade vibrations the damping term in Equation 3.1 has already been dropped. The forces on the right-hand side of the equation are the aerodynamic forces $\mathbf{F}_i^A(t)$ due to blade vibration $\mathbf{F}_i^V(t)$ and those coming from the forcing $\mathbf{F}_i^F(t)$ which may have various origins. Naturally, the interaction of these forces may be non-linear but under the supposition of small vibration amplitudes a linear superposition is sufficient which is a common simplification also employed by Schmitt [100], Kemme [63], Duta [26] and many others. The segregated consideration of the fluid forces allows to address the different aeroelastic problems individually. By setting

$\underline{\mathbf{F}}_i^F(t) = 0$ flutter analyses can be conducted involving the determination of the aeroelastic parameters and stability margins. On the contrary when $\underline{\mathbf{F}}_i^V(t)$ is set to zero forced response analyses in the absence of aerodynamics can be performed. Furthermore, both effects can be studied simultaneously enabling investigations of the aerodynamics' influence on forced blade vibrations.

The solution of Equation 3.1 is assumed to be of complex exponential type and can be written as

$$\underline{\mathbf{x}}_i(t) = \hat{\mathbf{x}}_i \cdot e^{\lambda_i t} \quad (3.2)$$

with $\lambda_i = -\delta_i + j\omega_i$ being the eigenvalue of the i -th blade. By setting the fluid forces to zero and since the mechanical damping has already been dropped ($\delta_i = 0$), the homogeneous eigenvalue problem can be set up as

$$\{ \mathbf{K}_i + \lambda_i^2 \mathbf{M}_i \} \hat{\mathbf{x}}_i = \mathbf{0}. \quad (3.3)$$

The solution of Equation 3.3 yields the N in-vacuo eigenvalues $\lambda_{i,n} = j\omega_{i,n}$ and mode shapes $\Phi_{i,n}$ of an isolated blade in the absence of aerodynamic forces. With the help of this mode shape, Equation 3.1 can be transformed to modal space with the modal coordinate $\underline{q}_{i,n}(t)$ of the mode shape under investigation through

$$\underline{\mathbf{x}}_{i,n}(t) = \Phi_{i,n} \cdot \underline{q}_{i,n}(t) \quad (3.4)$$

yielding

$$\mathbf{M}_i \Phi_{i,n} \ddot{\underline{q}}_{i,n}(t) + \mathbf{K}_i \Phi_{i,n} \underline{q}_{i,n}(t) = \underline{\mathbf{F}}_i^A(t) = \underline{\mathbf{F}}_i^V(t) + \underline{\mathbf{F}}_i^F(t). \quad (3.5)$$

This modal model of a blade possesses the so called *orthogonality properties* which can be stated as follows

$$\Phi_{i,n}^T \mathbf{M}_i \Phi_{i,k} = \begin{cases} m_{g,n} & \text{for } n = k \\ 0 & \text{for } n \neq k \end{cases} \quad \text{and} \quad \Phi_{i,n}^T \mathbf{K}_i \Phi_{i,k} = \begin{cases} k_{g,n} & \text{for } n = k \\ 0 & \text{for } n \neq k \end{cases} \quad (3.6)$$

in which $m_{g,n}$ is the modal mass and $k_{g,n}$ the modal stiffness of the n -th mode shape respectively. These modal values are not universal since they depend on the scaling of the

mode shapes. However it is found that the ratio of modal stiffness and mass is unique, it equals $\omega_{i,n}^2 = k_{g,n}/m_{g,n}$. A further simplification of the modal model can be achieved by mass normalisation of the mode shape by

$$\Psi_{i,n} = \frac{\Phi_{i,n}}{\sqrt{m_{g,n}}}. \quad (3.7)$$

As a result of the mass normalisation process the orthogonality properties become

$$\Psi_{i,n}^T \mathbf{M}_i \Psi_{i,n} = \mathbf{I} \quad \text{and} \quad \Psi_{i,n}^T \mathbf{K}_i \Psi_{i,n} = \omega_{i,n}^2 \quad (3.8)$$

with \mathbf{I} being the identity matrix.

The equations of motion of the single blades with the natural angular undamped frequencies $\omega_{i,n}$ with the corresponding mode shapes $\Psi_{i,n}$ can now be combined in a single modal equation

$$\begin{pmatrix} \ddot{\underline{q}}_{0,n}(t) \\ \vdots \\ \ddot{\underline{q}}_{i,n}(t) \\ \vdots \\ \ddot{\underline{q}}_{N-1,n}(t) \end{pmatrix} + \begin{bmatrix} \omega_{0,n}^2 & 0 & \dots & 0 \\ 0 & \ddots & & \vdots \\ \vdots & & \omega_{i,n}^2 & \\ 0 & \dots & 0 & \omega_{N-1,n}^2 \end{bmatrix} \begin{pmatrix} \underline{q}_{0,n}(t) \\ \vdots \\ \underline{q}_{i,n}(t) \\ \vdots \\ \underline{q}_{N-1,n}(t) \end{pmatrix} = \underbrace{\begin{pmatrix} \Psi_{0,n}^T \\ \vdots \\ \Psi_{i,n}^T \\ \vdots \\ \Psi_{N-1,n}^T \end{pmatrix}}_{\underline{\mathbf{f}}_n = \{\underline{f}_{i,n}\}} \begin{pmatrix} \underline{\mathbf{F}}_0^A(t) \\ \vdots \\ \underline{\mathbf{F}}_i^A(t) \\ \vdots \\ \underline{\mathbf{F}}_{N-1}^A(t) \end{pmatrix} \quad (3.9)$$

in which $\underline{\mathbf{f}}_n(t)$ is the vector of the modal aerodynamic forces. The result is a modal equation of individual blade motion with the right hand side representing influences of aerodynamic forces which is valid for tuned ($\omega_i = \omega_{\text{tuned}}$) and mistuned systems. However in this form, the aerodynamic forces are still unknown and the blades are mechanically and aerodynamically uncoupled.

3.2 Aerodynamic Model for Aerodynamically Coupled Blade Vibrations

For the presentation of the aerodynamic model only the aerodynamic forces due to vibration of the blades are of interest and the excitation forces are set to zero, $\underline{\mathbf{F}}_i^F(t) = 0$. If the remaining aerodynamic forces due to vibration of the blades are taken to be known then the

modal displacements of Equation 3.9 are still uncoupled. However, the modal aerodynamic force $\underline{f}_i(t) = \underline{\Psi}_i^T \underline{F}_i^V(t)$ of the i -th blade vibrating in a particular mode shape¹ is not only depending on the vibration of the particular blade itself but also on the vibration of the neighbouring ones which is summarised in the most general form in Equation 3.10. In fact, there are various influences on the fluid forces. Apart from the parameters of the blade movement like displacement $\underline{q}_i(t)$, velocity $\underline{\dot{q}}_i(t)$ and acceleration $\underline{\ddot{q}}_i(t)$ and geometric influences also the flow conditions effect the modal forces. The values of mach number, reduced frequency and speed of sound clearly have an influence on the propagation of disturbances coming from the blade vibration and hence on the modal forces. All these effects are taken account of by the variable $\beta_i(t)$. According to Crawley [22] only the relative distance between the blade under consideration and the neighbouring blades is of interest. Exemplarily Equation 3.10 represents the modal force acting on the i -th blade of the blade assembly as the sum of the influence of the vibrating blade exerting on itself $\underline{f}_{i=0}(t)$ and the influences coming from the direct suction side $\underline{f}_{N-1}(t)$ and pressure side neighbour $\underline{f}_1(t)$ respectively.

$$\begin{aligned} \underline{f}_{i=0}(t) &= \underline{f}_0(\underline{q}_0(t), \underline{\dot{q}}_0(t), \underline{\ddot{q}}_0(t), \beta_0(t)) \\ &+ \underline{f}_1(\underline{q}_1(t), \underline{\dot{q}}_1(t), \underline{\ddot{q}}_1(t), \beta_1(t)) \\ &+ \underline{f}_{N-1}(\underline{q}_{N-1}(t), \underline{\dot{q}}_{N-1}(t), \underline{\ddot{q}}_{N-1}(t), \beta_{N-1}(t)) \\ &+ \dots \end{aligned} \quad (3.10)$$

The idea of linearly combining the influences from neighbouring, vibrating blades is called aerodynamic influence coefficient (AIC) technique and has been introduced by Hanamura et al. in 1980 [48].

The physical interpretation of the influence coefficients is shown in Figure 3.1. The vibration of a single blade, the reference blade $i = 0$, induces changes in the flow field which lead to unsteady fluid forces on the reference blade itself ($\hat{\underline{L}}_0$) as well as on the blades adjacent to the suction side $\hat{\underline{L}}_{+n}$ and to the pressure side $\hat{\underline{L}}_{N-n}$ of the reference blade. The motion of the reference blade can be of arbitrary type which is indicated by $\underline{\Psi}$. On the supposition that the unsteady fluid forces are depending linearly on the blade amplitude, not only single mode shapes can be considered but also the superposition of several different ones. Therefore, so called inter-mode influence coefficients have to be determined as done by Kahl [61] for example. The focus of this work is on the analysis of a single family of modes with neighbouring modes being clearly separated from each other. In the case that all blades vibrate at a time, the influences displayed in Figure 3.1 superpose on each blade i of the assembly to the relevant modal force $\underline{f}_i(t)$. As a result the right-hand side of Equation 3.9 can be rewritten as follows

¹For reasons of clarity and comprehensibility the derivation of the equations is restricted to a single mode shape with the index being left out $\underline{\Psi}_n = \underline{\Psi}$.

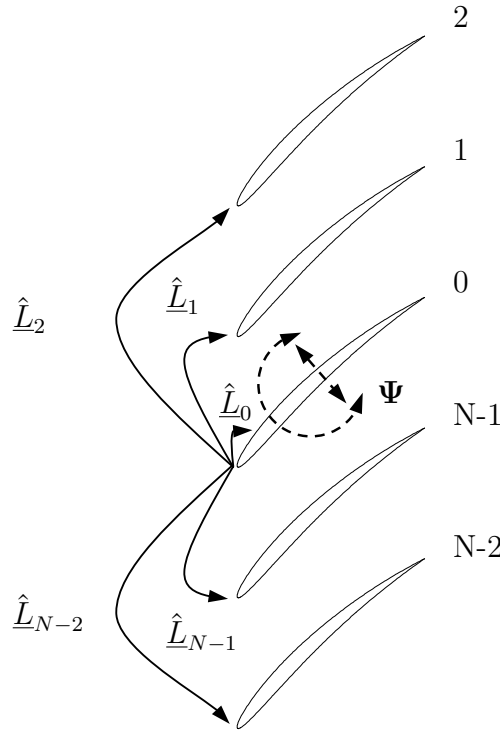


Figure 3.1: Idea of Aerodynamic Influence Coefficients

$$\{f_i(t)\} = \underbrace{\begin{bmatrix} \hat{L}_0 & \hat{L}_{N-1} & \cdots & \hat{L}_1 \\ \hat{L}_1 & \hat{L}_0 & \hat{L}_{N-1} & \cdots \\ \cdots & \hat{L}_1 & \hat{L}_0 & \hat{L}_{N-1} \\ \hat{L}_{N-1} & \cdots & \hat{L}_1 & \hat{L}_0 \end{bmatrix}}_{\hat{\underline{L}}} \begin{Bmatrix} q_0(t) \\ \vdots \\ q_i(t) \\ \vdots \\ q_{N-1}(t) \end{Bmatrix}. \quad (3.11)$$

Here $\hat{\underline{L}}$ is a complex, circulant matrix containing the influence coefficients. This matrix is not symmetric due to different influences on pressure and suction side neighbours. Equation 3.11 gives a vivid description of how the influence coefficients work. Considering the reference blade $i = 0$ once again, the vibration of blade $i = 1$ activates the influence coefficient \hat{L}_{N-1} which represents the fluid force coming from the closest suction side neighbour (see also Figure 3.1). One peculiarity which is worth to be mentioned is the consequently stabilising influence coming from \hat{L}_0 shown by Crawley and Hall [23]. In other words, a single vibrating blade in gas flow will always be damped by the fluid forces induced by its own vibration.

The determination of the influence coefficients can be done in experiments, see Vogt [115] for example, or in simulations, see e.g. Kahl [61], by letting the reference blade vibrate while recording the modal forces on the neighbouring blades simultaneously. The equations concerning the determination of the influence coefficients are presented in Section 3.4.

Finally Equation 3.9 can be expressed in matrix notation employing the influence coefficients matrix as given in Equation 3.11

$$\ddot{\underline{q}}(t) + [\text{diag} \{ \omega_i^2 \} - \hat{\underline{L}}] \underline{q}(t) = \mathbf{0}. \quad (3.12)$$

This equation is the most general form of the aeroelastic equation of motion of tuned and mistuned bladed disks vibrating in gas flow. Further simplifications can be introduced for the computation of tuned blade vibrations which are going to be presented in the following section.

3.3 Kinematic Formulation for Tuned Systems

The basis for the computation of aerodynamically coupled turbomachinery vibrations is established with the Equations 3.9 and 3.11. In the following, these equations are transferred to travelling wave mode coordinates which are the relevant vibrations of tuned rotors as described in Section 2.1. Starting from the dynamic model according to Equation 3.9 and using a representation of the aerodynamic influences that is depending on a kinematic description of the rotor relevant travelling wave mode vibrations, the equation of motions can be decoupled resulting in equations that allow to treat every single travelling wave mode separately. On the contrary to the general description of the blade vibrations in blade individual coordinates as presented in Section 3.2 for mistuned systems, the tuned system exhibits kinematic relationships between the single blade vibrations of an assembly. According to Lane's theorem [73], the vibrations of a blade assembly appearing as travelling wave modes are characterised by a constant interblade phase angle. Following the notation of Crawley [22] the interblade phase angle σ_n ² of the n -th travelling wave mode of an assembly with N blades is defined by

$$\sigma_n = \frac{2\pi \cdot n}{N}, \quad n = 0, 1, \dots, N - 1. \quad (3.13)$$

In case of $n = 0$, or $n = N/2$ in case of even blade numbers, the resulting interblade phase angles $\sigma_0 = 0^\circ$ and $\sigma_{N/2} = 180^\circ$ are those of the corresponding standing waves. With the help of σ_n a kinematic relation between the displacement of the i -th blade and the modal displacement of the n -th mode involved in the vibration of the assembly can be given with

$$q_i(t) = \left\{ \sum_{n=0}^{N-1} \hat{q}_{\sigma_n} e^{j(\omega t + i \cdot \sigma_n)} \right\}_{\text{Re}}. \quad (3.14)$$

²Throughout this work the index n is used for the presentation of the general relations while it is dropped when specific values of σ are given.

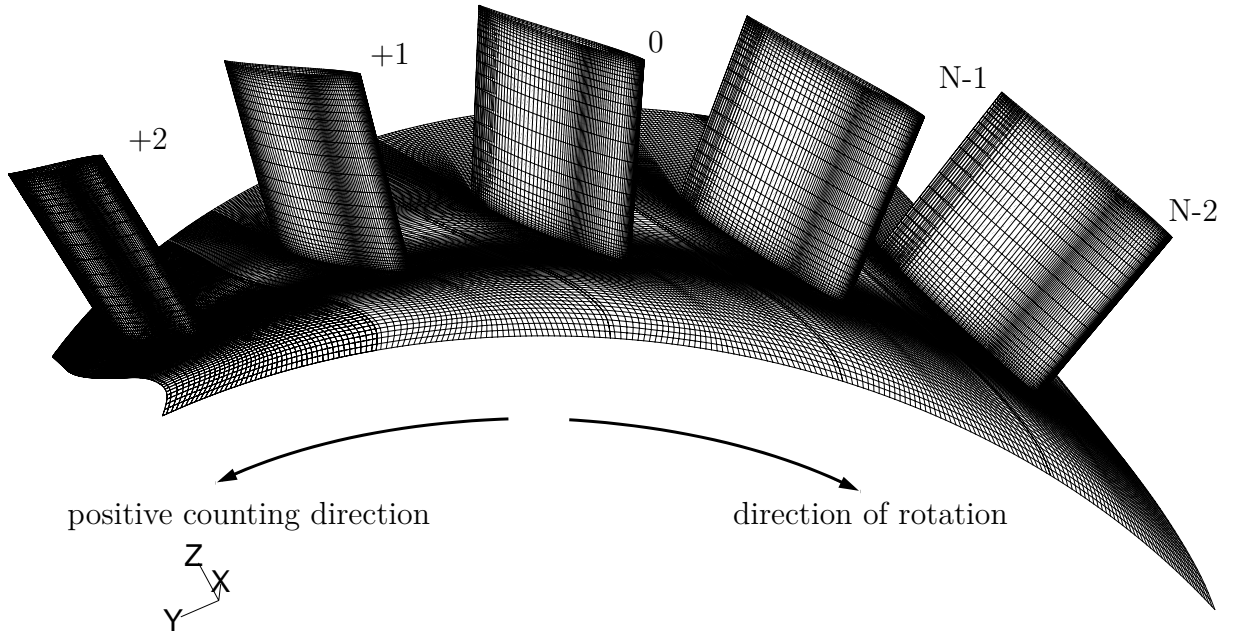


Figure 3.2: Annular cascade of the Standard Configuration 10

Here \hat{q}_{σ_n} is the amplitude and σ_n the interblade phase angle of the n -th mode participating in the vibration. As a consequence of this kinematic relationship and due to counting the blades in the opposite direction to the direction of rotation (Figure 3.2) positive interblade phase angles result in forward travelling waves (FTW) and negative ones in backward travelling waves (BTW) respectively. With the help of the interblade phase angle, Equation 3.12 which represents the aeroelastic equation of motion in blade individual coordinates where the blades are coupled through influence coefficients can be transformed into travelling wave mode coordinates $q_{\sigma_n}(t)$. First, the blade individual coordinates of the entire bladed assembly can be written as a function of the travelling wave mode coordinates employing the kinematic relation 3.14 as

$$\underline{\mathbf{q}}(t) = \{q_i(t)\} = \underbrace{\begin{bmatrix} \hat{E}_{0,0} & \cdots & \hat{E}_{0,N-1} \\ \vdots & & \vdots \\ \hat{E}_{i,0} & \cdots & \hat{E}_{i,N-1} \\ \vdots & & \vdots \\ \hat{E}_{N-1,0} & \cdots & \hat{E}_{N-1,N-1} \end{bmatrix}}_{\underline{\mathbf{E}}} \begin{Bmatrix} \hat{q}_{\sigma_0} \\ \vdots \\ \hat{q}_{\sigma_{N-1}} \end{Bmatrix} e^{j\omega t} \quad (3.15)$$

with $\underline{\mathbf{E}}$ being a complex matrix containing the exponential terms $\hat{E}_{k,l} = e^{j\frac{2\pi kl}{N}}$ of Equation 3.14 needed for the transformation from travelling wave mode to blade individual coordinates. Taking this kinematic relationship, the correlation of the travelling wave mode coordinate of a particular interblade phase angle σ_n and the corresponding modal force $\underline{f}_{\sigma_n}(t)$ reads

$$\underline{f}_{\sigma_n}(t) = \hat{\underline{C}}_{\sigma_n} \cdot \underline{q}_{\sigma_n}(t) \quad (3.16)$$

with $\hat{\underline{C}}_{\sigma_n}$ being the complex travelling wave mode coefficient of the n -th mode. The equation above is analogous to Equation 3.11 which is the general description for tuned and mistuned systems. The transformation of the travelling wave mode coefficients into blade individual aerodynamic influence coefficients and vice versa can be done via complex Fourier transformation

$$\hat{\underline{L}}_i = \frac{1}{N} \sum_{n=0}^{N-1} \hat{\underline{C}}_{\sigma_n} e^{j\frac{2\pi in}{N}} \quad (3.17)$$

and

$$\hat{\underline{C}}_{\sigma_n} = \sum_{i=0}^{N-1} \hat{\underline{L}}_i e^{-j\frac{2\pi in}{N}}. \quad (3.18)$$

With the kinematic relation of Equation 3.15 and the formulation for modal forces of travelling wave modes 3.16 the equation of motion given by Equation 3.9 can be decoupled yielding an equation of motion in travelling wave mode coordinates as

$$\begin{Bmatrix} \ddot{\underline{q}}_{\sigma_0}(t) \\ \vdots \\ \ddot{\underline{q}}_{\sigma_n}(t) \\ \vdots \\ \ddot{\underline{q}}_{\sigma_{N-1}}(t) \end{Bmatrix} + \begin{bmatrix} \omega_{\sigma_0}^2 & 0 & \dots & 0 \\ 0 & \ddots & & \vdots \\ \vdots & & \omega_{\sigma_n}^2 & \\ 0 & \dots & 0 & \ddots & 0 \\ 0 & \dots & 0 & \omega_{\sigma_{N-1}}^2 \end{bmatrix} \begin{Bmatrix} \underline{q}_{\sigma_0}(t) \\ \vdots \\ \underline{q}_{\sigma_n}(t) \\ \vdots \\ \underline{q}_{\sigma_{N-1}}(t) \end{Bmatrix} = \begin{Bmatrix} \underline{f}_{\sigma_0}(t) \\ \vdots \\ \underline{f}_{\sigma_n}(t) \\ \vdots \\ \underline{f}_{\sigma_{N-1}}(t) \end{Bmatrix}, \quad (3.19)$$

with

$$\begin{Bmatrix} \underline{f}_{\sigma_0}(t) \\ \vdots \\ \underline{f}_{\sigma_n}(t) \\ \vdots \\ \underline{f}_{\sigma_{N-1}}(t) \end{Bmatrix} = \underbrace{\begin{bmatrix} \hat{\underline{C}}_{\sigma_0} & 0 & \dots & 0 \\ 0 & \ddots & & \vdots \\ \vdots & & \hat{\underline{C}}_{\sigma_n} & \\ 0 & \dots & 0 & \ddots & 0 \\ 0 & \dots & 0 & \hat{\underline{C}}_{\sigma_{N-1}} \end{bmatrix}}_{\underline{C}} \begin{Bmatrix} \underline{q}_{\sigma_0}(t) \\ \vdots \\ \underline{q}_{\sigma_n}(t) \\ \vdots \\ \underline{q}_{\sigma_{N-1}}(t) \end{Bmatrix}. \quad (3.20)$$

Finally the aeroelastic equation of motion in travelling wave mode coordinates can be written in tensor notation

$$\ddot{\mathbf{q}}_{\sigma}(t) + [\text{diag} \{ \omega_{\sigma_n}^2 \} - \hat{\mathbf{C}}] \mathbf{q}_{\sigma}(t) = \mathbf{0}. \quad (3.21)$$

Equation 3.19 is the so called flutter equation with $\hat{\mathbf{C}}$ being a diagonal matrix that contains the travelling wave mode coefficients. The equation consists of N decoupled equations for the N travelling wave modes of a bladed assembly. The representation in travelling wave mode coordinates is the most suitable as it describes the assembly vibrations of a tuned system as they actually appear while the formulation in blade individual coordinates allows to take care of every blade vibration separately. However, for tuned systems both formulations give identical results.

3.4 Determination of Force and Moment Coefficients

In the previous sections the usage of force coefficients for the formulation of aeroelastic equations of motion in blade individual (influence coefficients) and travelling wave mode coordinates (travelling wave mode coefficients) has been presented in detail. The following paragraphs are going to address the determination of the relevant force coefficients. In this context, force coefficients can be considered as proportionality factors between the modal coordinates and the corresponding modal forces. Furthermore, a basic distinction can be made between simple, rigid blade motion and more general, flexible blade deformation. However, all coefficients are derived under the assumption of harmonic blade vibration. In the following paragraphs all force coefficients are denoted by $\hat{\mathbf{C}}_x$ with x referring to type of motion. Naturally, the equations are valid for the determination of the influence coefficients too for which the modal forces on the particular blade are normalised with the vibration amplitude of the reference blade.

3.4.1 Coefficients for Rigid Blade Motion

Rigid blade motion is often used in academic research and may be of translational or rotational type. From here on the translational movements are referred to as heaving motion and the rotational movements as pitching motion respectively.

Heaving Motion

If the direction of heaving is taken to be \mathbf{e}_y , then the unsteady aerodynamic force due to heaving motion can be calculated by integration of the complex local unsteady aerodynamic force over the entire blade surface through

$$\underline{f}(t) = \oint_s \underline{p}(s, t) \mathbf{n}^T(s) \mathbf{e}_y h ds. \quad (3.22)$$

Here $\underline{p}(s, t)$ is the unsteady pressure, $\mathbf{n}(s, t)$ the face normal vector and b the blade span. The unsteady pressure is written as complex value since it harmonically varies with the blade vibration and reaches its maximum time-shifted. The force coefficient needed for the aeroelastic equation of motion can be calculated from the complex modal force amplitude with the corresponding heaving displacement amplitude \hat{y} through

$$\hat{C}_L = \frac{\hat{f}}{\hat{y}}. \quad (3.23)$$

In this form the force coefficient conforms to the complex amplitude of the modal force normalised with the relevant displacement amplitude.

Pitching Motion

When pitching blade motion in one degree of freedom is considered, the aeroelastic equations of motion can be formulated using the blade's moment of inertia and the aerodynamic moment instead. Consequently, moment coefficients are used instead of force coefficients. In contrast to the heaving motion, the moment arm of a point on the blade surface $\{\mathbf{r}(s) - \mathbf{r}_0\}$ is required for the determination of the unsteady aerodynamic moment

$$\underline{M}(t) = \oint_s \underline{p}(s, t) [\{\mathbf{r}(s) - \mathbf{r}_0\} \times \mathbf{n}(s)]^T \mathbf{e}_z h ds \quad (3.24)$$

which is integrated over the entire blade surface to give the global aerodynamic moment which is normalised with the pitching amplitude $\hat{\alpha}$ to yield the moment coefficient

$$\hat{C}_M = \frac{\hat{M}}{\hat{\alpha}}. \quad (3.25)$$

3.4.2 Coefficients for General Motion

The aeroelastic analysis of real blade geometries features flexible blade mode shapes as shown in Figure 2.1. In the previous section the aeroelastic equations of motion have already been defined using modal transformation. The corresponding modal force coefficients are calculated from the unsteady modal force given by

$$\underline{f}(t) = \int_A \underline{p}(t) \underline{\Psi}^T \mathbf{n} dA \quad (3.26)$$

with $\underline{\Psi}$ being the mode shape vector and $\mathbf{n}(t)$ the normal face vector of a blade surface element $dA(t)$. In the equation above the normal face vector and the area of the corresponding blade surface element are explicitly depending on time which is the result of elastic blade deformation. Finally the complex modal force coefficient can be calculated by normalisation of the complex force amplitude with the modal displacement amplitude \hat{q} :

$$\hat{C}_{\Psi} = \frac{\hat{f}}{\hat{q}}. \quad (3.27)$$

3.5 Determination of Aeroelastic Eigenvalues

The basis for the analysis of the aeroelastic stability is founded by equations 3.12 and 3.21. From these the aeroelastic parameters, meaning the aerodynamic damping and the aeroelastic vibration frequency can be obtained by determination of the aeroelastic eigenvalues. The calculation procedure is exemplarily described for the flutter equation 3.21 of tuned systems.

Assuming the solution to be of complex exponential type

$$\underline{q}_{\sigma_n}(t) = \hat{q}_{\sigma_n} e^{\underline{\lambda}_{a,\sigma_n} t} \quad (3.28)$$

with

$$\underline{\lambda}_{a,\sigma_n} = -\delta_{a,\sigma_n} + j\omega_{a,\sigma_n} \quad (3.29)$$

the homogenous, complex eigenvalue problem is defined as

$$\left[\text{diag} \left\{ \underline{\lambda}_{a,\sigma_n}^2 + \omega_{\sigma_n}^2 \right\} - \hat{\underline{C}} \right] \hat{q}_{\sigma_n} = \mathbf{0}. \quad (3.30)$$

Here, $\omega_{\sigma_n}^2$ is the structural vibration frequency and $\underline{\lambda}_{a,\sigma_n}$ is the aeroelastic eigenvalue of the interblade phase angle σ_n with the corresponding decay rate of the damped or excited vibration δ_{a,σ_n} and the aeroelastic angular frequency ω_{a,σ_n} . Since the matrix of travelling wave mode coefficients $\hat{\underline{C}}$ (Equation 3.19) is a diagonal matrix, the equations are decoupled and every travelling wave mode can be regarded separately by

$$\underline{\lambda}_{a,\sigma_n}^2 + \omega_{\sigma_n}^2 - \hat{C}_{\sigma_n} = 0. \quad (3.31)$$

As a result the n -th aeroelastic eigenvalue can be easily determined through

$$\lambda_{a,\sigma_n} = \pm \sqrt{\hat{C}_{\sigma_n} - \omega_{\sigma_n}^2}. \quad (3.32)$$

Since only positive angular frequencies have physical relevance only the solution of 3.32 with positive imaginary part is considered. The aeroelastic parameters can now be determined from the aeroelastic eigenvalue λ_{a,σ_n} . From the general solution of a damped single degree of freedom oscillator the correlation between the structural undamped natural frequency ω_0 and the damped angular frequency ω as well as the damping which is present in the system δ is known to be

$$\omega_0^2 = \delta^2 + \omega^2 \quad (3.33)$$

which can be adapted for the aeroelastic system yielding

$$\omega_{\sigma_n} = \sqrt{\delta_{a,\sigma_n}^2 + \omega_{a,\sigma_n}^2} = \sqrt{\{\lambda_{a,\sigma_n}\}_{\text{Re}}^2 + \{\lambda_{a,\sigma_n}\}_{\text{Im}}^2}. \quad (3.34)$$

Usually the decay rate is much smaller than the aeroelastic frequency ($\delta_{a,\sigma_n}^2 \ll \omega_{a,\sigma_n}^2$). Hence, the aerodynamic damping as ratio of critical damping ζ_{a,σ_n} can be described as

$$\zeta_{a,\sigma_n} = \frac{\delta_{a,\sigma_n}}{\omega_{\sigma_n}} = -\frac{\{\lambda_{a,\sigma_n}\}_{\text{Re}}}{\sqrt{\{\lambda_{a,\sigma_n}\}_{\text{Re}}^2 + \{\lambda_{a,\sigma_n}\}_{\text{Im}}^2}} \approx -\frac{\{\lambda_{a,\sigma_n}\}_{\text{Re}}}{\{\lambda_{a,\sigma_n}\}_{\text{Im}}} \quad (3.35)$$

while the aeroelastic frequency f_{a,σ_n} can be directly calculated from the imaginary part of the aeroelastic eigenvalue by

$$f_{a,\sigma_n} = \frac{\{\lambda_{a,\sigma_n}\}_{\text{Im}}}{2\pi}. \quad (3.36)$$

It has to be emphasised that the preceding equations are only valid for tuned systems where the aeroelastic equation of motion can be decoupled for each interblade phase angle. The determination of the aeroelastic eigenvalues of mistuned systems involves the solution of the homogeneous eigenvalue problem derived from the aeroelastic equation of motion with influence coefficients, Equation 3.12, which can be accomplished with any standard numerical software.

Chapter 4

Equivalent Blisk Model

The equivalent blisk model (EBM), developed by Beirow in 2009 [7], is a surrogate mechanical model that represents the fundamental features of blisk vibration behaviour. The EBM must clearly be seen in contrast to reduced order models (ROM)¹, such as the CMS models [20] or the SNM model [124] which base on finite-element models and which give rise to the possibility of calculating blade displacements quantitatively. Unlike reduced order models, the EBM is made up of lumped masses, springs and dashpots and allows, when properly adapted to hardware, qualitative analyses of the basic effects of mistuned blisk vibration. Due to the fact that the number of DOF is even lower than those of high fidelity reduced order models, sensitivity studies become feasible with comparatively low effort. Nevertheless the analysis is restrained to a single family of modes. In addition to the mechanical properties of blisks also aerodynamic influences can be incorporated which allows to scrutinise the major effects of the aeroelasticity of mistuned blisks. To date, the aerodynamic influences are considered within the EBM by using interblade springs and dashpots, the so called equivalent aerodynamic elements. The original process of parameter identification for these elements is fairly challenging and has been enhanced now.

The scope of this chapter is to give an overview about the wide distribution of lumped mass models, to present the fundamentals of the EBM and to outline the processes of model setup and integration of aerodynamic influences.

4.1 Overview about Lumped Mass Models

A short overview about lumped mass models employed in the open literature has already been given by Beirow [7] and will be repeated here for the sake of completeness.

One of the first to use a lumped mass model was J.T. Wagner [116] who proposed the model shown in Figure 4.1 in 1967. His model included an elastic foundation of a disk without mass

¹A detailed summary of Reduced Order Models can be found in section 1.2.

to take care of the reduction of blade alone frequencies due to the blades being mounted on a flexible disk.

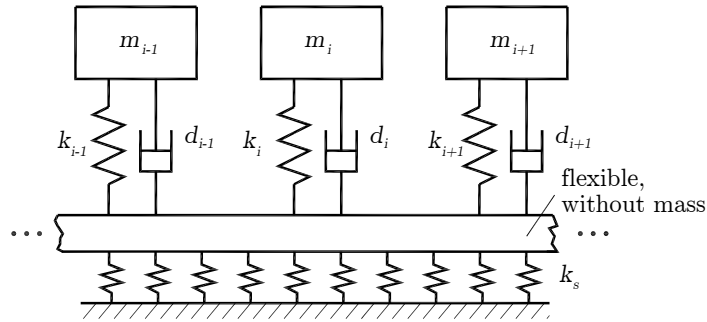


Figure 4.1: Lumped mass model with flexible disk (according to Wagner [116] taken from Beirow [7])

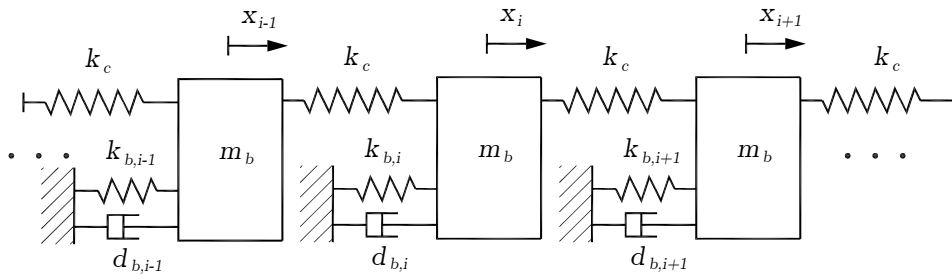


Figure 4.2: Lumped mass model with interblade connectors (according to Sinha [105] taken from Beirow [7])

Another approach is displayed in Figure 4.2. Here the mechanical coupling is considered by interblade spring elements k_c while the structural parameters of each blade are adjusted by springs and dashpots connected to ground. Similar models have been used by Wei and Pierre [117], Sinha and Chen [105], Mignolet et al. [81] or Kenyon et al. [64]. A similar model with a slight extension, in terms of interblade dashpots, has been employed by Lin and Mignolet [76], [80] who studied the influence of damping mistuning on the forced response of mistuned bladed disks.

The model deployed by Happawana et al. [49], shown in Figure 4.3, is almost the same with minimal modifications. Instead of linear spring elements, torsion springs are used as connection to the disk-like basis while the coupling between the discrete blade masses is realised via linear springs as well. This model has been used for the analysis of the effect of small deterministic parameter perturbations on the forced response of nearly periodic systems as a representation of strongly coupled bladed disks.

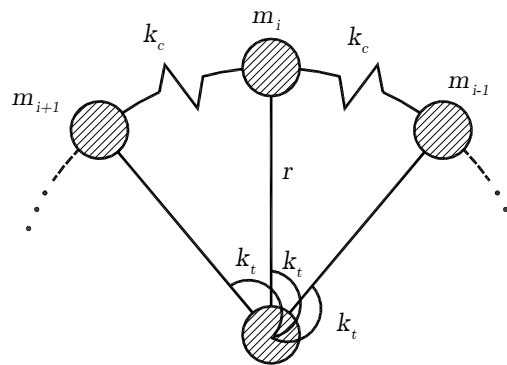


Figure 4.3: Lumped mass model with interblade connectors (taken from Beirrow [7])

More sophisticated models as presented by Griffin and Hoosac [46] and [45] or Ottarson and Pierre [111] employ two or three degrees of freedom per sector. The model given by Griffin and Hoosac [46] uses beam like elements instead of linear springs. In an extended version Griffin also included springs and dashpots between the blade masses to consider aerodynamic forces in the analyses [45]. One of the achievements of his approach was that he was able to compute relative amplitudes which are comparable with those from engine measurements of a fan stage.

Furthermore Basu and Griffin [6] suggested a model which uses a finite-element model of an axisymmetric plate represented by shell elements as disk to which the single degrees of freedom per blade are connected via linear springs. The model also includes aerodynamic forces and was used to study the influence of the fluid density on mistuning effects.

For the purpose of simulating the aeroelastic behaviour of a rotor manufactured from carbon fibre reinforced plastics Kahl [61] used an enhanced version of Sinha's model [105] with aerodynamic influence coefficients included.

In summary, the use of lumped mass models is a common procedure for the analysis of mistuned bladed disks which has been mainly restricted to research purposes. Their ability to give reasonable results has been approved by many researchers. Hence, a lumped mass model was chosen for the analysis of the fundamental vibration behaviour of a mistuned blisk with aerodynamic effects included.

4.2 EBM Fundamentals

On the basis of the aforementioned diversity of lumped mass models, an equivalent blisk model has been developed which comprises two degrees of freedom per blade sector as shown in Figure 4.4. Here the spring, dashpot and mass with the index *sec* represent the disk part of the sector. Additionally, the springs k_c are used to adjust the amount of mechanical

coupling within the disk. And finally the elements with index b are used to adapt the blades' properties to measured data. The next sections present the methodology of setting up the equivalent blisk model and the necessary modifications to consider aerodynamic influences.

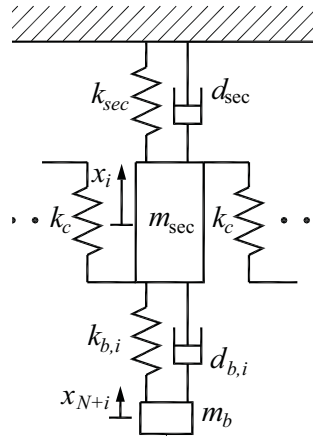


Figure 4.4: EBM blade sector model

4.2.1 Structural Parameter Identification

The adaption of the EBM parameters to the mechanical properties of a test piece comprises two basic steps. These are the assessment of the disk properties and the adaption of the blade parameters to measured mistuning data. The adaption of the blade parameters simultaneously serves as a correction of the measured blade frequencies to yield proper blade alone frequencies. Since the focus of this work is on the simulation of the effects of aeroelasticity on mistuned bladed disks, the measured mistuning patterns rely on the work of Klauke [68], Beirow [7] and Strehlau [110] who describe the methodology of mistuning measurement in detail.

In contrast, the composition of the EBM is an essential part and will be repeated here for reasons of thoroughness. The methodology follows the procedure presented by Beirow [7], its single steps are illustrated in Figure 4.5 and explained in detail in the following paragraphs.

Step 1

The basis of the derivation of disk and blade parameters is founded by FE analyses. First, disk and blades are analysed separately to gain their physical masses m_d and $m_{b,i}$. Since the blade masses are regarded to be perfectly identical in the tuned as well as in the mistuned case, $m_{b,i}$ simplifies to m_b . Concerning the disk parameters, an FE analysis of the blisk with the blades being modeled as rigid bodies is initially conducted. As a result, the natural frequencies of the disk, as exemplarily presented in Figure 4.6, can be plotted against the number of nodal diameters or CSM respectively. With the knowledge of the disk mass

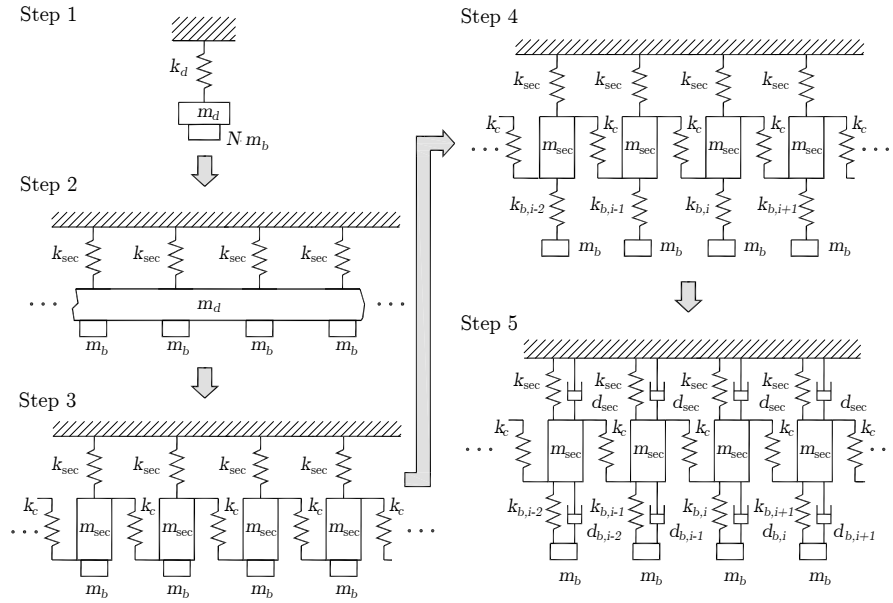


Figure 4.5: Steps of EBM setup (taken from Beirrow [7])

and the natural frequency associated with the minimum CSM, the disk stiffness k_d can be calculated from a simple SDOF relation by

$$\omega_{d, \text{CSM}_{\min}} = \sqrt{\frac{k_d}{m_d + N \cdot m_b}}. \quad (4.1)$$

The determination of the disk stiffness therefore contains the entire mass of the blisk which is the reason that the blades are included in the FE analysis of the disk.

Step 2

Since the EBM represents an entire blisk as an assembly of N single sectors, the disk stiffness is split into N springs representing the sector stiffnesses k_{sec} by

$$k_{sec} = \frac{k_d}{N}. \quad (4.2)$$

Step 3

In the same manner as in step two, the disk mass is split into N sectors, each having a sector mass of $m_{sec} = m_d/N$. Furthermore, the frequency of the maximum CSM of the same family of modes can be determined from Figure 4.6. In order to take account of the flexibility of the disk, coupling stiffnesses k_c are introduced. With the help of a parameter variation, the

sector stiffness is varied until the difference in frequency of the maximum CSM of EBM and FE-model becomes minimal.

Step 4

After the disk parameters have been identified, the blade masses are detached from the disk and blade stiffnesses $k_{b,i}$ are introduced. Similarly to the identification of the disk stiffness, the blade stiffnesses can be computed using an SDOF approach through

$$k_{b,i} = 4\pi^2 f_{b,i}^2 m_{eff}. \quad (4.3)$$

Here the frequencies $f_{b,i}$ are the results of a measurement campaign. It has to be noted that initially these measured frequencies are regarded to be blade alone frequencies. Hence, the disk is considered to be rigid during the identification of the blade stiffnesses. Consequently, the blade natural frequencies will not conform to those obtained from the measurement when the disk is regarded to be flexible. To take account of that effect, an iterative correction of the blade parameters is carried out after the very last setup step. As a result, the effectively vibrating blade mass changes. The idea is that not all parts of the blade take part in the vibration process. Therefore, a certain amount of the blade mass is considered to be associated with the disk vibration. The remaining mass is the effectively vibrating blade mass called m_{eff} . Details about the correction methodology are presented by Beirow [7]. In case of a tuned system, all blade stiffnesses are the same and therefore $k_{b,i} = k_b$.

Step 5

The final step comprises the integration of the mechanical damping. Both, the values of disk damping d_d and blade damping $d_{b,i}$ are results of modal analysis. In accordance with step 2, the disk damping is split into N individual sector dashpots by

$$d_{sec} = \frac{d_d}{N}. \quad (4.4)$$

Again, in case of a tuned system the blade damping values are identical for all blades and hence $d_{b,i} = d_b$.

Finally, by applying the momentum equation to the identified EBM, a system of $2N$ equations of motion emerges:

$$\mathbf{M}\ddot{\mathbf{x}}(t) + \mathbf{D}\dot{\mathbf{x}}(t) + \mathbf{K}\mathbf{x}(t) = \mathbf{F}^A(t) = \mathbf{F}^V(t) + \mathbf{F}^F(t). \quad (4.5)$$

The matrices in equation 4.5 are the diagonal mass matrix

$$\mathbf{M} = \left[\begin{array}{cccc|ccc} m_{sec} & 0 & \dots & 0 & 0 & \dots & 0 \\ 0 & \ddots & \ddots & \vdots & \vdots & & \vdots \\ \vdots & \ddots & \ddots & 0 & 0 & \dots & 0 \\ 0 & \dots & 0 & m_{sec} & 0 & \dots & 0 \\ \hline 0 & \dots & 0 & 0 & m_{eff} & 0 & \dots & 0 \\ \vdots & & & \vdots & 0 & \ddots & \ddots & \vdots \\ 0 & \dots & 0 & 0 & \vdots & \ddots & \ddots & 0 \\ 0 & \dots & 0 & 0 & 0 & \dots & 0 & m_{eff} \end{array} \right], \quad (4.6)$$

the symmetric damping matrix with $d_i^* = d_{sec} + d_{b,i}$

$$\mathbf{D} = \left[\begin{array}{cccc|cccc} d_1^* & 0 & \dots & 0 & -d_{b,1} & 0 & \dots & 0 \\ 0 & d_i^* & \ddots & \vdots & 0 & -d_{b,i} & \ddots & \vdots \\ \vdots & \ddots & \ddots & 0 & \vdots & \ddots & \ddots & 0 \\ 0 & \dots & 0 & d_N^* & 0 & \dots & 0 & -d_{b,N} \\ \hline -d_{b,1} & 0 & \dots & 0 & d_{b,1} & 0 & \dots & 0 \\ 0 & -d_{b,i} & \ddots & \vdots & 0 & d_{b,i} & \ddots & \vdots \\ \vdots & \ddots & \ddots & 0 & \vdots & \ddots & \ddots & 0 \\ 0 & \dots & 0 & -d_{b,N} & 0 & \dots & 0 & d_{b,N} \end{array} \right] \quad (4.7)$$

and the symmetric stiffness matrix with $k_i^* = k_{sec} + 2k_c + k_{b,i}$.

$$\mathbf{K} = \left[\begin{array}{cccccc|cccccc} k_1^* & -k_c & 0 & \dots & 0 & -k_c & -k_{b,1} & 0 & 0 & \dots & 0 & 0 \\ -k_c & \ddots & \ddots & \ddots & & 0 & 0 & \ddots & \ddots & \ddots & & 0 \\ 0 & \ddots & k_i^* & -k_c & \ddots & \vdots & 0 & \ddots & -k_{b,i} & 0 & \ddots & \vdots \\ \vdots & \ddots & -k_c & \ddots & \ddots & 0 & \vdots & \ddots & 0 & \ddots & \ddots & 0 \\ 0 & & \ddots & \ddots & k_{N-1}^* & -k_c & 0 & & \ddots & \ddots & -k_{b,N-1} & 0 \\ -k_c & 0 & \dots & 0 & -k_c & k_N^* & 0 & 0 & \dots & 0 & 0 & -k_{b,N} \\ \hline -k_{b,1} & 0 & 0 & \dots & 0 & 0 & k_{b,1} & 0 & 0 & \dots & 0 & 0 \\ 0 & \ddots & \ddots & \ddots & & 0 & 0 & \ddots & \ddots & \ddots & & 0 \\ 0 & \ddots & -k_{b,i} & 0 & \ddots & \vdots & 0 & \ddots & k_{b,i} & 0 & \ddots & \vdots \\ \vdots & \ddots & 0 & \ddots & \ddots & 0 & \vdots & \ddots & 0 & \ddots & \ddots & 0 \\ 0 & & \ddots & \ddots & -k_{b,N-1} & 0 & 0 & & \ddots & \ddots & k_{b,N-1} & 0 \\ 0 & 0 & \dots & 0 & 0 & -k_{b,N} & 0 & 0 & \dots & 0 & 0 & k_{b,N} \end{array} \right] \quad (4.8)$$

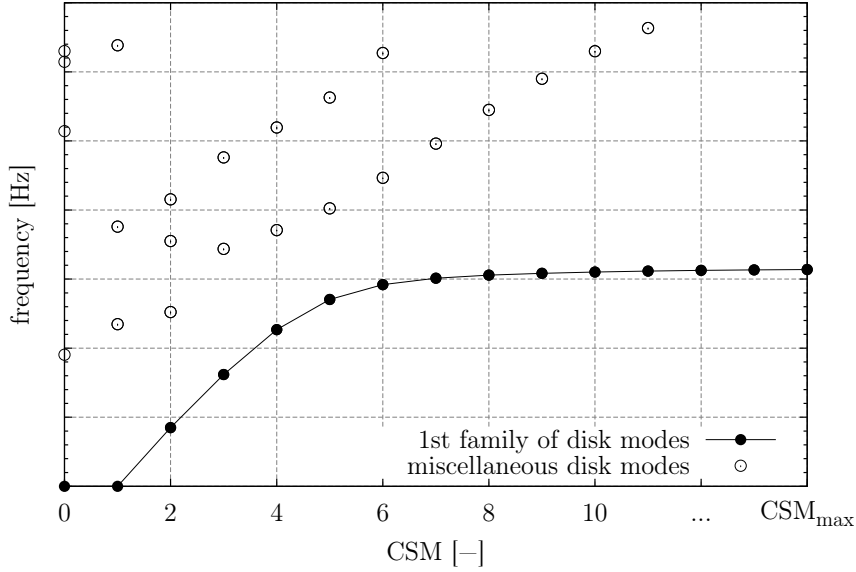


Figure 4.6: Sample diagram of disk natural frequencies versus CSM

4.2.2 Equivalent Aerodynamic Elements

As discussed in section 2.3, the aerodynamics significantly influence the vibrational behaviour of blisks. To account for these effects, the EBM is extended with additional springs, masses and dashpots (the so called equivalent aerodynamic elements) representing the aerodynamic forces from a mechanical point of view. Additionally, the usage of aerodynamic influence coefficients is presented in section 4.2.3.

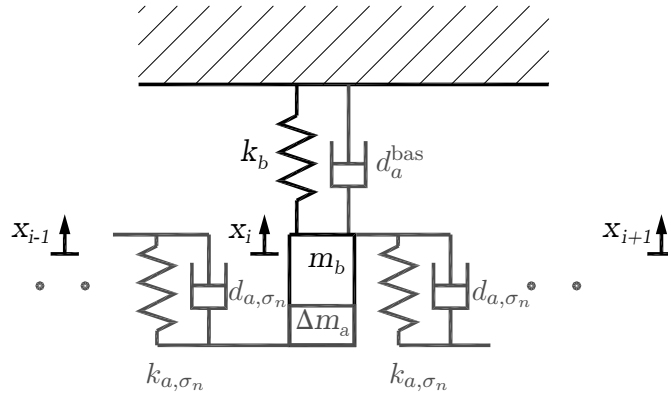


Figure 4.7: Schematic model of aerodynamic elements of one sector

The idea of equivalent aerodynamic elements is shown in Figure 4.7. Basically the elements can be distinguished between interblade phase angle dependent parameters k_{a,σ_n} , d_{a,σ_n} and independent ones d_a^{bas} , Δm_a . Concerning the interblade phase angle dependent values, k_{a,σ_n}

takes account of the aerodynamic stiffening and softening effects and d_{a,σ_n} describes the aerodynamic damping as viscous damping. Obviously, when the interblade phase angle σ_n becomes zero, only the co-vibrating air mass Δm_a remains while the forces due to k_{a,σ_n} and d_{a,σ_n} become zero. Apparently, even at $\sigma = 0^\circ$ aerodynamic damping exists. Hence, a dashpot is introduced with d_a^{bas} which provides damping in case of zero interblade phase angle. The method that has been employed for the parameter identification so far is presented in [7]. Here, a new procedure is described which employs the aeroelastic eigenvalues of the tuned system as derived in Section 3.5.

The aim of the identification procedure is to obtain values for the equivalent aerodynamic elements as functions of the interblade phase angle. As a consequence the elements' parameters can be varied depending on the interblade phase angle during the simulations which is essential for the computation of mistuned blisk vibrations where the phase angles are not the same between adjacent blades. During the identification procedure a single sector, as displayed in Figure 4.7, will be considered. For this sector the momentum equation reads

$$(\Delta m_a + m)\ddot{x}_i + (d_a^{\text{bas}} + 2d_{a,\sigma_n})\dot{x}_i - d_{a,\sigma_n}(\dot{x}_{i-1} + \dot{x}_{i+1}) + (2k_{a,\sigma_n} + k)x_i - k_{a,\sigma_n}(x_{i-1} + x_{i+1})x_i = 0 \quad (4.9)$$

Since the identification is performed on the basis of the tuned aeroelastic eigenvalues, the individual blade displacements x_{i-1} , x_i and x_{i+1} and the appendant time derivatives due to assembly vibrations in a particular interblade phase angle σ can be expressed through

$$\begin{aligned} x_{i+k} &= \hat{x}_i \sin(\omega t + k \cdot \sigma_n) \\ \dot{x}_{i+k} &= \hat{x}_i \omega \cos(\omega t + k \cdot \sigma_n). \end{aligned} \quad \text{for } k = -1, 0, 1 \quad (4.10)$$

By replacing the blade displacements x_{i-1} and x_{i+1} and velocities \dot{x}_{i-1} and \dot{x}_{i+1} with the corresponding terms from Equation 4.10, Equation 4.9 becomes

$$m^* \ddot{x}_i + d_{\sigma_n}^* \dot{x}_i + k_{\sigma_n}^* x_i = 0. \quad (4.11)$$

Here the parameters related to aerodynamic mass, damping and stiffness are

$$\begin{aligned} m^* &= \Delta m_a + m_b, \\ d_{\sigma_n}^* &= d_a^{\text{bas}} + 2d_{a,\sigma_n}(1 - \cos(\sigma_n)) \quad \text{and} \\ k_{\sigma_n}^* &= k_b + 2k_{a,\sigma_n}(1 - \cos(\sigma_n)). \end{aligned}$$

If, analogously to Section 3.5, the solution is assumed to be of complex exponential type, the eigenvalues of Equation 4.11 can be calculated to

$$\lambda_{1,2} = -\zeta_{\sigma_n}^* \omega_{0,\sigma_n}^* \pm i \underbrace{\omega_{0,\sigma_n}^* \sqrt{1 - \zeta_{\sigma_n}^{*2}}}_{\omega_{\sigma_n}^*}. \quad (4.12)$$

From the aeroelastic eigenvalues of the tuned system λ_{a,σ_n} , the aerodynamic damping ζ_{a,σ_n} and the aeroelastic angular frequency ω_{a,σ_n} are known (see Section 3.5), hence it can be written

$$\zeta_{\sigma_n}^* = \frac{-\{\lambda_{a,\sigma_n}\}_{\text{Re}}}{\omega_{0,\sigma_n}^*} = \frac{d_{\sigma_n}^*}{2m^* \omega_{0,\sigma_n}^*} = \frac{d_a^{\text{bas}} + 2d_{a,\sigma_n}(1 - \cos(\sigma_n))}{2\sqrt{(\Delta m_a + m_b)(k_b + 2k_{a,\sigma_n}(1 - \cos(\sigma_n)))}} \quad (4.13)$$

with

$$\omega_{0,\sigma_n}^* = \sqrt{\{\lambda_{a,\sigma_n}\}_{\text{Re}}^2 + \{\lambda_{a,\sigma_n}\}_{\text{Im}}^2} \quad (4.14)$$

and

$$\omega_{\sigma_n}^* = \{\lambda_{a,\sigma_n}\}_{\text{Im}} = \sqrt{\frac{k_b + 2k_{a,\sigma_n}(1 - \cos(\sigma_n))}{\Delta m_a + m_b}} \sqrt{1 - \zeta_{\sigma_n}^{*2}}. \quad (4.15)$$

This leaves us with four unknowns (the parameters of the aerodynamic elements) and only two equations Equations 4.13 and 4.15. Starting with the identification for $\sigma = 0^\circ$ the terms related to k_{a,σ_n} and d_{a,σ_n} become zero. Hence, only the unknown dashpot d_a^{bas} and the co-vibrating fluid mass Δm_a remain unknown. Furthermore, the angular frequency that is used to determine the aerodynamic forces is known, this is the structural natural angular frequency ω_{0,σ_n}^* . Consequently Equation 4.13 can be written as

$$\zeta_{\sigma=0^\circ}^* = \frac{-\{\lambda_{a,\sigma=0^\circ}\}_{\text{Re}}}{\omega_{0,\sigma=0^\circ}^*} = \frac{d_{\sigma=0^\circ}^*}{2m^* \omega_{0,\sigma=0^\circ}^*} = \frac{d_a^{\text{bas}}}{2\sqrt{(\Delta m_a + m_b)k_b}} \quad (4.16)$$

and Equation 4.15 becomes

$$\omega_{\sigma=0^\circ}^* = \{\lambda_{a,\sigma=0^\circ}\}_{\text{Im}} = \sqrt{\frac{k_b}{\Delta m_a + m_b}} \sqrt{1 - \zeta_{\sigma=0^\circ}^{*2}}. \quad (4.17)$$

Equation 4.17 can also be written as

$$\omega_{\sigma=0^\circ}^{*2} \left(\frac{\Delta m_a}{k_b} + \frac{1}{\omega_{0,\sigma_n}^{*2}} \right) = 1 - \zeta_{\sigma=0^\circ}^{*2}. \quad (4.18)$$

After rearrangement of Equation 4.18, the co-vibrating fluid mass can be determined via

$$\Delta m_a = m_b \left[\frac{\omega_{0,\sigma=0^\circ}^{*2}}{\omega_{\sigma=0^\circ}^{*2}} (1 - \zeta_{\sigma=0^\circ}^{*2}) - 1 \right]. \quad (4.19)$$

Consecutively, the dashpot d_a^{bas} can be calculated from Equation 4.16

$$d_a^{\text{bas}} = 2\zeta_{\sigma=0^\circ}^* \sqrt{k_b(\Delta m_a + m_b)}. \quad (4.20)$$

Finally, the remaining unknowns can be directly calculated from the aeroelastic eigenvalues of the specific interblade phase angles by rearranging Equation 4.15 to yield k_{a,σ_n}

$$k_{a,\sigma_n} = \frac{\omega_{\sigma_n}^{*2} \frac{(\Delta m_a + m_b)}{1 - \zeta_{\sigma_n}^{*2}} - k_b}{2(1 - \cos(\sigma_n))} \quad \sigma_n \neq 0^\circ \quad (4.21)$$

and Equation 4.13 obtaining d_{a,σ_n}

$$d_{a,\sigma_n} = \frac{2\zeta_{\sigma_n}^* \sqrt{(\Delta m_a + m_b)(k_b + k_{a,\sigma_n})} - d_a^{\text{bas}}}{2(1 - \cos(\sigma_n))} \quad \sigma_n \neq 0^\circ. \quad (4.22)$$

In the tuned case, the identified parameters can be directly included into the EBM corresponding to the IBPA of the CSM under consideration. Concerning the simulation of mistuned systems an iterative adaption of these parameters with respect to the interblade phase angle occurring between adjacent blades has to be performed. In practice, the parameters of the aerodynamic elements are initially adjusted according to the interblade phase angle of the excitation. During the calculation procedure they are continuously adapted to the instantaneous value of the interblade phase angle between adjacent blades.

4.2.3 Aerodynamic Influence Coefficients

On the contrary to the previously presented method of equivalent aerodynamic elements, the influence of the aerodynamic forces due to blade motion is considered in form of aerodynamic influence coefficients as well. The determination of these force coefficients is described in Section 3.5 in detail. The following section addresses the integration of these coefficients into the EBM which involves a suitable scaling with respect to the effectively vibrating blade mass.

Due to differences in the calculation procedure of the AIC and the usage of them within the EBM, a scaling of the influence coefficients becomes necessary. In Section 3.4.2 the

determination of the influence coefficients is described in detail. The starting point are the equations for the determination of force coefficients of general motion. According to Equations 3.26 and 3.27 the i -th coefficient L_i of a blade vibrating in mode Ψ is defined as

$$\hat{L}_i^\Psi = \frac{\Psi^T \hat{\mathbf{F}}_i^V}{\hat{q}_0^\Psi} \quad \text{for } i = 0, 1, \dots, N-1. \quad (4.23)$$

Here Ψ^T is the mass normalised mode shape, $\hat{\mathbf{F}}_i^V$ is the vector of complex amplitudes of the aerodynamic force of the i -th blade due to vibration of the reference blade in mode Ψ with the modal displacement amplitude \hat{q}_0^Ψ . Therefore, the coefficients determined by Equation 4.23 are mass normalised as well. Assuming that the normalisation procedure has been done with the effectively vibrating blade mass m_{eff} , the equation above can be reformulated using the actual mode shape $\Phi = \Psi \cdot \sqrt{m_{eff}}$ and the appropriate EBM blade displacement $\underline{x}_0^\Phi(t) = \underline{x}_0^\Psi(t)/\sqrt{m_{eff}}$ as

$$\hat{L}_i^\Psi = \frac{1}{m_{eff}} \cdot \underbrace{\frac{\Phi^T \hat{\mathbf{F}}_i^V}{\hat{x}_0^\Phi}}_{\hat{L}_i^\Phi}. \quad (4.24)$$

Hence, the aerodynamic forces due to blade vibration of the EBM vibrating in mode Φ can be expressed as

$$\underline{\mathbf{F}}^V(t) = \hat{\mathbf{L}}^\Phi \cdot \underline{\mathbf{x}}^\Phi(t) = \hat{\mathbf{L}}^\Psi \cdot m_{eff} \cdot \underline{\mathbf{x}}^\Phi(t). \quad (4.25)$$

Since the aerodynamic influence coefficients only act on the blade DOF, the entries in the matrix $\hat{\mathbf{L}}^\Phi$ acting on the DOF of the disk are zero. Hence the influence coefficients matrix reads

$$\hat{\mathbf{L}}^\Phi = \left[\begin{array}{cccc|cccc} 0 & 0 & \dots & 0 & 0 & 0 & \dots & 0 \\ 0 & 0 & \ddots & \vdots & 0 & 0 & \ddots & \vdots \\ \vdots & \ddots & \ddots & 0 & \vdots & \ddots & \ddots & 0 \\ 0 & \dots & 0 & 0 & 0 & \dots & 0 & 0 \\ \hline 0 & 0 & \dots & 0 & \hat{L}_0^\Phi & \hat{L}_{N-1}^\Phi & \dots & \hat{L}_1^\Phi \\ 0 & 0 & \ddots & \vdots & \hat{L}_1^\Phi & \hat{L}_0^\Phi & \hat{L}_{N-1}^\Phi & \dots \\ \vdots & \ddots & \ddots & 0 & \dots & \hat{L}_1^\Phi & \hat{L}_0^\Phi & \hat{L}_{N-1}^\Phi \\ 0 & \dots & 0 & 0 & \hat{L}_{N-1}^\Phi & \dots & \hat{L}_1^\Phi & \hat{L}_0^\Phi \end{array} \right]. \quad (4.26)$$

The aerodynamic forces due to blade vibration on the right hand side of the EBM equation of motion in complex notation

$$M\ddot{\mathbf{x}}^\Phi(t) + D\dot{\mathbf{x}}^\Phi(t) + K\mathbf{x}^\Phi(t) = \underline{\mathbf{F}}^V(t) + \underline{\mathbf{F}}^F(t) = \hat{\underline{\mathbf{L}}}^\Phi \cdot \mathbf{x}^\Phi(t) + \underline{\mathbf{F}}^F(t) \quad (4.27)$$

can be written in full as

$$\hat{\underline{\mathbf{L}}}^\Phi \cdot \mathbf{x}^\Phi(t) = \underbrace{\left\{ \hat{\underline{\mathbf{L}}}_{\text{Re}}^\Phi \cdot \mathbf{x}_{\text{Re}}^\Phi(t) - \hat{\underline{\mathbf{L}}}_{\text{Im}}^\Phi \cdot \mathbf{x}_{\text{Im}}^\Phi(t) \right\}}_{\text{real part}} + j \cdot \underbrace{\left\{ \hat{\underline{\mathbf{L}}}_{\text{Re}}^\Phi \cdot \mathbf{x}_{\text{Im}}^\Phi(t) + \hat{\underline{\mathbf{L}}}_{\text{Im}}^\Phi \cdot \mathbf{x}_{\text{Re}}^\Phi(t) \right\}}_{\text{imaginary part}}. \quad (4.28)$$

As the objective is to break the equations down to real quantities, only the real part of Equation 4.28 is taken into consideration. It can be further simplified to

$$\left\{ \hat{\underline{\mathbf{L}}}^\Phi \cdot \mathbf{x}^\Phi(t) \right\}_{\text{Re}} = \hat{\underline{\mathbf{L}}}_{\text{Re}}^\Phi \cdot \mathbf{x}_{\text{Re}}^\Phi(t) - \hat{\underline{\mathbf{L}}}_{\text{Im}}^\Phi \cdot \mathbf{x}_{\text{Im}}^\Phi(t) = \hat{\underline{\mathbf{L}}}_{\text{Re}}^\Phi \cdot \underbrace{\hat{\mathbf{x}}^\Phi \cos(\omega t)}_{\mathbf{x}^\Phi(t)} - \hat{\underline{\mathbf{L}}}_{\text{Im}}^\Phi \cdot \underbrace{\hat{\mathbf{x}}^\Phi \sin(\omega t)}_{\frac{-\dot{\mathbf{x}}^\Phi(t)}{\omega}} \quad (4.29)$$

$$\left\{ \hat{\underline{\mathbf{L}}}^\Phi \cdot \mathbf{x}^\Phi(t) \right\}_{\text{Re}} = \hat{\underline{\mathbf{L}}}_{\text{Re}}^\Phi \cdot \mathbf{x}^\Phi(t) + \hat{\underline{\mathbf{L}}}_{\text{Im}}^\Phi \cdot \frac{\dot{\mathbf{x}}^\Phi(t)}{\omega} \quad (4.30)$$

Substituting the right hand side of Equation 4.27 with Equation 4.30 yields the equation of motion of the EBM with aerodynamic influence coefficients included in real notation

$$M\ddot{\mathbf{x}}^\Phi(t) + \left[D - \frac{\hat{\underline{\mathbf{L}}}_{\text{Im}}^\Phi}{\omega} \right] \dot{\mathbf{x}}^\Phi(t) + \left[K - \hat{\underline{\mathbf{L}}}_{\text{Re}}^\Phi \right] \mathbf{x}^\Phi(t) = \underline{\mathbf{F}}^F(t). \quad (4.31)$$

This equation can readily be used for numerical time integration for flutter and forced response analyses or can easily be transformed into the frequency domain. Both procedures are presented in the following sections.

4.3 Time Marching for Flutter and Forced Response Analysis

This section presents the numerical time integration of the EBM equation of motion in real notation with aerodynamic influence coefficients included employing the implicit Newmark

scheme [85]. The scheme developed by Newmark in 1959 is well established in the numerical time integration of the equations of motion in aeroelastic computations, e.g. Sayma et al. [99] or Schmitt [100]. Its major advantages, the second-order-accuracy and the unconditional stability with respect to the time step size, make it the method of choice. Again, the basis for the time integration is the equation of motion with external excitation forces $\mathbf{F}^F(t)$, Equation 4.31. In case of flutter analyses, the excitation forces are simply set to zero. The complete equation in semi-discrete form reads²

$$M\ddot{\mathbf{x}}_{n+1} + \left[\mathbf{D} - \frac{\hat{\mathbf{L}}_{\text{Im}}}{\omega} \right] \dot{\mathbf{x}}_{n+1} + \left[\mathbf{K} - \hat{\mathbf{L}}_{\text{Re}} \right] \mathbf{x}_{n+1} = \mathbf{F}_{n+1}^F. \quad (4.32)$$

In this formulation, the values of acceleration $\ddot{\mathbf{x}}_{n+1}$, velocity $\dot{\mathbf{x}}_{n+1}$ and displacement \mathbf{x}_{n+1} are evaluated at the future time instant t_{n+1} and are therefore unknown. As a result, assumptions for velocity and displacement as functions of the acceleration have to be made within the time interval Δt . The classical Newmark scheme is formulated in such a way that the following approaches are used for the unknown velocity $\dot{\mathbf{x}}_{n+1}$ and displacement \mathbf{x}_{n+1} respectively

$$\dot{\mathbf{x}}_{n+1} = \dot{\mathbf{x}}_n + [(1 - \delta)\ddot{\mathbf{x}}_n + \delta\ddot{\mathbf{x}}_{n+1}] \Delta t \quad \text{and} \quad (4.33)$$

$$\mathbf{x}_{n+1} = \mathbf{x}_n + \dot{\mathbf{x}}_n \Delta t + [(0.5 - \beta)\ddot{\mathbf{x}}_n + \beta\ddot{\mathbf{x}}_{n+1}] \Delta t^2 \quad (4.34)$$

Here the variables subscripted with n denote the particular values of the last time step³, which are known at the time $\dot{\mathbf{x}}_{n+1}$ and \mathbf{x}_{n+1} are calculated. Depending on the choice of the constants β and δ different assumptions for the acceleration can be made. If the constants are chosen to $\beta = 1/6$ and $\delta = 1/2$ a linear acceleration gradient is assumed. In the present work a constant average acceleration is presumed within one time interval, hence the constants are chosen to

$$\beta = 0.25 \quad \text{and} \quad \delta = 0.5.$$

Given that we know the values of $\ddot{\mathbf{x}}_n$, $\dot{\mathbf{x}}_n$ and \mathbf{x}_n we have three unknowns and two equations, 4.33 and 4.34. Taking the equation of motion 4.32 as third and replacing the unknown displacement and velocity with Equations 4.33 and 4.34 leads to

²The superscript which denotes a particular mode shape is dropped now.

³At the beginning of the computation, these values are calculated from the initial conditions according to the considered assembly vibration.

$$\begin{aligned}
& \left\{ \mathbf{M} + \left[\mathbf{D} - \frac{\hat{\mathbf{L}}_{\text{Im}}}{\omega} \right] \Delta t \delta + \left[\mathbf{K} - \hat{\mathbf{L}}_{\text{Re}} \right] \Delta t^2 \beta \right\} \ddot{\mathbf{x}}_{n+1} = \mathbf{F}_{n+1}^F - \dots \\
& \dots \left[\mathbf{D} - \frac{\hat{\mathbf{L}}_{\text{Im}}}{\omega} \right] \cdot [\dot{\mathbf{x}}_n + \Delta t(1 - \delta)\ddot{\mathbf{x}}_n] - \dots \\
& \dots \left[\mathbf{K} - \hat{\mathbf{L}}_{\text{Re}} \right] \cdot [\mathbf{x}_n + \Delta t\dot{\mathbf{x}}_n + \Delta t^2(0.5 - \beta)\ddot{\mathbf{x}}_n].
\end{aligned} \tag{4.35}$$

The resultant equation contains only values that are known a priori (mass, stiffness, damping and influence coefficients matrices) or which are the results of the latest time step ($\ddot{\mathbf{x}}_n$, $\dot{\mathbf{x}}_n$, \mathbf{x}_n). Since the nodal diameter of the excitation force can be explicitly specified, the value of \mathbf{F}_{n+1}^F can be calculated using force amplitudes of unity or those obtained from CFD-analysis. For a given cyclic symmetry mode which is going to be analysed the excitation force for one blade i of the assembly can be calculated through

$$F_i^F(t) = m_{eff} \sum_{EO=1}^n \hat{F}_{EO} \cos(\Omega_{EO}t + i\sigma_{CSM} + \varphi_{EO}), \quad i = 0, 1, \dots, N - 1. \tag{4.36}$$

Here, \hat{F}_{EO} is the amplitude of a specific engine order EO excitation, Ω_{EO} is the excitation frequency, σ_{CSM} is the interblade phase angle of the assembly due to the considered CSM and φ_{EO} characterises the phase difference between the different engine orders. It has to be mentioned that not all engine orders contribute to the forcing of a specific CSM but only those are significant that have the same number of nodal lines. The problem of excitation aliasing has been addressed in Section 2.3.2.

The only unknown that remains is the acceleration at the future time step $\ddot{\mathbf{x}}_{n+1}$ which can be explicitly calculated by solving Equation 4.35. Ultimately, the displacement and velocity at the future time instant t_{n+1} can be calculated subsequently with Equations 4.33 and 4.34 respectively.

Plausibility Check of Time Integration

In order to assure the proper functionality of the numerical time integration some plausibility checks have been performed. For that reason, influence coefficients of the compressor rotor model presented in Chapter 7 calculated for one frequency of the first blade mode have been used to compare the EBM time integration results with analytical solutions. For that purpose, without loss of generality, the disk was regarded to be rigid and a tuned system without mechanical blade damping has been considered. The imaginary part of the influence coefficients along with the resultant damping curves is presented in Figure 4.8.

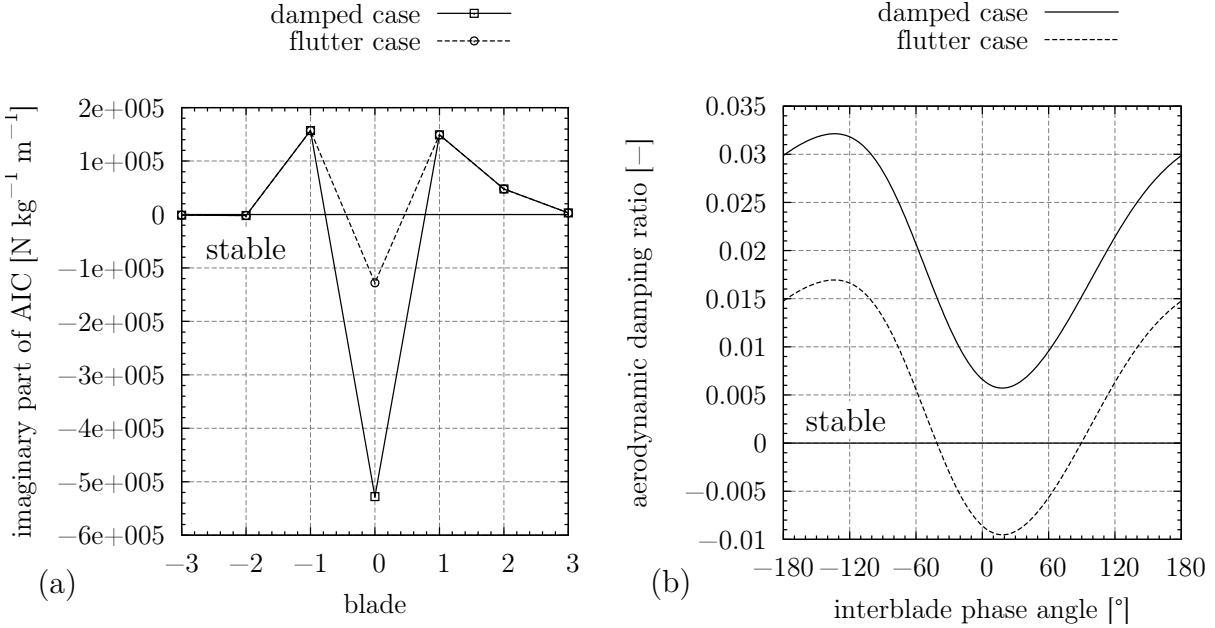


Figure 4.8: Imaginary part of AIC (a) and resultant damping curves (b)

Two different cases have been considered. The so called *damped case* represents the influence coefficients of the nominal rotor, while the zeroth influence coefficient of the *flutter case* has been increased by 75% of its original value. Consequently, the eigeninfluence of a vibrating blade as well as the average damping value of the interblade phase angle dependent aerodynamic damping are reduced. Finally, this leads to a significant lowering of the entire damping curve of approximately 2% with respect to the ratio of critical damping and an unstable region between interblade phase angles of $\sigma = -41^\circ$ and $\sigma = -89^\circ$. This was done to demonstrate the ability of performing flutter computations with the EBM.

The analytical solutions can be calculated employing the force coefficients in travelling wave mode coordinates which requires a transformation from blade individual influence coefficients \hat{L}_i to travelling wave mode coefficients \hat{C}_{σ_n} according to Equation 3.18. In a tuned system every blade exhibits the same vibratory motion, the only difference is the phase angle between adjacent blades. For a given interblade phase angle the corresponding travelling wave mode coefficient is calculated using the AIC shown in Figure 4.8 together with the corresponding aerodynamic damping ratio. Analogously to Equation 4.31 an equation of motion can be formulated for each travelling wave mode with the corresponding interblade phase angle σ_n :

$$m\ddot{x} - \frac{\hat{C}_{\sigma_n, \text{Im}}}{\omega} \dot{x} + [k - \hat{C}_{\sigma_n, \text{Re}}] x = F^F. \quad (4.37)$$

The solution of this equation is straight forward and the results of four different computations are presented in Figure 4.9. At first the free vibration of the *damped case* given an

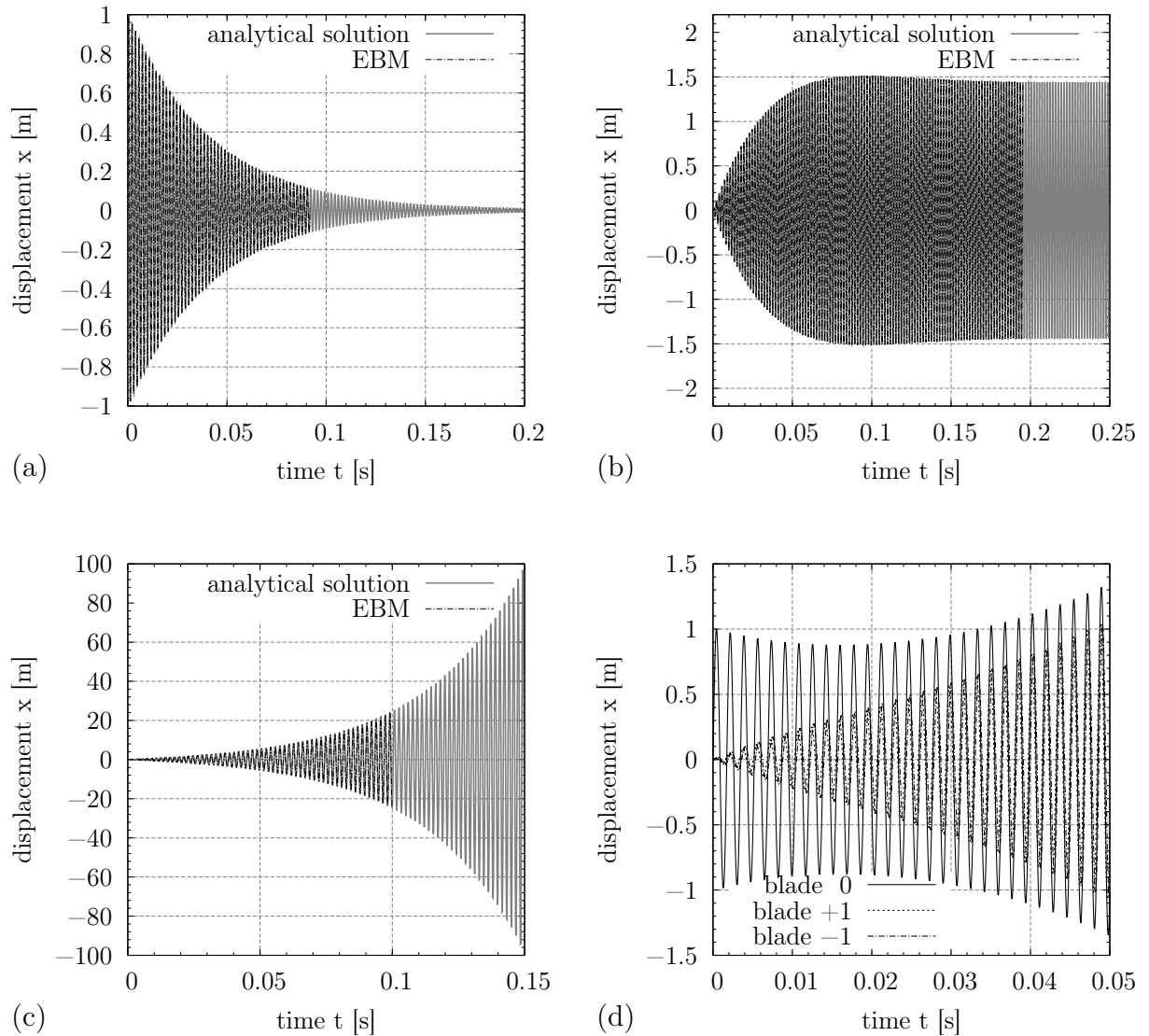


Figure 4.9: Results for free damped vibration $\sigma = 0^\circ$ (a), forced damped vibration $\sigma = 45^\circ$ (b), forced vibration of the flutter case $\sigma = 45^\circ$ (c) and initial excitation of a single blade of the flutter case (d)

initial velocity according to an interblade phase angle of $\sigma = 0^\circ$ and the forced vibration at $\sigma = 45^\circ$ are demonstrated, Figure 4.9 (a) and (b). Both EBM results show excellent agreement in terms of blade amplitudes as well as with respect to the aeroelastic frequency. The same conclusion can be drawn for the forced vibration of the *flutter case* at $\sigma = 45^\circ$ as shown in Figure 4.9 (c). Concerning the last diagram, only one blade (blade 0) has been given an initial velocity. First, the initially excited blade is damped which is caused by the negative imaginary part of the influence coefficients, see Figure 4.8. Due to the influence coefficients \hat{L}_{-1} and \hat{L}_{+1} having an exciting influence, the neighbouring blades blade +1 and

blade -1 are forced and start to vibrate too. As soon as the vibration amplitudes are high enough, their exciting influence leads to an increasing displacement of blade 0 as well. The results obtained with the EBM are plausible and the numerical time integration provides reasonable results too.

4.4 Forced Response in the Frequency Domain

As the numerical time integration is comparatively time consuming, the equation of motion can be transformed to the frequency domain which reduces the total computational time and makes parameter studies with a large amount of simulations feasible. Initially, the EBM equation of motion 4.31 with the excitation force $\mathbf{F}^F(t)$ on the right hand side is Fourier transformed yielding

$$\underline{\mathbf{X}}(j\Omega) = \left\{ -\Omega^2 \mathbf{M} + j\Omega \left[\mathbf{D} - \frac{\hat{\mathbf{L}}_{\text{Im}}^\Phi(\Omega)}{\Omega} \right] + \left[\mathbf{K} - \hat{\mathbf{L}}_{\text{Re}}^\Phi(\Omega) \right] \right\}^{-1} \underline{\mathbf{F}}^F(j\Omega) \quad (4.38)$$

$$= \underline{\mathbf{H}}(j\Omega) \underline{\mathbf{F}}^F(j\Omega). \quad (4.39)$$

Here $\underline{\mathbf{H}}(j\Omega)$ represents the transfer matrix and $\underline{\mathbf{F}}^F(j\Omega)$ is the Fourier transform of the excitation force.

The values of the transfer matrix explicitly depend on the excitation frequency which makes a computation of the matrix entries at every frequency increment necessary. Moreover, the influence coefficients are directly depending on the frequency at which they are determined which is taken into consideration by an interpolation procedure. Therefore the influence coefficients are computed at three designated frequencies and they are then interpolated using a quadratic interpolation for the frequency of interest. It has to be mentioned that the assumption of quadratic dependency only holds true for a small frequency range. The interpolation of influence coefficients has been validated with bidirectionally coupled FSI computations of a 2D compressor rotor model for which the results are presented in Chapter 6.

Chapter 5

Standard Configuration 10

In order to verify the aeroelastic methods and to demonstrate the ability to calculate turbomachinery aeroelasticity with Fluent, a standard configuration was chosen as test case. The simulation of turbomachinery aeroelasticity with Fluent has already been the object of research of Schrape et al. [101], [102]. However, the previous work dealt with two-dimensional analyses only. Nevertheless these results provide the basis for the following analysis of three-dimensional turbomachinery aeroelasticity. The main focus of this chapter is on the validation of the routines used for the determination of force coefficients, aerodynamic influence coefficients and the aeroelastic eigenvalues.

5.1 Model

The geometry of the standard configuration 10 (SC10) is part of the collection of standard configuration of the "Workshop of Aeroelasticity" from the group of Prof. Fransson [34]. This collection contains results from experiments and simulations of numerous test cases for different blade cascades of compressor and turbine configurations. These results can be used to validate new numerical methods and codes by comparing them to those obtained by other researchers.

With the aim of performing aeroelastic analyses of a modern high pressure compressor, a test case was sought that requires the analysis of a complex, three-dimensional, unsteady flow. This was found in the SC10 with a compressor-like annular blade cascade in subsonic and transonic flow. The interesting feature of the SC10 is that apart from two-dimensional results, also results of three-dimensional flow simulations with separation and blockage are available.

From the SC10 aeroelastic sample cases defined in [34] containing heaving and pitching motions at subsonic and transonic flow the test cases number 2 and 3 for pitching and number 10 and 11 for heaving have been chosen. Additionally a three-dimensional test case with in-

viscid and viscous simulations is taken into consideration. Due to lack of experimental data, the validation process is done by performing a code-to-code comparison. The results that serve as reference for this work are those obtained by Repar et al. [91]. These simulations feature comparisons between inviscid and viscous two- and three-dimensional simulations obtained with different types of steady and non-reflecting boundary conditions (NRBC). Apart from Repar et al. also Hall [47], who focused on two-dimensional inviscid computations, and Montgomery and Verdon [83] intensively analysed the SC10¹.

5.1.1 Parameters and Flow Conditions

The geometry of the standard configuration 10 has been proposed by Verdon in 1987 [113]. It bases on a NACA 5506 definition with an altered thickness distribution to close the profile in a wedge shaped trailing edge. The blade satisfies the Kutta condition at the trailing edge. Additionally, the SC10 has been extended to a three-dimensional test case by Montgomery and Verdon [83] with the flow of the two-dimensional inviscid case representing flow conditions at midspan. The three-dimensional annular cascade features 24 straight blades without tip gap, the geometric parameters are summarised in Table 5.1. During unsteady simulations of heaving and pitching motions, the blades are assumed to slide over walls at hub and casing respectively.

Table 5.1: Parameters of the SC10 annular cascade

geometric parameters		
profil	modified NACA 5506	
blade number	$N [-]$	24
chord length	$c [m]$	0.1
stagger angle	$\gamma [^\circ]$	45
pitch to chord ratio at midspan	$t = p/c$	1.0
aspect ratio	h/c	0.849
radius at hub	$R_1 [m]$	3.395
radius at casing	$R_2 [m]$	4.244

The flow is subsonic with an inlet mach number of $Ma_1 = 0.7$ and an inlet angle of $\beta_1 = 55^\circ$. In case of the annular cascade the inlet angle is constant at all radii.

For all flow conditions a pitching motion with an amplitude of $\hat{\alpha} = 2.0^\circ$ has been simulated. Furthermore a heaving motion with an amplitude of $\hat{y} = 0.01c$ in the direction normal to blade chord was simulated with the two-dimensional model. For the aeroelastic simulations a reduced frequency, Equation 2.18, based on full chord length, of $\omega^* = 0.5$ has been used. The details for all simulation conditions are summarised in Table 5.2.

¹Simulations have also been performed by Huff [56], Hoehn [54], Ayer [3] and Kemme [63].

Table 5.2: Aerodynamic and aeroelastic parameters

flow condition		steady	
		2D	3D
inlet mach number	Ma_1	0.7	
inlet angle	$\beta_1 [^\circ]$	55	
Reynolds number (Navier-Stokes Sim.)	Re	$1.25 \cdot 10^6$	

flow condition		unsteady	
		2D	3D
reduced frequency	ω^*	0.5	
amplitude heaving motion	$\hat{y} [m]$	0.01c	-
pitching axis coordinates	$x_\alpha, y_\alpha [m]$	0.5c, 0.05c	
amplitude pitching motion	$\hat{\alpha} [^\circ]$	2.0	

5.1.2 Reference Results

In order to be able to evaluate the results of the simulations, the reference results of Repar et al. are summarised shortly. Repar et al. solved the time-linearised Euler equations as well as the time-linearised Navier-Stokes equations applying the Spalart-Allmaras one equation turbulence model. The simulations presented in this work have been conducted with the same turbulence model, aiming at a correlation of the results as good as possible. Moreover, the application of the Spalart-Allmaras turbulence model to turbomachinery simulations has provided adequate results in a great number of cases. The study conducted by Bardina et al. [5] confirms the decision, proving that the Spalart-Allmaras model yields reasonable results for complex flows simultaneously showing excellent performance.

Concerning the time linearisation employed by Repar et al., it was assumed that the unsteady flow field can be modeled as a superposition of the steady state flow field and small harmonic linear perturbations, details about the method can be found in [89]. As a premise for the validity of this assumption, the flow field should not contain strong non-linearities such as shocks and separation bubbles. Shocks, whose position may vary considerably during blade motion, have a major effect on the aerodynamic damping. The proper prediction of the shock position is a tough task even with non-linear methods, see Grueber [43] for an investigation of viscous effects on aerodynamic damping for example. Further difficulties may be posed by separation bubbles. The area where separation occurs may well increase when blades vibrate and hence increase non-linearity in fluid forces. The assumption of small vibration amplitudes reduces the non-linear effects and makes a time-linearised treatment of the flow acceptable.

Concerning the boundary conditions of the unsteady simulations, Repar et al. used Giles' two-dimensional non-reflecting boundary conditions [40] for the two-dimensional computa-

tions. For the three-dimensional simulations, one-dimensional and three-dimensional [90] non-reflecting boundary conditions have been applied.

5.1.3 Details about the Numerical Simulations

The numerical simulations have been conducted with the commercial CFD solver Fluent 6.3.26.

The inviscid simulations involve the numerical solution of the non-linear Euler equations. On the contrary, during the viscous computations the Navier-Stokes equations in combination with the one-equation turbulence model from Spalart-Allmaras [107] with wall functions are solved. Concerning the solver settings, the implicit density based solver with cell-based gradient evaluation has been used for all simulations. The determination of the flow variables at the cell faces has been realised with second order accurate upwind-discretisation schemes. The convective fluxes at the cell boundaries are approximated using Roe's flux differencing scheme.

When it comes to unsteady simulations, first order implicit time integration has been employed. Although a second order scheme is included in Fluent and its use would be desirable, it has not been available with deforming meshes in the current version. During simulation it is ensured that the unsteady residuals estimated in each time step decrease to the level of the residuals of the steady state simulations. The choice of an appropriate time step size is a trade-off between numerical accuracy and the time needed for the simulation. In a previous work Schrape has analysed the influence of the time step size on the results of aerodynamic damping and aeroelastic frequency of fluid-structure coupled simulations in Fluent [101]. He estimated the error in aerodynamic damping due to numerical dissipation obtained with 110 time steps per vibration cycle to approximately 2%. Concerning the simulations of SC10 preliminary investigations have shown that a resolution of 150 time steps per vibration cycle provides sufficiently accurate results. An increase of the number of time steps by factors of two or four did not alter the results significantly. Consequently, unless otherwise stated, a resolution of 150 time steps per vibration cycle is used for all upcoming computations.

The CFD meshes employed in the computations are adopted from Schrape [102] and Grueber [43] and have been created with the Fluent appendant meshing software Gambit 2.4.6. The application of such structured grids to aeroelastic simulations of a NACA profile has already been validated by Schrape. The boundaries have been designated pressure inlet and pressure outlet conditions and periodic boundary conditions at the lateral boundaries. In case of viscous computations the blades have been assigned no-slip condition on the blade surfaces. Moreover, 1D NRBC have been assigned to the outlet in case of unsteady computations.

5.2 2D Model

5.2.1 Inviscid Steady State Simulations

The block structured mesh of a single passage for the inviscid simulations is displayed in Figure 5.1. The mesh consists of seven blocks with one C-mesh block located directly around the profile geometry featuring 87x5 nodes in the near-profile C-mesh and 187x43 nodes in the fluid domain.

In order to quantify the numerical error of this mesh a grid study has been conducted. Therefore, seven different meshes with successively doubled number of grid points in the x- and y-direction, which quadruples the total number of grid points, have been simulated. The mesh with the lowest resolution consists of 1400 elements (50x20 nodes) the one with the highest resolution of 5.242.880 elements (500x100 nodes). In order to guarantee a proper grid quality with reference to the aspect ratio of the elements and their minimum angles, the scalability has been ensured so that the quality features remain almost unchanged.

For all meshes a steady state CFD simulation with an inlet mach number of $Ma_1 = 0.7$ has been performed. The flow is subsonic in the entire fluid domain for this particular inlet condition. Apart from the residuals, global values have been used to judge the discretisation error. With respect to the following unsteady computation of the aerodynamic damping the lift coefficient c_L

$$c_L = \frac{1}{c(p_{t,1} - p_1)} \oint_s p(s) \mathbf{n}(s) \mathbf{e}_y ds \quad (5.1)$$

and moment coefficient c_M

$$c_M = \frac{1}{c^2(p_{t,1} - p_1)} \oint_s p(s) [\{\mathbf{r}(s) - \mathbf{r}_0\} \times \mathbf{n}(s)] \mathbf{e}_z ds \quad (5.2)$$

have been chosen as their values directly influence the accuracy of the aerodynamic damping. Because of the successive refinement, the numerical error due to discretisation decreases constantly and the flow coefficients converge towards grid independent values. Using the Richardson Extrapolation, see Appendix A for details, the grid independent values of c_L and c_M can be extrapolated and the discretisation error can be determined as the deviation from these values. The global coefficients for aerodynamic lift c_L and aerodynamic moment c_M are displayed in Figure 5.2.

As expected, both values converge towards constant values. Finally, the mesh with the highest resolution has a deviation of only -0.18% in c_L and -0.89% c_M with respect to the extrapolated values. Ultimately, the mesh was adapted to the flow situation. The results of this mesh with 8900 elements are included in Figure 5.2 too. The deviation from the

extrapolated values are only -1.0% (c_L) and -0.40% (c_M) which is regarded as sufficient for the upcoming simulations.

The simulation of the steady state flow with the final mesh results in the isentropic mach number plot displayed in Figure 5.3. The isentropic mach number can be calculated from the static pressure distribution on the blade surface according to Equation 5.3.

$$Ma_{is}(x) = \sqrt{\left(\frac{2}{\kappa - 1}\right) \left[\left(\frac{p_{t,1}}{p(x)}\right)^{\frac{1-\kappa}{\kappa}} - 1 \right]} \quad (5.3)$$

The mass averaged total pressure at the inlet $p_{t,1}$ has been taken as reference total pressure. Actually, the stagnation pressure at the leading edge is supposed to equal the total pressure at the inlet which leads to an isentropic mach number of zero at the leading edge stagnation point. In practical applications the discretisation mostly does not resolve the stagnation point properly. Additionally, when using cell-centered finite-volume methods the cell center closest to the wall has always a finite distance from the wall and the values on the blade surface are obtained by extrapolation procedures. Altogether this affects the minimum of the isentropic mach number which is approximately $Ma_{is,min} = 0.2$. Even the reference results of Repar et al. show a minimum isentropic mach number of $Ma_{is,min} = 0.17$. Overall, a good correlation between the results of Repar et al. and the present Fluent simulations are observed.

5.2.2 Inviscid Unsteady Simulations

This section deals with the determination of the aeroelastic eigenvalues of the cascade at inviscid flow conditions. Therefore, unidirectionally coupled fluid-structure-interaction simulations have been performed following two different approaches. First, a finite number of multi-passage simulations have been conducted, followed by a single computation for the determination of the aerodynamic influence coefficients.

Regarding the first approach, the number of passages considered in a multi-passage computation depends on the interblade phase angle σ_n for which the eigenvalues shall be computed. The number of passages and hence the number of blades required can be calculated by assigning the desired interblade phase angle to the first travelling wave mode $n = 1$ and rearranging Equation 3.13 to solve for the number of blades N which yields

$$N = \frac{2\pi}{\sigma_{n=1}}. \quad (5.4)$$

By applying periodic boundary conditions at the upper and lower boundaries of the multi-passage setup the number of blades which is present in the computations directly determines

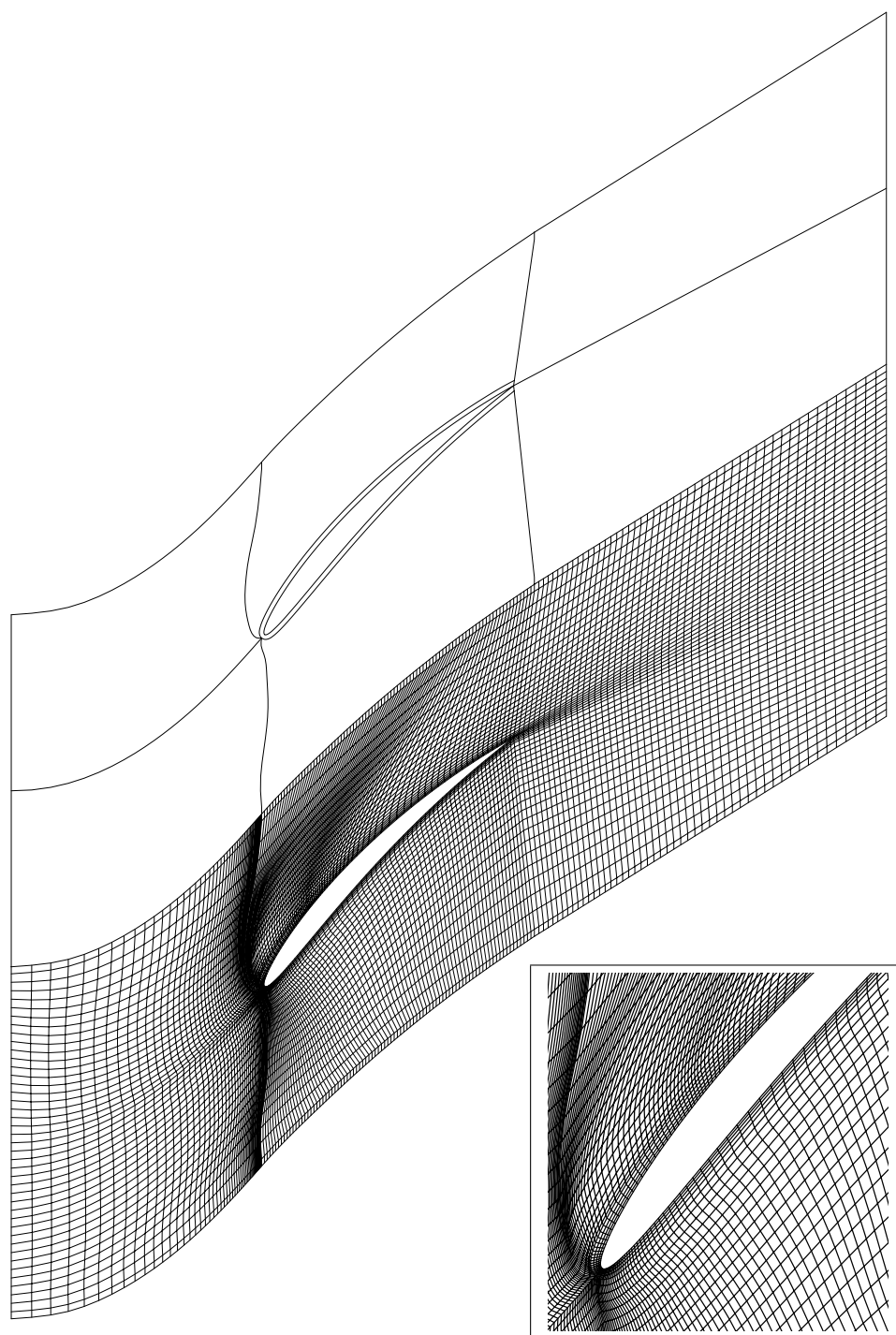


Figure 5.1: Block structure and mesh for the 2D Euler simulations (187x43 nodes)

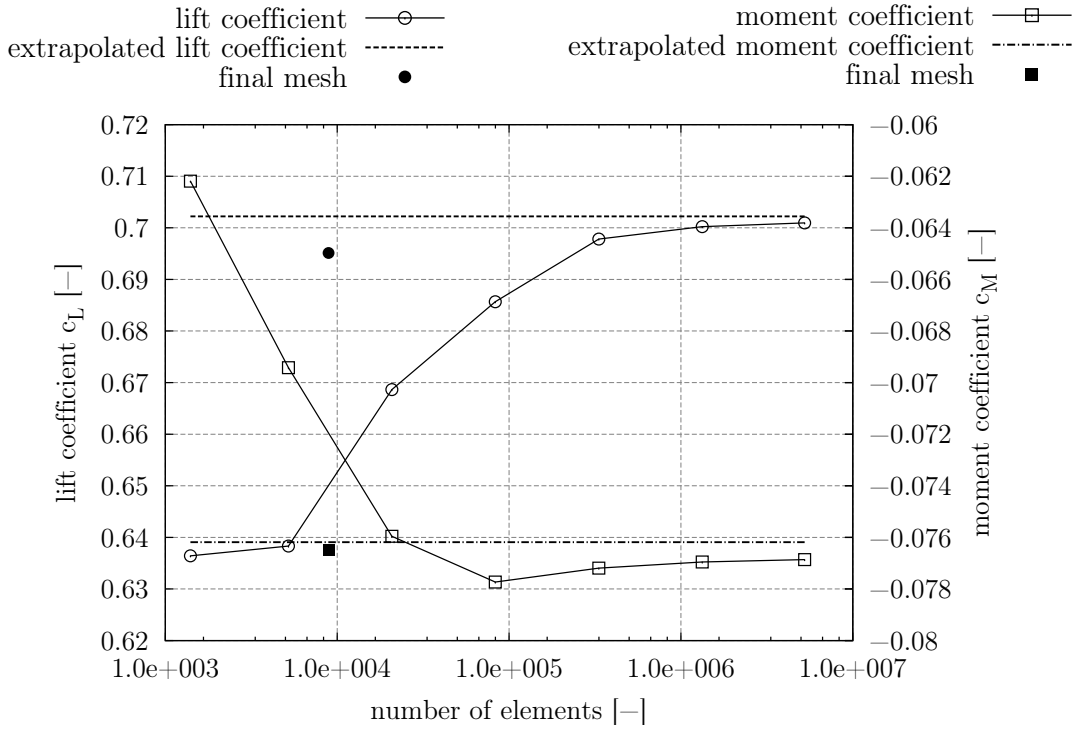


Figure 5.2: Lift coefficient and moment coefficient as function of element numbers, $Ma_1 = 0.7$

the minimum resolvable interblade phase angle, see also [102] for details. During the simulations, the instantaneous pressure fluctuations are recorded which allows for a determination of the relevant force coefficients. These coefficients can then be used to calculate the aeroelastic parameters according to Equations 3.32 to 3.36. Amplitude and phase angle of the calculated force coefficients are regarded to be adequately converged when the change of the magnitude of the force coefficients of two consecutive vibration cycles has degraded to less than 0.1%.

With respect to the determination of the aerodynamic influence coefficients, a cascade of 10 blades has been used. It has to be mentioned that the number of passages is not arbitrary chosen but a trade-off between the total computational time needed and accuracy desired. That is to say, if the number of passages is too low the perturbations propagating from the moving reference blade to the rest of the blades in the domain will pass through the periodic boundaries and superimpose with the true fluctuations on the blade on the other side of the boundary which leads to a misinterpretation of the influence coefficients. In compressor applications the influence of the vibrating blade on the direct neighbouring blades is the greatest while the influence on the rest of the blades in the domain is quite low. Experience gained on the SC10 simulations showed that computations with 10 passages provided sufficiently accurate results. In these simulations only one blade (blade no. 5) vibrates and the unsteady pressure fluctuations are recorded on each blade leading to the aerodynamic influence coefficients. With the help of the transformation given by Equation 3.18, these

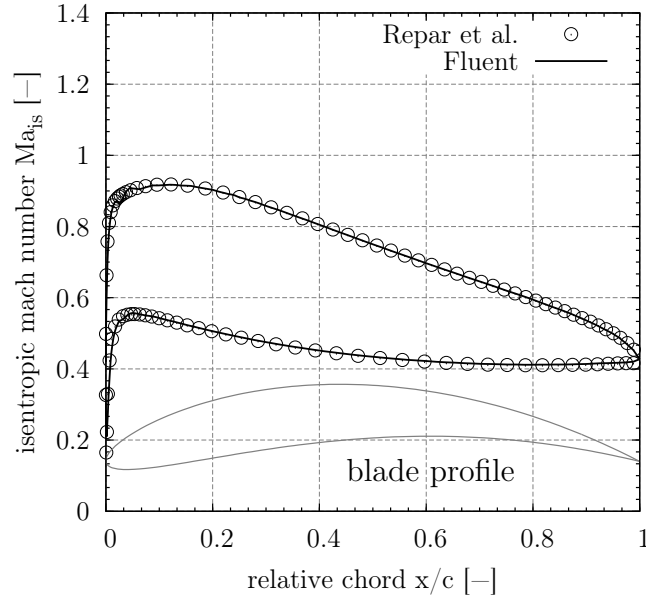


Figure 5.3: Isentropic mach number for inviscid, subsonic ($Ma_1 = 0.7$) flow conditions

influence coefficients can be transformed to the interblade phase angle dependent travelling wave mode force coefficients which enables the calculation of the aeroelastic eigenvalue of a particular travelling wave mode following Equation 3.32.

The results of the abovementioned simulations of heaving motion at subsonic flow conditions are presented in Figures 5.4 and 5.5. The charts display the aerodynamic influence coefficients and the corresponding curves of the aerodynamic damping parameters. For the comparison of the different results, the normalised aerodynamic damping parameter has been chosen which can be calculated from the aerodynamic damping, Equation 3.35, for heaving motion through

$$\Xi = \frac{2m\omega_{\sigma_n}^2 \zeta_{a,\sigma_n}}{h(p_{t,1} - p_1)} \quad (5.5)$$

and for pitching motion

$$\Xi = \frac{2J\omega_{\sigma_n}^2 \zeta_{a,\sigma_n}}{hc^2(p_{t,1} - p_1)}. \quad (5.6)$$

The diagrams of aerodynamic damping parameter contain the same reference curve computed by Repar et al. with Giles' 2D non-reflecting boundary conditions. In contrast, the Fluent results shown have been obtained with 1D NRBC at the outlet and steady pressure inlet boundary conditions. In addition to the standard mesh which has been described in the previous section, a second one with extended inlet and outlet duct has been employed in the computations. At this, the inlet and outlet boundaries are located about 10 chord

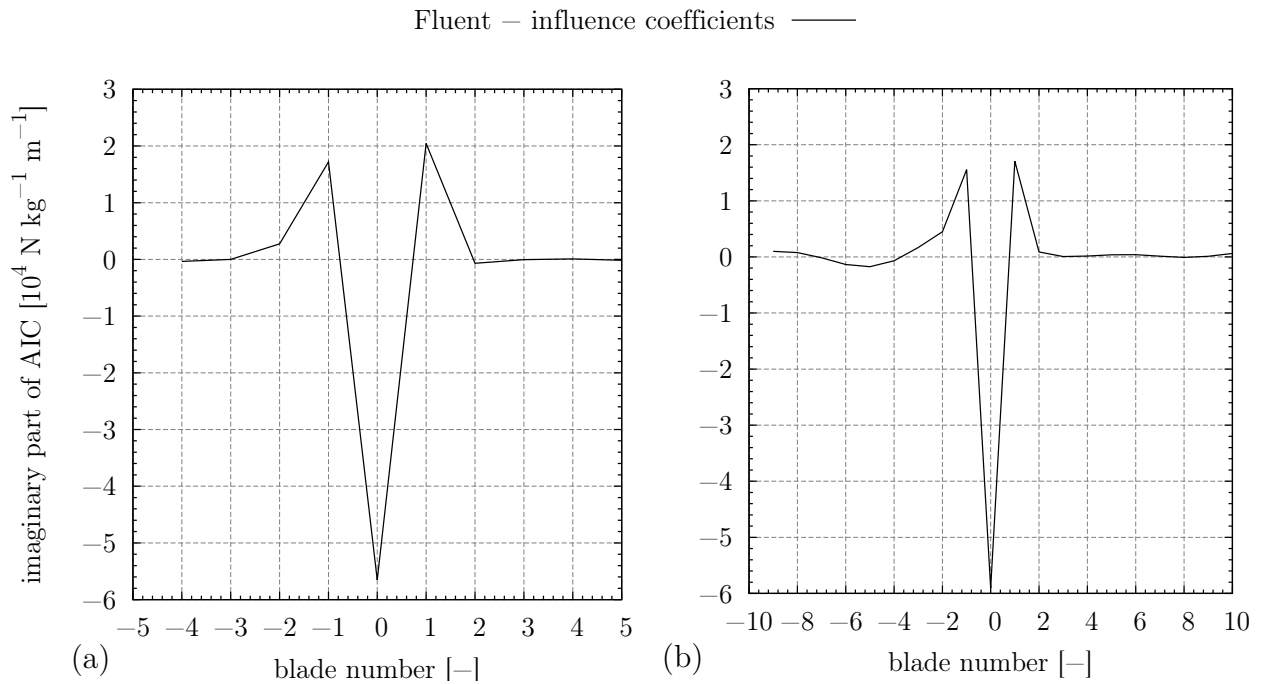


Figure 5.4: Aerodynamic influence coefficients of heaving motion at subsonic flow conditions ($Ma_1 = 0.7$) on (a) standard mesh and (b) on extended mesh

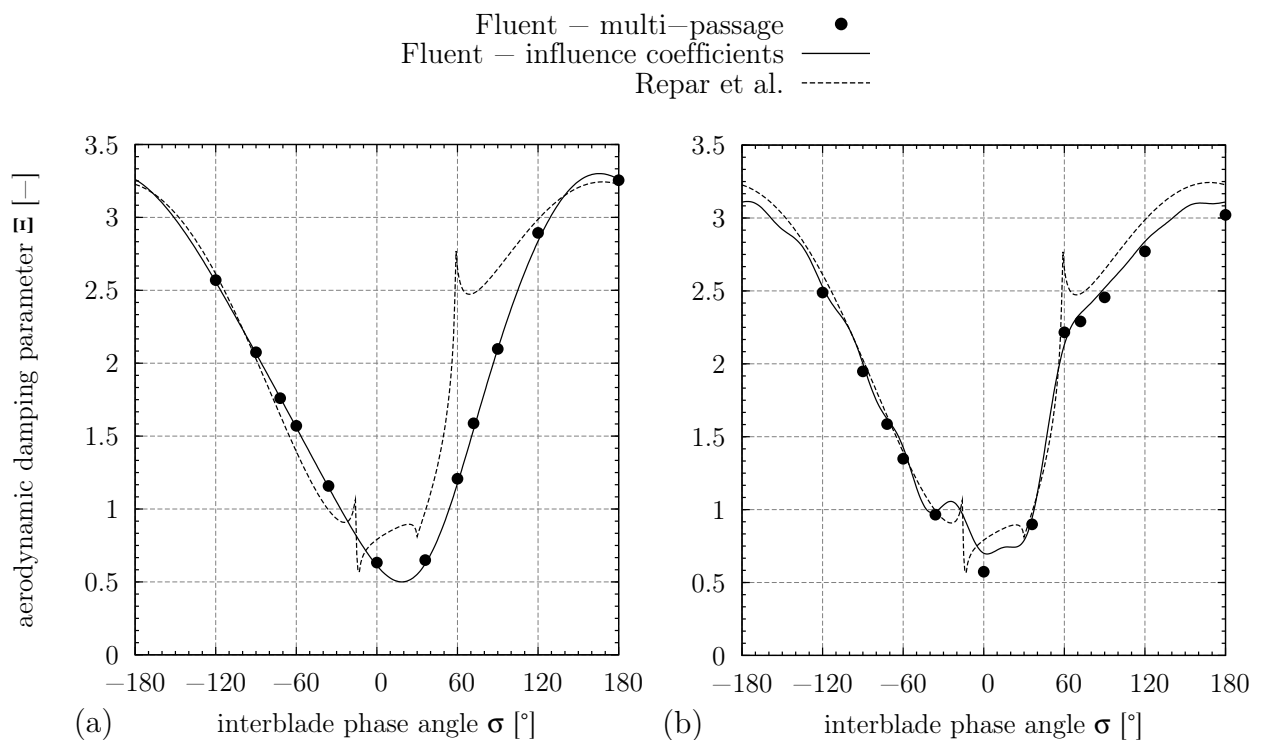


Figure 5.5: Aerodynamic damping parameter as function of interblade phase angle for heaving motion at subsonic flow conditions ($Ma_1 = 0.7$) on (a) standard mesh and (b) on extended mesh

lengths away from the airfoil geometry. This has been done to take account of the aeroacoustic resonances occurring between $-16^\circ < \sigma < 58^\circ$ where acoustic modes are cut-on. Additionally, the cascade has been extended to 20 blade passages.

First the results obtained with the standard mesh, shown in Figures 5.4 and 5.5 (a), are discussed. Comparing the different results, an excellent agreement between multi-passage and influence coefficients simulations can be observed on the standard mesh, justifying the assumption that the aerodynamic influence can be linearly superposed to yield proper travelling wave mode force coefficients. On the other hand, the comparison with the results of Repar et al. shows lack of agreement in the region of acoustic resonance for multi-passage as well as for influence coefficients simulations. The difference is most obvious at the resonance at $\sigma = 58^\circ$ where the aerodynamic damping determined with Fluent is about 55% lower than the reference value of Repar et al. This particular deviation is certainly attributed to the reflectivity of the steady pressure inlet boundary conditions. Comparing the curves outside the resonance region Fluent agrees quite well with the reference results. Here all modes are cut-off and the influence of the boundary conditions' reflectivity is the lowest. The extension of the fluid domain is a common practice to reduce the spurious reflections. By locating the boundaries some chord lengths away from the profile and coarsening the mesh towards the boundaries, the dissipation of the waves can be increased leading to less reflections. Moreover, the number of blade passages has been increased from 10 to 20 to check if the influences on the blades further away from the reference blade have really decreased down to zero. The results obtained with such an extended mesh are shown in Figures 5.4 and 5.5 (b). Obviously, the Fluent results match better with the reference values. Especially the difference in aerodynamic damping at $\sigma = 58^\circ$ reduces to about 17%. Anyhow, it has to be admitted that the agreement also gets worse which is especially the case for $-180^\circ < \sigma < -120^\circ$ and $120^\circ < \sigma < 180^\circ$. However, the eminent agreement of multi-passage and influence coefficients computations is still obvious even in the region of the acoustic resonances which is also a result of the greater number of influence coefficients. From Figure 5.4 (b) it can be seen that the imaginary part of the influence coefficients further away from the moving blade is still different from zero and hence should not be neglected. All in all, the comparison is still quite well with the Fluent results giving more conservative values in the presence of acoustic resonance which is especially interesting for practical issues.

Additionally, simulations of pitching blade motion with 2° amplitude have been conducted for which the results are displayed in Figure 5.6. In general, the same observations as for the heaving motion can be made although the agreement of Fluent results obtained with the extended mesh is better than with the heaving blade motion which is also confirmed by the improved agreement in the region outside the acoustic resonance. Furthermore, the comparatively large number of influence coefficients results in a surprisingly excellent match of influence coefficients and multi-passage results capturing also the peaks in aerodynamic damping at $\sigma = -16^\circ$ and $\sigma = 58^\circ$. The improved compliance is also supported by Figure 5.7

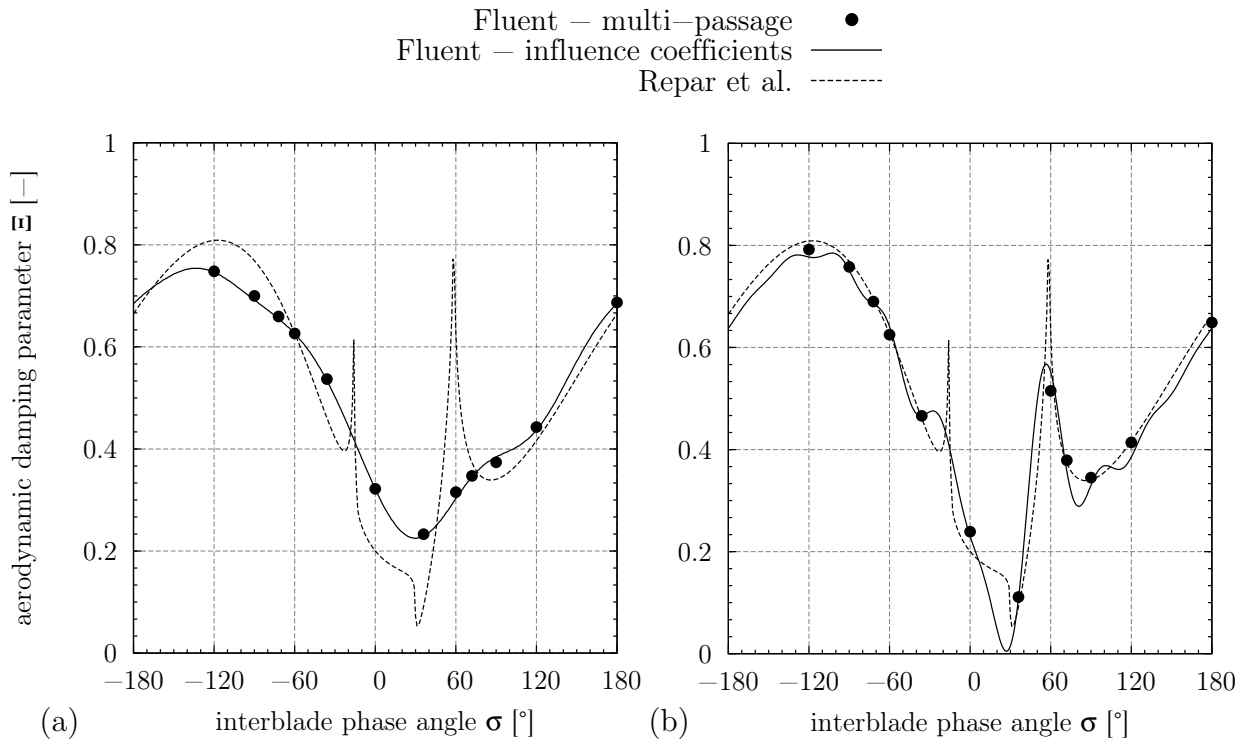


Figure 5.6: Aerodynamic damping parameter as function of interblade phase angle for pitching motion at subsonic flow conditions ($Ma_1 = 0.7$) on (a) standard mesh and (b) on extended mesh

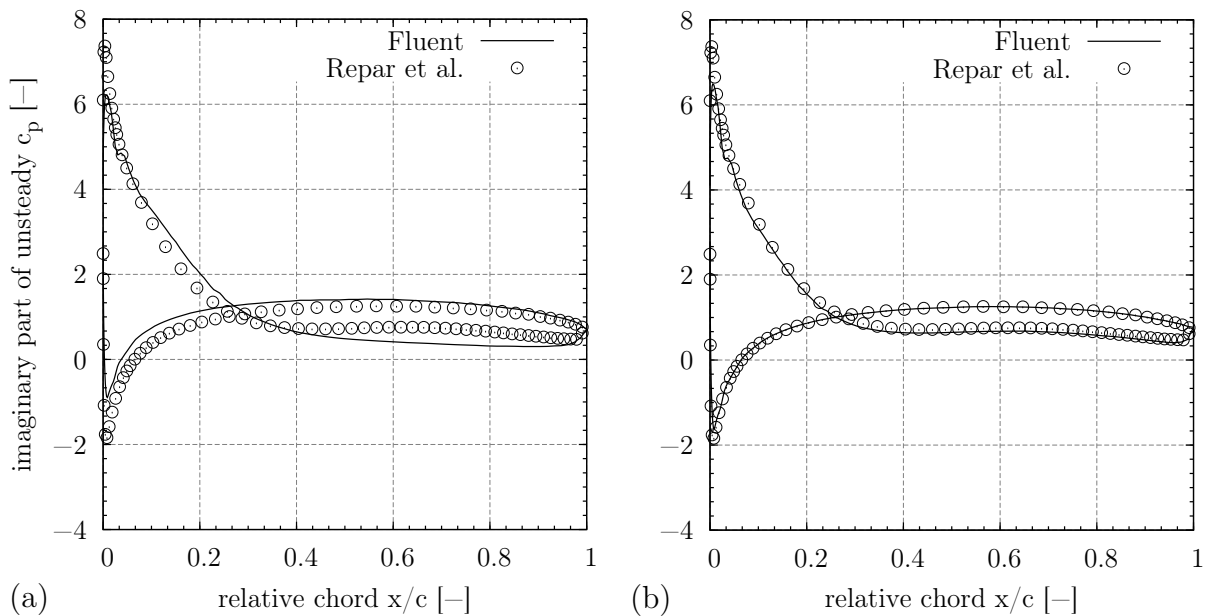


Figure 5.7: Imaginary part of the unsteady pressure coefficient for pitching motion at subsonic flow conditions ($Ma_1 = 0.7$, $\sigma = 90^\circ$) on (a) standard mesh and (b) on extended mesh

showing the imaginary part of the unsteady pressure coefficient. Here the results match best for the extended mesh which shows excellent agreement with the reference results.

5.2.3 Viscous Steady State Simulations

After the aeroelastic simulations at inviscid flow conditions went well, the inclusion of viscous effects shall be analysed next, as a preparation for the three-dimensional viscous simulations. In order to take account of the viscous effects, turbulence is modeled using the one equation eddy viscosity model from Spalart-Allmaras. Additionally, the molecular viscosity is computed as a function of temperature according to Sutherland's law. The mesh is the same as employed in the inviscid simulations with the C-mesh in the near-wall region being adapted to give proper boundary layer resolution.

Concerning the first cell height and the near-wall mesh resolution, the suggestion in Fluent is to set up the mesh such that for the dimensionless wall distance values of $y+ \geq 30$ emerge if wall functions are going to be used. If the boundary layer should be resolved in detail values of $y+ \approx 1$ are recommended. In order to get a better understanding of how the near-wall spacing influences the results, five different variations of C-meshes have been analysed. The parameters varied are the first cell height, the growth factor and the number of cells in the C-mesh region. For each mesh the boundary layer profiles are computed for two representative positions at the suction side of the airfoil at $x/c = 0.505$ and at $x/c = 0.765$. In Figure 5.8 the dimensionless tangential velocity

$$u+ = \frac{u_{\text{tan}}}{u_{\tau}} = u_{\text{tan}} \cdot \sqrt{\frac{\rho}{\tau}} \quad (5.7)$$

is displayed as a function of dimensionless wall distance

$$y+ = \Delta y \frac{u_{\tau}}{\nu_{\text{visc}}} \quad (5.8)$$

where u_{τ} is the shear velocity, ρ is the fluid density, τ the wall shear stress, ν_{visc} the kinematic viscosity and Δy the distance of the first cell center from the wall. To allow for a proper comparison, the theoretical boundary profiles of the viscous sublayer and the logarithmic region are plotted as well. The results confirm the recommendations made concerning the near wall resolution. Looking at the computations without wall-functions first ($y+ < 1$ and $y+ > 1$), a very good agreement between both mesh resolutions and the analytical curves can be found. On the other hand, if wall-functions are employed the first cell height is an important parameter to obtain proper results. If the resultant $y+$ values are around values of 30, notable differences occur leading to deviations of up to 18% with respect to the free stream velocity for the mesh with $y+ < 30$. Furthermore, when first cell heights are used leading to $y+$ -plus values slightly higher than 30 ($y+ > 30$) or well above 100 ($y+ > 100$)

the deviations decrease culminating in an excellent agreement of the computations with the finest and the coarsest near-wall mesh in the logarithmic boundary layer region and the free stream. Since the computational effort for two-dimensional computations is comparatively small, the near-wall spacing of $y^+ > 1$ has been used for all upcoming viscous simulations.

A detail of the C-mesh at the leading edge of the airfoil is displayed in Figure 5.9 (a) together with the isentropic mach number of viscous steady state simulation at subsonic flow conditions. Again, the agreement between the Fluent results and the reference results of Repar et al. is quite well which is certainly due to employing the same turbulence model, hence no significant differences have been expected.

5.2.4 Viscous Unsteady Simulations

In contrast to the inviscid simulations, only the pitching motion was simulated for the viscous flow condition. The results are presented in Figure 5.10 in contrast to results of Repar et al. obtained with 1D NRBC, Figure 5.10 (a), and those computed with Giles' 2D NRBC, Figure 5.10 (b). First of all, an eminent match of influence coefficients and multi-passage computations is noted. Concerning the comparison with the reference results, the agreement with the Fluent computations is sufficient for the results obtained on the standard mesh. Here, the biggest deviations occur for small positive interblade phase angles which is probably due to lack of non-reflecting boundary conditions at the inlet. This assumption is also supported by the results obtained on the extended mesh. Comparing them with the reference results of Repar et al. the match is much better than with the standard mesh, especially in the region $0^\circ < \sigma < 50^\circ$. Furthermore the improvement in compliance is the same as already observed for pitching at inviscid flow conditions.

The results of the aeroelastic computations of 2D standard configuration 10 can be summarised shortly:

- excellent agreement of multi-passage and influence coefficients computations is observed for all computations,
- the match of Fluent computations on standard mesh and reference results with high fidelity boundary conditions is sufficient due to lack of proper NRBC at the inlet with the biggest deviations appearing at low interblade phase angles and near resonant condition,
- the compliance increases when an extended mesh is employed in the computations with the influence coefficients being capable of reproducing acoustic resonances when the inlet and outlet boundaries are located further away from the profile and the number of blade passages and hence of the computed AIC is increased.

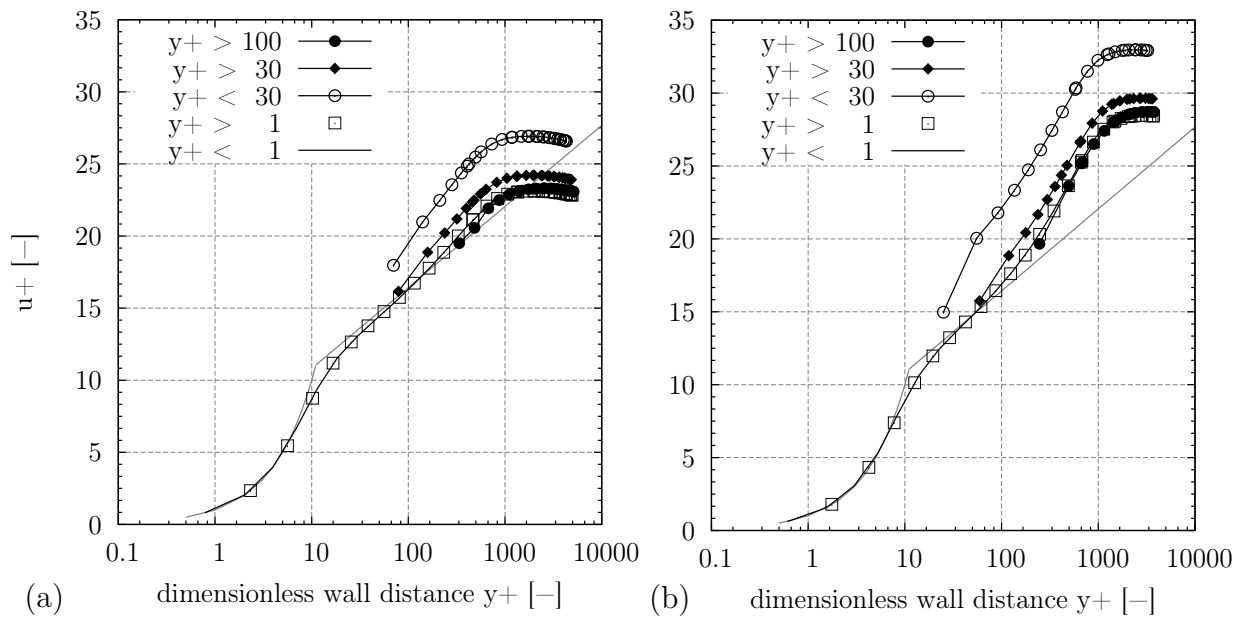


Figure 5.8: Near wall velocity profiles at (a) $x/c = 0.505$ and (b) $x/c = 0.765$

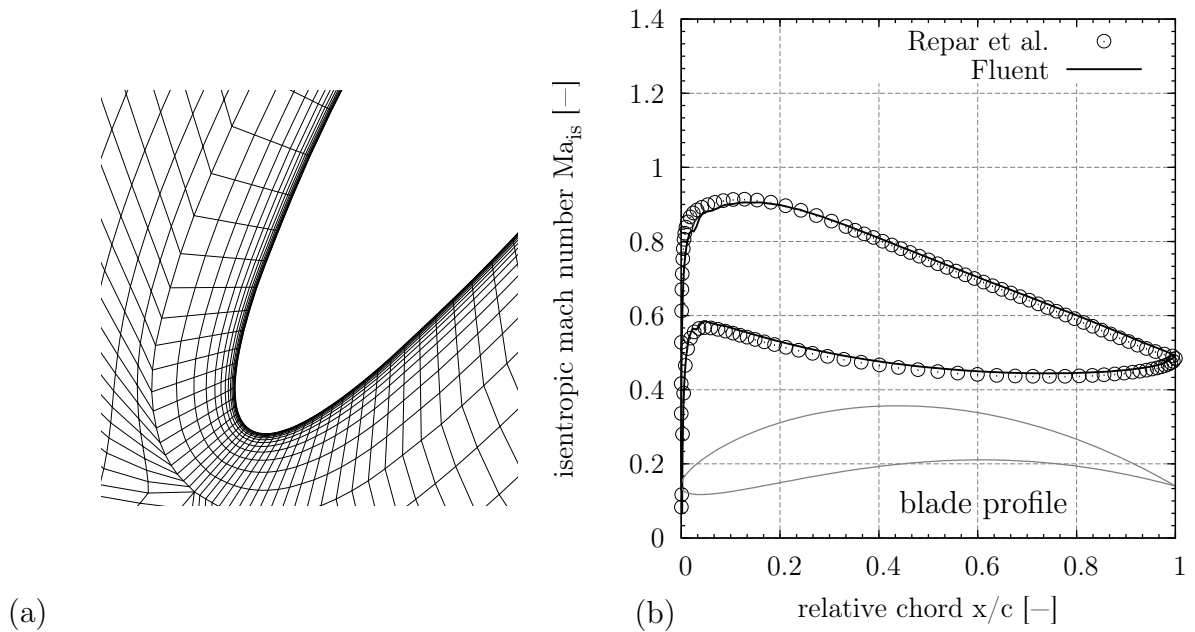


Figure 5.9: Mesh detail of C-mesh (a) and isentropic mach number (b) for viscous, subsonic flow condition, $Ma_1 = 0.7$

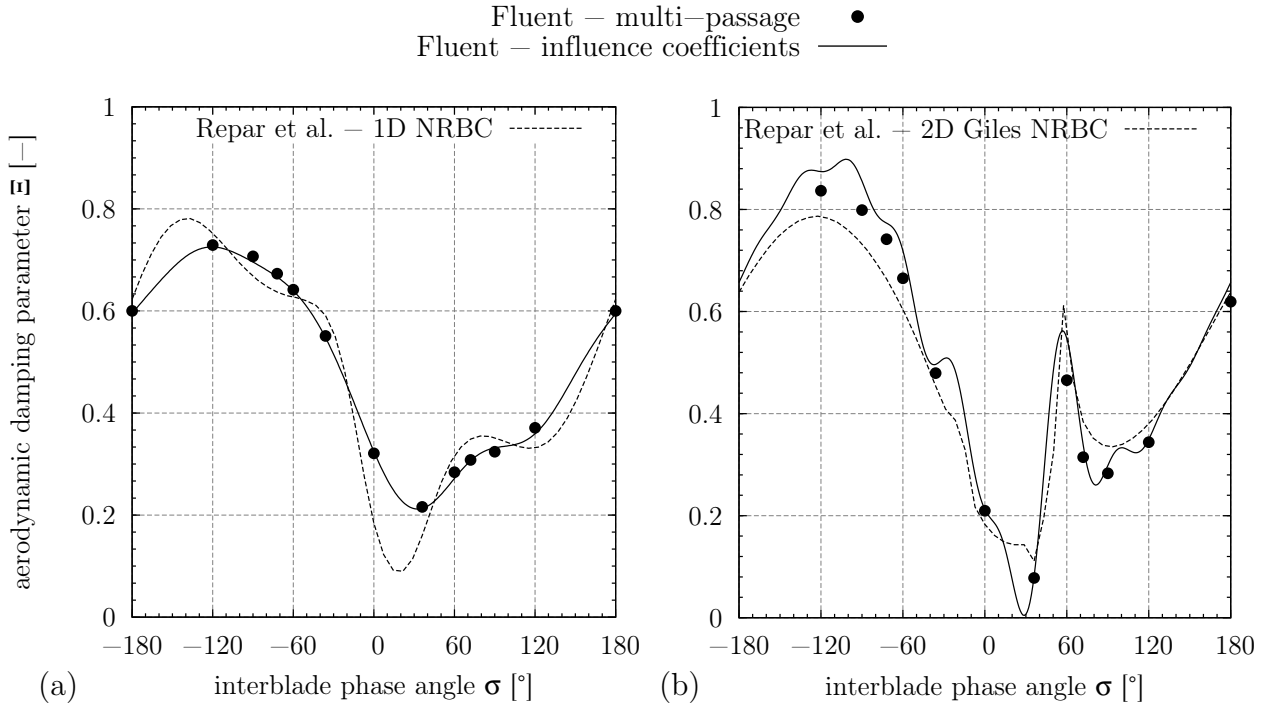


Figure 5.10: Aerodynamic damping parameter as function of interblade phase angle for pitching motion at subsonic, viscid flow conditions ($Ma_1 = 0.7$) on (a) standard mesh and (b) on extended mesh

5.3 3D Model

After the two-dimensional models have been analysed, the three-dimensional annular cascade of the SC10 has been simulated. Therefore, the 2D cross section of the profile previously employed in the 2D simulations is used to construct the 24 straight (untwisted) blades of the cascade. The parameters of the resulting annular cascade have been summarised in Table 5.1. There is no tip gap modeled and the blade is assumed to slide over hub and casing during blade motion. Following the proposal of Repar et al., the annular cascade was assumed to be stationary which is in contrast to the computations performed by Kemme [63] and Montgomery and Verdon [83] who simulated a rotating cascade. Hence, the inlet flow angle is constant over the entire cascade height.

The objective of the simulations is to verify the methods used before on a three-dimensional cascade with complex flow features. Although only a simple blade pitching motion is applied, the calculation of the force as well as the influence coefficients is carried out in two different ways. On the one hand, the coefficients are determined by simply calculating the aerodynamic moment according to Equations 3.24 and 3.25. Since these equations only hold true for simple pitching motion, the relevant coefficients are also determined employing the most general form of Equations 3.26 and 3.27. This is done with regard to the upcoming simulations of a real compressor blade with flexible blade mode shapes.

In the course of the analysis of the annular cascade, the inviscid flow condition is considered first, providing a basis for the discussion of the influences of the viscous flow features. The meshes comprise 14 radial layers for the inviscid simulations and 33 radial layers for the viscous computations employing wall-functions at hub and casing giving an average $y+$ value of $y+ \approx 100$. The mesh in a radial section is the same as previously used in the two-dimensional inviscid and viscous computations, respectively. The number of nodes per blade passage is 147488 for the inviscid mesh and 394284 for the viscous one.

Since the focus of the simulations is not on the detailed analysis of the influences of boundary conditions on the attainable results but on the validation of the calculation methods and due to CPU restrictions, computations with inlet and outlet relatively close to the profile² have been carried out only. In case of unsteady simulations, the 1D NRBC available in Fluent has been used at the outlet.

The following sections present the results of the inviscid and viscous computations at the same time which allows for a holistic analysis of the different flow effects.

5.3.1 Steady State Simulations

At first the results of steady state computations are presented in Figures 5.11 and 5.12. All plots show an excellent agreement between the present results and the ones obtained by Repar et al. In Figure 5.11 the isentropic mach number is shown at two distinct radial cuts. The 3D inviscid results vary only little on the two radial positions. Furthermore, as it was intended to, the inviscid results at 50% span compare very well with the 2D computations.

In contrast, both mach number plots of the viscous flow condition show significant differences compared to the two-dimensional results. The reason for the deviations of the viscous flow results is the consideration of viscosity influences on the one hand side and a flow separation at the suction side of the airfoil on the other side. This separation occurs between the hub and approximately 40% blade span and induces a massive blockage of the passage which makes a reduction of the static outlet pressure of about 11% necessary to adjust the inlet mach number to $Ma_1 = 0.7$. The numerical oil streak pattern of the steady state solution is shown in Figure 5.13. In addition to the visual evaluation of the flow pattern, the friction coefficient presented in Figure 5.12 indicates flow separation too. At 10% span the flow is detached over almost 60% of blade chord while it is attached over the entire chord length at 50% span. The quite promising results of the steady state simulations give rise to unsteady simulations of pitching blade motion presented in the following section.

²The boundaries are located about one chord length away from leading and trailing edge respectively. This configuration corresponds to the standard mesh used in the two-dimensional simulations.

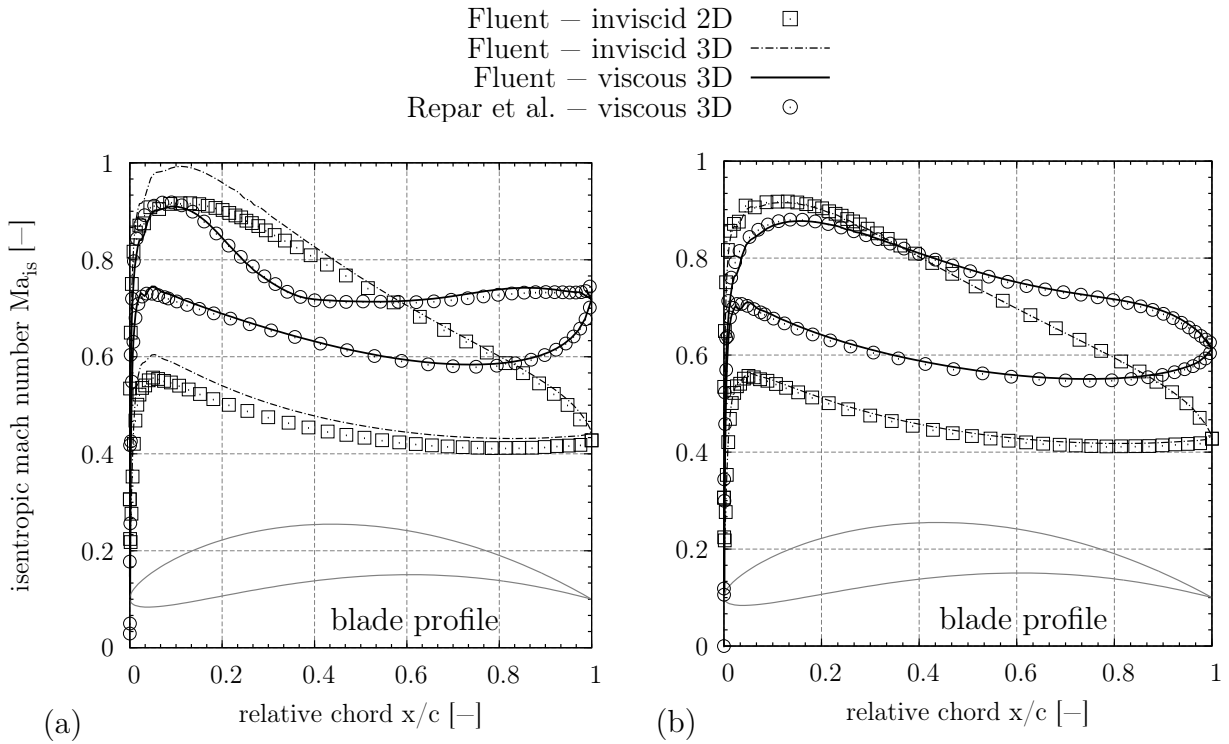


Figure 5.11: Isentropic mach number of inviscid and viscid computations at (a) 10% span and (b) 50% span

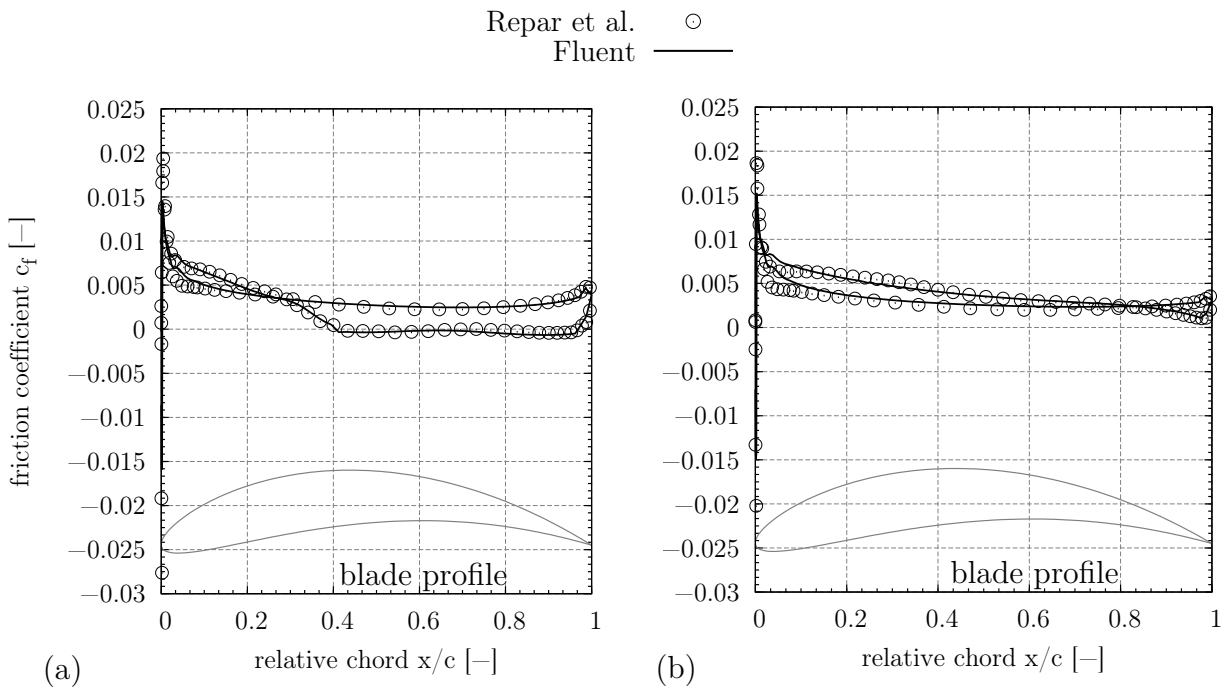


Figure 5.12: Friction coefficient of viscid computations at (a) 10% span and (b) 50% span

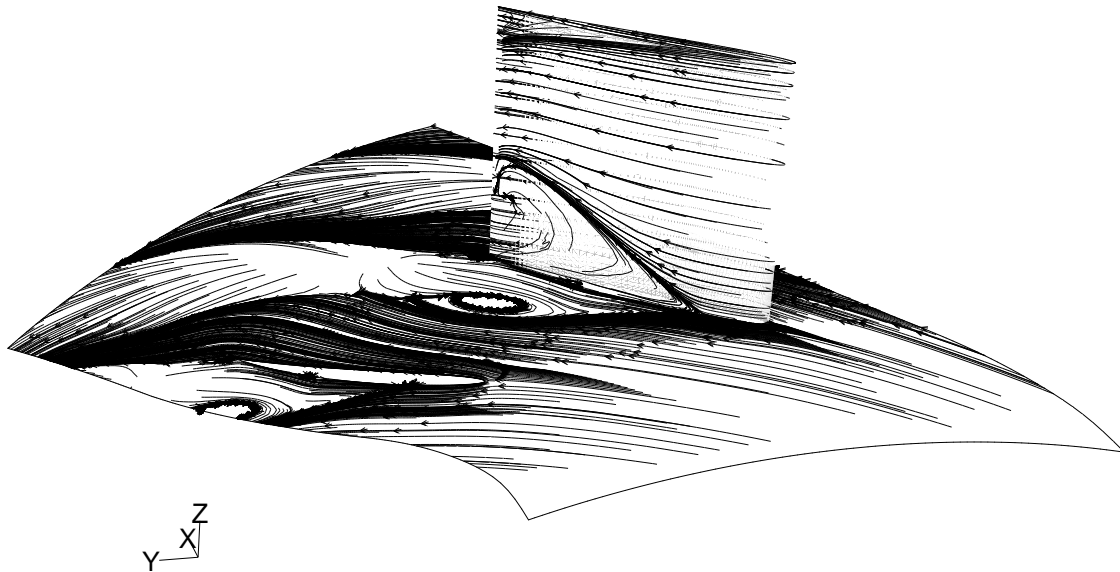


Figure 5.13: Numerical oil streak pattern of 3D steady state, viscous computations

5.3.2 Unsteady Simulations

The unsteady computations have been carried out for the pitching motion only, for inviscid and viscous flow conditions. With the 2D simulations, it has been shown that the number of passages involved in the determination of the influence coefficients is essential for the quality of the results. Therefore the 3D annular cascade has been simulated as full assembly regarding the maximum number of influences possible. For the inviscid simulations, two different meshes have been considered. In addition to the standard mesh, an extended mesh with the inlet being located at about five chord lengths from the airfoil away has been simulated. Since non-reflecting boundary conditions are used at the outlet, only the inlet is placed further upstream. The results of the inviscid simulations are presented in Figure 5.14.

Here, the influence of the additional inlet duct is clearly visible. While the results obtained on the standard mesh show considerable differences especially at low IBPA, which is comparable to the results of the 2D computations, the results of the extended mesh compare a little better with the reference results obtained by Repar et al. Furthermore, Fluent predicts an acoustic resonance peak at $\sigma = 63^\circ$ which is not present in the reference results attributed to the usage of 1D NRBC only. Additionally, a comparison between employing simple coefficients for rigid body pitching motion and coefficients for general motion is given in the chart. As expected, both approaches give the same results allowing for analyses of more complex mode shapes. Analogously to the 2D computations, the comparison of multi-passage simulations and influence coefficients is excellent.

For the viscous, unsteady simulations only the standard mesh with steady boundary conditions at the inlet and 1D NRBC at the outlet has been simulated. Simulations with an

extended mesh have been spared out due to CPU restrictions. It has been shown with the 2D computations that the methods are capable of capturing acoustic resonances when proper boundary conditions are used but since in real turbomachinery applications the "boundaries" in front of and behind a blade row always combine certain amounts of permeability and reflection of pressure fluctuations neither the steady numerical boundary conditions nor the non-reflecting ones will reproduce real engine conditions. Of course the aim should always be to gain results to be easily interpretable but since the focus here is not on the analysis of the influences of the numerical boundary conditions but on the validation of the aeroelastic methods the comparison is restricted to reference results with 1D NRBC obtained by Repar et al. only. The results of the standard mesh showed regular agreement for the 3D inviscid annular cascade with the greatest differences being eliminated when an extended mesh is used.

Taking a look at the results of the 3D viscous cascade, the match of the values computed on the standard mesh with the reference results obtained with 1D NRBC is even better than observed for all previous simulations. It is somewhat surprising that the greatest differences now occur at $\sigma = 180^\circ$ while the compliance at $\sigma = 0^\circ$ is rather good. This is the inverse effect compared to the inviscid computations. At $\sigma = 180^\circ$ Repar et al. predict unstable condition with negative damping while the Fluent results show positive damping well above zero. Finally the global analysis of the results suggest the assumption that non-linear effects might be of great importance for the 3D viscous cascade. It can be stated that the differences in the numerical treatment of Repar et al. employing a linear solver and Fluent considering the non-linear Navier-Stokes equations plus additional effects of the numerical boundary conditions add up to the deviations between the results obtained with Fluent and the reference results. However, due to experience gained from the previous computations the major effect is probably attributed to the steady boundary conditions at the inlet.

Another issue is the poor agreement of multi-passage and influence coefficients results. For the integration of the influence coefficients into the EBM, it is necessary that the aerodynamics they represent are sufficiently comparable with the multi-passage results. If the emphasis is on a qualitative representation of interblade phase angle dependent aerodynamic effects, the influence coefficients as calculated with Fluent should be adequate. But if the effects are intended to be modeled as determined in multi-passage computations the influence coefficients can be determined by transformation from the travelling wave mode coefficients to blade individual influence coefficients as described by Equation 3.17. With the help of these influence coefficients the entire damping curve can be reconstructed from the multi-passage results as shown in Figure 5.15.

In summary, the following statements can be made:

- Excellent agreement of multi-passage and influence coefficients computations is observed for inviscid computations,

-
- the match of inviscid Fluent computations on the standard mesh with the reference results obtained with high fidelity boundary conditions is sufficient due to lack of proper NRBC at the inlet with the biggest deviations appearing at low interblade phase angles and near resonant conditions,
 - the compliance increases when the mesh is extended at the inlet with the influence coefficients being capable of reproducing acoustic resonances,
 - in case of viscous computations, the agreement is better for small interblade phase angles while considerable differences occur at greater ones,
 - on the contrary to all previous computations of the SC10, the results of viscous aerodynamic influence coefficients and multi-passage computations show significant differences which can be overcome by reconstruction of the influence coefficients from travelling wave mode coefficients.

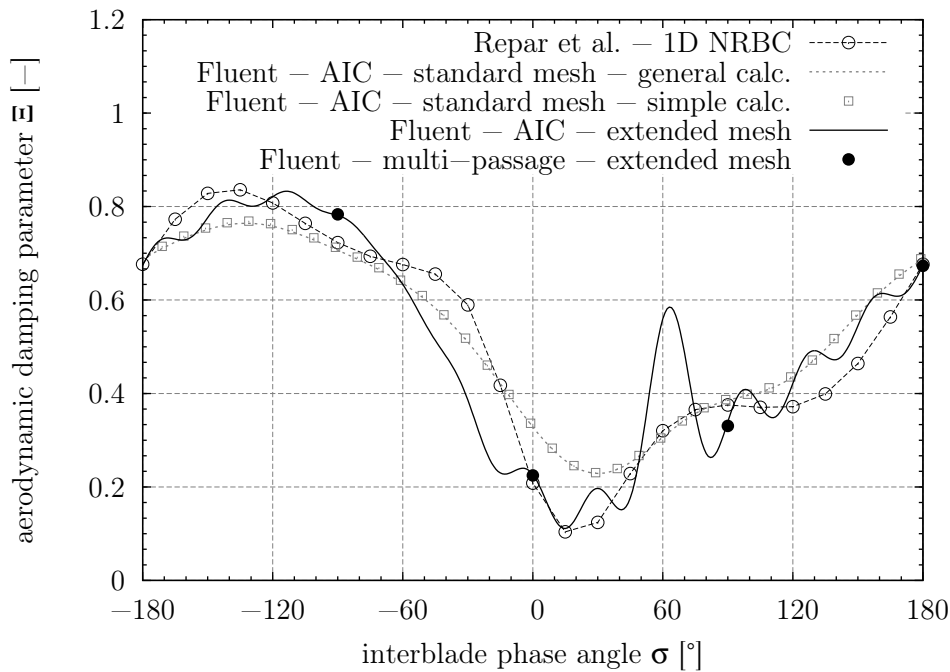


Figure 5.14: Aerodynamic damping parameter of pitching motion at inviscid subsonic flow condition

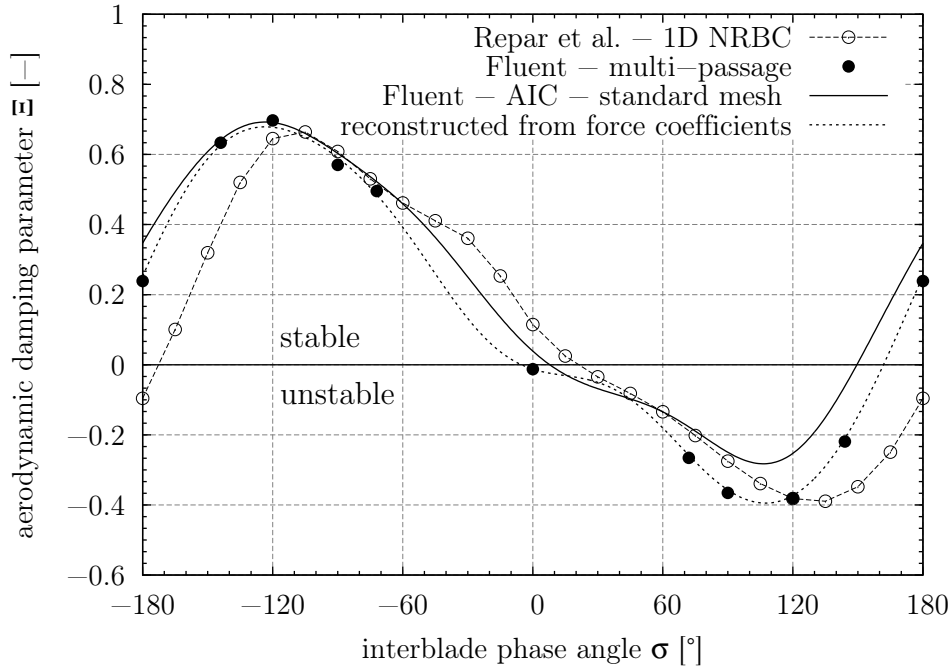


Figure 5.15: Aerodynamic damping parameter of pitching motion at viscous, subsonic flow condition

Chapter 6

E3E - Rotor 6

Using two stages of a modern high pressure compressor (HPC), the aeroelastic analysis of blisk rotors employing the equivalent blisk model is presented exemplarily. For this purpose a 2D model of an HPC rear stage and a front stage 3D model of the same compressor have been analysed. The analyses feature bidirectionally coupled fluid structure interaction simulations (FSI) and experimentally determined mistuning patterns.

The analyses are subdivided into the following parts:

Initially the 2D model of the Engine 3E's¹ (E3E) rotor 6 has been simulated to obtain the aeroelastic eigenvalues and forced response computations of a random mistuning distribution have been conducted comparing different treatment of aerodynamic forces in the model. Within the analyses, EBM computations with equivalent aerodynamic elements as presented in Section 4.2.2 and aerodynamic influence coefficients as described in sections 3.2 and 4.2.3 have been employed. Additionally, bidirectionally coupled fluid structure interaction simulations with the commercial CFD code Fluent have been performed and the results have been compared to the one obtained with the EBM. Subsequently, structural and aeroelastic computations of a 3D model of the E3E's rotor 1 have been performed. Therefore the modal parameters of the mistuned system have been derived from experimental results. According to these results a FE model as well as an EBM model of the rotor 1 have been updated. Consequently, the tuned system has been derived from the mistuned one with the tuned natural frequencies being the mean values of the mistuned ones. With the knowledge of the tuned quantities, the vibration induced fluid forces and hence the aerodynamic damping values have been determined. Afterwards, forced response analyses were conducted using the EBM representing the tuned and the mistuned system respectively. During these analyses the parameters of structural and/or aerodynamic coupling have been varied.

¹The E3E - Technology program aims at jet engine improvements concerning topics of economy, efficiency and environment.

6.1 The E3E High Pressure Compressor

The aeroelastic analyses have been carried out using the high pressure compressor of the E3E. Within the E3E engine propulsion technology program the 9 stage HPC has been the subject of intensive research. The HPC features rotor blisks with modern aerodynamic blade design features. Figure 6.1 exemplarily displays a conventional blade which is connected with the disk through slots and a modern rotor in blisk design. The focus of the present work are the rotors of the first and sixth stage of the HPC. The blisks analysed within this work correspond to phase I of the E3E program. Details about the E3E program have been summarised by Klinger et al. [70] for example. The advantages and disadvantages arising from the blisk design have been addressed in Chapter 1.

The condition of maximum take-off (MTO) has been chosen as operating point for which the analyses are going to be conducted. According to Grieb [44] the MTO condition is the most significant one when judging the structural integrity of civil turbofan engine compressors and hence one of the most interesting ones concerning structural and aeroelastic analyses.

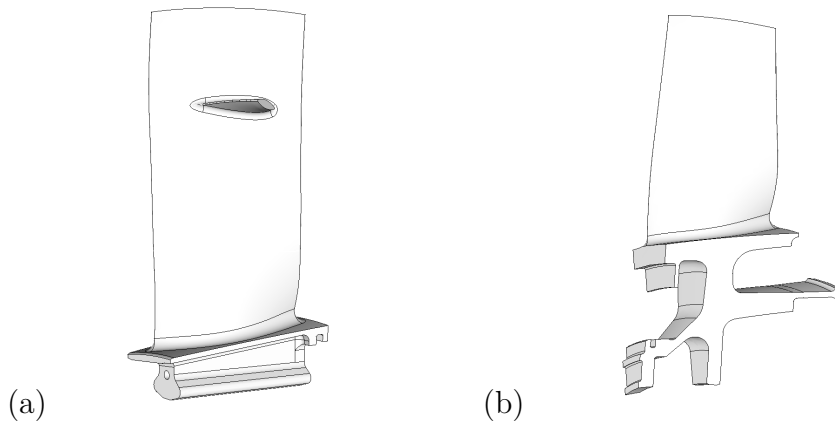


Figure 6.1: Initial blade with root (a) and improved rotor blisk design (b)

6.2 2D Linear Cascade of Rotor 6

Prior to the extensive analyses of the mistuned rotor 1 blisk, two-dimensional computations for a meanline approximation of the rotor 6 have been performed. The objective is, to apply the aeroelastic methods validated in the previous chapter, at a rather academic example, to a 2D model which is derived from real engine hardware and to validate EBM simulations with aerodynamic effects included against bidirectionally coupled fluid-structure-interaction simulations of the tuned and a mistuned cascade. Throughout the entire section, the EBM model of rotor 6 features an infinitely stiff disc which means that blade vibrations are only coupled through aerodynamic forces.

The vibrations of the rotor 6 linear cascade have previously been investigated by Schrape et al. [102]. The focus of this work was on the determination of the aerodynamic damping and the aeroelastic frequency of the cascade to provide input for the identification of the equivalent aerodynamic elements [7], [9]². The investigated blade motion is a single degree of freedom heaving motion in the direction normal to the blade chord.

In the work of Schrape et al. the aeroelastic coupling was realised via MpCCI which is a commercial FSI tool that has been used to couple Abaqus and Fluent. On the contrary to that, the current work makes use of User-Defined-Functions (UDF) available in Fluent. Equally to sections 5.2.2 and 5.2.4 one UDF is used to realise a unidirectional coupling where only the blade displacements are transferred to Fluent to deform the mesh in the fluid domain while the blade motion remains unaffected by the aerodynamic forces. Additionally, a second UDF is employed which facilitates a bidirectional coupling between blade motion and the flow by solving SDOF equations of motion and allows for forced response simulations of the tuned and mistuned cascade in Fluent. These simulations are then used to validate EBM results obtained with aerodynamic influence coefficients included.

The 3D model of the rotor 6 blisk is displayed in Figure 6.2 (a). As can be seen from the cross sections, Figure 6.2 (b), the blade is almost two-dimensional with only low twist from hub to tip. Consequently, a projection of the midspan cross section to a two-dimensional plane is used to set up a linear cascade of the rotor 6. The blade height was assumed to be half the blade span of the 3D model. This is the same approximation that has previously been used by Nipkau in 2007 [87]. As already mentioned, MTO operating conditions of have been chosen. A summary of the relevant parameters is given in Table 6.1.

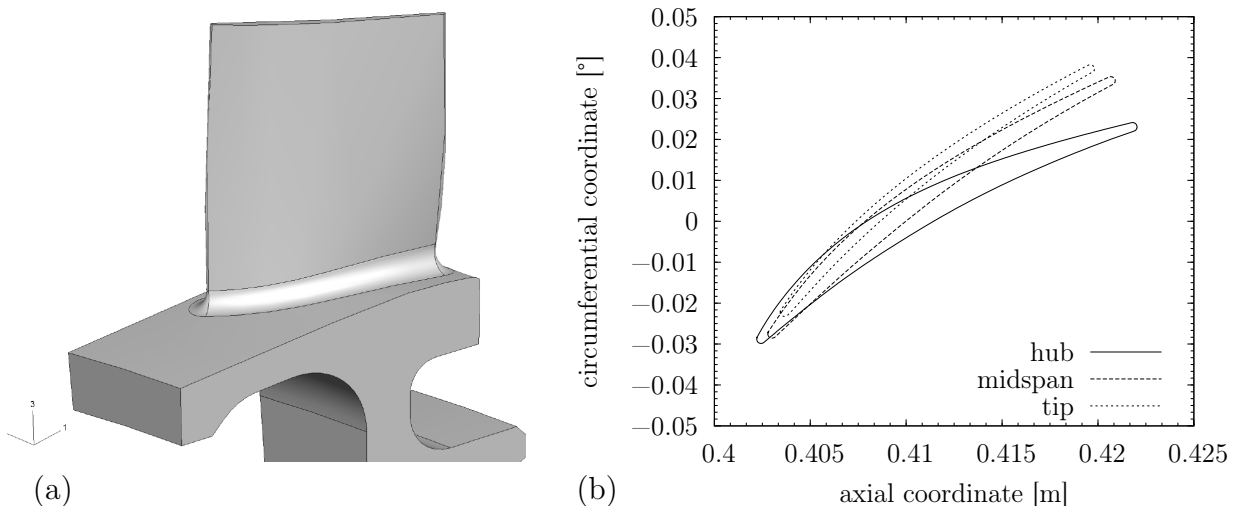


Figure 6.2: 3D FE model (a) and blade sections (b) of rotor 6

²The former identification process has been replaced by the one given in Section 4.2.2.

Table 6.1: Operating conditions E3E rotor 6

structural parameters		
number of blades rotor 6	N	87
number of blades in the cascade	N_{2D}	9
speed of rotation	Ω_r [rad/s]	1597.71
aerodynamic parameters		
mach number at inlet (midspan)	$Ma_{1,rel}$	0.76
velocity angle at inlet (midspan)	$\beta_{1,rel}$ [°]	49.2
chord length (midspan)	c [m]	0.023
Reynolds number (midspan)	Re	$1.3 \cdot 10^6$
pressure ratio	Π	1.292
aeroelastic parameters		
reduced frequency (chord at midspan)	ω^*	1.04
blade mass ratio	μ	95
amplitude of vibration	\hat{y}	0.01c

The mesh employed in the computations is a semi-structured one with quadrilateral cells in the near wall boundary layer region while the rest of the domain is meshed using triangular elements. Analogously to the computations of the SC10, the simulations feature the one-equation turbulence model of Spalart and Allmaras with wall-functions. The mesh, shown in Figure 6.3, comprises a total number 4805 nodes in a single passage domain with 10 cell layers used to resolve the near wall region with an average y-plus of about 60. Again, the numerical boundary conditions are a pressure inlet with prescribed total pressure, total temperature and velocity angles, a static pressure outlet condition, no slip wall boundary condition on the blade surface and periodic boundary conditions at the upper and lower passage boundaries. Concerning the solver settings, the explicit density based solver with node-based gradient evaluation has been used for the rotor 6 computations. On the contrary to the simulations of the SC10 only steady boundary conditions have been used at inlet and outlet. This has been done in the awareness that pressure waves may not pass the boundary and influence the results of the aeroelastic computations. Nevertheless, since the same conditions have been used during all simulations, the computations have been consistently carried out.

The previous work showed a good comparison between the results of two- and three-dimensional CFD simulations with respect to steady state flow solutions and aeroelastic simulations. Nonetheless, the focus of this section is on the comparison of bidirectionally coupled FSI simulations and EBM computations that is why no correlations with three-dimensional computations are presented here. For details about the correlation with 3D computations see Schrape et al. [102].

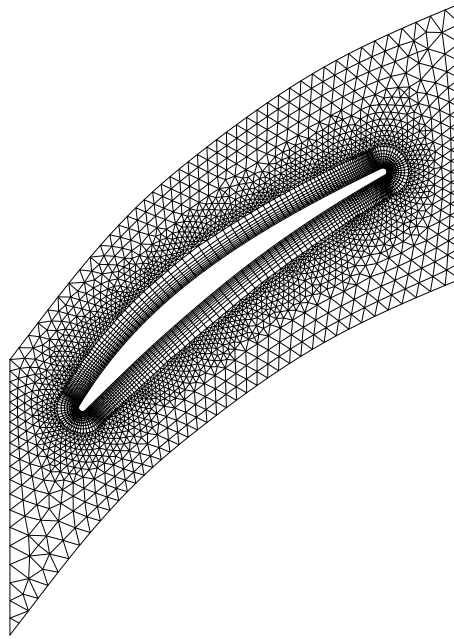


Figure 6.3: 2D section model of rotor 6

6.2.1 Tuned Cascade Results

In order to characterise the aeroelastic behaviour of the tuned cascade, uni- and bidirectionally coupled FSI simulations of heaving motion have been performed to identify the aeroelastic eigenvalues. The objective of these computations is to identify the interblade phase angle dependent aeroelastic parameters of the tuned cascade. First, unidirectional simulations with prescribed blade motion have been analysed. Analogously to the computations performed on the standard configuration 10, multi-passage computations have been conducted employing a number of single passages corresponding to the desired interblade phase angle of a travelling wave mode and the aeroelastic computations have been regarded as fully converged when the change of magnitude of the force coefficients evaluated for two consecutive vibration cycles has degraded to less than 0.1%. Throughout the unsteady simulations a temporal resolution of 150 time steps per vibration cycle has been used.

Naturally, the aeroelastic vibration frequency is not known a priori. Hence the structural natural frequency of the 1st flap blade mode of the 3D FE model ($f=2578\text{Hz}$) has been used initially. After the first eigenvalues have been calculated, the simulations are repeated with the aeroelastic frequency obtained from the imaginary part of the eigenvalues.

Moreover, a cascade configuration consisting of nine blades has been used to calculate the aerodynamic influence coefficients. Making use of the transformation given by Equation 3.18, these influence coefficients can be used to determine the interblade phase angle dependent travelling wave mode force coefficients, Equation 3.18, and hence the aeroelastic eigenvalues of the particular travelling wave modes. The influence coefficients are computed to integrate

the aerodynamic influences in the EBM and to enable comparisons with bidirectionally coupled FSI simulations. The imaginary part of the calculated influence coefficients calculated at the structural natural frequency (2578Hz) and at frequencies $\pm 10\%$ are displayed in Figure 6.4. It shows that, as expected, the influences on the direct neighbouring blades are the greatest while the rest of the blades is only little effected by the vibration of the reference blade. Hence, for this particular model, nine influence coefficients are enough to reproduce the aerodynamic influences of all blades vibrating in travelling wave modes.

The results of the aforementioned simulations, presented in Figure 6.5, show no significant differences between the various aeroelastic methods. The eigenvalues determined by unidirectional simulations with structural and aeroelastic frequency are nearly the same. Exemplarily, the aeroelastic frequency of a vibration at $\sigma = 0^\circ$ is only 5‰ lower than the structural frequency. The reason for that is that in turbomachinery applications the additional stiffness coming from the fluid forces is usually much smaller than the mechanical stiffness of the blade. Especially in rear stages of compressors, the vibration of low aspect ratio blades with low flexibility is dominated by the blade stiffness.

Furthermore, the eigenvalues computed from the aerodynamic influence coefficients are plotted in Figure 6.5. Here, the results also agree quite well with the unidirectional multi-passage simulations. Anyway, it must be stated that the differences in aeroelastic frequency are slightly greater with positive interblade phase angle than for the corresponding negative ones. While there is almost no difference between the eigenvalues apparent for $\sigma = 0^\circ$ the discrepancy at $\sigma = 180^\circ$ is clearly visible.

In addition to the linear methods, bidirectionally coupled FSI simulations of blade vibrations in travelling wave modes, taking account of all non-linearities, have been performed with the multi-passage approach. Therefore an UDF has been written for Fluent which calculates the modal forces induced by unsteady pressure fluctuations due to blade movement at each instant in time as given by Equation 3.22. These modal forces are used on the right hand side of the blades' equations of motion which are solved by numerical time integration employing the Newmark-scheme as explained in Section 4.3 in detail. The displacements calculated are then used to deform the mesh in the fluid domain. That way an explicit, sequential coupling algorithm is realised. Since no iteration is performed within one time step, comparatively small time step sizes are required. Anyway, the temporal resolution of 150 time steps per vibration cycle is sufficient which has already been proven by Schrape et al. [101]. To initiate the vibrations, the blades are given initial boundary conditions. Due to the influence of the fluid forces, the blades will either be damped (positive damping) or excited (negative damping) and the aerodynamic damping can be determined from the decay rate. The aeroelastic frequency instead is calculated by fitting sinusoidal functions with non-linear least squares method to the resulting displacement curves.

The objective of the bidirectionally coupled FSI simulations is to compare influence coefficients results with constant amplitude neglecting the influences from fluid forces with the

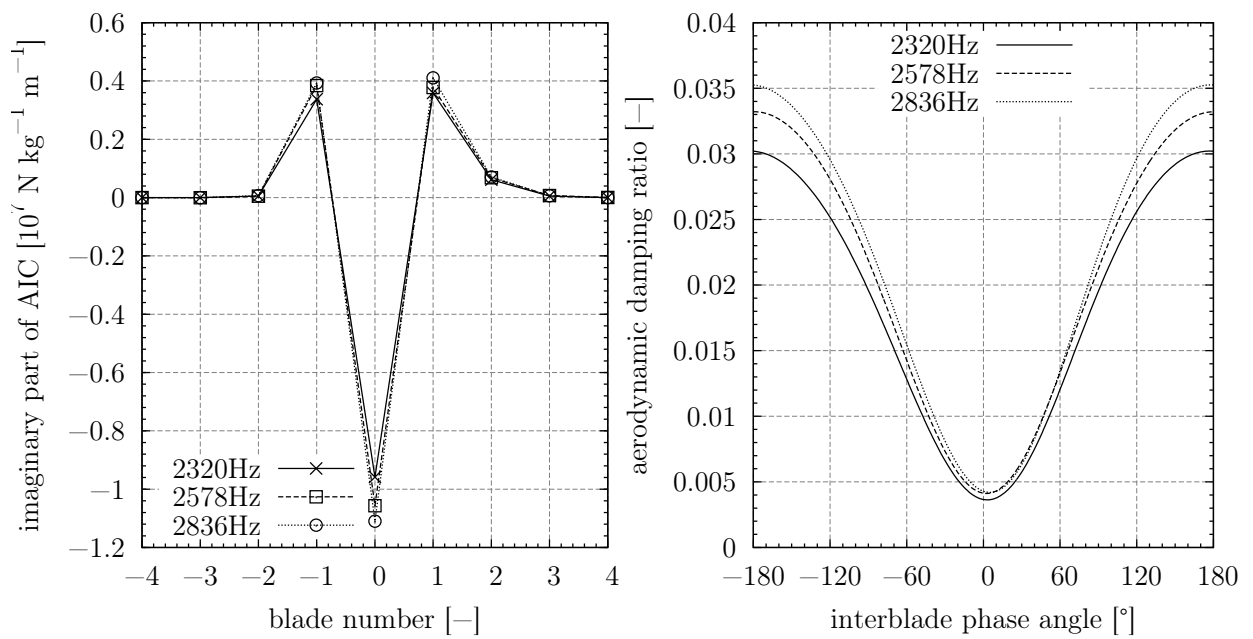


Figure 6.4: Imaginary part of AIC (a) and aerodynamic damping ratio (b) for $\pm 10\%$ frequency deviation

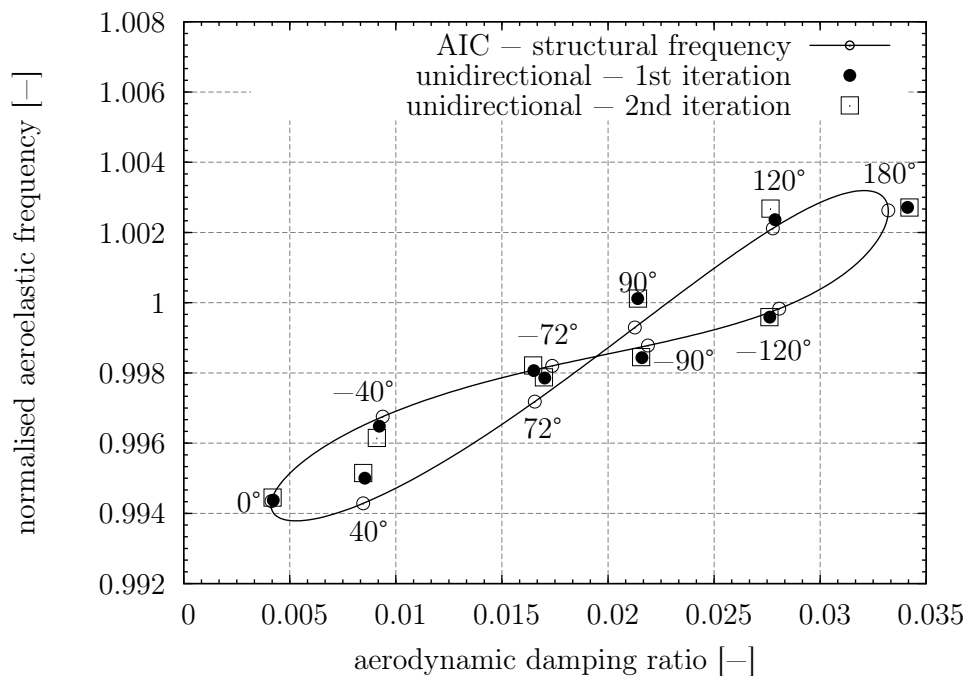


Figure 6.5: Results of unidirectional FSI computations

results of a full interaction model taking account of all non-linear effects. Furthermore, a good agreement of the eigenvalues of these simulation methods is essential for the comparison of bidirectionally coupled forced response simulations of the tuned and the mistuned cascade with EBM computations. The results of these computations are presented in Figure 6.6. Once again a satisfying comparison can be observed. Especially the results of unidirectional and bidirectional multi-passage computations match very well except for $\sigma = 180^\circ$ where the greatest differences occur. The good agreement of the two methods, especially concerning the aeroelastic frequency, confirms the assumption that the blade mass ratio is comparatively high resulting in a minor relevance of the fluid forces' impact on the vibration frequency. The results additionally indicate linear correlation of blade displacement amplitude and fluid forces which corresponds to the results obtained by Schrape et al. [102] who showed for the 2D model of rotor 6 that the work done per vibration cycle and the kinetic energy of the blade go linearly with each other.

Subsequently, the aerodynamic influence coefficients as well as equivalent aerodynamic elements, derived from the aeroelastic eigenvalues, have been used in EBM forced response computations to compare its results to bidirectionally coupled forced response simulations. The simulations have been performed in preparation of the mistuned cascade simulations. For that purpose, an interblade phase angle of $\sigma = 120^\circ$ has been chosen because of it showing superb agreement of the aeroelastic parameters obtained with influence coefficients and those from bidirectionally coupled FSI computations. Another advantage is that it only needs a cascade of three passages for the bidirectional simulations which saves computational time.

At this point it has to be mentioned again that no disk flexibility is regarded during the computations of rotor 6. Hence, since no information about real excitation forces is available, the force amplitude of the excitation can be calculated from simple SDOF relation with a given displacement amplitude. The displacement amplitude is the same as used in the aeroelastic eigenvalue analysis, given in Table 6.1. Furthermore no mechanical damping has been considered.

The results are presented in Figure 6.7 containing the frequency response functions of bidirectionally coupled FSI simulations, EBM computations with aerodynamic influence coefficients and equivalent aerodynamic elements. The displacements have been normalised with the displacement at resonance and the forcing frequency has been normalised with the structural natural frequency. Both EBM computations show remarkable agreement with the bidirectionally coupled simulations which is hardly surprising because of the excellent match of eigenvalues calculated with the bidirectional coupling and influence coefficients for $\sigma = 120^\circ$, see Figure 6.6. Since the parameters of the equivalent aerodynamic elements have been determined with the eigenvalues calculated with influence coefficients, the match of the EBM computations is perfect. From the aeroelastic eigenvalues in Figure 6.6 it could be expected that the maximum response of the aerodynamically coupled results is shifted to a frequency greater than the structural natural frequency which reflects in all present results.

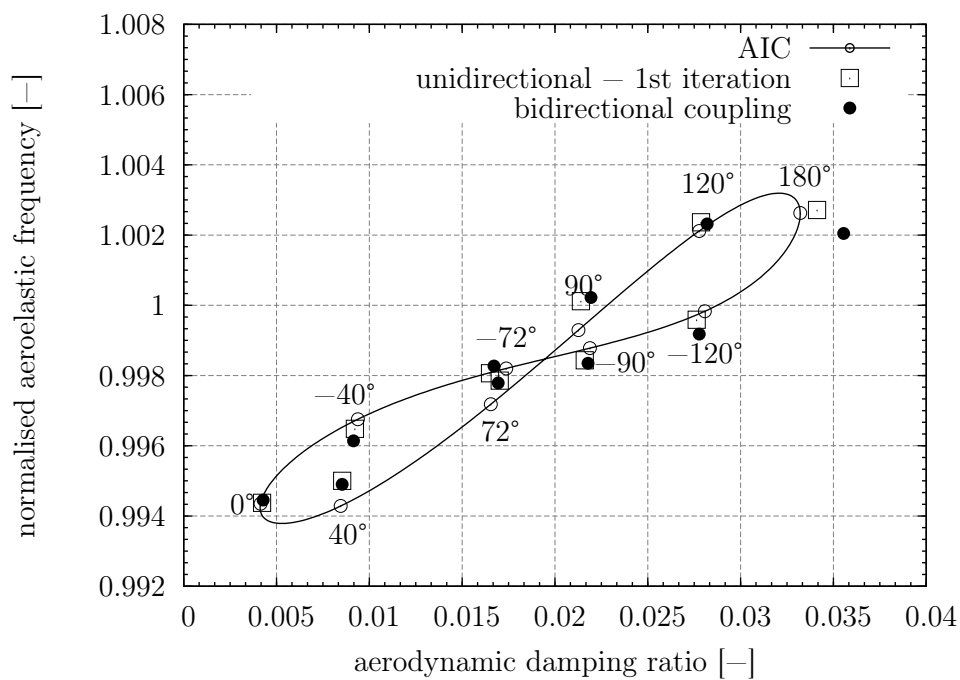
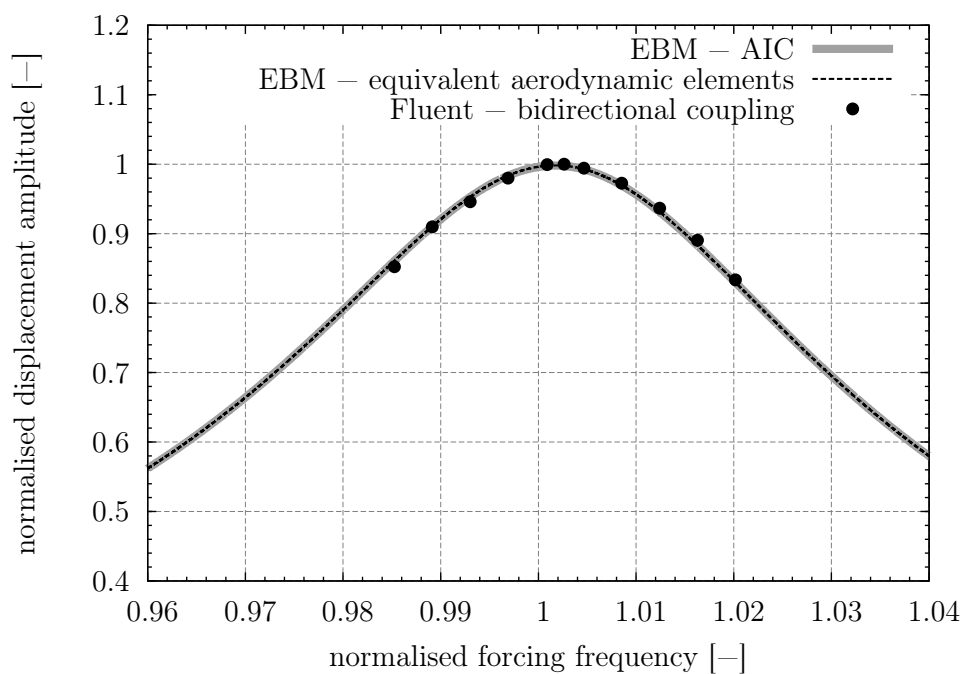


Figure 6.6: Results of influence coefficients and bidirectional FSI simulations

Figure 6.7: Frequency response function of tuned rotor 6 cascade, $\sigma = 120^\circ$

Concerning the aeroelastic simulations performed on the tuned cascade it can be summarised that all uni- and bidirectional methods deliver comparable results with respect to the aeroelastic parameters of the cascade, confirming the assumption that the fluid forces' influence on the vibration frequency is of minor importance. Moreover, the agreement of multi-passage and influence coefficients simulations justifies the supposition that the aerodynamic influences can be superposed linearly. Finally, the comparison of bidirectionally coupled FSI simulations of cascade forced response and EBM computations with aerodynamic influence coefficients included showed that the EBM is able to capture the main flow effects of amplitude mitigation and frequency shifting of a particular travelling wave mode.

6.2.2 Mistuned Cascade Results

In addition to the tuned cascade, a mistuned one has been simulated. This has been done for three reasons. First, analogously to the tuned cascade, the validation of the mistuned EBM with aerodynamic influence coefficients shall be done by comparing the results to bidirectionally coupled FSI simulations. The second objective is to check whether the performance of the equivalent aerodynamic elements, compared to the influence coefficients, is as good as in the tuned case. And last but not least it shall be demonstrated that the EBM is able to reproduce the same effects as observed by Kahl [61] and Petrov [92]. Kahl employing a lumped mass model with a single degree of freedom per blade sector and Petrov using his ROM (see Section 1.2 for details) showed that the maximum displacement amplification factor can drop well below the tuned response in case of mistuned bladed disk forced response analysed with aerodynamic forces included. With the example of the mistuned rotor 6 cascade, with rigid disk, it shall be demonstrated that this effect is mainly due to the interblade phase angle dependent treatment of aerodynamic damping. Moreover it will be shown that an attenuation below the tuned response depends on the amount of aerodynamic damping present in the tuned case and that it strongly depends on the max to min ratio of the damping curve as well.

For the forced response computations, two different engine order excitations corresponding to interblade phase angles of $\sigma_1 = 120^\circ$ and $\sigma_2 = 40^\circ$ have been chosen. Both forced response analyses are carried out on a cascade of nine blade passages, corresponding to a minimum educible interblade phase angle of $\sigma = 40^\circ$. At first, a random mistuning pattern with a standard deviation of $\sigma_{\text{STD}} = 0.5\%$ has been created, displayed in Figure 6.8. Next, this particular pattern has been used in bidirectional FSI simulations and EBM computations.

Concerning the equivalent aerodynamic elements, some additional effort has to be made during simulation of mistuned systems. The additional masses, dashpots and stiffnesses have discrete values and are all the same when considering a particular interblade phase angle. This is somehow equivalent to travelling wave mode coefficients which are also the same for each blade in tuned blade vibrations. On the contrary, when mistuning is regarded and influence coefficients are used, the aerodynamic forces superpose on each blade depending on

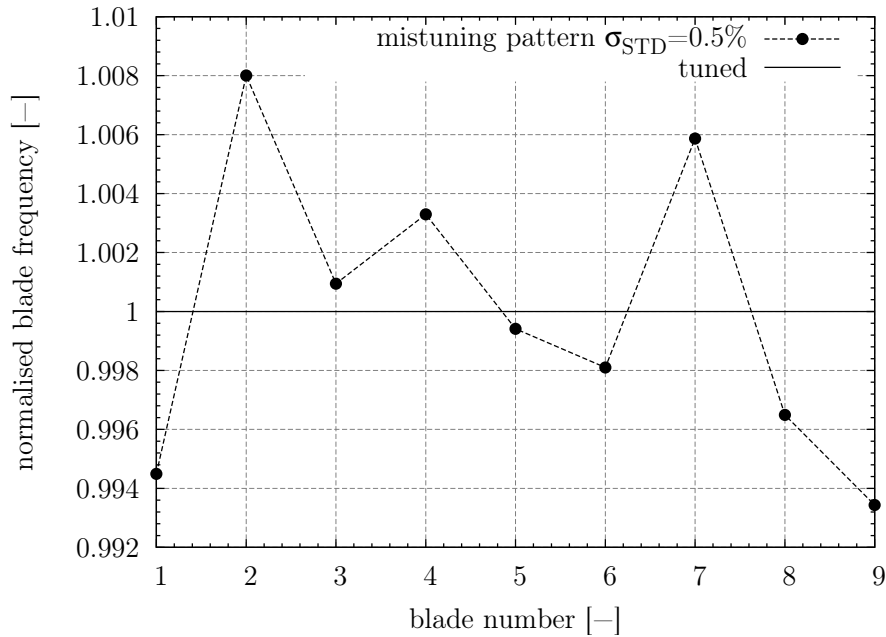


Figure 6.8: Mistuning pattern of rotor 6 cascade, $\sigma_{\text{STD}} = 0.5\%$

the interblade phase angle of the rest of the blades in the cascade. In order to recreate this behaviour an iterative adaption of the equivalent aerodynamic elements' parameters has to be performed. The simulations in the frequency domain are initially started with the tuned parameters corresponding to the interblade phase angle of the excitation. As a result of the computation, the phase angles between adjacent blades will be different from the tuned one. Subsequently the parameters of the aerodynamic elements are adapted according to these phase angles and the computation is repeated. This iterative adaption is repeated until the interblade phase angles do not change significantly over a computational step. The frequency response functions of the blades in the cascade are presented in Figure 6.10, the displacements have been normalised with the tuned response displacement magnitude.

Since every blade features a different natural frequency in a mistuned system, the frequency dependency of the aerodynamic forces has been taken into consideration by calculating the influence coefficients at frequencies $\pm 10\%$ ³ of the structural natural frequency too, shown in Figure 6.4. During the computation, the influence coefficients have been interpolated according to the frequency of the excitation by quadratic interpolation. The interpolated real and imaginary parts of the zeroth influence coefficient are exemplarily shown in Figure 6.9. It has to be mentioned that the quadratic interpolation should be only applied to small frequency ranges because it can only give qualitative results.

First, for the validation of the mistuned EBM, the interblade phase angle of the excitation is chosen to $\sigma_f = 120^\circ$ with an identical excitation force as in the tuned computation presented in the previous section. The frequency response functions of the different computations are

³The range of $\pm 10\%$ is important for the subsequent computations of mistuning up to $\sigma_{\text{STD}} = 10\%$.

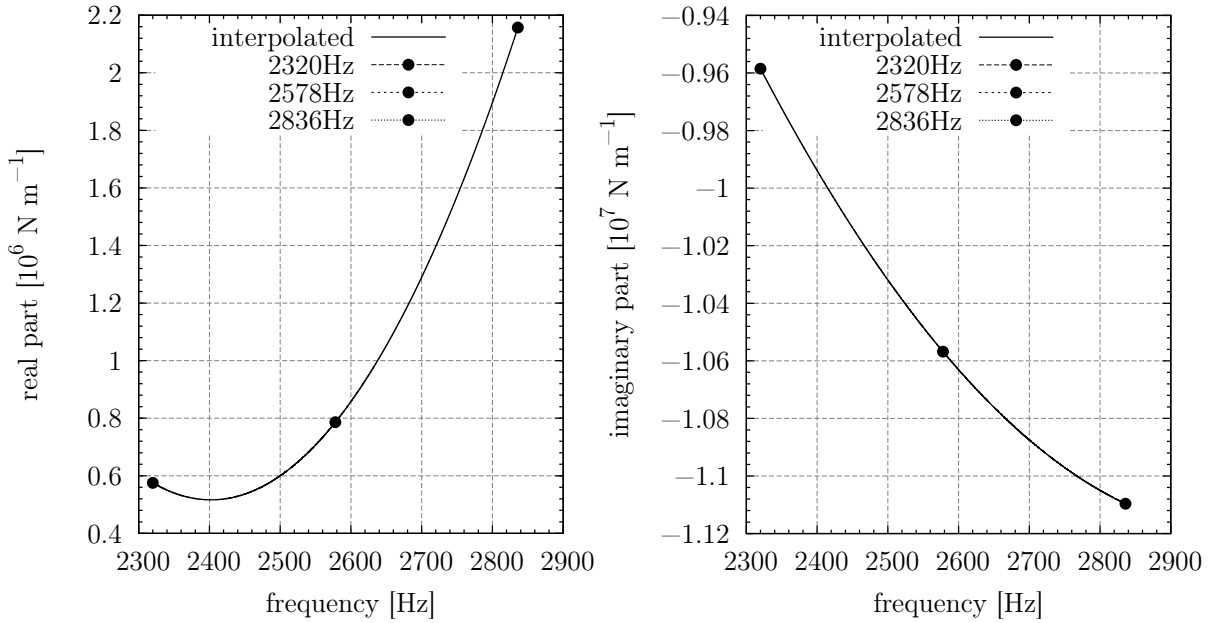


Figure 6.9: Interpolated zeroth influence coefficient as function of frequency

presented in Figure 6.10. At first sight, the considerable agreement of the bidirectional and EBM computations is apparent. Regarding the maximum blade displacement amplitude, the EBM results obtained with influence coefficients feature an average deviation of only $\pm 3.7\%$ with a maximum of -8.3% associated with blade 4. The difference in resonance frequency on the other hand is approximately $\pm 0.07\%$. Although the differences of the results obtained with equivalent aerodynamic elements appear to be much greater they only differ by $\pm 5.5\%$ with respect to the displacement amplitude and approx. $\pm 0.3\%$ regarding the resonance frequency. In summary, it can be stated that both methods are able to reproduce the aerodynamic influences due to mistuned blade vibrations giving adequate results with the aerodynamic influence coefficients tending to be a little closer to the bidirectionally coupled simulations.

In the following analysis the methods have been compared to one another in terms of greater mistuning ranges and the ability to reproduce maximum blade responses lower than the tuned one. Therefore, the mistuning pattern previously involved in the simulations, see Figure 6.8, has been scaled to yield 500 patterns with standard deviations ranging from $\sigma_{\text{STD},\text{min}} = 0.02\%$ to $\sigma_{\text{STD},\text{max}} = 10.0\%$. A forced response analysis of all these patterns is conducted for an interblade phase angle of $\sigma_f = 40^\circ$ whose aerodynamic damping is close to the minimum of all damping values. Due to CPU restrictions only 3 carefully selected patterns have been simulated during the bidirectional FSI computations, these are the pattern resulting in maximum amplification at $\sigma_{\text{STD},1} = 0.84\%$ and two patterns with large $\sigma_{\text{STD},2} = 4.0\%$ and very large mistuning $\sigma_{\text{STD},3} = 8.0\%$.

The EBM computations are carried out prior to the bidirectionally coupled FSI simulations to identify the resonance frequency of the blade showing maximum response. Initially, forced

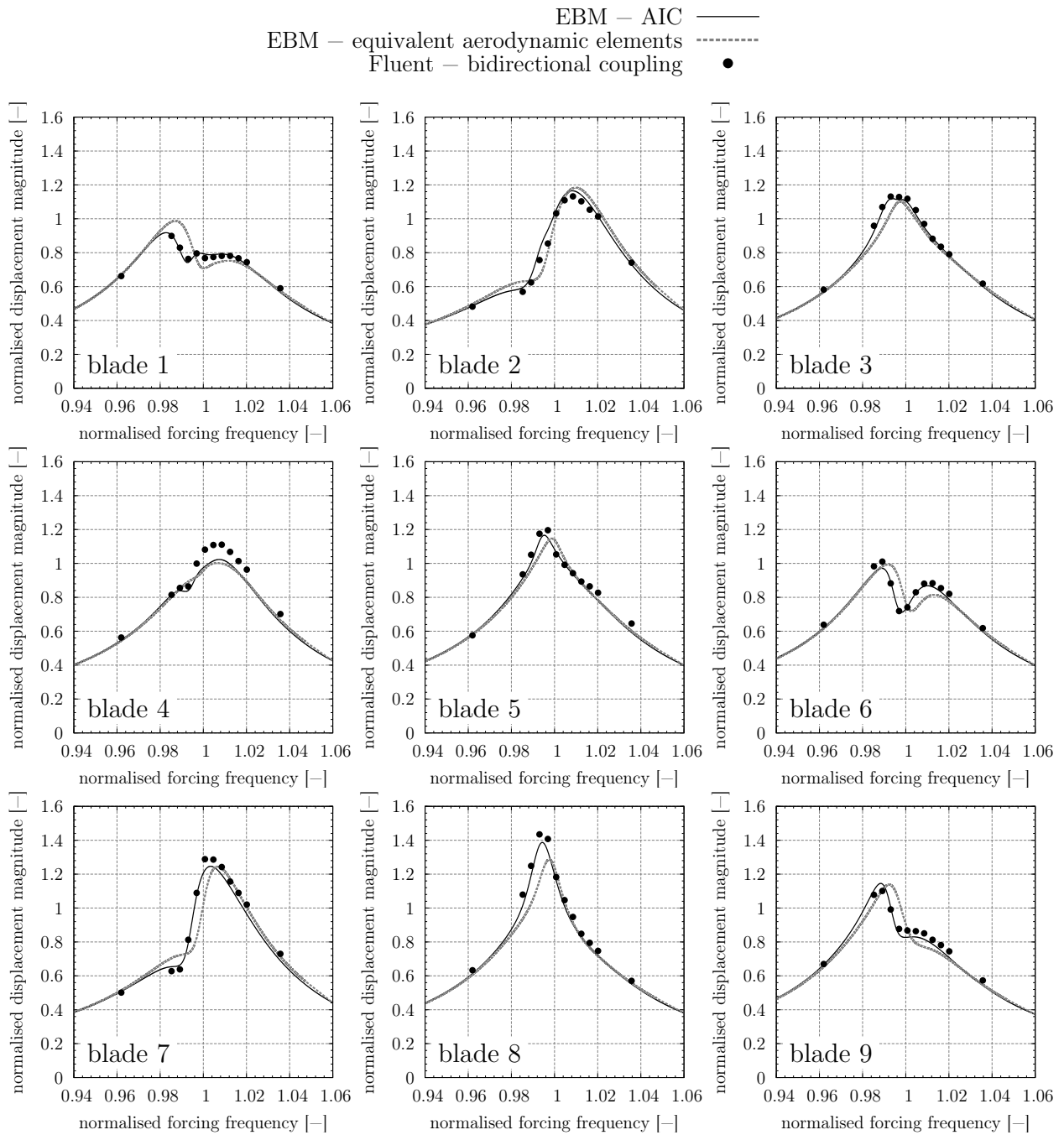


Figure 6.10: Frequency response functions of mistuned rotor 6, $\sigma_f = 120^\circ$

response computations of the tuned system have been performed employing the aeroelastic frequency as excitation frequency to yield the tuned blade displacement which has been found to be approx. 4.7% higher with the EBM computations compared to the bidirectionally coupled FSI simulations. This is consistent with the comparison of the eigenvalues previously shown in Figure 6.6 indicating a slightly lower damping for the bidirectional simulations. The results of all computations are displayed in Figure 6.11 showing the dis-

placement amplification factor, see Equation 2.9 for details, versus the standard deviation of the mistuning patterns. At this, each curve has been normalised with its corresponding tuned displacement amplitude.

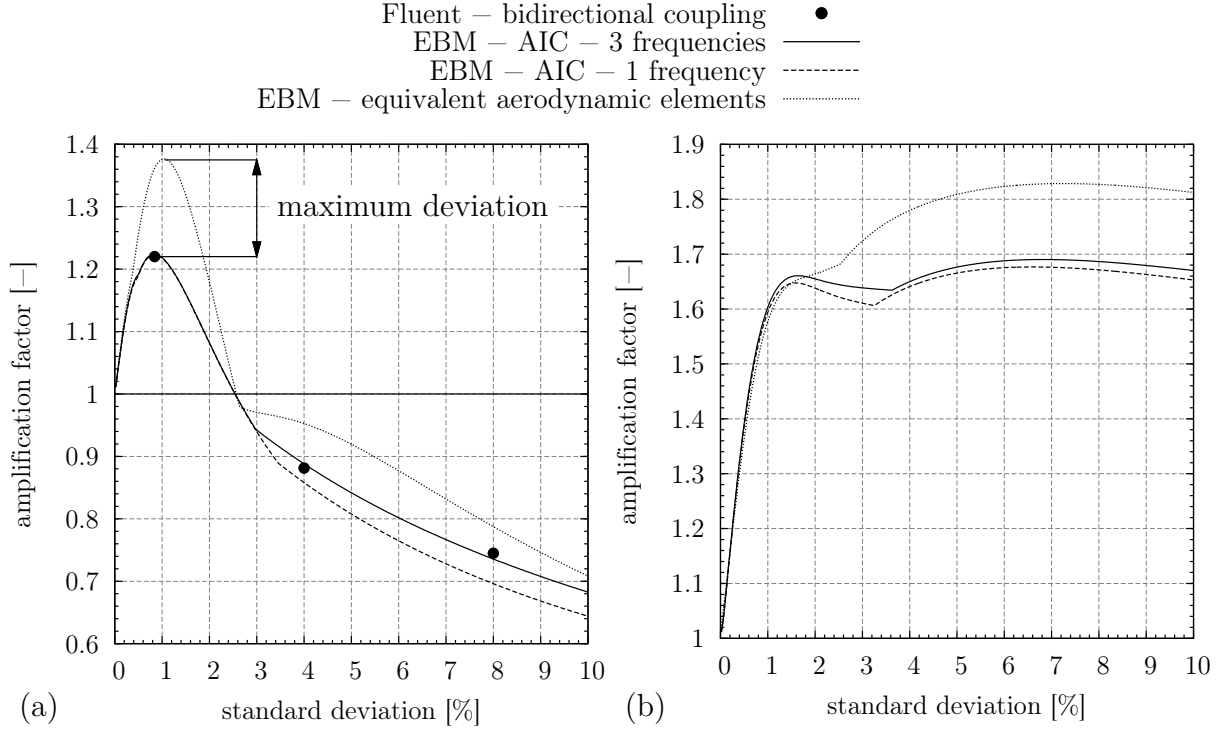


Figure 6.11: Amplification factor versus standard deviation of 500 scaled mistuning patterns, $\sigma_f = 40^\circ$ (a) and $\sigma_f = 120^\circ$ (b)

It can be seen that the correlation of bidirectionally coupled FSI simulations and EBM computations conducted with frequency depending influence coefficients is astonishing. In contrast, when constant influence coefficients are used, computed for a vibration at the structural natural frequency, the match of both EBM computations is very well up to $\sigma_{STD} \approx 3.0\%$. From that point on, the effect of frequency dependency of the aerodynamic forces becomes greater and the differences grow larger with increasing standard deviation when constant influence coefficients are used. Additionally, the results obtained with equivalent aerodynamic elements have been included in the diagram. It can be seen that all results compare quite well up to a standard deviation of approximately 0.3% from which on the aerodynamic elements' deviations grow up to a maximum difference in the amplification factor of 0.16. This effect is probably due to the increasing deviation of the mistuned eigenvalues from the tuned ones for which the parameters of the aerodynamic elements have been identified. Consequently, from the point of maximum deviation the differences decrease with increasing standard deviation, agreeing with the result of the variable influence coefficients at $\sigma_{STD} \approx 2.5\%$ where both methods yield a maximum blade response equal to the tuned one.

The interesting thing to see is that the computations yielded, as it has been expected, amplification factors significantly lower than 1.0, even though a completely rigid disk has been assumed. An amplitude reduction of up to 30% can be observed for this particular mistuning pattern. However, it has to be admitted that the present study has been conducted for a heaving motion with a large max to min ratio of the interblade phase angle dependent aerodynamic damping curve. Nevertheless since a rigid disk and no structural damping has been used, the reduction of the maximum blade amplitude below the tuned response can only be a result of the interblade phase angle dependency of the aerodynamic damping. The greater the max to min ratio of aerodynamic damping gets, the more likely is a mitigation of the maximum blade response below the tuned one. In order to study this effect, additional EBM computations have been performed with variations of the max to min ratio of the aerodynamic damping which can be achieved through adaption of the influence coefficients. For this purpose the influence coefficients L_{+1} and L_{-1} which have the major effect one the max to min ratio have been successively reduced in steps of 20%. The resulting damping plots along with the corresponding graphs of displacement amplification versus standard deviation are presented in Figure 6.12 (a) and (b) respectively.

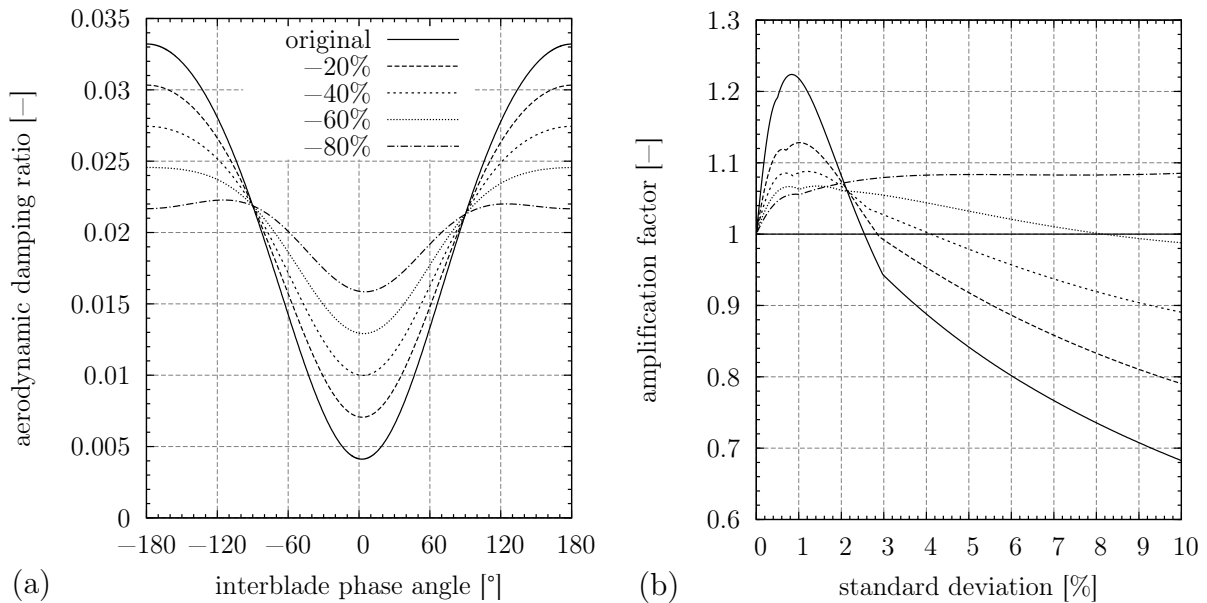


Figure 6.12: Aerodynamic damping (a) and amplification factor (b) obtained with adapted aerodynamic influence coefficients, $\sigma_f = 40^\circ$

As expected, the displacement amplification factors which have been below 1.0 before increase with decreasing max to min ratio of the aerodynamic damping. Another important issue is the phase angle of the excitation which is, in combination with the max to min ratio, essential for the reduction of the maximum mistuned response below the tuned one. The excitation employed in the previous computations features an interblade phase angle near to the one showing minimum aerodynamic damping ($\sigma = 2.4^\circ$). In the forced response of the tuned cascade every blade features the aerodynamic damping corresponding to the

phase angle of the excitation. Since in a mistuned system, the interblade phase angles between adjacent blades are not the same for the entire cascade, every blade is subjected to a different portion of aerodynamic damping. If the phase angle of the excitation is associated with minimum aerodynamic damping, or close to it, than the phase angles occurring in the forced response of the mistuned cascade are inevitably exhibiting higher damping values than in the tuned cascade. The opposite effect can be observed when the phase angle of the excitation is close to the maximum of the damping curve. Consequently the amplification factors of a forced response with $\sigma_f = 120^\circ$, also shown in Figure 6.11, exceed the tuned response for all standard deviations. Considering Figure 6.12 (b) again, the amplification factors that have been greater than 1.0 decrease with decreasing max to min ratio. A clear dependency of the amplification factor behaviour on the shape of the damping curve becomes obvious. This finding is especially interesting for higher blade modes for which the max to min ratio of the aerodynamic damping commonly becomes smaller and the effect is supposed to be less pronounced than for the present example. Moreover, an infinitely stiff disk has been used here, hence studies with mechanical coupling are desirable. As a consequence of the aforementioned explanations, the analyses presented in the following chapter comprise the simulation of the aeroelastic behaviour of higher blade modes with mechanical coupling included.

The findings of this chapter can be summarised shortly:

- The computations of the aeroelastic parameters with different uni- and bidirectionally coupled methods all yield comparable results,
- consequently, the tuned frequency response functions of bidirectionally coupled FSI simulations and EBM computations with different aerodynamic treatment agree perfectly,
- the frequency response functions of a randomly mistuned cascade with 0.5% standard deviation excited with $\sigma_f = 120^\circ$ show proper compliance of EBM with influence coefficients and bidirectionally coupled FSI computations while the equivalent aerodynamic elements exhibit greater deviations, especially with respect to the aeroelastic frequency,
- for greater standard deviations and an excitation with $\sigma_f = 40^\circ$ an eminent agreement of EBM computations with influence coefficients and bidirectionally coupled FSI simulations has been observed while the equivalent aerodynamic elements showed qualitatively satisfactory behaviour with greater differences,
- furthermore, a maximum blade displacement attenuation below the tuned response has been obtained for an excitation with an IBPA close to the one exhibiting minimum aerodynamic damping with the effect clearly depending on the max to min ratio of the aerodynamic damping.

Chapter 7

E3E - Rotor 1

The analyses of the previous section have been concerned with the analysis of linear cascade blade vibrations. Several assumptions such as a rigid disk, a simple heaving motion and rigid blades allowed to study the major effects of aerodynamic influences on mistuned blade vibrations. In a next step a 3D model of the stage 1 rotor of the E3E featuring flexible disk, flexible blade mode shapes and mistuning patterns determined by experimental modal analysis, is going to be analysed. The following studies comprise the simulation of the steady and the unsteady flow for the determination of the aeroelastic eigenvalues and the aerodynamic influence coefficients as well as EBM computations of the mistuned system with aerodynamic effects included focusing on the three fundamental modes and one mode at a higher frequency.

7.1 Steady State Numerical Flow Solution

The analysis of the steady state flow was performed with a single flow passage in Rolls-Royce's in-house aeroelasticity code Au3D, see Sayma [99] and Vahdati [112] for details about the code. On the contrary to the previous simulations Au3D has been used instead of Fluent because of it being a well validated code which is specialised for the use in turbomachinery analysis. Its advantages in unsteady, aeroelastic simulations are the availability of one-dimensional non-reflecting boundary conditions at inlet and outlet and phase-lagged boundary conditions. Analogously to the previous simulations, the one-equation turbulence model of Spalart-Allmaras has been used. The aeroelastic methods previously applied to Fluent results have been adapted to be used in Au3D by Giersch [39].

The flow boundary conditions are taken as defined in the aerodynamic design process. The values at the boundaries are specified as radial profiles. The most important design parameters are summarised in Table 7.1. Since the boundary conditions from design base on simplified flow models, a single passage multi blade row computation with the directly

Table 7.1: Operating conditions E3E rotor 1

structural parameters		
number of blades rotor 1	N	29
speed of rotation	Ω_r [rad/s]	1597.71
aerodynamic parameters		
relative mach number at inlet (midspan)	$Ma_{1,rel}$	0.82
relative velocity angle at inlet (midspan)	$\beta_{1,rel}$ [°]	54.7
Reynolds number (midspan)	Re	$1.65 \cdot 10^6$
rotor 1 pressure ratio	Π	1.43
aeroelastic parameters		
reduced frequency (chord at midspan)	ω^*	0.8 ... 6
mass ratio	μ	250

up- and downstream located stator vanes along with the strut in front of the HPC has been simulated in addition to single blade row computations with the boundary conditions from design applied to inlet and outlet of the passage. The first three blade rows of the HPC as well as the strut are illustrated in Figure 7.1.

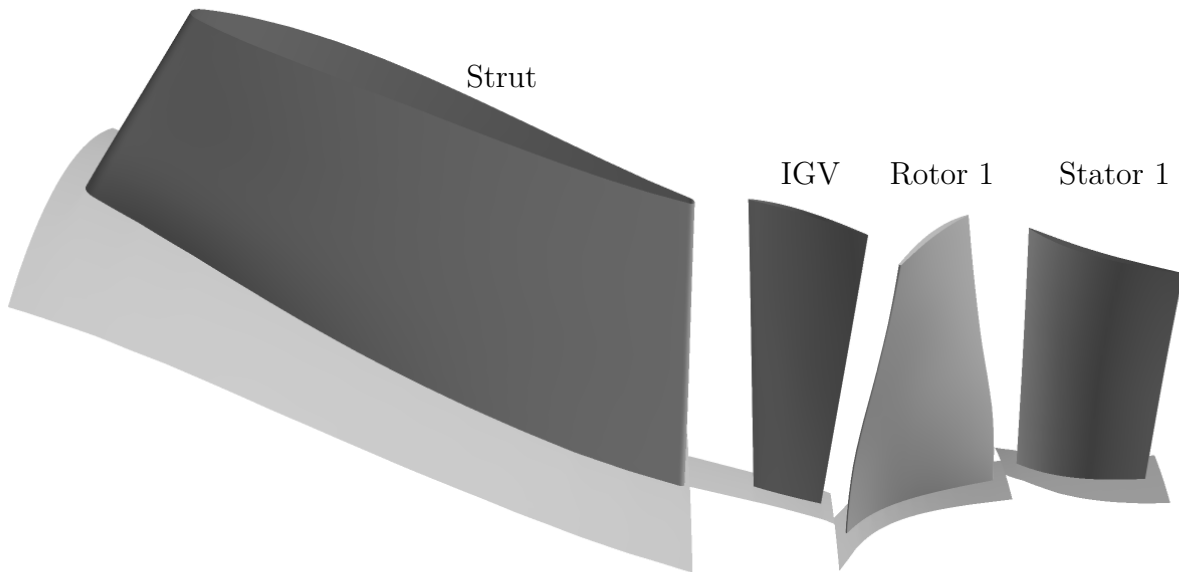


Figure 7.1: Strut and first three blade rows of the E3E-HPC

The characteristic of the first stage, with inlet guide vane (IGV) and strut in front of it, is displayed in Figure 7.2. The speedline corresponds to the speed of rotation as given in Table 7.1, the pressure ratio was controlled by variation of the outlet static pressure. The operating point is indicated by the black filled symbols while the design point is indicated by the grey filled symbols. It can be seen from the characteristic that the deviation of the

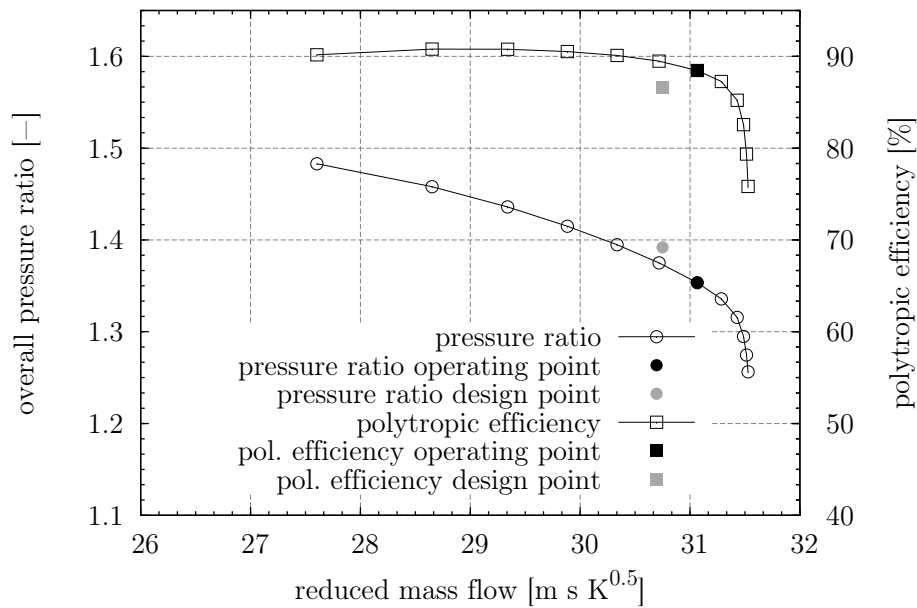


Figure 7.2: Engine characteristic of multi blade row at maximum take-off condition

computational results from the design intent is in an acceptable range. Additional explanations for the differences can be found by analysis of the steady state flow solution. Hence the steady state solution of the single blade row rotor passage is going to be discussed. Since no experimental data is available the analysis completely bases on the results of the numerical solutions. Therefore, a single passage with boundary conditions specified as intended from design has been simulated. As the tip gap of the rotor has a significant influence on the flow it is taken into consideration. On the contrary to the rotor, the vanes are modeled without any gaps and fillets. Hence, the focus of the following section is on qualitative judgment of the flow solution and its influence on the vibration behaviour of the rotor. Subsequently, the steady state flow of the whole stage, including the IGV and the strut, has been simulated and compared to the results of the single blade row. In order to be able to adapt the compressor aerodynamics to the operating conditions at part speed conditions IGV and stator 1 are designed as variable stator vanes (VSV), their positions are adjusted in accordance with the VSV-schedule.

The hybrid rotor mesh is made up of an O-mesh (12x246 nodes) in the vicinity of the blade and prism elements in the rest of the domain. The radial resolution is realised with 46 mesh layers with the mesh spacing getting denser in the vicinity of hub and casing to ensure proper boundary layer resolution. The mesh has been adapted step by step to guarantee having at least 10 cells in the boundary layer and an average y-plus of approximately 70. The total number of nodes in the passage is 265.000.

The results of the steady state computations are presented in Figure 7.3 and Figure 7.4. Here the values of relative velocity angle, relative inlet mach number, static pressure, total

pressure and specific mass flow are compared between design, single and multi blade row simulations. Concerning the multi blade row simulations, mixing planes have been used at the blade row interfaces circumferentially averaging the flow parameters at this boundary. At first sight, the results of the computations agree satisfactorily with the design specification.

Comparing the single results with each other the first thing that catches the eye is the influence of the wall boundary layers. Due to the reduction of the effective flow area the velocity of the mean flow as well as the specific mass flow increase, see Figures 7.3 (d) and 7.4 (d). The effect becomes even more clear for the results of the multi blade row computation.

At the inlet, total pressure and absolute velocity angles are prescribed and kept constant during simulation. This leads to smaller boundary layer thickness in the regions close to hub and casing thus to less blockage. Since the absolute velocity angle is fixed, the tangential component of the absolute velocity has to increase to compensate the increase in axial velocity. As a consequence the relative velocity angle is reduced, Figure 7.3 (a), and the inlet mach number increases due to the greater axial velocity, Figure 7.3 (b). In case of the multi blade row computation, the velocity angles at the inlet of the rotor passage are not prescribed but a result of the upstream inlet guide vane. As a result, they differ from the design specification. Nevertheless, the relative velocity angle compares well with the single passage computation which is due to the smaller tangential velocity components compensating the larger axial velocity components, 7.3 (a).

Additionally, the flow solution at the outlet of the rotor passage is presented in Figure 7.4. Here the excellent agreement of the specific mass flow of design and multi blade row computation catches the eye, Figure 7.4 (d), while the single blade row solution shows considerable differences compared to the design specification. The perfect match of the static pressure profile of the single blade row solution is attributed to the pressure outlet boundary conditions which fixes the static pressure profile at the outlet.

In Figure 7.5 the pressure coefficient of the steady state solution on the blade and at various spanwise sections of rotor 1 taken from the multi blade row computation is displayed. Additionally, the relative mach number at different radial sections is presented in Figure 7.6. All the plots indicate a shock on the suction side of the blade whose position varies between approximately 20% and 60% relative chord and which is getting stronger from hub to tip. This finding is quite important, since the shock position may considerably vary during blade vibration of the upcoming unsteady computations which may influence the aeroelastic parameters and which might pose the limit for the usage of influence coefficients.

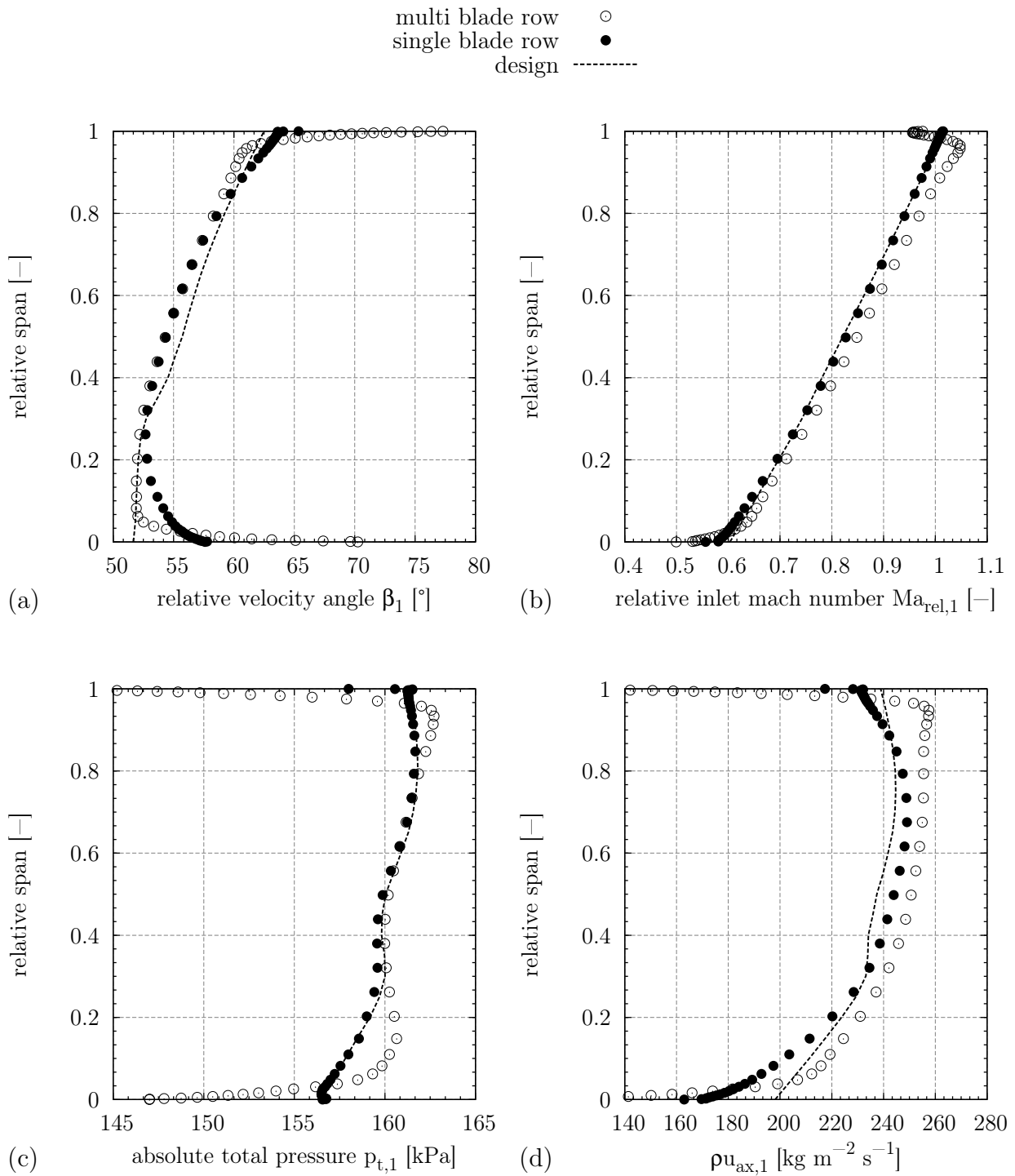


Figure 7.3: Radial distributions of relative velocity angle (a), relative mach number (b), absolute total pressure (c) and specific mass flow (d) at the inlet of rotor 1

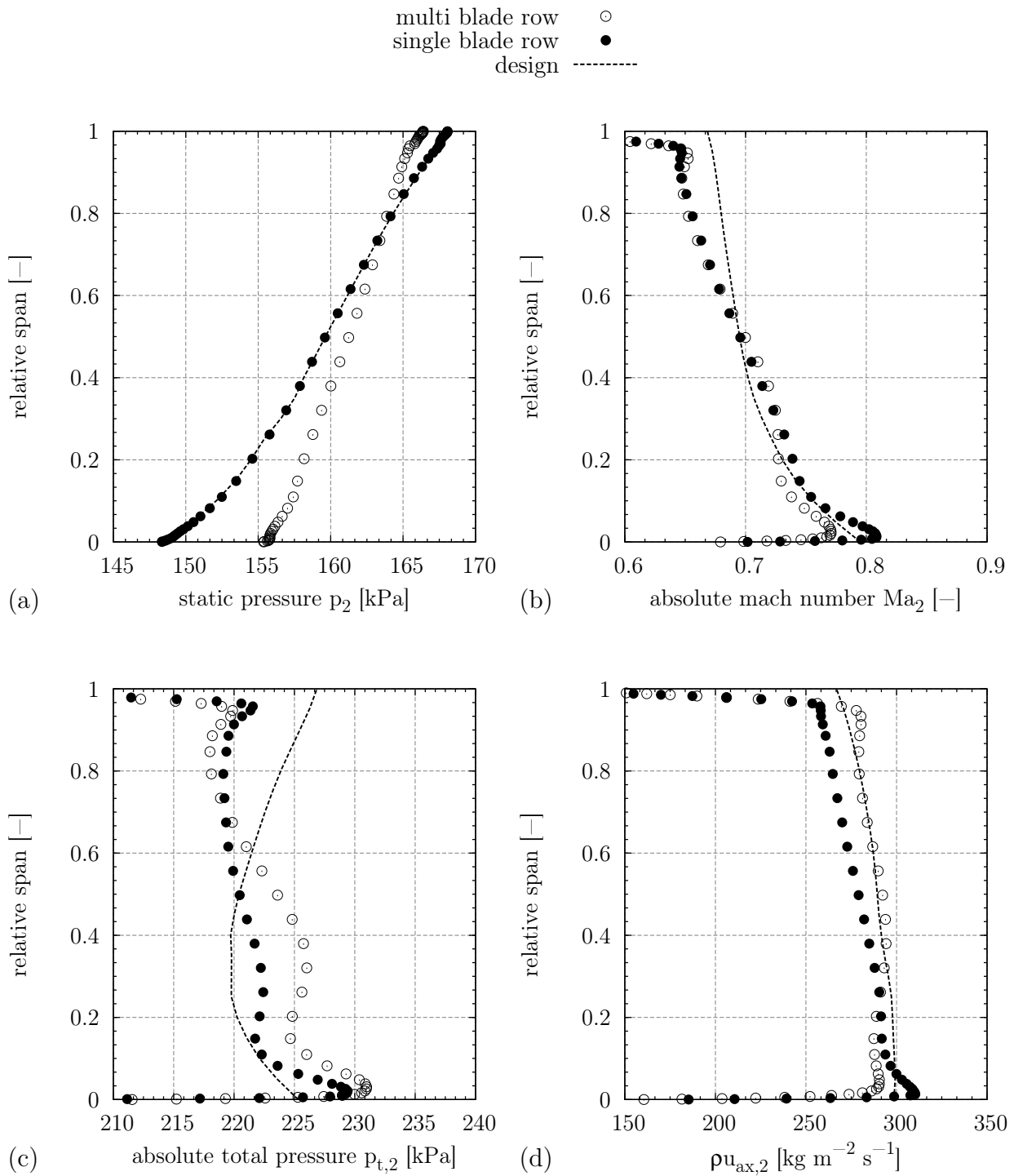


Figure 7.4: Radial distributions of static pressure (a), absolute mach number (b), absolute total pressure (c) and specific mass flow (d) at the outlet of rotor 1

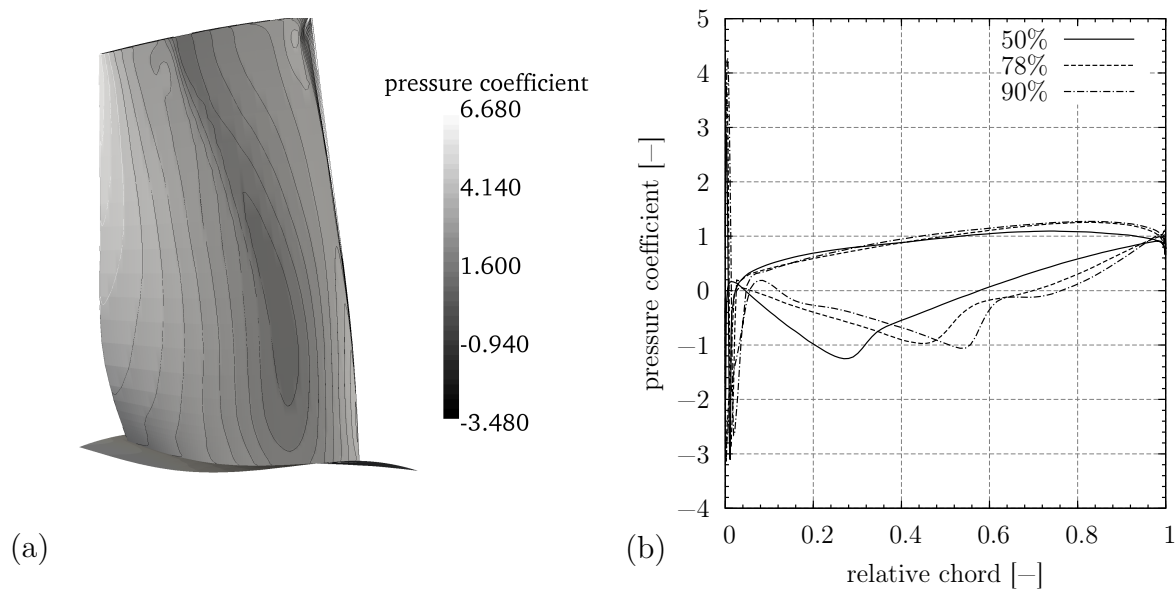


Figure 7.5: Pressure coefficient on blade surface (a) and at blade span sections (b) from multi-blade row computations

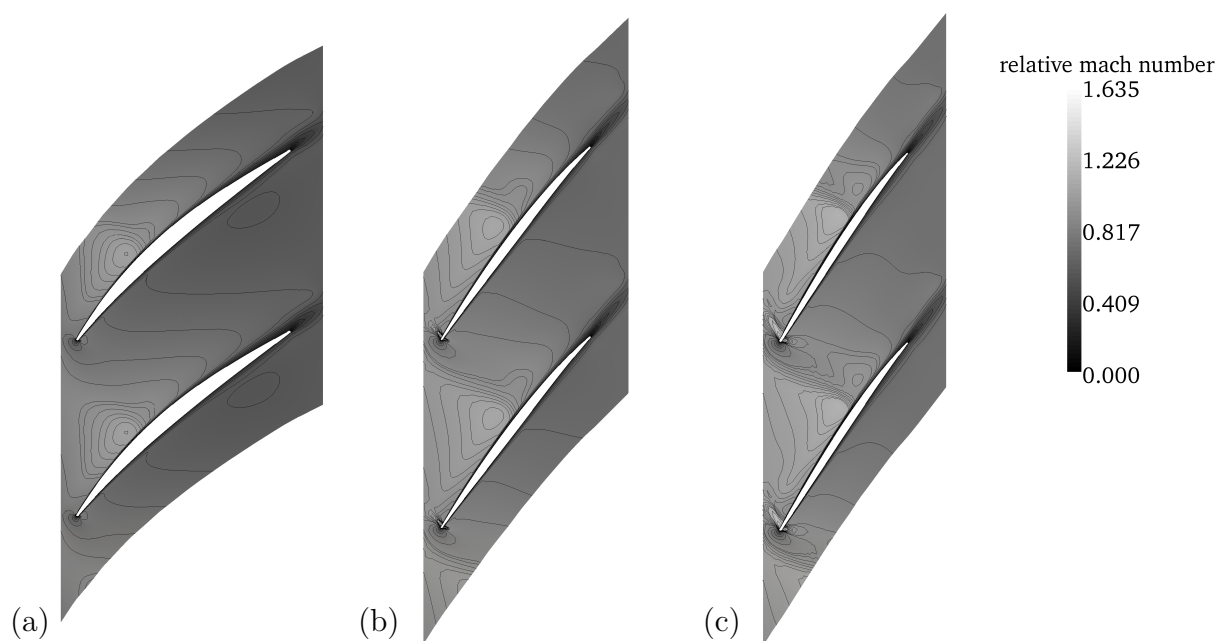


Figure 7.6: Relative mach number at 50% span (a), 78% span (b) and 90% span (c) (multi-blade row computation)

7.2 Modal Analysis

The modal analysis of the rotor 1 blisk comprises experimental analysis of the mistuned rotor 1 blisk as well as FE analyses of the mistuned and tuned numerical model. The following section presents the numerical analysis of the tuned blisk followed by the results of experimental modal analysis of the mistuned rotor 1 blisk and the subsequent model updating process.

7.2.1 Tuned System

Prior to the determination of the aeroelastic parameters, the modal parameters have been calculated from finite-element computations giving the natural frequencies and mode shapes of the blade modes of interest. For that purpose, a cyclic-symmetric model of the tuned blisk, as displayed in Figure 6.1 (b), has been analysed with the commercial FE-code Abaqus. During the analysis the influences of temperature and pressure forces on the modal parameters have been neglected while centrifugal forces are considered. As a result, a frequency versus cyclic symmetry mode (CSM) diagram can be constructed as displayed in Figure 7.8. The frequency lines of the first 6 blade modes are displayed along with scattered disk modes crossing the blade mode lines. The blade dominated modes have been identified by relating the strain energy of blade and disk, as presented by Klauke [68], and with the help of the partial modal assurance criterion (PMAC), see Allemang [2] for details. According to Klauke, an assembly mode can be regarded as blade dominated mode when the percentage of strain energy in the blade is greater than 90%. Furthermore, if the blade's percentage on the total strain energy is between 65% and 90% the assembly modes are considered as coupled modes. If the percentage is lower than 65% the assembly modes are dominated by disk deformation and hence identified as disk dominated modes. The issue of frequency veering and crossing has been extensively addressed by Klauke et al. [69]. With the help of the PMAC

$$PMAC = \frac{(\Phi_1^T \Phi_2)^2}{(\Phi_1^T \Phi_1)(\Phi_2^T \Phi_2)} \quad (7.1)$$

the blade mode shapes of the assembly modes (index 1) can be assigned to the corresponding blade mode family (index 2). For values of $PMAC = 1.0$ the compared modes are completely linearly dependent while values of $PMAC \geq 0.9$ indicate great similarity and modes yielding values of $PMAC < 0.9$ show only few correlation. A clear distinction between blade- and disk-dominated modes is not always possible in regions of frequency veering and crossing, especially when frequencies of a single CSM are very close. In forced response computations all modes within the frequency range of the excitation will be excited yielding complex blisk vibration behaviour. For details about the analysis of veering and crossing the reader is referred to Klauke et al. [69] for example. It shows that, due to mechanical coupling through the disk, the frequencies of the interesting modes 1 to 3 and mode 6, shown in Figure 7.7,

clearly depend on the considered CSM. Table 7.2 summarises the frequency variations of the different modes. It lists the minimum and maximum frequencies of the blade modes under consideration as well as the frequency associated with the maximum CSM (f_{14}) which is the one least affected by mechanical coupling effects. The percentages in brackets represent the deviation to the frequency of the maximum CSM. It is commonly agreed that blade vibrations tend to couple more over the disk for flap wise blade modes than for torsional modes which also reflects in the rotor 1 results because the 1st (mode 1) and 2nd flap mode (mode 2) show greater frequency variations than 1st torsion (mode 3) and the tram line mode (mode 7). Nevertheless, when mistuning is introduced the tuned CSM split up into MCSM, as described in Section 2.2 which is the more realistic case. Consequently, the results of mistuned system analyses are presented in the following section.

Table 7.2: Frequencies of rotor 1

blade mode	f_{\min} [Hz]	f_{14} [Hz]	f_{\max} [Hz]
1	561.65 (CSM 2,-5.0%)	591.08	671.58 (CSM 0,+13.6%)
2	1379.4 (CSM 3,-6.2%)	1470.4	1574.5 (CSM 0,+7.1%)
3	1797.9 (CSM 4,-0.2%)	1802.3	1824.6 (CSM 0,+1.2%)
6	4372.1 (CSM 3,-1.1%)	4422.0	4422.0 (CSM 14)

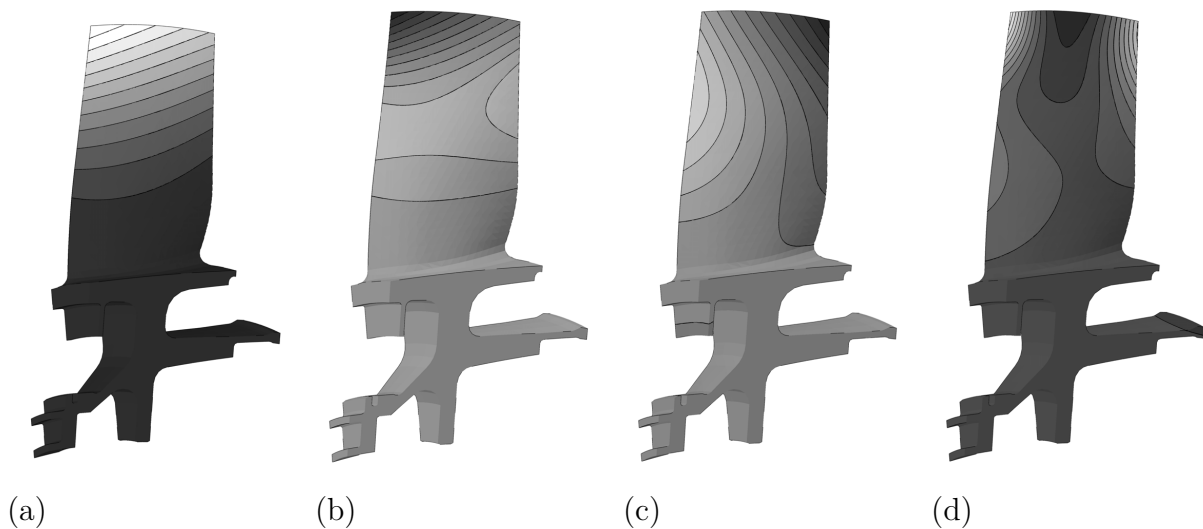


Figure 7.7: Displacement in viewing direction of selected blade modes of rotor 1 - 1st flap (a), 2nd flap (b), 1st torsion (c) and tram line (d)

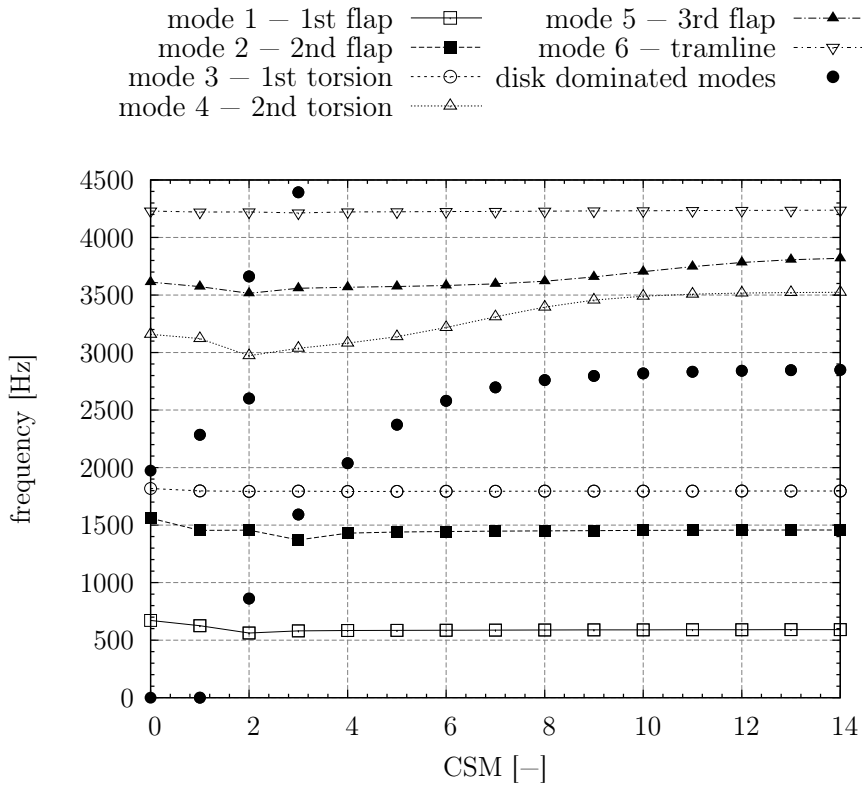


Figure 7.8: Natural frequencies versus CSM

7.2.2 Mistuned System

In order to analyse the aeroelastic behaviour of the mistuned rotor 1 blisk, mistuning patterns of real hardware have been determined by experimental modal analysis. The mistuning patterns employed in the current work are the outcome of the work of Klauke [68], Beirow [7] and Strehlau [110]. The methodology employed during measurement is described in detail by Beirow and Kuehnhorn [8]. The approach can be summarised in short as follows. Prior to the measurement campaign every blade, except the one to be measured, is equipped with a suitable additional mass introducing an intentional detuning of the entire system. During measurement the blade under consideration is excited with a modal hammer and the blade velocity is measured with non-contact laser doppler vibrometry (LDV). From the frequency response function the resonance frequency and the material damping can be identified.

In a next step, the measured blade frequencies and damping values are used in a model updating process to adapt the FE-model of the entire blisk at rest to the present hardware. In doing so, the measurement process is reproduced numerically. Iteratively the Young's Modulus of the blade under consideration is adapted to fit the measured frequency. This procedure is repeated for every blade of the assembly. The reader is referred to the work of Strehlau [110] for details about the entire process.

Subsequently, the system is analysed in the same manner while undergoing rotation to obtain the blade alone frequencies during operation. For simplicity the effects of temperature on the Young's Modulus as well as pressure forces from the gas flow are neglected henceforth.

Exemplarily, the measured frequencies¹ of the 1st flap mode (mode 1) together with the frequencies obtained from FE analysis after model updating process are displayed in Figure 7.9 (a). It shows that with the adaption of the FE-model to hardware, numerical analysis produces the same results as obtained by measurement. It has also been shown by Hoenisch and Kuehhorn [55] that the frequency response functions of all blades measured while exciting at a single point on the blisk correlate very well with those obtained in numerical analyses.

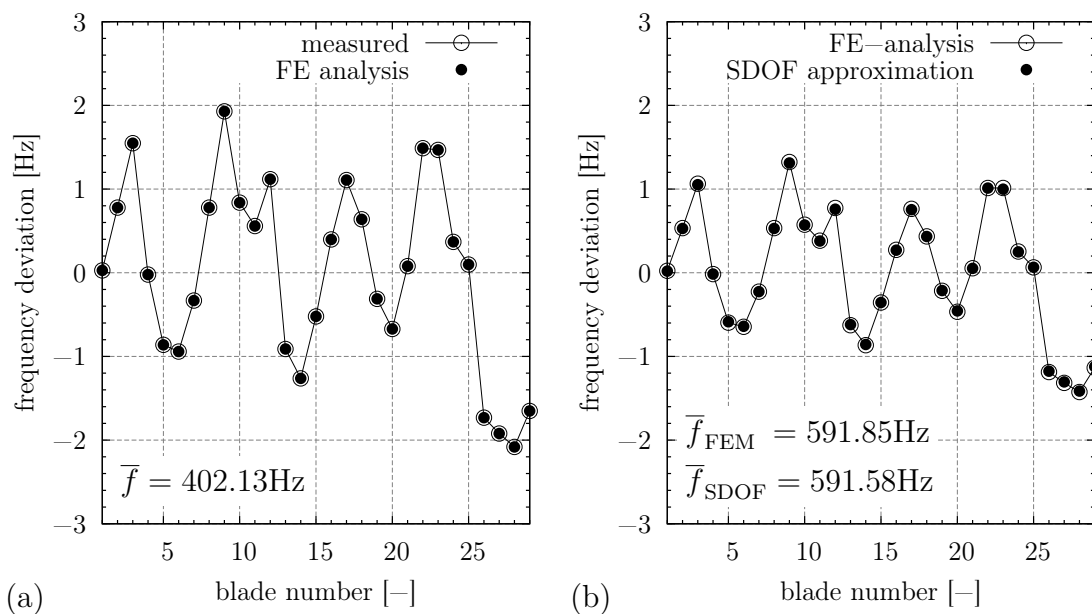


Figure 7.9: Measured and numerically determined frequencies of mode 1 (1st flap) at rest (a) and blade frequencies of the rotating system (b)

Since the rotor is under the influence of centrifugal forces under operating conditions, the blade frequencies have been determined from FE-analysis with centrifugal load, due to rotation at the speed given in Table 7.1, as well. The result of this computation is presented in Figure 7.9 (b). Comparing the blade frequencies at rest and under rotation a reduction of the mistuning effect can be observed for the latter condition which can be quantified by the standard deviations of the frequencies at rest $\sigma_{\text{STD},0} = 0.28\%$ and at rotation $\sigma_{\text{STD},\Omega} = 0.13\%$. This finding is in agreement with observations made by Feiner [30] for example. Additional computations have been carried out with the method presented in Section 2.2 to outline

¹The results of the modal analysis of the mistuned blisk are presented in form of blade frequencies rather than MCSM which consider the entire system because the perspective of individual blade vibration is the same as for the influence coefficients used to incorporate aerodynamic influences in the EBM.

the possibility of calculating the blade frequencies at rotation by simple SDOF approximation rather than by costly FE-simulations. Therefore Equation 2.16 is used evaluating the additional stiffness coming from the centrifugal forces according to the difference of the frequencies of the maximum CSM 14. As can be seen in Figure 7.9 (b) the frequencies obtained with the SDOF approximation match very well with the FE results. The deviation of approximately 0.05% is of minor impact and can be neglected. However, it must be stressed that this observations are made here at the example of 1st flap mode. Therefore the same calculations have been made for the rest of the modes considered in this work for which the blade frequency plots are presented in Appendix B. It shows that the influence of the centrifugal forces is greatest for the 1st flap mode while the effect on the absolute frequency variation is smaller for the 2nd flap mode and that it has almost no effect on the 1st torsion and tram line modes, see also Table 7.3. Concerning the comparison of FE- and SDOF-results the agreement is excellent with a maximum deviation of the mean frequencies of both methods of 0.53% associated with 2nd flap mode. With regard to the absolute frequency variation, the greatest deviation from the FE-results is observed for 1st torsion mode with -0.12% which is the same order of magnitude as for the deviation of its mean value.

Table 7.3: Standard deviations of frequency mistuning

blade mode	σ_{STD} at rest [%]	σ_{STD} at rotation [%]
1	0.28	0.13
2	0.2	0.15
3	0.129	0.124
6	0.119	0.118

7.3 Identification of Aeroelastic Parameters

For the EBM forced response computations with aerodynamic effects included the aerodynamic influence coefficients need to be computed. In order to evaluate the validity of these influence coefficients the aeroelastic parameters, meaning the aerodynamic damping and the aeroelastic frequency, are determined by unidirectionally coupled FSI simulations as well. All simulations feature a rigid disk, constant vibration frequency and constant mode shape. Hence, in case of unidirectionally coupled FSI simulations, the blade vibrations differ from each other only by the interblade phase angle between adjacent blades.

For the influence coefficients computations a partial blade assembly consisting of seven blades is used. At the boundaries 1D non-reflecting boundary conditions have been applied. The blade mode shapes are interpolated onto the CFD mesh to let the reference blade vibrate at constant amplitude. Analogously to all previous computations, the influence coefficients

have been regarded as sufficiently converged when the change in their magnitudes is less than 0.1% compared to the previous vibration cycle. The influence coefficients have been computed for the mean value of the mistuned blade frequencies of the four blade modes analysed in the previous section as well as for frequencies $\pm 10\%$ of the mean frequencies to take account of the frequency deviations of mistuning patterns with standard deviations of up to $\sigma_{\text{STD}} = 10\%$.

Additionally, unidirectionally coupled FSI computations have been performed for four CSM (-10,-4,4,10) employing the mean blade frequencies. On the contrary to the unidirectional computations performed on SC10 and rotor 6 in Fluent, the present simulations have been performed with Au3D employing single passages with phase-lagged-boundary conditions as presented by Erdos et al. [27]. At this, the flow solution at the periodic boundaries is stored for the number of time steps needed to resolve a particular interblade phase angle and prescribed time lagged on the opposite boundary. The disadvantage of higher memory consumption, because of storing the flow solutions, is outweighed by the gain in CPU time. During the computation, the work done by the blade is determined after each vibration cycle and the aerodynamic damping is calculated using the energy method according to Equation 2.22.

The results of the aforementioned computations are displayed in Figure 7.10 indicating excellent agreement of the influence coefficients and single passage simulations. Moreover, the matching of both methods implies that the influence of the shock on the suction side is of minor importance. Investigations of the pressure coefficient at several blade sections during a vibration cycle support the impression that the shock position does not change significantly. Hence it can be stated that the influence coefficients are well suited for a reproduction of the interblade phase angle dependent aeroelastic behaviour of rotor 1. Furthermore, great differences in the aerodynamic damping due to a change of the vibration frequency can be observed to some extent. Considering the differences between the minimum and maximum vibration frequencies at the interblade phase angle with maximum aerodynamic damping, an increase of up to 80% is reached for blade mode 6. In fact, the biggest change in the absolute value of the aerodynamic damping is achieved for blade mode 1 where a difference of $\Delta\zeta_a \approx 0.015$ occurs. These numbers underline the importance of a frequency dependent treatment of the aerodynamic influences as accomplished in the present work.

7.4 Rotor 1 EBM Model

For the analysis of the forced response vibrations of the tuned and mistuned rotor 1 blisk an EBM model has been set up. The model takes account of disk flexibility, material damping of disk and blades as well as frequency and interblade phase angle dependent aerodynamic damping. The analyses comprise the investigation of the aerodynamic forces' influence on the eigenvalues of rotor 1, the computation of the tuned forced response and the intensive

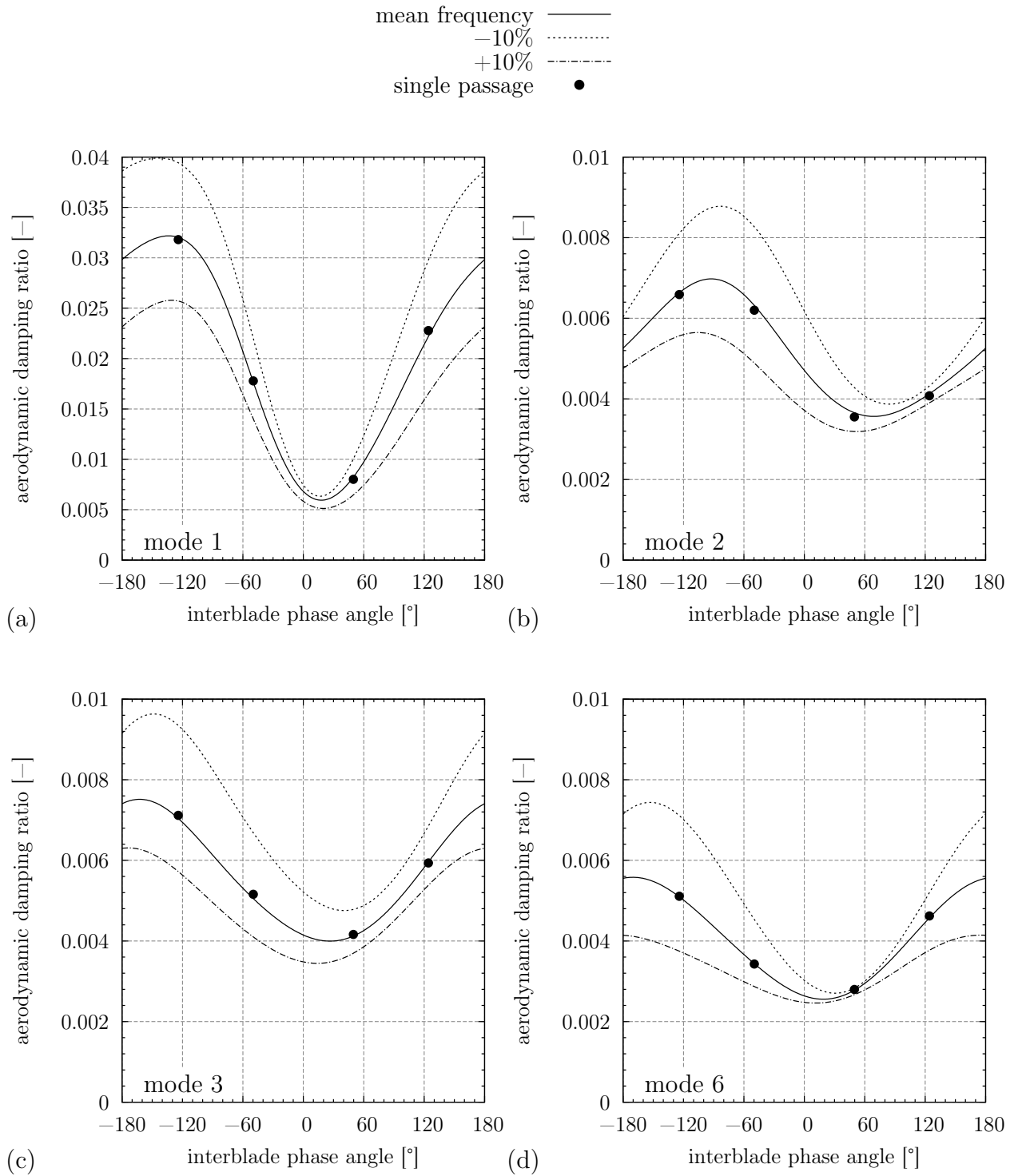


Figure 7.10: Aerodynamic damping for 1st flap mode (a), 2nd flap mode (b), 1st torsion mode (c) and tram line mode (d)

examination of the mistuned system including probabilistic analyses which give rise to a statistical assessment of mistuned blisk vibration features.

7.4.1 Identification of EBM Parameters

As already discussed in Chapter 4, the EBM has to be set up for each blade mode individually. It can be seen from Figure 7.8 that the modes 1 to 3 belong to the same disk mode family. Hence, the same disk parameters can be used for all of them. Nevertheless, an additional FE computation is necessary to obtain the lowest and highest frequencies of the first disk mode family (e.g. zero nodal circles).

For each blade mode a FE model featuring nearly rigid blades with a Young's Modulus ratio of blade and disk of ($E_b/E_d \approx 10$) has been exposed to centrifugal loading. As a result, the lowest frequency of the first disk mode family, associated with CSM 2 and the maximum frequency associated with CSM 14 are computed for the first and second disk mode family. The values of disk and blade mass are known from design to be $m_d = 7.796\text{kg}$ and $m_b = 9.699 \cdot 10^{-2}\text{kg}$ respectively. The frequencies in combination with the disk mass specify the EBM disk parameters of disk stiffness k_d and coupling stiffness k_c .

Next, the blade parameters are identified according to the blade frequencies calculated by SDOF approximation from the measured mistuning patterns as presented in Section 7.2.2. The blade stiffnesses $k_{b,i}$ are calculated directly from the approximated blade frequencies assuming a rigid disk. The blade mechanical damping values incorporated by the blade dampers $d_{b,i}$ are calculated from the measured blade frequency response function. Subsequent to the identification of the blade stiffness and damping, the disk flexibility is enabled which will lead to a change in blade frequencies. Hence they are corrected to fit the measured values by adapting the effectively vibrating blade mass which can be expressed in percentage of the physical blade mass as listed in Table 7.4. It can be seen that the effective blade mass is greatest for the 1st flap mode. This is not surprising since it is apparent from Figure 7.7 that this is the mode which has the biggest part of the blade participating in the vibration. Finally the aerodynamic influence coefficients, scaled with the effective blade mass, are incorporated as described in Section 4.2.3.

Table 7.4: Effective blade masses of rotor 1

blade mode	$m_{\text{eff}}/m_b[\%]$
1	37.31
2	12.94
3	12.72
6	15.71

In summary, the EBM model is adapted to the mistuned rotor 1 blisk and the tuned system

is derived afterwards adjusting the tuned values of blade frequency and damping to the mean values of the mistuned counterparts.

7.4.2 Eigenvalues of Tuned EBM

In order to check the plausibility of the identified models, eigenvalues of the tuned EBM without aerodynamic influences have been compared to FE results. Additionally, the eigenvalues of the aeroelastic system have been compared to the aeroelastic eigenvalues calculated under the assumption of a rigid disk as presented in Section 7.3. That way, the change in aeroelastic eigenvalues due to disk flexibility and therefore mechanical coupling can be evaluated.

The natural frequencies of the considered blade modes in the EBM without aerodynamic forces plotted versus the CSM are presented in Figure 7.11 showing acceptable agreement for the first three modes and greater differences for mode 6. It shows that for all blade modes the best match can be observed for the maximum CSM where the mechanical coupling has the lowest impact. On the contrary, the closer the considered CSM is to the region of blade and disk mode crossing the bigger the deviations to the FE results get. Furthermore, the mismatch enlarges for modes at higher frequencies and becomes greatest for mode 6 (tram line mode). Nevertheless it can be stated that the EBM is capable of modeling the effects of disk flexibility qualitatively with the excellence in correlation increasing with increasing distance from the frequency crossing regions.

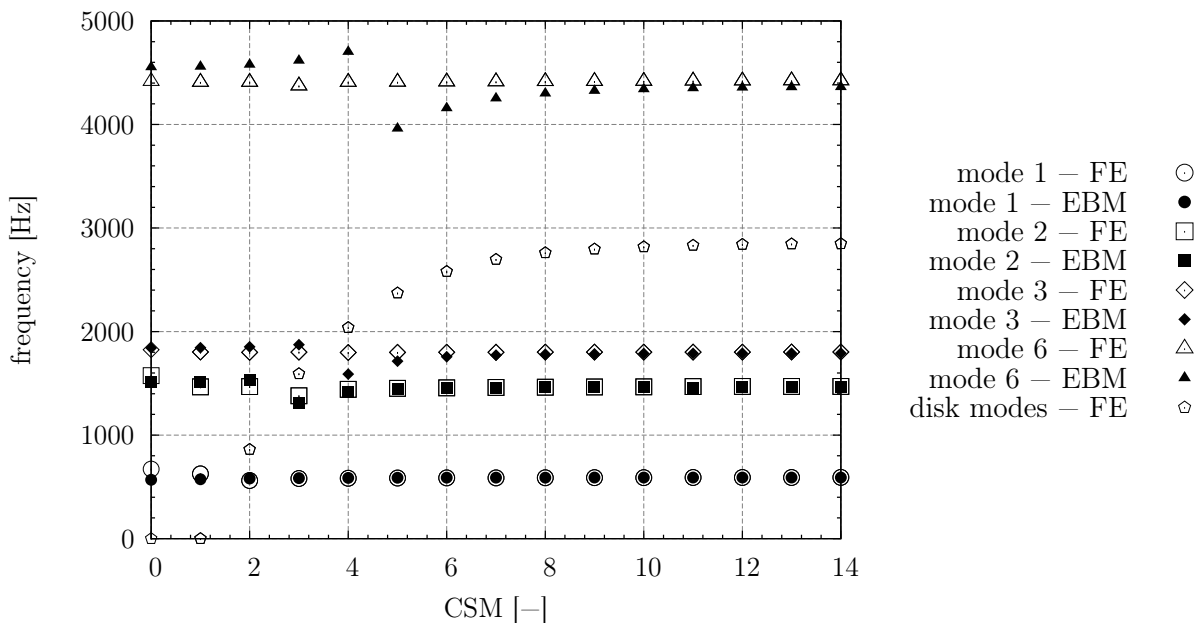


Figure 7.11: Frequency versus CSM diagram

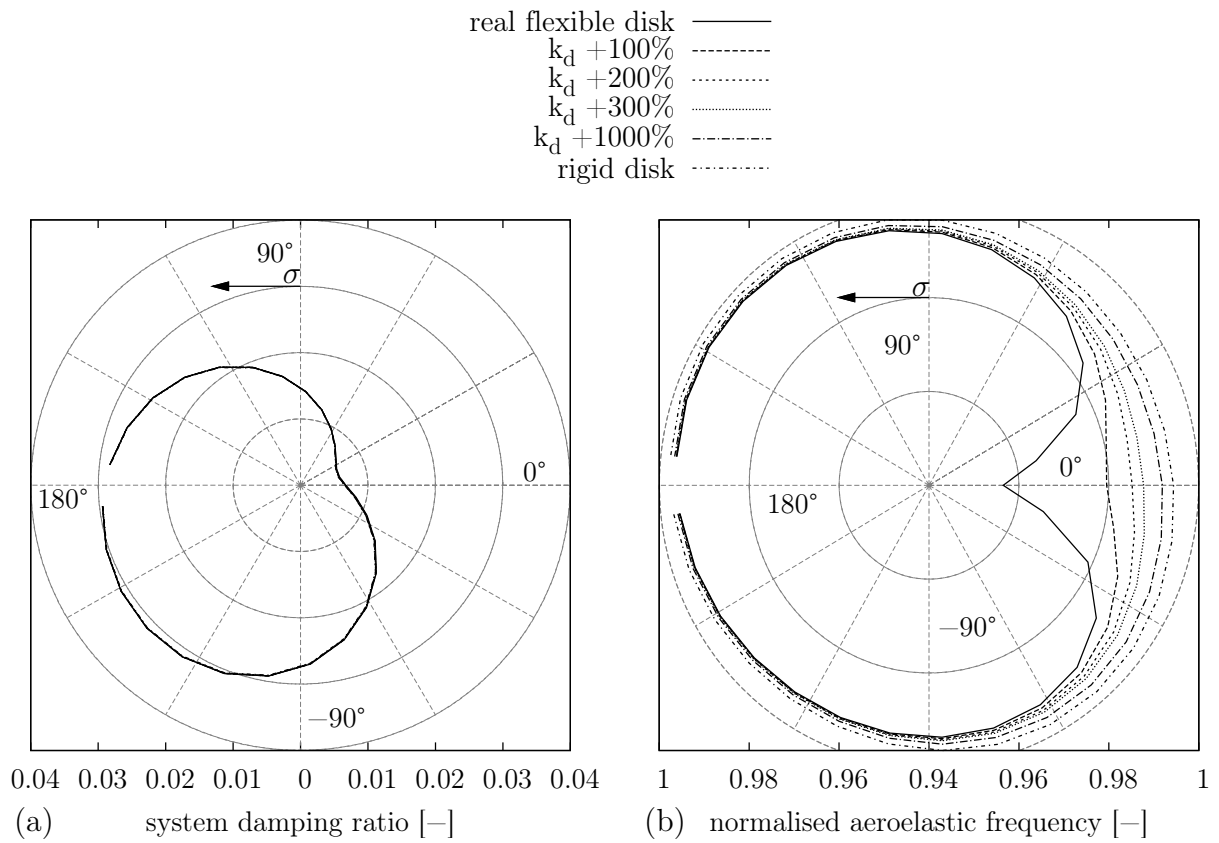


Figure 7.12: System damping (a) and aeroelastic frequency (b) of mode 1

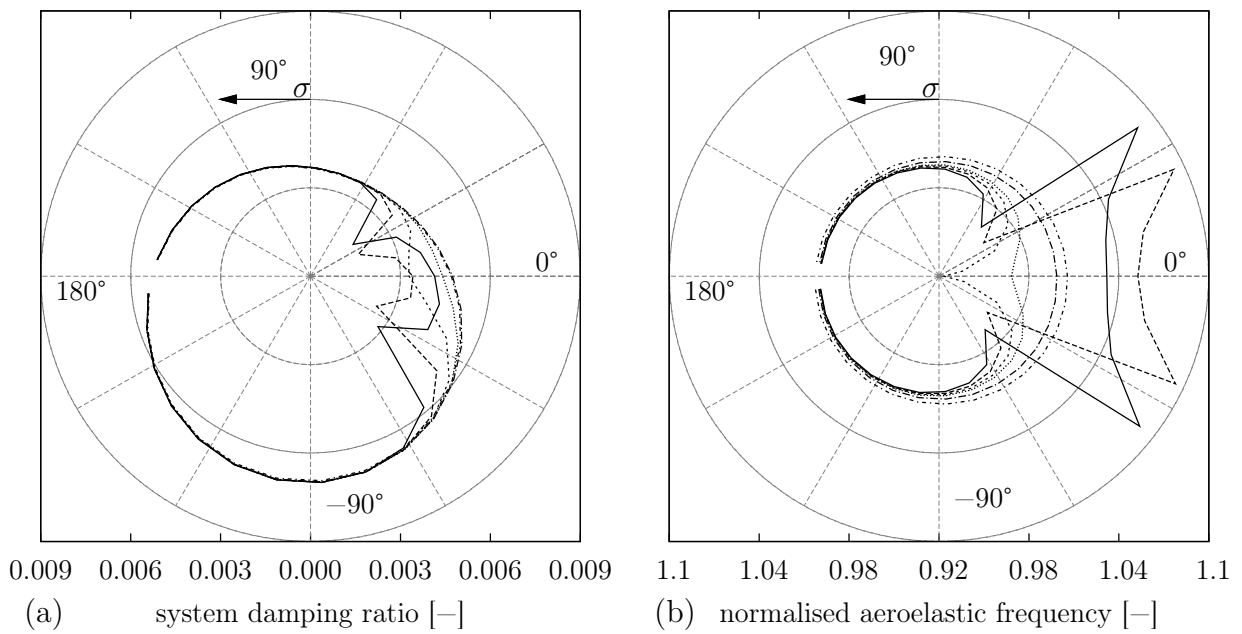


Figure 7.13: System damping (a) and aeroelastic frequency (b) of mode 2

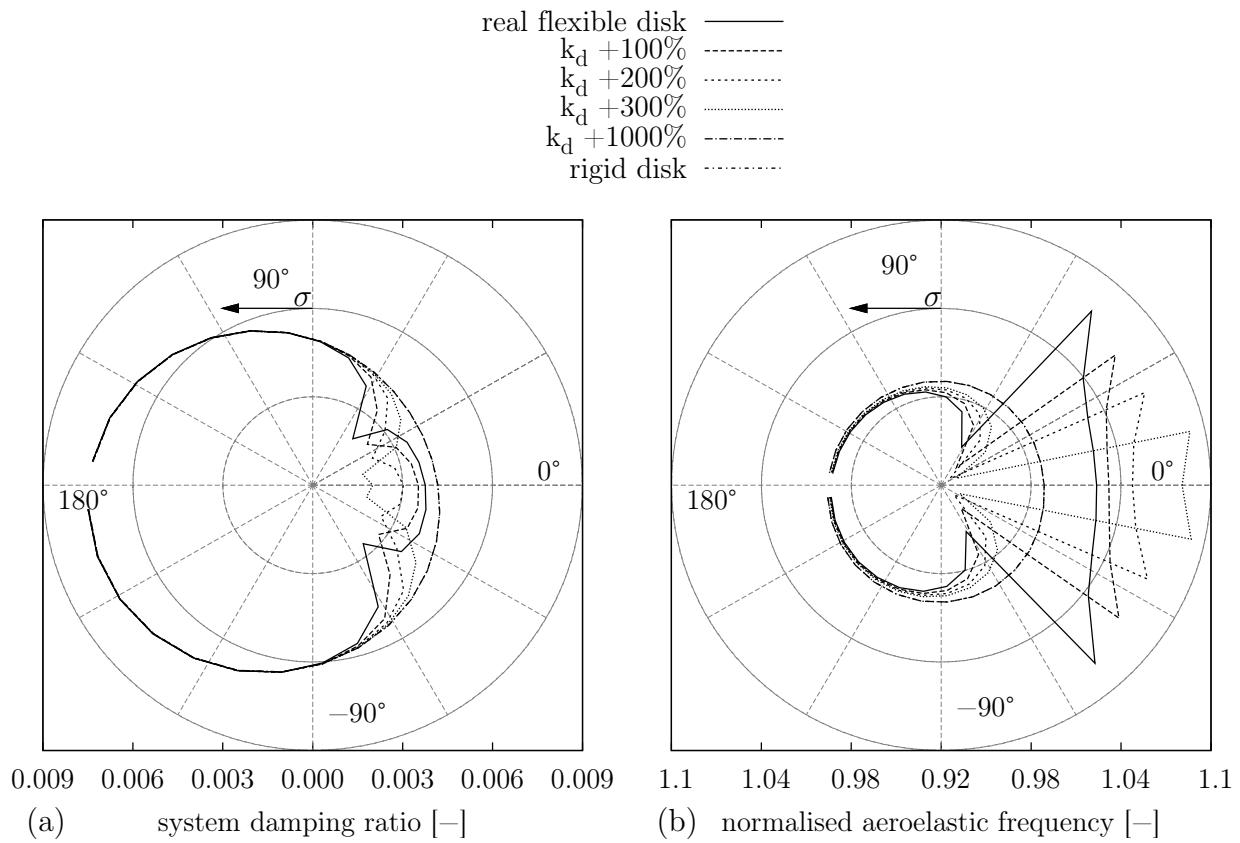


Figure 7.14: System damping (a) and aeroelastic frequency (b) of mode 3

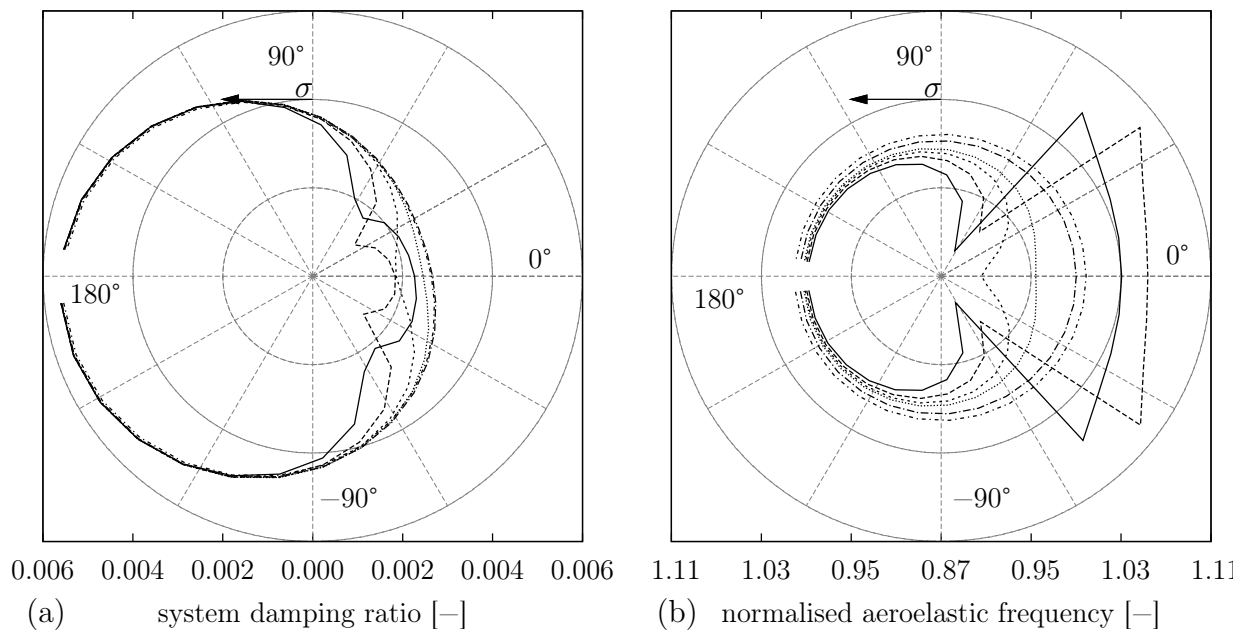


Figure 7.15: System damping (a) and aeroelastic frequency (b) of mode 6

Furthermore, the aeroelastic system parameters for the 1st flap mode are presented in Figure 7.12. At this, the system damping and the aeroelastic frequency are displayed in two separate plots as function of the disk stiffness k_d which has been increased from its original value until rigid disk condition as assumed in the identification process of the influence coefficients is reached. It shows that the sum of mechanical and aerodynamic damping is clearly dominated by the aerodynamic damping and that no quantitative change in system damping due to increased disk stiffness can be detected. The contrary is the case for the aeroelastic system frequency where the maximum resonance frequency drop is approximately 3.5% for $\sigma = 0^\circ$. Considering the rest of the CSM this change decreases with increasing number of nodal diameters (value of interblade phase angle) showing almost no difference for the highest CSM which is not very surprising since the highest CSM commonly shows lowest susceptibility to mechanical coupling.

Analogous analyses have been repeated for the rest of the blade modes for which the results are presented in Figures 7.13 to 7.15. Considering the aeroelastic system properties of these modes, the impact of mechanical coupling becomes obvious. The lower the disk stiffness is, the more mechanical coupling is introduced which leads to a significant reduction of the system damping of up to -52% for CSM=-3 of mode 2. As can be seen from the damping plot of mode 3, the CSM showing the greatest damping reduction may vary depending on the degree of mechanical coupling. Here the relevant CSM are in the range of -4 to 4. The CSM showing maximum deviation from the damping values determined under rigid disk assumption is always that one associated with the frequency crossing of a disk mode. Comparing the aeroelastic frequency² plots with the system damping, it appears that while the system damping is always lower than the corresponding values of a system with rigid disk, the aeroelastic system frequency may well increase. At this, it depends whether the CSM, and hence the interblade phase angle, is higher than the CSM at the frequency crossing or lower. The aeroelastic frequency will decrease moderately for the former one while notably differences are observed in the latter case. The change of the CSM associated with the maximum difference is the same as for the system damping and is attributed to the increase of the disk frequencies. As can be seen from Figure 7.11 for the real flexible disk the frequency crossing occurs at CSM=3 for mode 2 and at CSM=4 for mode 3. When the disk stiffness is increased the CSM where frequency crossing appears is shifted to lower CSM due to a shift of all disk modes to higher frequencies. Again, for all the modes the effect on CSM greater than 5 is of minor importance. When a certain amount of disk stiffness is present all disk modes exhibit higher frequencies than the lowest blade frequency and the results appear as for the curve of a rigid disk.

²The aeroelastic frequencies have been normalised with the tuned structural frequency.

7.4.3 Eigenvalues of Mistuned EBM

After the influence of the aerodynamics on the tuned rotor blisk has been analysed, mistuning is introduced into the EBM. Therefore, the blade stiffnesses are adapted according to the mistuning patterns presented in Figure 7.9 for mode 1 and in Figures B.1 to B.3 for the rest of the modes. Initially, the eigenvalues of the system without aerodynamic forces are compared. As described in Section 2.2 mistuning leads to a split of the double modes resulting in two eigenvalues with different natural frequencies close to the tuned one. The mistuned natural frequencies are displayed in Figure 7.16 showing the expected deviations. For this plot, the frequencies have been assigned to the dominating Fourier coefficients DFT_{\max} of the spatial Fourier decomposition of the mode shapes which correlates with the CSM in case of the tuned system while it does not necessarily reflect the number of zero-displacement-crossings of the mistuned system. Details about this topic are also presented in Section 2.2. That is why there are four eigenvalues present for $DFT_{\max} = 14$ while there is non for $DFT_{\max} = 12$ and only one for $DFT_{\max} = 13$. It also shows, as has been described by Wei and Pierre [117] that even small mistuning as determined for mode 1 ($\sigma_{\text{STD},\Omega} = 0.13\%$) can lead to a significant change in natural frequencies and that the deviations from the mean value are greatest for higher eigenvalues.

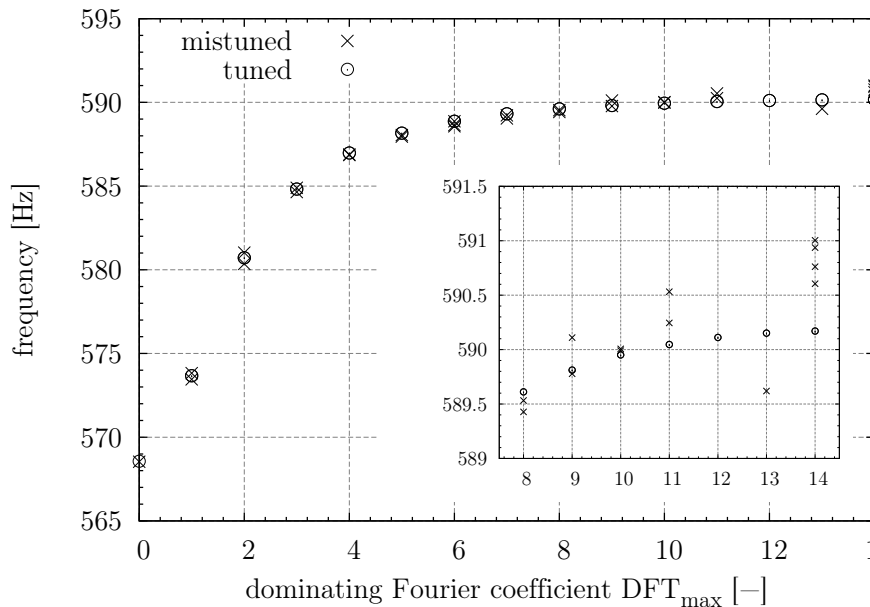


Figure 7.16: Mistuned natural frequencies versus dominating Fourier coefficients (MCSM), mode 1

The Fourier coefficients and the mode shapes of the eigenvalues with and without aerodynamic influence for $DFT_{\max} = 3$ and $DFT_{\max} = 14$ are displayed in Figures 7.19 and 7.20. Concerning the deviations from the tuned mode shapes, the rather small standard deviation already results in massive differences especially for higher DFT_{\max} . In the case of

$DFT_{\max} = 14$ the mode shape is strongly localised with the displacements being restricted mainly to blades 15 to 19 which also reflects in the localisation parameter of $\psi = 62.98\%$. The impact of the aerodynamics on the mode shapes is quite different depending on the dominating Fourier coefficient. Considering $DFT_{\max} = 3$ first, Figure 7.19, the mode shape changes only slightly which is also confirmed by a rather small decrease of the Fourier coefficients 4 to 9. The localisation parameter, described in Section 2.2, remains almost constant with $\psi = 5.06\%$ without aerodynamics and with $\psi = 4.35\%$ when aerodynamics are regarded. On the other hand, the aerodynamics provide a massive reduction of the additional Fourier coefficients introduced by mistuning for $DFT_{\max} = 14$ which leads to a mitigation of the mistuning effects and which is the reason that the dominance of $DFT_{\max} = 14$ becomes even greater and the mode shapes becomes more comparable to the tuned one. Consequently the localisation parameter drops to $\psi = 14.45\%$ indicating that more blades can take part in the vibration distributing the vibration energy more uniformly over the assembly. An excerpt from the rest of the mode shapes of mode 1 and the remaining blade modes is presented in Appendix C.

Comparing the mode shapes of the different blade modes for $DFT_{\max} = 3$ and $DFT_{\max} = 14$, the impact of mistuning is quite different with and without aerodynamic influences. Considering $DFT_{\max} = 3$ first, the spatial Fourier decomposition shows content of Fourier coefficients from 1 to 9 for mode 1 which is mitigated when aerodynamic forces are taken into consideration. For mode 2 only very small additional coefficients can be observed which is the reason that the mode shapes compare very well with the tuned one. The impact of the aerodynamics is considerably lower than for mode 1. The same is assessed for the mode shapes of mode 3 and mode 6.

On the other hand, when the mode shapes with $DFT_{\max} = 14$ are analysed the opposite is the case. For mode 1 significant magnitudes of Fourier coefficients greater than 3 can be observed in the case without aerodynamic forces which are reduced by factors of up to 2 while increasing $DFT_{\max} = 14$ by a factor of approximately 3.5 with aerodynamics considered. For mode 2 the situation is quite similar although an increase only by factor 2.5 is achieved for $DFT_{\max} = 14$ and the coefficients for 8 and 11 even rise when aerodynamics are regarded. The same can be observed for mode 3 and mode 6 while the latter one even shows a reduction of the magnitude of the dominating Fourier coefficient while an increase of the 13th coefficient occurs at the same time which does not lead to an improvement at all. The additional Fourier coefficients that are found are the reason that the corresponding CSM are also excited in forced response analysis even if only a single engine order excitation is present. Similarly, a mode shape containing additional Fourier coefficients can be excited by any of the corresponding CSM leading to complex vibration behaviour.

Lastly, the aeroelastic eigenvalues of the considered modes are plotted in Figure 7.17 and 7.18. In Section 2.3.1 the influence of mistuning on the aeroelastic stability has been described. At first sight, no significant differences between the tuned and mistuned eigenvalues can be determined which is due to the comparatively small mistuning as given in Table 7.3. If a

closer look is taken at the least stable eigenvalues marginal increases of the aerodynamic damping can be detected, see Table 7.5 which presents the relative change with respect to the tuned damping value. Those eigenvalues associated with the highest Fourier coefficients show greater changes which is mainly attributed to the previously presented frequency split and a cause of the considerable magnitudes of additional Fourier coefficients.

Table 7.5: Stability increase due to mistuning

mode	least tuned damping [-]	least mistuned damping [-]	damping rise [%]
1	0.005891436	0.005946409	0.009331
2	0.001784594	0.001799221	0.008196
3	0.002064080	0.002064999	0.000445
6	0.001726258	0.001730629	0.002532

7.4.4 Forced Response of Tuned and Mistuned EBM

The analysis of the tuned and mistuned forced response is performed to analyse the sensitivity of the rotor 1 blisk to blade frequency deviations due to mistuning. Since the focus is on the qualitative differences introduced by blade mistuning, the forcing amplitude is set to unity for all computations allowing for a comparison of the results of different engine order excitations. The computations are carried out in the frequency domain as described in Section 4.4 yielding frequency response functions, amplification factors and localisation parameters as result. For the computations, it is still assumed that, despite of the frequency mistuning, the blade mode shapes remain constant. Concerning the aerodynamic forces, the frequency dependency is considered by interpolating the aerodynamic influence coefficients as presented in Section 6.2.2 from the coefficients of three computations using the structural natural frequency and values of $\pm 10\%$ as shown in Figure 7.10.

The tuned forced response founds the basis for the analysis of the impact of mistuning on the blade responses. Its computation is straight forward and its results are the blade amplitudes and frequencies at resonance. Special attention has to be paid to frequency veering and crossing regions. As described in Section 2.1 the vibrations of different blade and/or disk modes may couple in these regions. Since the aerodynamic influence coefficients are only valid for a single blade mode family, the frequency range in the affected crossing regions was restricted to the range of the blade dominated frequencies covering also the frequency deviations introduced by mistuning. For the computations without aerodynamics a frequency resolution of 0.01Hz has been used while frequency steps of 0.025Hz have been employed when aerodynamic forces have been considered.

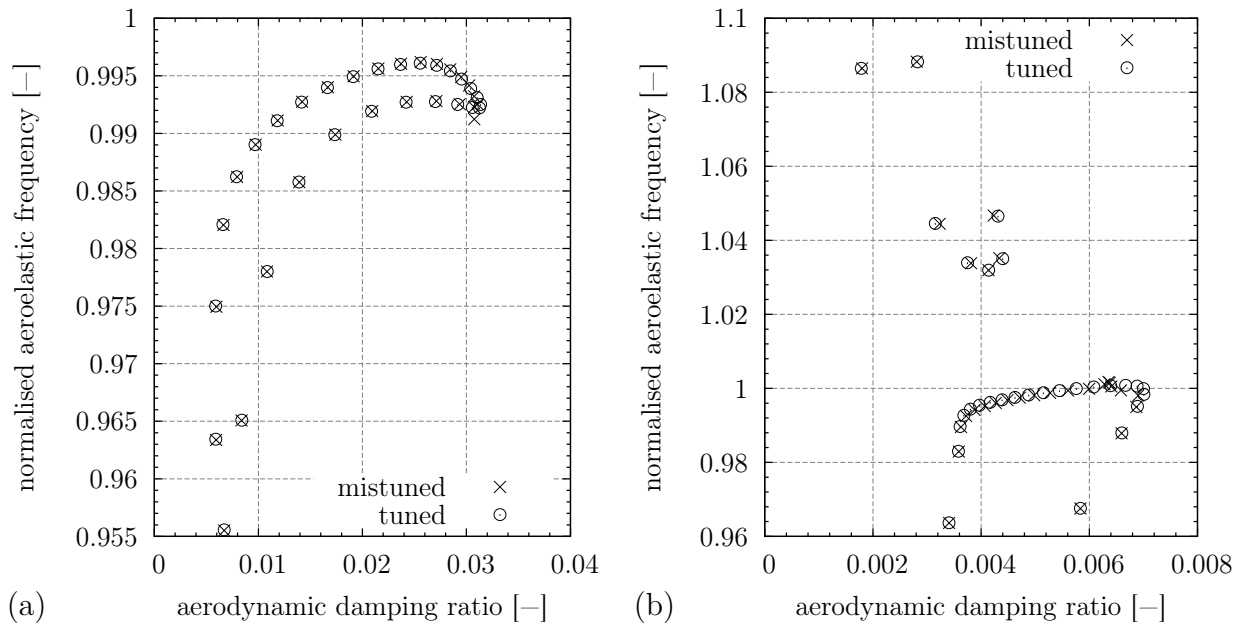


Figure 7.17: Aeroelastic eigenvalues of mode 1 (a) and mode 2 (b)

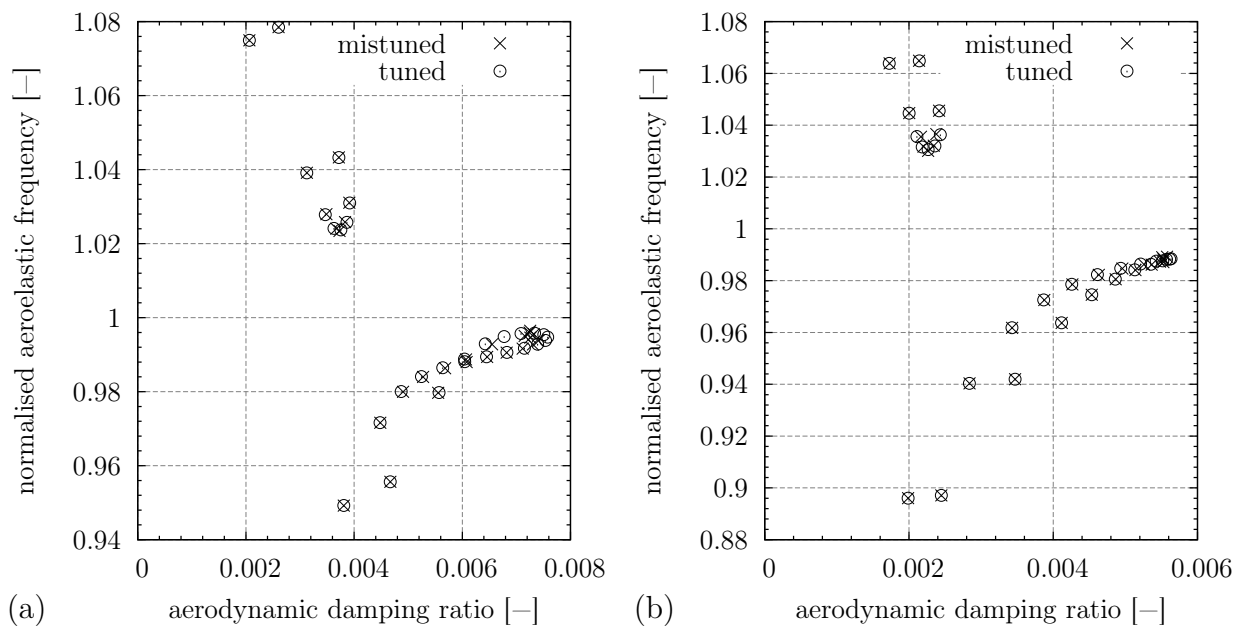


Figure 7.18: Aeroelastic eigenvalues of mode 3 (a) and mode 6 (b)

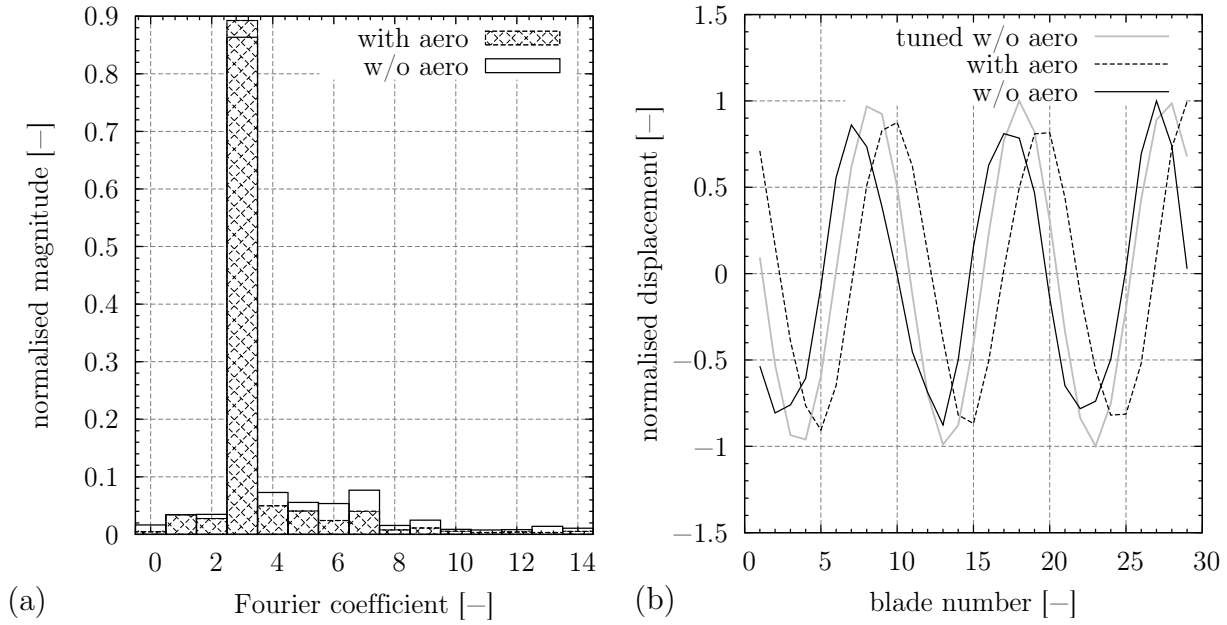


Figure 7.19: Fourier coefficients (a) and mode shape (b) of mode 1, $DFT_{\max} = 3$

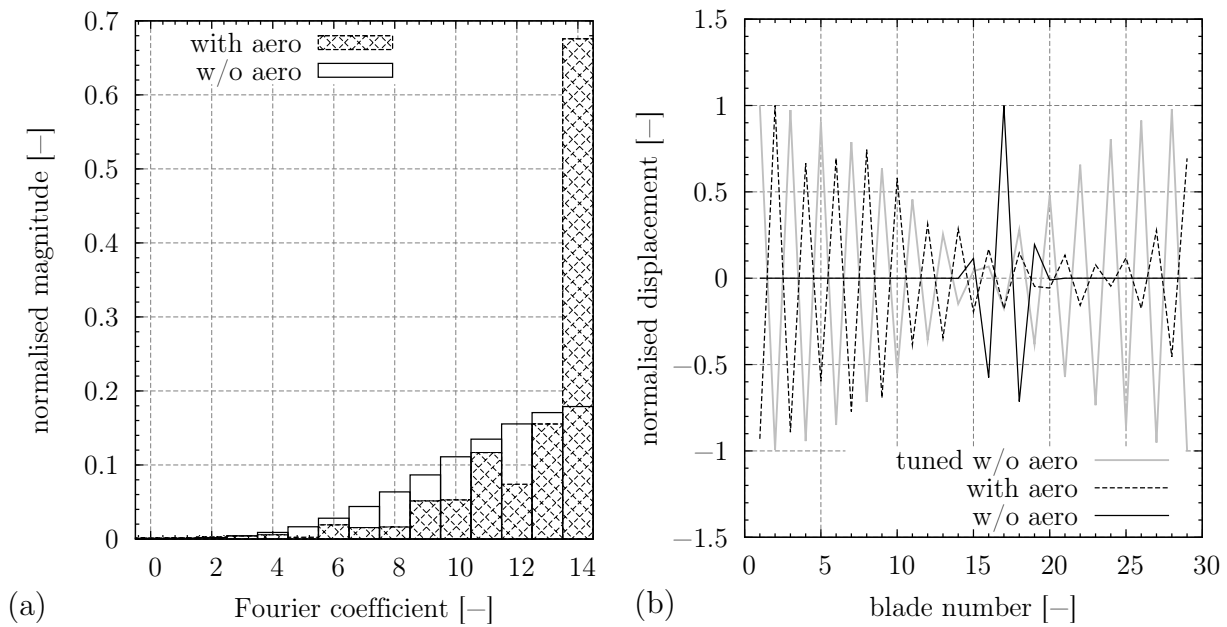


Figure 7.20: Fourier coefficients (a) and mode shape (b) of mode 1, $DFT_{\max} = 14$

Measured Mistuning Patterns

At first, the forced response of mistuning patterns obtained from blade by blade measurements (and corrected by the offset introduced by centrifugal forces) is analysed for different scenarios of aerodynamic damping and various engine order excitations. In Figure 7.21 the frequency response functions of the tuned and mistuned system, normalised with the maximum tuned blade response without, with constant and with blade individual aerodynamic damping are displayed for an excitation of mode 1 with an engine order exciting a 7 nodal diameter pattern (nd 7)³. In case of the mistuned system the envelope of all blade displacements is shown. This particular engine order has been exemplarily chosen because of its forced response showing the maximum blade displacement amplification in the absence of aerodynamic forces.

Considering the mistuned system without any aerodynamic damping no single peak can be found anymore. Instead, as previously described, all mode shapes containing additional Fourier coefficients corresponding to the engine order of the excitation are also forced resulting in numerous peaks besides the resonance peak. The Fourier decomposition of the blade displacement at the circumference at the frequency of maximum blade displacement (also displayed in Figure 7.21) shows significant content of higher CSM leading to a localisation parameter of $\psi = 29.69\%$ and a displacement amplification of approximately 42%. When aerodynamic forces are included in the computations an immense reduction of the mistuning effect is achieved. The results shown in Figure 7.21 (b) have been obtained with every blade featuring the same, constant aerodynamic damping and aerodynamic stiffness due to the interblade phase angle of the excitation thus no aerodynamic coupling between the blades. This can be realised by applying the corresponding travelling wave mode coefficient as zeroth and only influence coefficient. On the contrary, the results of Figure 7.21 (c) are the outcome of a computation with blade individual damping realised via aerodynamic influence coefficients. This means that the blades are aerodynamically coupled and that the blade damping is explicitly depending on the vibration of the adjacent blades. However, only little difference can be determined between the two computations. The reason for that is the rather small standard deviation of the frequency mistuning of only $\sigma_{\text{STD},\Omega} = 0.13\%$. Although these small deviations are strong enough to notably alter the forced response of the system without aerodynamic forces, the impact of the aerodynamics is sufficient to mitigate the additional Fourier coefficients resulting in a vibration mode close to the tuned one. This assumption is confirmed by the results of the Fourier decomposition showing a clearly dominating seventh coefficient for the computations with aerodynamic damping. Consequently, the localisation parameter drops down to $\psi = 1.14\%$ in case of constant aerodynamics and $\psi = 2.17\%$ respectively. These values indicate almost tuned behaviour which is also the reason that the blade individual, aerodynamic treatment gives nearly the same results. In both

³Positive nodal diameters indicate blisk vibration in a forward travelling wave and negative ones backward travelling waves respectively.

cases the displacement amplification is clearly reduced to values of $\nu = 1.03$ and $\nu = 1.06$ respectively.

Analogous comparisons of the forced response of the engine order showing maximum amplification in the case without aerodynamics have been performed for the rest of the considered blade modes shown in Appendix D. The observations made for mode 1 remain the same for the other modes. Especially the results of the computations employing constant and blade individual aerodynamic damping are very much the same. Since the standard deviations of the mistuning patterns are comparatively small the question arises whether the effect of the different aerodynamic treatment is similar when the standard deviation increases.

This question has already been addressed by several researchers. In the work of Klauke [68] probabilistic analyses of mistuning patterns featuring up to 3% standard deviation of the frequency mistuning have been performed in the absence of aerodynamic forces. Concerning greater deviations Nikolic [86] investigated the forced responses of a system with frequency deviations of up to 40% but only without considering aerodynamic coupling. This so called *large mistuning* concept has been the subject matter of Petrov's work as well, [93], [92], [94], [95]. He scrutinised the forced response behaviour of mistuned bladed disks with frequency deviations up to $\sigma_{\text{STD}} = 10\%$ including the influences coming from the aerodynamics. He found that with interblade phase angle dependent aerodynamic damping the maximum mistuned blade response may be reduced to 40% of its tuned counterpart. On the contrary, his computations featuring constant aerodynamic damping as determined from tuned assembly simulations did not show this phenomenon. Anyway, his computations were restricted to a single aerodynamic damping characteristic involving huge max to min ratios as usually observed for first flap modes.

In order to analyse the dependency of the forced response on the mistuning strength, similar simulations of patterns with standard deviations of up to 10% have been carried out for the four previously analysed blade modes featuring different max to min ratios of the aerodynamic damping. First, the measured mistuning patterns have been scaled to standard deviations between 0% and 10%. The strategy is similar to the computations performed on the 2D rotor 6 model in Section 6.2.2 indicating a correlation of the degree of mistuned response reduction and the max to min ratio of the aerodynamic damping. Furthermore, since measured mistuning distributions of a single blisk can not cover the entire variety of mistuning patterns occurring in a fleet of engines, probabilistic forced response analyses of randomly generated mistuning patterns have been conducted. The intention of these computations is to give a detailed insight into the effects arising when blade modes with lower aerodynamic damping and smaller max to min ratios are considered. Moreover the conditions needed to achieve a reduction below the tuned response are pointed out.

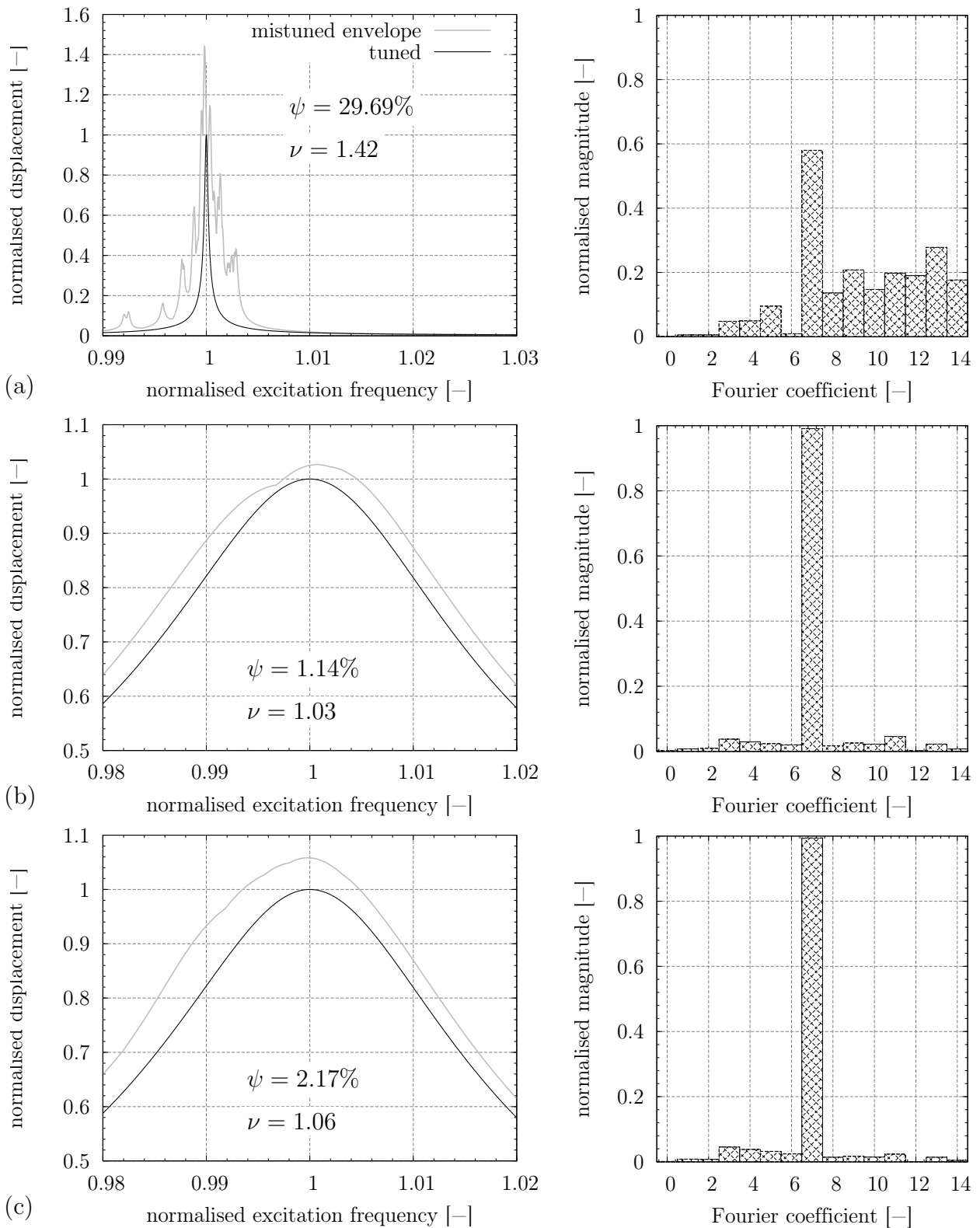


Figure 7.21: Frequency response function and Fourier coefficients of mistuned ODS at resonance frequency without aerodynamic damping (a), with constant damping (b) and with blade individual damping (c) - mode 1, nd 7

Scaled Mistuning Patterns

For the interpretation of the forced response of the scaled mistuning patterns, five engine order excitations have been considered for each blade mode, these are

- the engine order leading to maximum displacement amplification in the case without aerodynamic forces as already shown in Figure 7.21 and Figures D.1 to D.3,
- the engine orders exciting the nodal diameters with minimum and maximum aerodynamic damping and
- the engine orders giving minimum and maximum amplification at $\sigma_{STD} = 10\%$

which are summarised in Table 7.6⁴.

Table 7.6: Relevant engine orders and excited nodal diameters

condition	mode 1		mode 2		mode 3		mode 6	
	EO	nd	EO	nd	EO	nd	EO	nd
max. amplification w/o aero	7	7	13	13	0	0	14	14
min. aerodynamic damping	1/2	1/2	5/6	5/6	2	2	1/2	1/2
min. amplification	1	1	8	8	1	1	4	4
max. aerodynamic damping	18	-11	22/21	-7/-8	16	-13	15	-14
max. amplification	19	-10	26	-3	18	-11	16	-13

It has to be mentioned that in cases where two engine orders are given in the table, the minimum and maximum values of aerodynamic damping are not associated with integral numbers of nodal diameters but feature IBPA in between the given ones. In all other cases the extremes have been close to the listed engine orders.

The amplification factors of the nodal diameters⁵ excited by the chosen engine orders are presented in Figures 7.22 to 7.25. Considering blade mode 1 first, the massive differences between the computations with constant aerodynamic damping and those with blade individual one are apparent. While the differences are rather small for $\sigma_{STD} \ll 1\%$, which has also been observed for the results of the measured mistuning patterns, considerable deviations occur for greater standard deviations with the maximum being associated with nd 1 where the maximum mistuned response is almost twice as high as with blade individual damping. Moreover, the curves obtained with constant damping seem to converge towards a common amplification factor of approximately 1.2. From Table 7.6 it can be seen that for

⁴The given nodal diameters correspond to the aerodynamic damping curve of the nominal system.

⁵The results are labeled with the nodal diameters excited by the chosen engine orders in the tuned case.

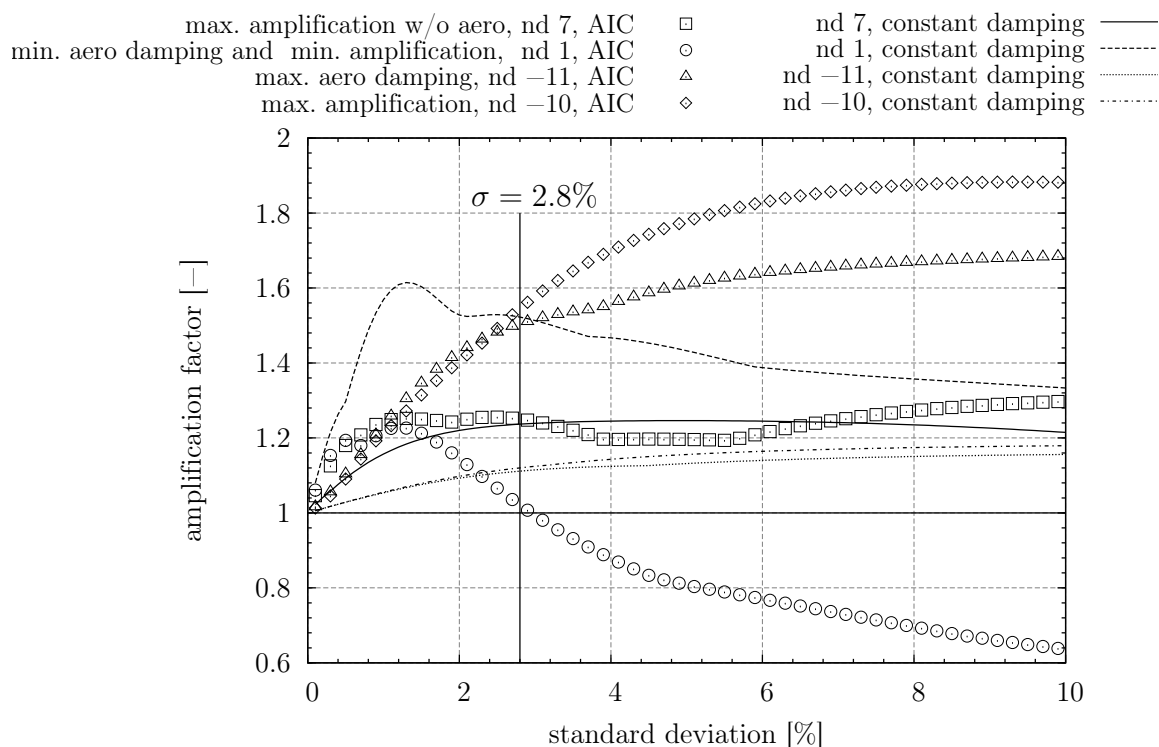


Figure 7.22: Amplification factors of forced response with scaled mistuning patterns - mode 1

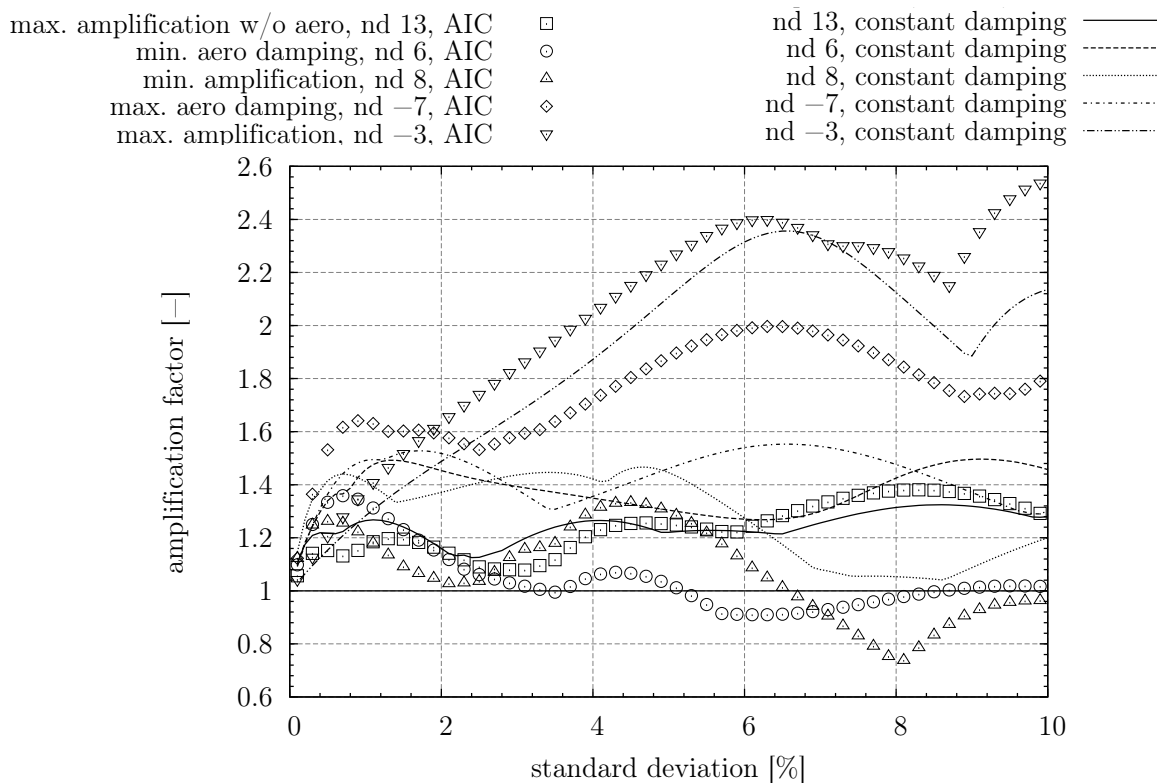


Figure 7.23: Amplification factors of forced response with scaled mistuning patterns - mode 2

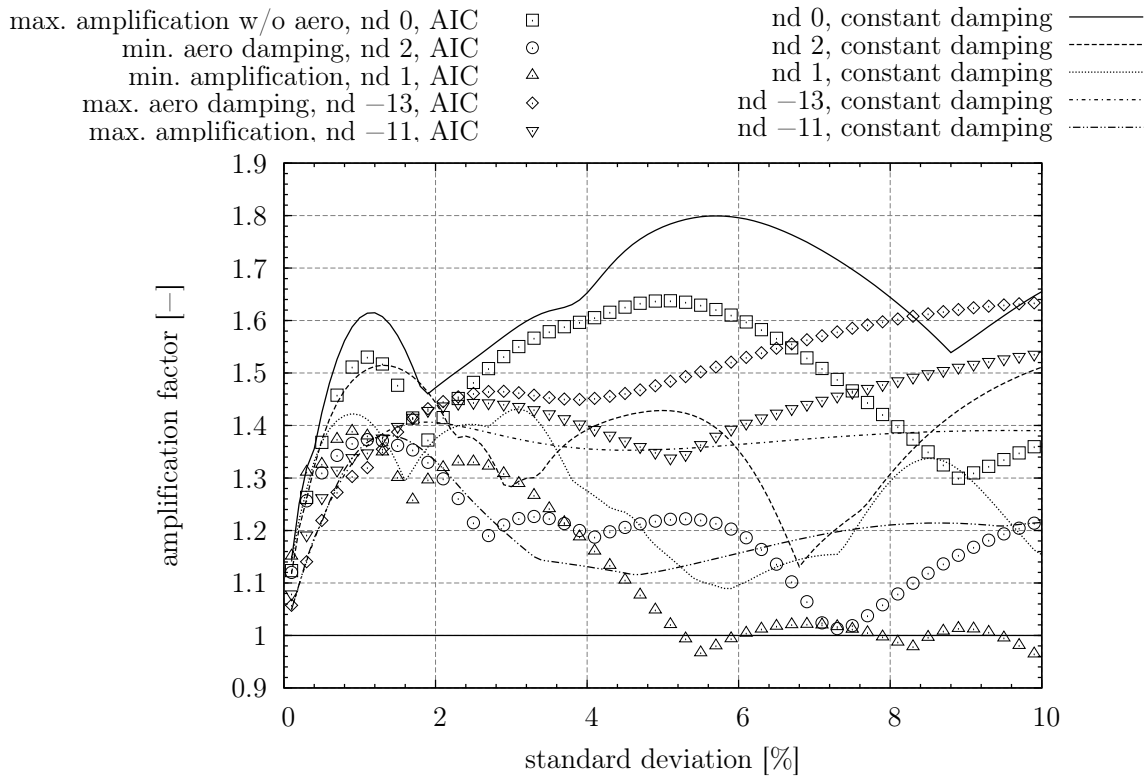


Figure 7.24: Amplification factors of forced response with scaled mistuning patterns - mode 3

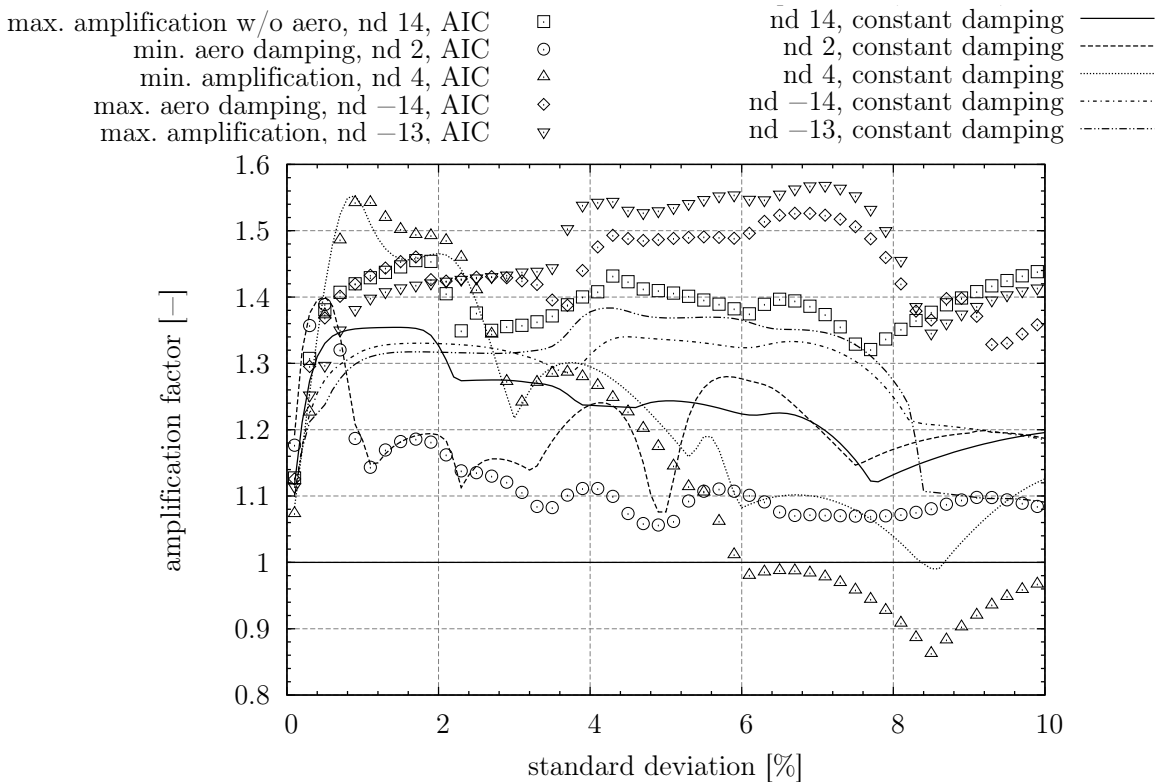


Figure 7.25: Amplification factors of forced response with scaled mistuning patterns - mode 6

mode 1 the nodal diameters with minimum aerodynamic damping and minimum amplification factor are identical (nd 1). For this nd 1 significant reductions of up to 36% with respect to the tuned response are achieved. Nevertheless, for $\sigma_{\text{STD}} < 2.8\%$ amplification factors of up to 1.24 are also reached. The computation of the nd 1 forced response with constant damping shows similar tendencies but with significantly different gradients especially for lower standard deviations. Concerning the nodal diameter with maximum amplification (nd -10) it is close to the one with maximum aerodynamic damping (nd -11) and these show similar behaviour. Yet, none of these forced responses shows a maximum blade displacement lower than the tuned one but on the contrary to nd 1 the amplification factors are consequently greater than the corresponding ones obtained with constant aerodynamic damping.

The situation for blade mode 2 is quite similar. Here, the nodal diameter exhibiting minimum aerodynamic damping (nd 6) is not the same as the one that shows the greatest amplitude reduction (nd 8). Nevertheless, nd 8 is very close to the minimum aerodynamic damping and shows likewise behaviour. Overall, nd 6 exhibits blade amplitudes lower than the tuned one over a greater standard deviation range while nd 8 drops below the tuned response for $\sigma_{\text{STD}} > 6.5\%$. Again, the nodal diameter corresponding to maximum aerodynamic damping (nd -7) shows significant amplification factors while the greatest ones are achieved for nd -3 which shows comparable behaviour as the counterpart with constant damping. On the contrary to the results of blade mode 1 the differences between blade individual and constant damping are not that great. Despite the smaller differences, no mitigation below the tuned response is achieved with constant damping likewise.

The findings also apply for the other two blade modes. Yet, the minimum amplification factors reached for blade mode 3 are only just below the tuned response while for blade mode 6 a reduction of approximately 18% is achieved. For mode 6 even the comparison of constant and blade individual damping becomes best. Taking nd 4 for example, both results match quite well up to $\sigma_{\text{STD}} \approx 5.0\%$ when the blade individual effects become dominant which leads to significantly lower amplification factors.

In the following, the phenomenon of maximum blade response reduction below the tuned one is going to be analysed in detail. All nodal diameters that show amplification factors slightly above or even below 1.0 at large standard deviations feature significantly higher responses below and around $\sigma_{\text{STD}} = 1.0\%$ as well. Both phenomena are attributed to a combination of structural and aerodynamic effects. On the one hand, the amount of structural coupling influences the achievable amplitude which has already been shown by Miyakozawa [82]. Likewise, the disk section of the rotor 1 blisk has been modified to yield the behaviour of an infinitely stiff disk resulting in a massive reduction of the amplification factors at low standard deviations, Figure 7.26 (a).

Another important factor are the aerodynamic forces. The impact of the max to min ratio of the interblade phase angle dependent aerodynamic damping has already been shown with the analysis of the rotor 6 in Section 6.2.2. Analogously, the $\pm 1\text{st}$ influence coefficients of mode

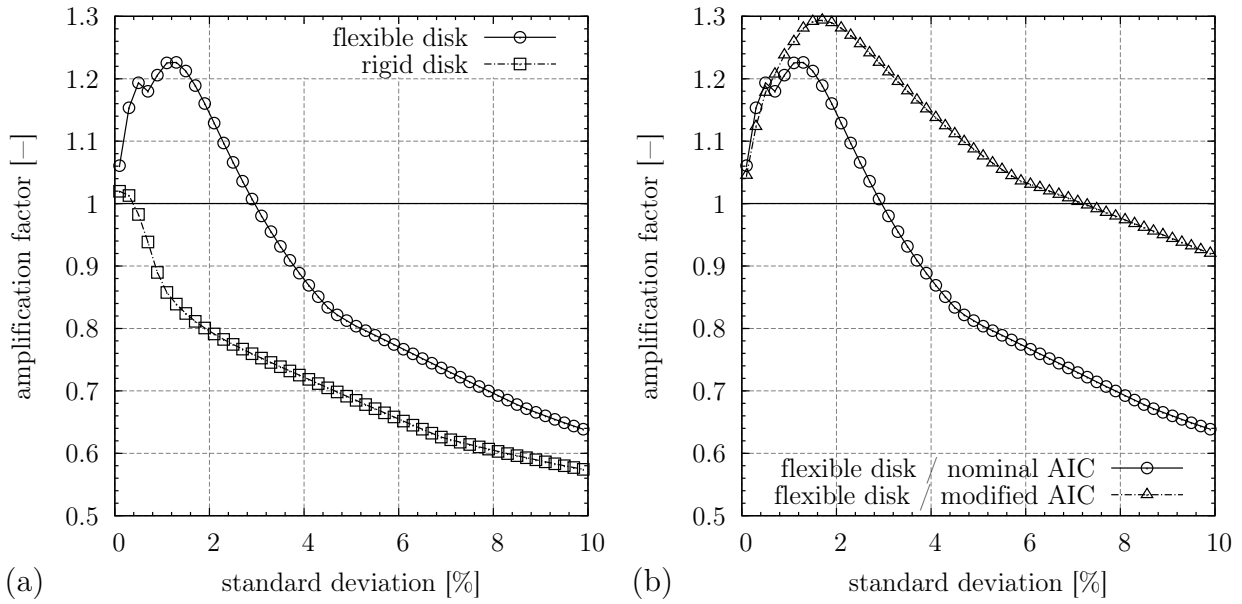


Figure 7.26: Variation of disk flexibility (a) and modified AIC (b) - mode 1 / nd 1

1 have been reduced by 50%. As a result, the amplification factors shown in Figure 7.26 (b) increase, shifting the point where the maximum blade response drops below the tuned one to $\sigma_{\text{STD}} = 7.3\%$. A significantly lower max to min ratio of the aerodynamic damping is a characteristic feature of higher blade modes. Hence it is quite obvious that such an immense reduction of the maximum blade response is more likely to occur with first flap modes or such with high max to min ratios of aerodynamic damping.

The characteristic behaviour of the amplification factor of a nodal diameter pattern is a result of localisation and frequency separation of the blades as has already been described by Klauke [68] and Brown [15]. Again, the physical mechanisms are discussed at the example of nd 1 of mode 1. Considering the case without aerodynamic damping first, Figure 7.27, the resonance frequencies of the blades are closely spaced if the frequency deviations are very small which expresses itself in low amplification factors and hence mode shapes similar to the tuned one. Due to the blade resonances being so close, vibration energy can be transferred from one blade to the other. At that point, the mistuning is not yet changing the circumferential distribution of the responses very much, Figure 7.28 (a), but though significant increase in the maximum blade response is observed. When the mistuning strength increases, the blade resonance frequencies separate more and more obstructing an exchange of vibration energy leading to a temporary decrease of blade amplitudes, Figure 7.28 (b). Finally when the mistuning is so strong that distinctively different resonance frequencies occur, the vibration energy concentrates on only the blades closest to the excitation frequency resulting in large localisation parameters and steadily increasing blade amplitudes, Figure 7.28 (c).

If the aerodynamics are taken into consideration the comparatively low localisation param-

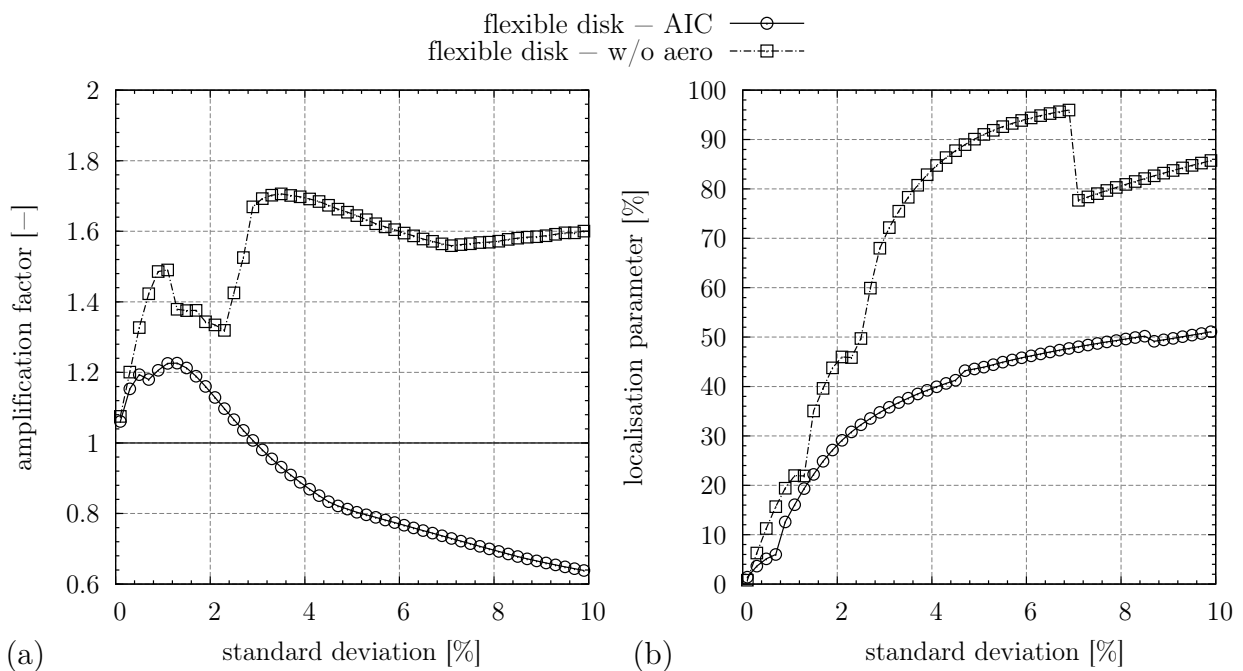


Figure 7.27: Amplification factor (a) and localisation parameter (b) of forced response with and w/o aerodynamics - mode 1 / nd 1

eter at small standard deviations results in interblade phase angles close to the tuned one. Hence the circumferential blade displacements as plotted in Figure 7.28 (a) are comparable for the system with and without aerodynamic damping and both still match quite good with the tuned CSM 1. The resultant aerodynamic damping admittedly reduces the displacement amplification but though, since the amount of damping is still similar to the tuned one and the energy transfer between the blades is still possible, a significant displacement amplification is the result. When the standard deviation increases the deviations from the tuned mode shape grow. This means that more CSM take part in the vibration which reveals in the Fourier decomposition by additional coefficients, Figure 7.28. Consequently, adjacent blades feature different interblade phase angles than in the tuned case. If the engine order excites the nodal diameter of minimum aerodynamic damping in the tuned case, every deviation from the tuned interblade phase angle will yield more damping and therefore an attenuation of maximum blade response in the mistuned case. The opposite is the case when the forced response of the nodal diameter corresponding to maximum aerodynamic damping is considered. In Figure 7.22 these differences are quite apparent. Depending on whether the nodal diameter of minimum or maximum damping is regarded, the amplification factors may considerably increase or decrease compared to the computations employing constant damping taken from the tuned system.

The findings of the analysis of scaled mistuning patterns are:

- The forced responses featuring maximum blade amplitudes lower than the tuned one

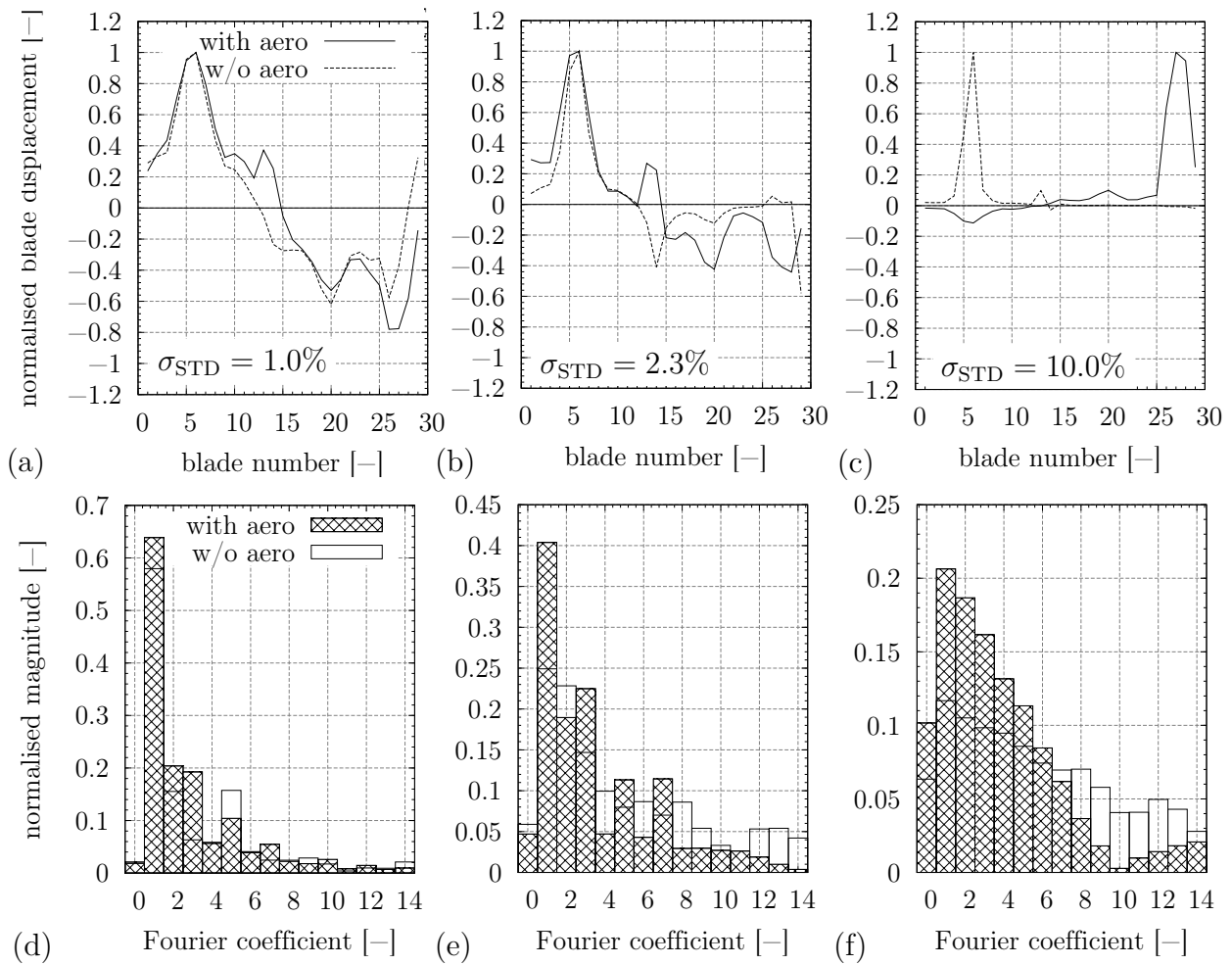


Figure 7.28: Circumferential blade displacements at resonance and corresponding Fourier coefficients - mode 1 / nd 1

are either assigned to those nodal diameters featuring minimum aerodynamic damping in the tuned case or are close to it,

- the biggest reduction is achieved for the blade mode having the largest max to min ratio in aerodynamic damping (mode 1),
- the largest amplification factors of rotor 1 mistuned forced response are occurring for the excitation of negative nodal diameters featuring maximum aerodynamic damping or being close to it,
- considerable differences in the effect of blade individual and constant aerodynamic damping are observed which decrease for smaller max to min ratios of the aerodynamic damping
- constant aerodynamic damping shows no potential to reduce the maximum blade response below the tuned one,

- even if an attenuation of the maximum blade response below the tuned one is achieved, considerable displacement amplification may occur at low standard deviations depending on the degree of structural coupling and the localisation strength.

Probabilistic Forced Response Analysis

Since the previous results are only an excerpt from all possible nodal diameter excitations, probabilistic analyses have been conducted to allow for a statistical evaluation of the problem. Therefore 10.000 random mistuning patterns have been created in the range of $0\% \leq \sigma_{\text{STD}} \leq 10\%$. According to Beirow [7] the distribution of the blade frequencies around its mean value can be best approximated with Weibull distributions which has been considered in the generation of these patterns.

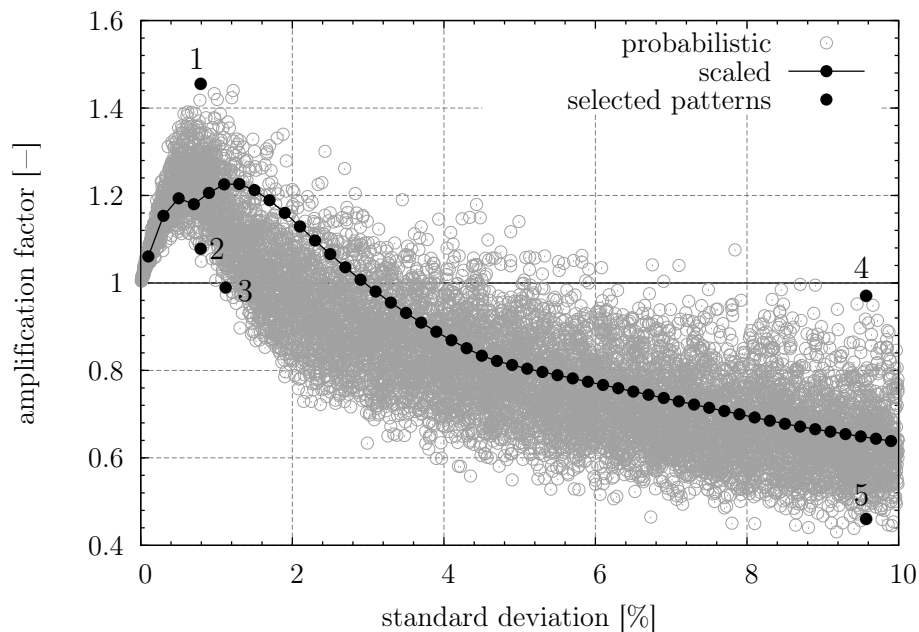


Figure 7.29: Amplification factors of forced response with random and scaled mistuning patterns - mode 1 / nd 1

First the results of nodal diameter 1 of mode 1 are presented in Figure 7.29 in comparison with the results of the scaled mistuning patterns. The maximum amplification occurring at $\sigma_{\text{STD}} = 0.79\%$ (pattern labeled with 1 in Figure 7.29) is more than twice as high as the corresponding value of the scaled pattern. Nevertheless, significantly lower amplification factors ($\approx -30\%$, as percentage of the corresponding value of the scaled pattern) are also observed at the same standard deviation (pattern number 2). Moreover, the lowest standard deviation where a mitigation of the maximum blade response below the tuned one is reached is shifted to a value of $\sigma_{\text{STD}} = 1.12\%$ (pattern 3). It shows, that the maximum achievable amplitude reduction in the considered range of frequency deviation increases to almost 60%.

However, by comparing the patterns number 4 and 5 with each other it becomes clear that although an immense reduction can be achieved at large standard deviations, considerably higher amplification factors just below the tuned response are also possible.

Additional computations have been conducted for all possible nodal diameters of the four blade modes considered in this work. The results of the nodal diameters that showed the minimum amplification factors, see Table 7.6, are presented in Figure 7.30⁶ (a). From the results of the scaled mistuning patterns it could be expected that the probability of the amplification factors to drop below 1.0 decreases with increasing mode number. This is exactly what can be observed from the diagrams. It shows that the probability is greatest for mode 1 for which almost 80% of all patterns yield maximum blade responses lower than the tuned one, see Figure 7.30(c). For mode 2 only 44% show the same reduction below 1.0. The value continuously decreases to 14% for mode 3 and only 0.7% for mode 6.

Next, Figures 7.31 (a) to (d) display the maximum amplification factor versus the excited nodal diameter, comparing computations with blade individual and constant aerodynamic damping for each of the four considered blade modes. The results of mode 1 show similar trends as observed in the analysis of the scaled mistuning patterns. For low numbers of nodal diameters, the maximum amplification is considerably reduced when blade individual damping is considered while the opposite is the case for higher numbers of nodal diameters. The maximum differences may reach values of about 100% of the tuned response. Nevertheless, similar results are obtained for nodal diameters between 6 and 8. Considering the rest of the blade modes, quite similar curves are obtained for blade modes 2, 3 and 6. Compared to the constant damping, the results of blade individual damping show an average reduction of the amplification factor of about 15% with respect to the tuned response for positive nodal diameters of mode 2. The opposite effect is noticeable for negative nodal diameters. Similar observations can be made for low numbers of nodal diameters for mode 3 and 6 while an increase of the maximum amplification factor emerges for higher numbers of nodal diameters. It catches one's eye that the curves of mode 2, 3 and 6 are on the same level of maximum amplification and that the curves show similar shapes. Concerning the constant aerodynamic damping, maximum amplification factors of approximately 2.8 and minimum values of about 1.8 appear for these three modes. For all blade modes except mode 2 the nodal diameters which show maximum and minimum amplification factors change when blade individual damping is considered. The difference is greatest for mode 1 where the maximum is associated either with nd 0 or nd -10 while the minimum may be either due to excitation of nd 14 or nd 4. It is also interesting to notice that the shape of the curve of maximum amplification is comparable to the damping curve (Figure 7.10) for mode 1. This observation supports the findings made for the scaled patterns of mode 1. Again, the reason for this is that blades featuring large amounts of aerodynamic damping in the tuned case can only get lower damping in the mistuned case which leads to greater amplification factors and vice versa. However, the theoretical limit given by Whitehead [119] of $\nu = \frac{1}{2}(1 + \sqrt{N}) = 3.19$

⁶Every 10th pattern is plotted for reasons of visibility.

is not reached by any of the results although the maximum amplification found for $nd -3$ gets quite close with $\nu = 3.18$. Nevertheless, Petrov [94] has shown that even if the analysis of a great number of randomly generated mistuning patterns does not exceed this theoretical limit, an optimisation aiming at a determination of the worst mistuning patterns may result in patterns which do so.

Finally, the statistics of the results of all possible nodal diameters are displayed in Figures 7.32 and 7.33. For the discussion, positive and negative nodal diameters have been considered separately. The first thing that strikes the eye is the almost uniform distribution of the amplification factors of positive nodal diameters belonging to mode 1. The amplification factors below 1.0 are dominated by low numbers of nodal diameters up to $nd 5$ for which the majority of the maximum blade responses is below the tuned one. Nevertheless, as previously described for the scaled patterns, amplification factors greater than 1 are also computed for low standard deviations which sums up with similar amplification factors of higher nodal diameters at low standard deviations to a higher probability density for factors slightly greater than one. For nodal diameters from 9 onwards the amplification factors increase quickly with increasing standard deviation being then normally distributed around an amplification factor of 1.6. These explanations have also been visualised with separate calculation of the probability density presented in Appendix E. The probability of all positive nodal diameters to yield amplification factors lower than 1.0 is about 31% which is almost as twice as high as for mode 2 where the probability decreases to about 17%. Considering blade mode 2, the distribution of amplification factors of positive and negative nodal diameters is quite similar. Nevertheless, for positive nodal diameters the greatest probability is achieved of amplification factors 30% lower than for negative nodal diameters. The probability to reach higher amplification factors decreases slowly with a 99 percentile of 2.89. Here, negative nodal diameters do not show any reduction below the tuned response which is very probable due to the fact that even the lowest negative nodal diameters are quite "far away" from the minimum aerodynamic damping associated with $nd 5/6$. The distributions of mode 3 and 6 are quite similar showing greatest probabilities for medium amplification factors between 1.2 and 1.4. The probability of positive nodal diameters to show maximum blade amplitudes lower than the tuned one decreases immensely to only 4.5% and 6.2% respectively. On the contrary to mode 2, also negative nodal diameters, mainly those of low order, show the specific reduction below the tuned response although the probabilities are only about 0.5% which is the result of the low nodal diameters being closer to the nd with minimum aerodynamic damping again, see Table 7.6.

The findings of the probabilistic analysis are:

- Even if large amplitude reductions below the tuned response can be achieved, blade responses close to the tuned one are also possible for the same amount of frequency deviation depending on the distribution of the blade frequencies around the circumference,

- the nodal diameters showing a massive amplitude reduction compared to the tuned case, also show considerable amplification factors for standard deviations around $\sigma_{\text{STD}} \approx 1\%$,
- whether a mitigation below the tuned response occurs or not depends on the relative distance of the excited nodal diameter from the one showing minimum aerodynamic damping which is the reason that all excited, negative nodal diameters of mode 2 result in maximum blade responses greater than the tuned one,
- the strength of amplitude attenuation also depends on the max to min ratio of the aerodynamic damping,
- considerable differences with regard to the maximum amplification factor associated with an nodal diameter may occur between the results of constant and blade individual damping with the deviations being greatest for mode 1 for which differences of up to 100% with respect to the tuned response are observed,
- the theoretical limit given by Whitehead is not reached by any of the computations, yet an excitation of nd -3 of mode 2 resulted in a maximum amplification of $\nu = 3.18$ in the mistuned case which is very close to the theoretical maximum of $\nu_{\text{max}} = 3.19$.

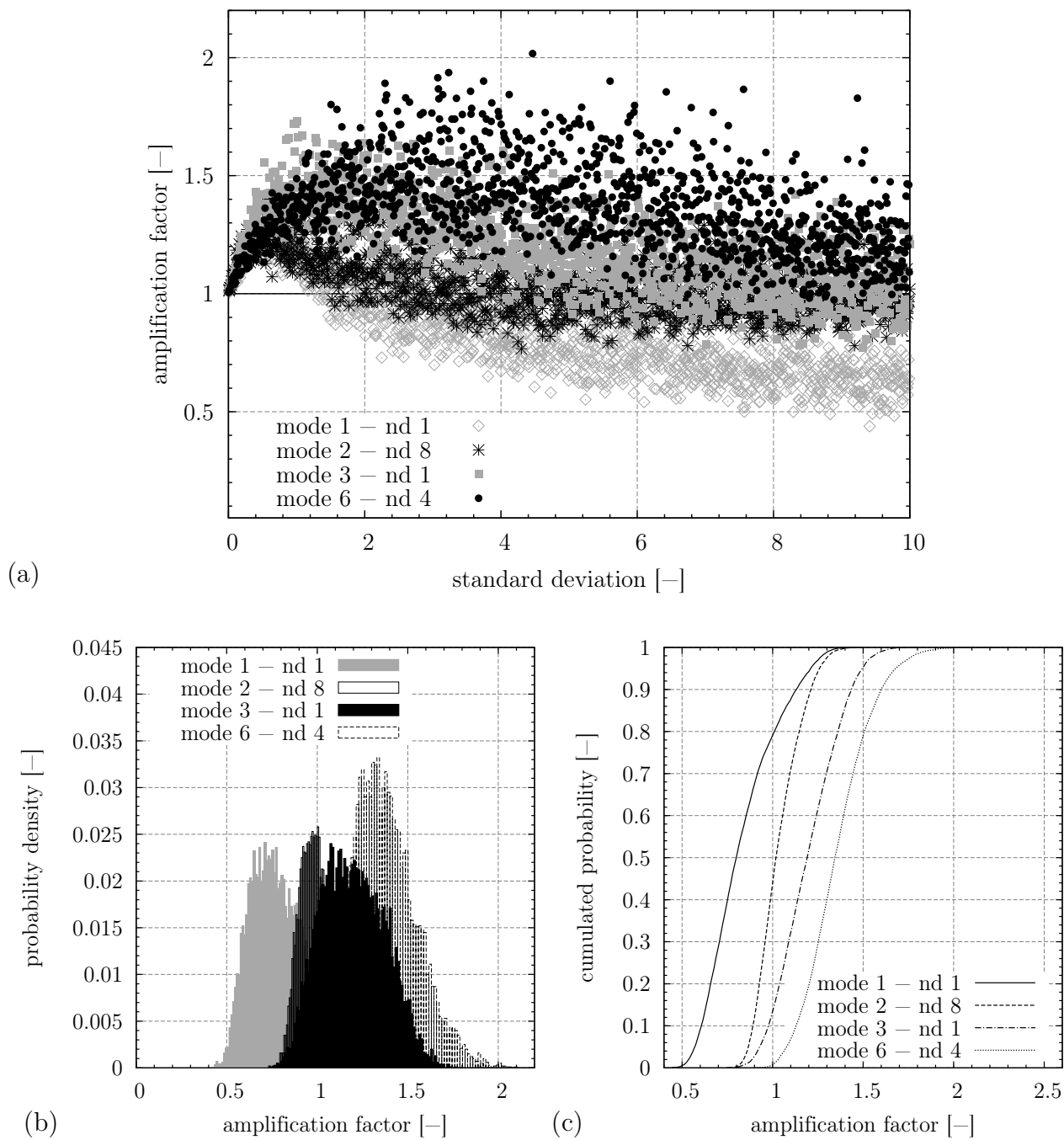


Figure 7.30: Amplification factors of forced response with random mistuning patterns for nodal diameters showing minimum amplification factors (a), corresponding probability densities (b) and cumulative density functions (c)

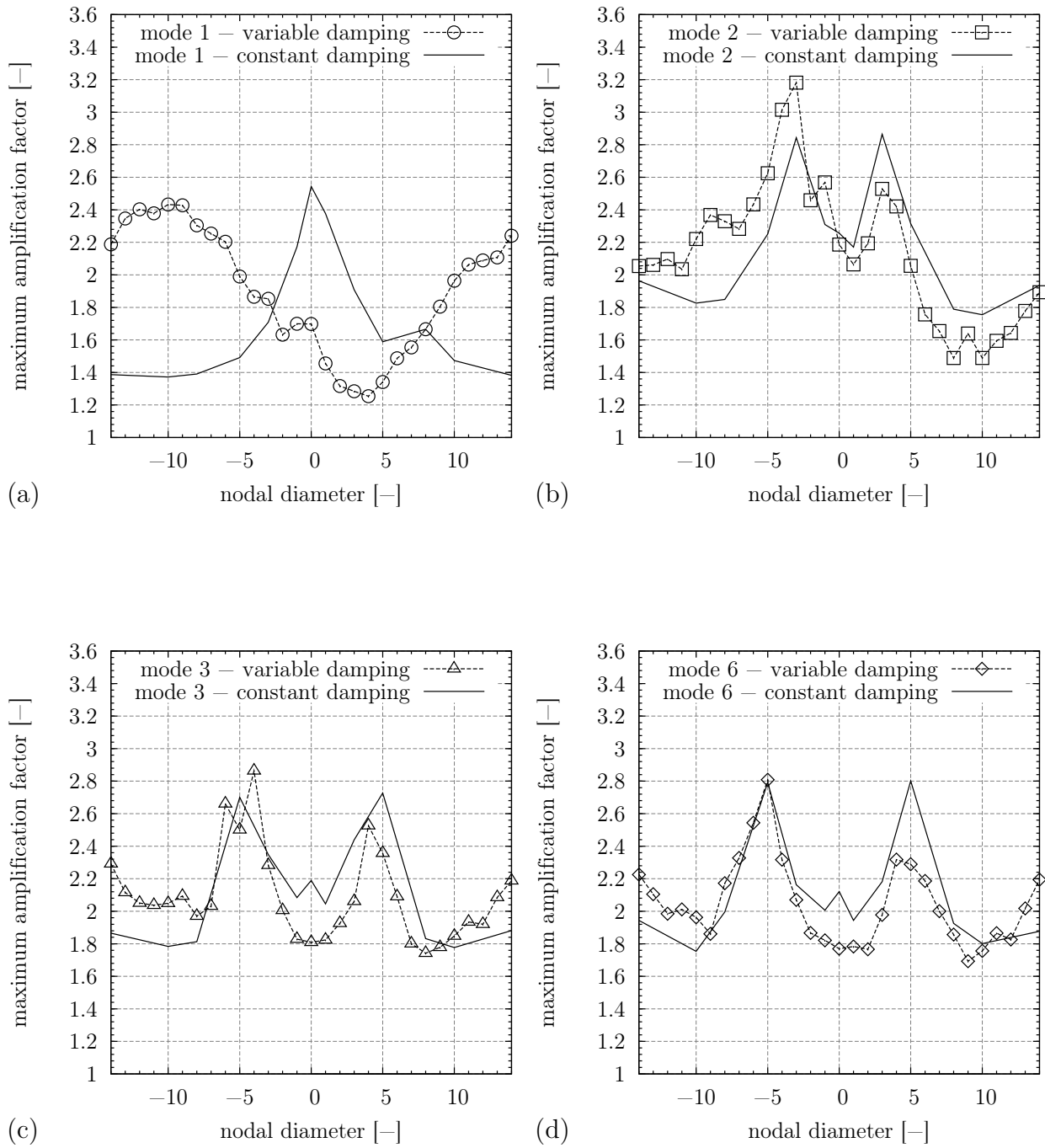


Figure 7.31: Comparison of maximum amplification factors obtained with blade individual and constant damping for blade mode 1 (a), mode 2 (b), mode 3 (c) and mode 6 (d)

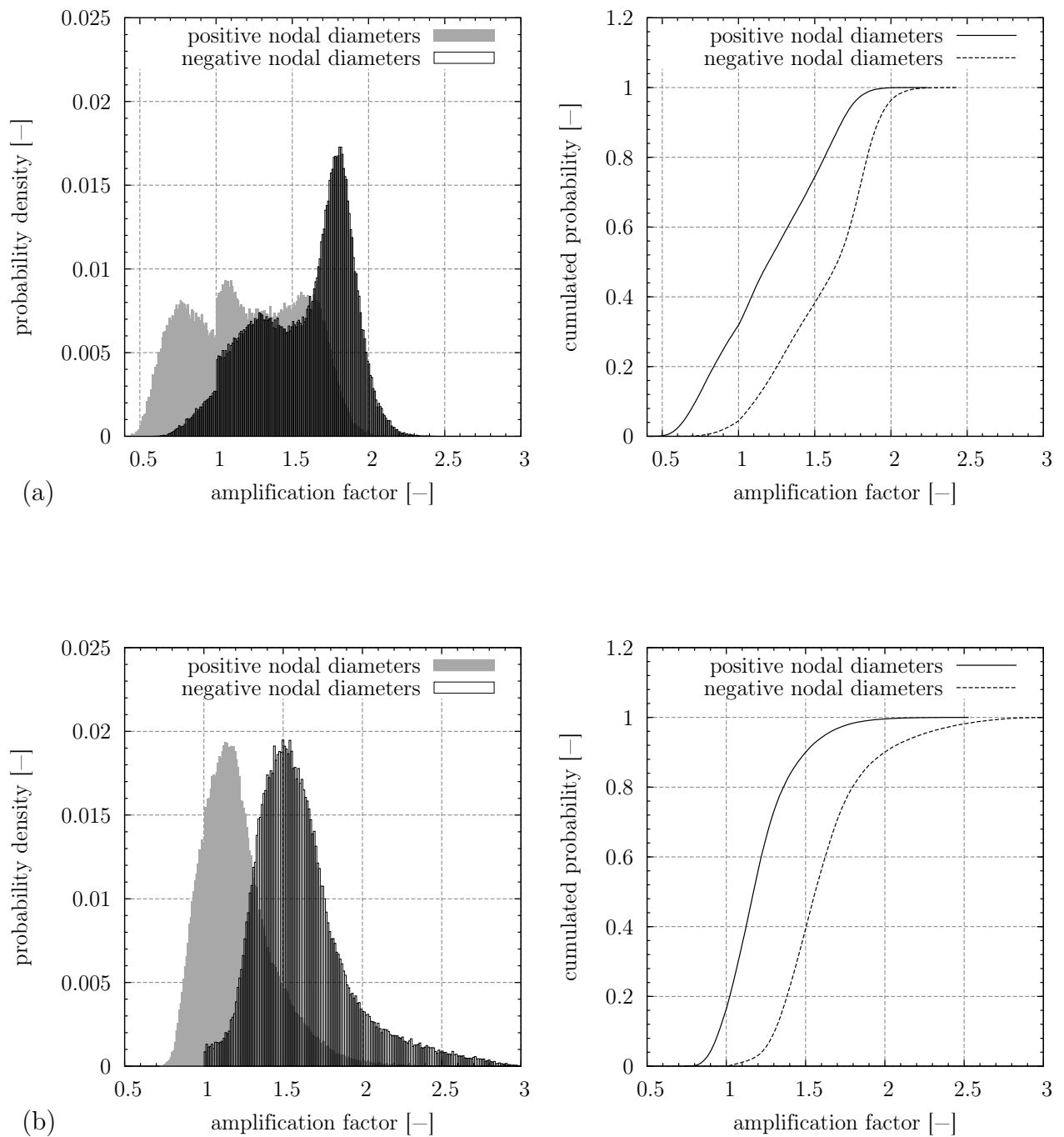


Figure 7.32: Probability density and cumulated probability for positive and negative nodal diameters - mode 1 (a) and mode 2 (b)

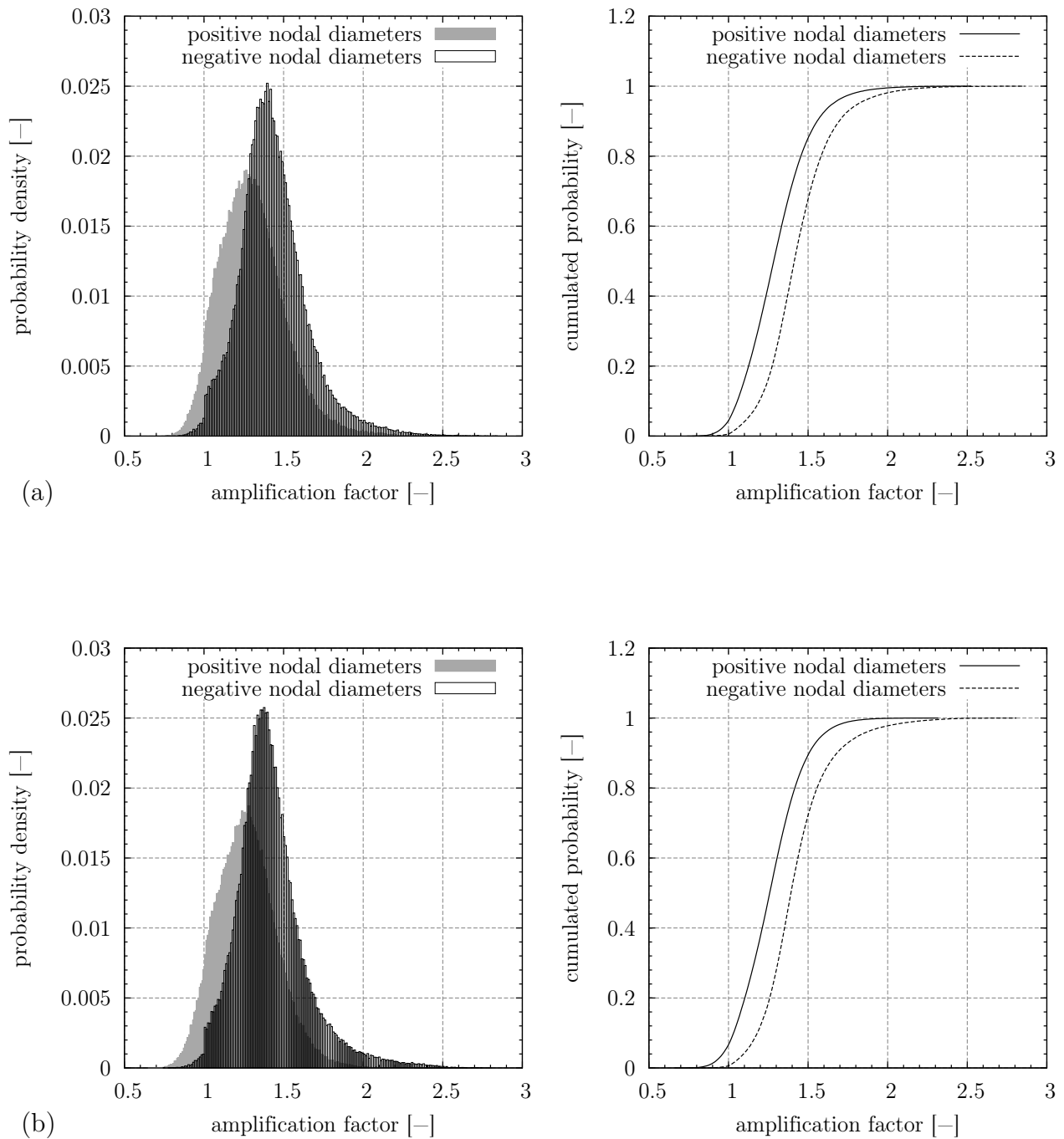


Figure 7.33: Probability density and cumulated probability for positive and negative nodal diameters - mode 3 (a) and mode 6 (b)

Chapter 8

Summary

The present thesis deals with the impact of the aerodynamics in aero engine compressors on mistuned blade vibrations. Therefore two different aerodynamic models, one using aerodynamic influence coefficients and one employing equivalent aerodynamic elements have been integrated into an equivalent blisk model to take account of aerodynamic damping forces.

After the presentation of the basics of bladed disk vibration and the aeroelastic methods, the aeroelastic parameters of the compressor like standard configuration 10 have been computed with the commercial CFD code Fluent and compared to reference results from other researchers in order to validate the calculation procedures. First, two-dimensional simulations of the unsteady flow during heaving and pitching motion have been conducted which all show excellent agreement of the aerodynamic damping parameters obtained with influence coefficients and multi-passage computations. The match of the 2D computations with the reference results is sufficient with the biggest differences occurring at low interblade phase angles and near acoustic resonances which is due to lack of proper non-reflecting boundary conditions. Consequently, the compliance can be increased when the boundaries are located some chord lengths away from the profile which leads to eminent agreement with the reference results with the influence coefficients being able to reproduce peaks in the aerodynamic damping parameter due to acoustic resonances. The same observations have been made for the inviscid 3D computations while in case of viscous simulations the deviations from the reference results were greater. At this, the biggest differences occurred at large interblade phase angles.

Subsequently the aeroelastic vibration behaviour of the two-dimensional E3E compressor rotor 6 model has been analysed with uni- and bidirectionally coupled FSI simulations as well as EBM computations of blade heaving motion assuming an infinitely stiff disk. Initially, the aeroelastic eigenvalues have been computed with uni- and bidirectionally coupled FSI computations showing great agreement of all results. Furthermore tuned forced response computations have been conducted for one particular interblade phase angle. In doing so, excellent agreement of bidirectionally coupled FSI simulations and EBM computations with

equivalent aerodynamic elements derived from the aeroelastic eigenvalues and aerodynamic influence coefficients was found. Moreover, a randomly mistuned rotor 6 cascade has been analysed in the same manner confirming the results of tuned forced response computations except for the equivalent aerodynamic elements which showed greater deviations than the aerodynamic influence coefficients especially with respect to the aeroelastic resonance frequency. Additional computations featuring 500 scaled mistuning patterns have been carried out, confirming the assumption that the aerodynamics are the major perpetrator in the mitigation of maximum mistuned blade response below the tuned one. In the course of the studies, the impact of the max to min ratio of the aerodynamic damping on the amplitude attenuation has been investigated showing considerable dependency of the attainable amplification reduction on the shape of the aerodynamic damping curve.

Ultimately, the aeroelastic parameters and mistuned forced response of four blade modes of the E3E compressor rotor 1 model has been computed featuring a flexible disk, mistuning patterns from experimental blade by blade measurements and probabilistic analyses of mistuned forced responses. At this, a satisfying match of the tuned eigenvalues of FE and EBM model, which have been adapted to real hardware, was achieved. Furthermore, a simple SDOF approximation has been used for deriving mistuning patterns at rotation from those measured at rest in experiments.

Concerning the beneficial effect of mistuning with respect to flutter stability, a slight increase of the least damped mistuned eigenvalues was observed which is actually very small due to the rather small frequency deviations of the measured mistuning patterns. Similarly, the impact of the measured mistuning patterns on the maximum blade forced response is rather small in the presence of aerodynamic forces which significantly reduce displacement amplification and mode shape localisation. Analogously to the computations of the rotor 6 cascade, the measured mistuning patterns have been scaled to standard deviations between $\sigma_{STD} = 0\% - 10\%$ resulting in maximum blade amplitudes significantly higher and lower than the tuned response. At this, considerable dependency on the max to min ratio of the aerodynamic damping, the degree of mechanical coupling and the engine order of the excitation has been observed. In detail, the maximum reduction below the tuned response was achieved with excitations at or close to the one exhibiting minimum aerodynamic damping in the tuned case while the maximum blade displacement amplification was observed for negative engine orders featuring maximum aerodynamic damping in the tuned case or being close to it. Moreover, considerable differences between using constant and blade individual aerodynamic damping have been noticed. Lastly, the results have been confirmed by probabilistic analyses of a large number of mistuning patterns. As a result, the difference between constant and blade individual damping has reached values of up to 100% with respect to the tuned blade response. Furthermore, it could be shown that with increasing mode number the probability of an attenuation of the maximum blade response below the tuned one decreases continuously.

All in all, it can be concluded that the aerodynamic influence coefficients provide an efficient

method of integrating aerodynamic influences in a structural model. However, the excellent agreement with bidirectionally coupled FSI simulations has been achieved in the absence of mechanical coupling and with simple blade motion of a 2D model only. Hence, a comparison with 3D computations including mechanical coupling is desirable. Furthermore, the agreement with high fidelity simulation methods is fantastic, though no correlation with engine data has been analysed so far.

Nevertheless, the EBM with aerodynamics provides an efficient and fast methodology for the fundamental analyses of the impact of mistuning on the flutter and forced response behaviour which shall make it a valuable tool in early design stages of aero engines.

Appendix A

Richardson Extrapolation

Within CFD simulations one of the most important things, if not the most important one is the quality of the numerical grid and hence the resultant discretisation error. There is a lot a CFD engineer can do to ensure a proper mesh quality prior to starting a simulation. But even if the grid is perfectly aligned with the flow, and the engineer has set up his mesh carefully, the numerical mesh remains a discrete representation of the fluid continuum and hence a discretisation error is inevitable. For the estimation of the numerical error due to discretisation, grid convergence studies are a reliable technique.

A popular method for the quantification of the numerical error is the Richardson Extrapolation first used by Lewis Fry Richardson in 1910. The Richardson Extrapolation is also known as " h^2 extrapolation" meaning that the extrapolation is done on the basis of the mesh spacing h . In the following, a short overview about the idea of the Richardson Extrapolation and the necessary equations are given. Further details are given by Roache [98] or Ferziger and Perić [33].

The intention of using the Richardson Extrapolation is to enhance the order of accuracy of a discrete solution on a particular numerical grid. The discrete solution f can be expressed as a function of the grid spacing h by

$$f = f_{\text{exact}} + g_1 h + g_2 h^2 + \dots + g_n h^n. \quad (\text{A.1})$$

Here, the functions g_n are defined as the correlation between the numerical error and the grid spacing. According to [98], for a second order accurate solution, the representation of the discrete solution simplifies to

$$f = f_{\text{exact}} + g_2 h^2 + H.O.T. \quad (\text{A.2})$$

with H.O.T. being "high order terms". In order to eliminate the leading error term g_2 , two

different discrete solutions f_1 and f_2 , calculated on a "fine" and on a "coarse" grid, can be combined to yield an enhanced guess for the exact solution

$$f_{\text{exact}} \cong f_1 + \frac{f_1 - f_2}{r_g^2 - 1} \quad (\text{A.3})$$

including the grid refinement ratio $r_g = h_2/h_1$. The above equation describes an estimation of the exact solution as a correction to the fine grid solution f_1 . Being of minor significance, the H.O.T. are omitted. In practical applications, a successive doubling of the grid spacing h , giving $r_g = 2$, is often used. Equation A.3 then reads

$$f_{\text{exact}} \cong \frac{4}{3}f_1 - \frac{1}{3}f_2. \quad (\text{A.4})$$

According to Roache, if the discrete solutions f_1 and f_2 are de facto second order accurate than the estimation of f_{exact} is of fourth order accuracy. In fact, if second order upwind schemes are used, only third order accurate estimations can be achieved.

Appendix B

Mistuning Patterns of Rotor 1

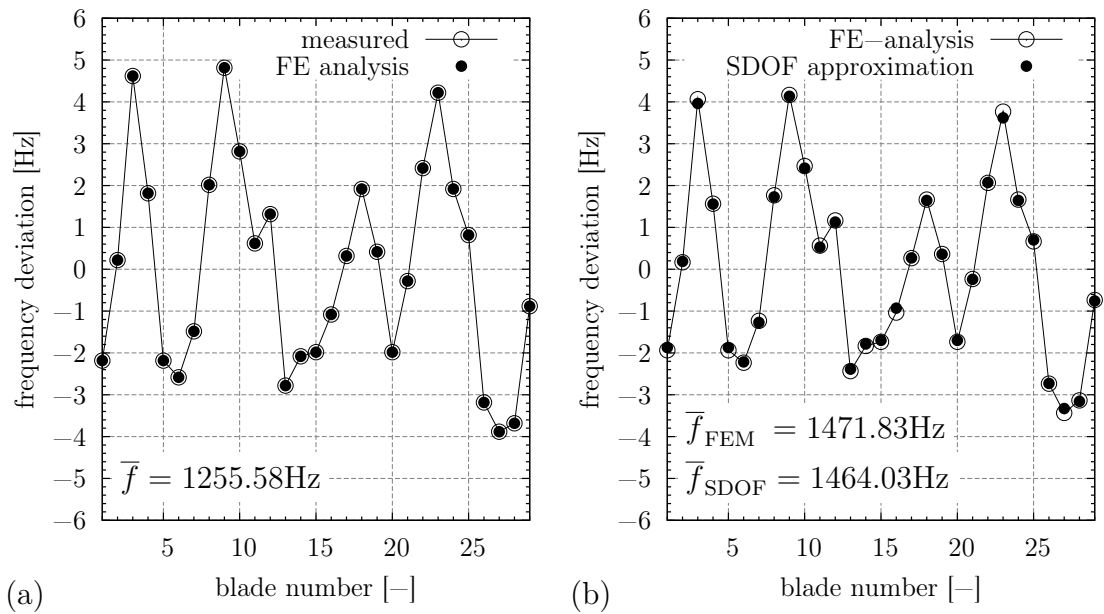


Figure B.1: Measured and numerically determined frequencies of mode 2 (2nd flap) at rest (a) and blade frequencies of the rotating system (b)

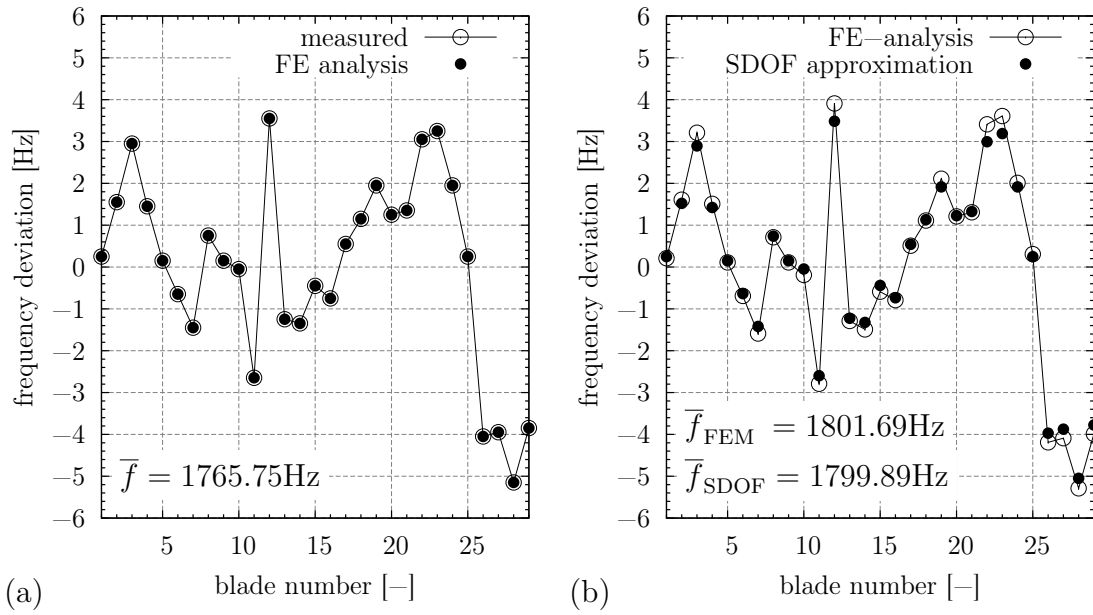


Figure B.2: Measured and numerically determined frequencies of mode 3 (1st torsion) at rest (a) and blade frequencies of the rotating system (b)

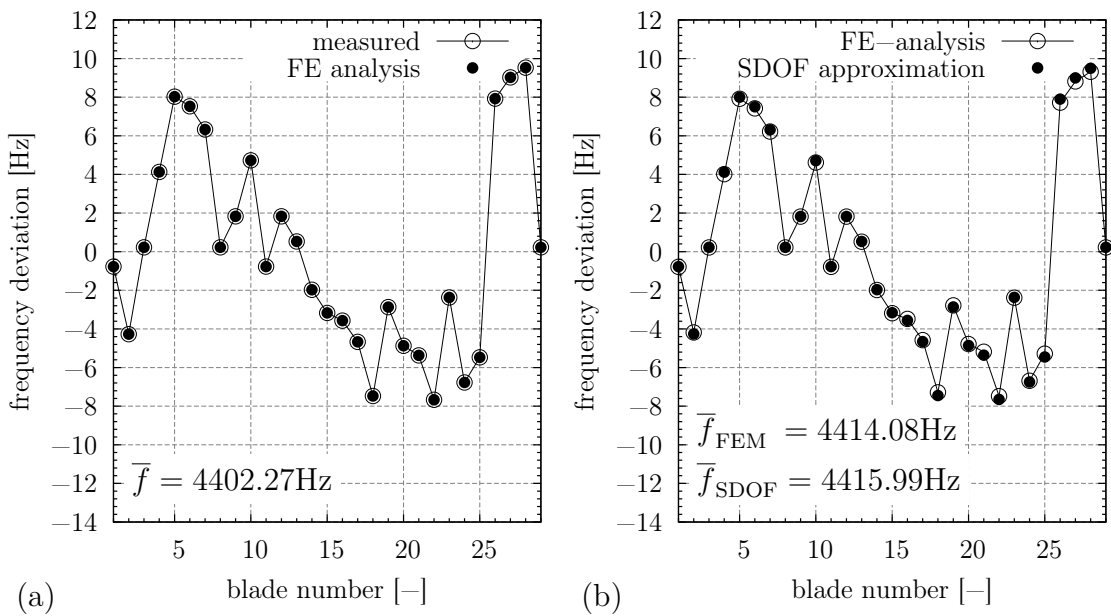


Figure B.3: Measured and numerically determined frequencies of mode 6 (tram line) at rest (a) and blade frequencies of the rotating system (b)

Appendix C

Eigenvalues of Mistuned Rotor 1 EBM Model

C.1 Mode 1 - 1st flap

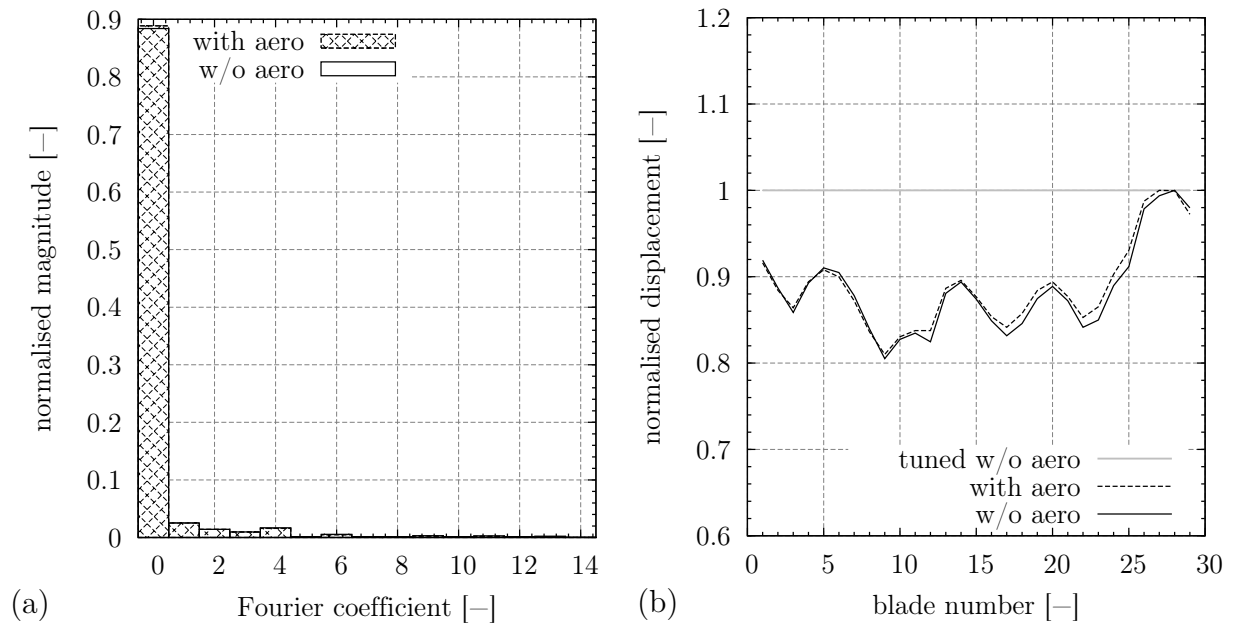
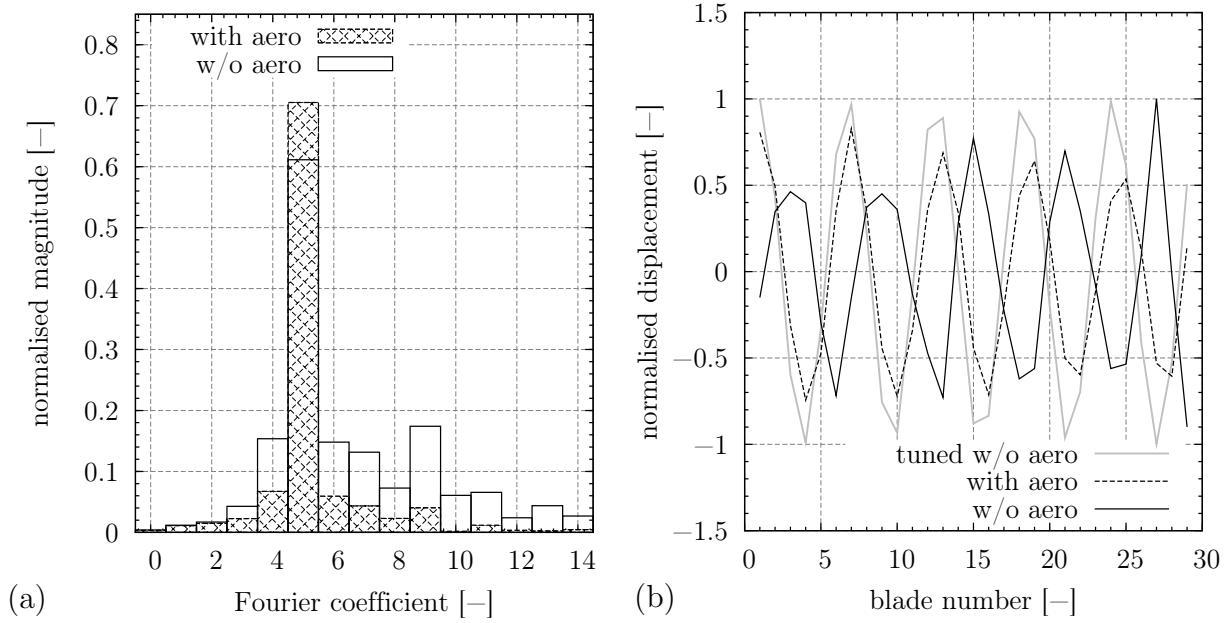
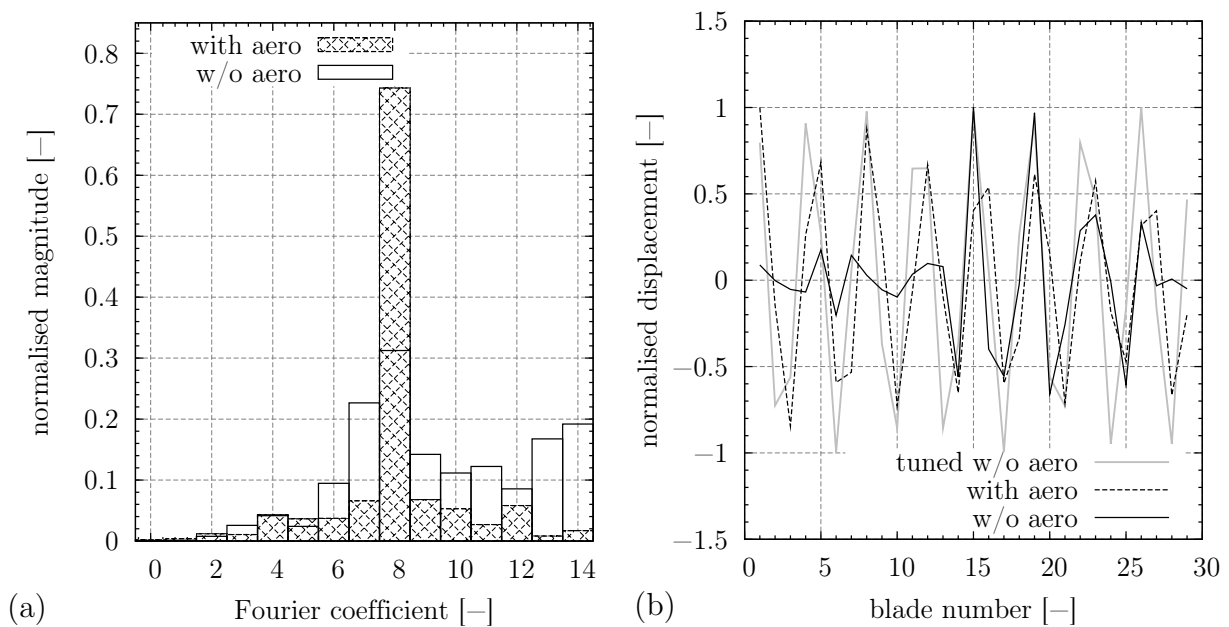


Figure C.1: Fourier coefficients (a) and mode shape (b) of mode 1, $DFT_{\max} = 0$

Figure C.2: Fourier coefficients (a) and mode shape (b) of mode 1, $DFT_{\max} = 5$ Figure C.3: Fourier coefficients (a) and mode shape (b) of mode 1, $DFT_{\max} = 8$

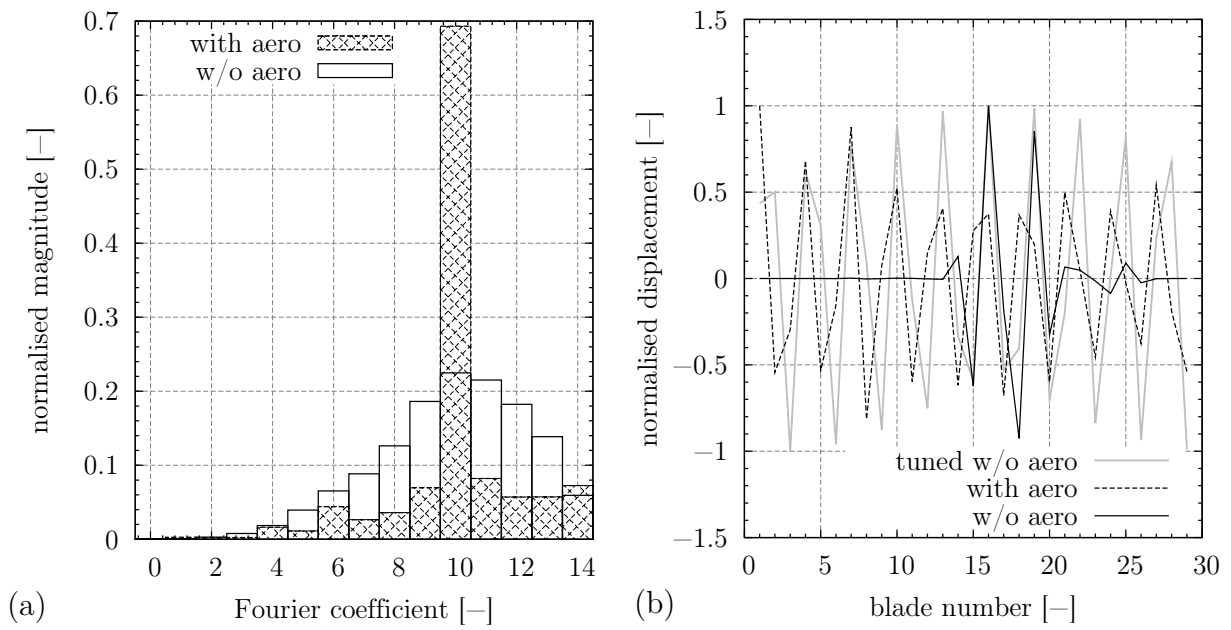


Figure C.4: Fourier coefficients (a) and mode shape (b) of mode 1, $DFT_{\max} = 10$

C.2 Mode 2 - 2nd flap

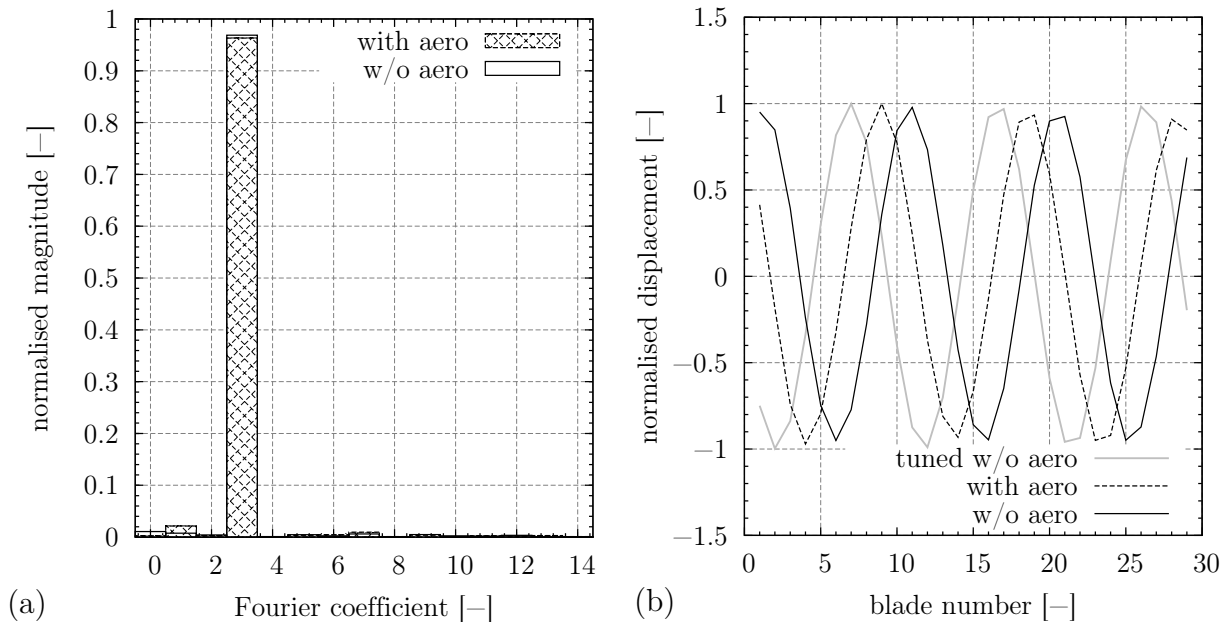


Figure C.5: Fourier coefficients (a) and mode shape (b) of mode 2, $DFT_{\max} = 3$

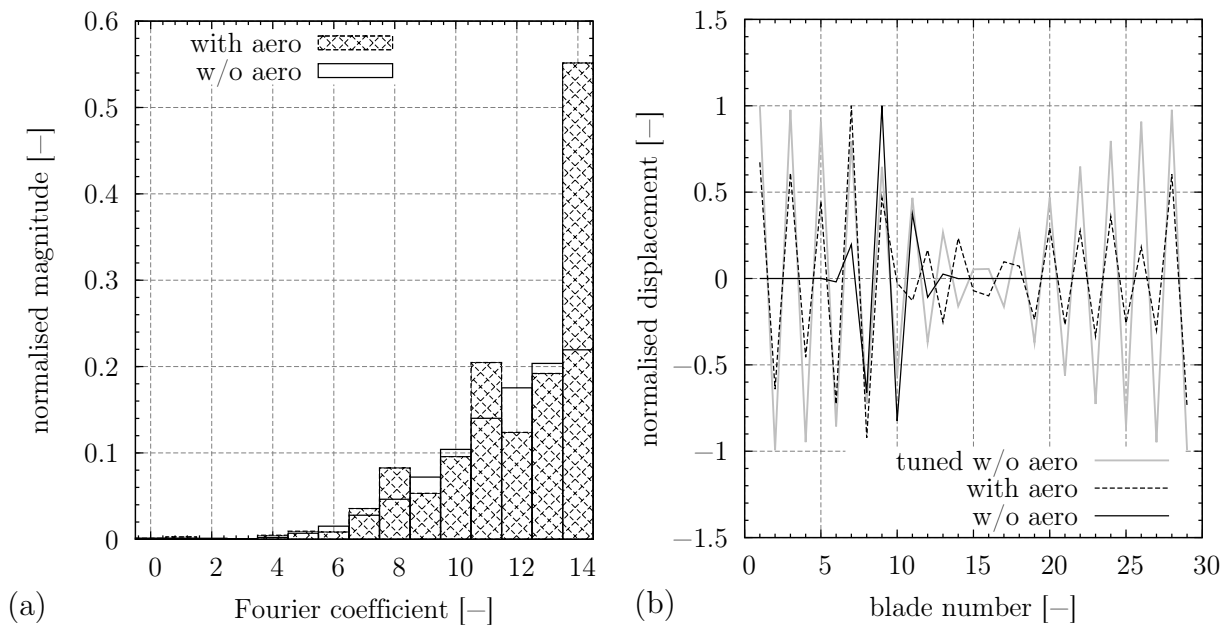


Figure C.6: Fourier coefficients (a) and mode shape (b) of mode 2, $DFT_{\max} = 14$

C.3 Mode 3 - 1st torsion

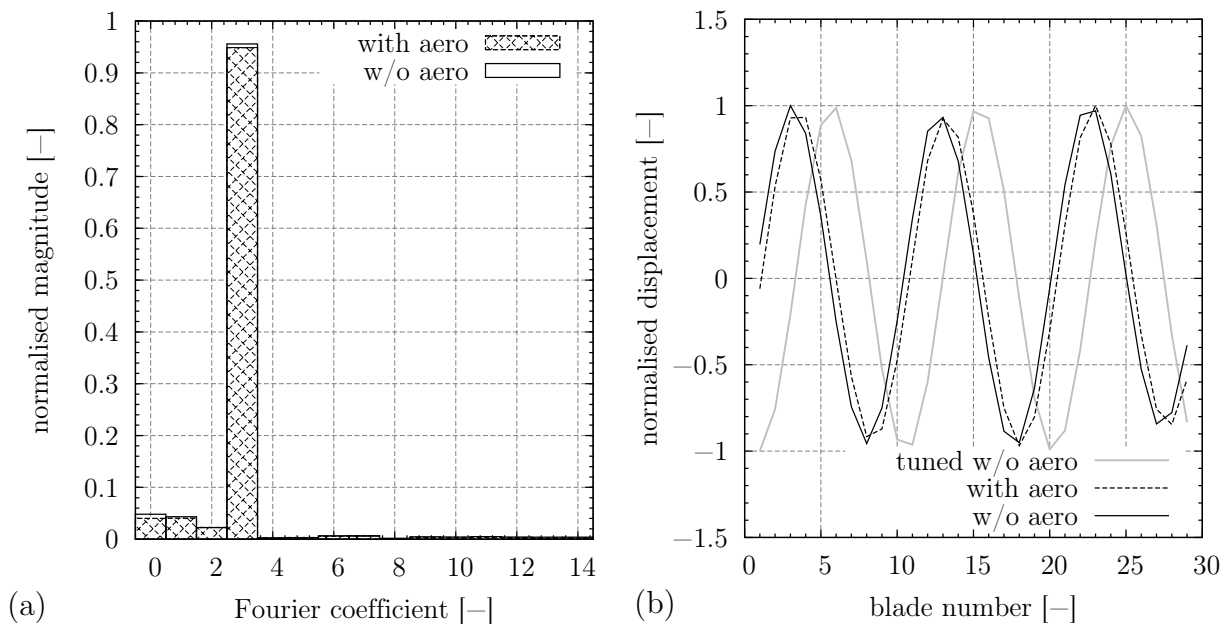


Figure C.7: Fourier coefficients (a) and mode shape (b) of mode 3, $DFT_{\max} = 3$

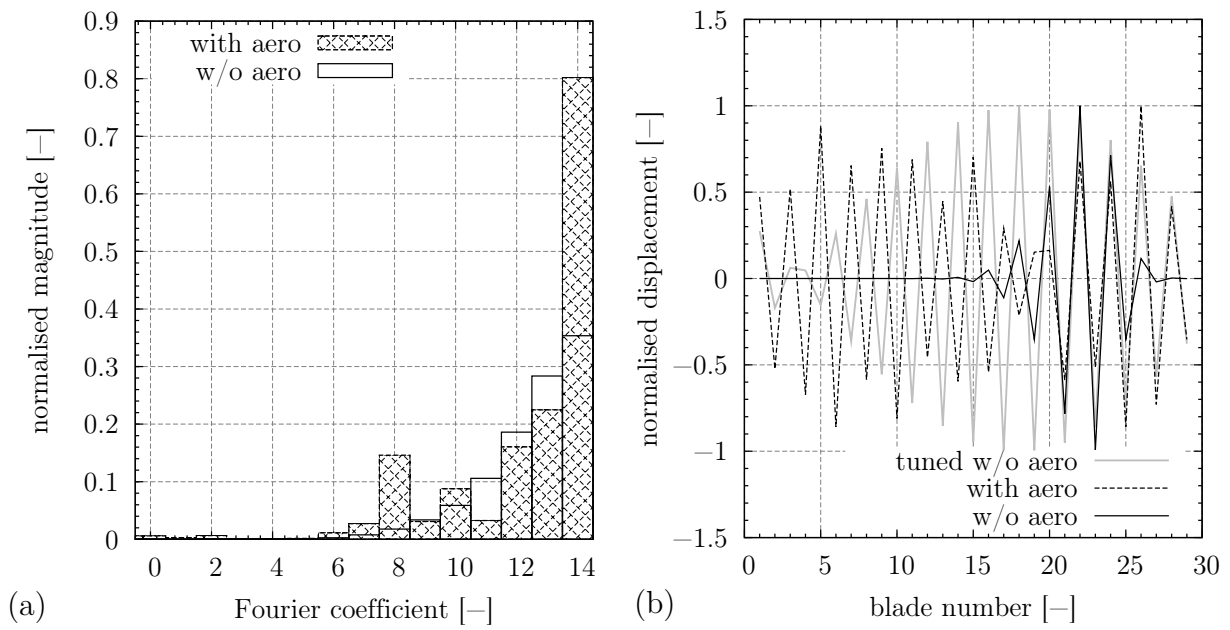


Figure C.8: Fourier coefficients (a) and mode shape (b) of mode 3, $DFT_{\max} = 14$

C.4 Mode 6 - tram line

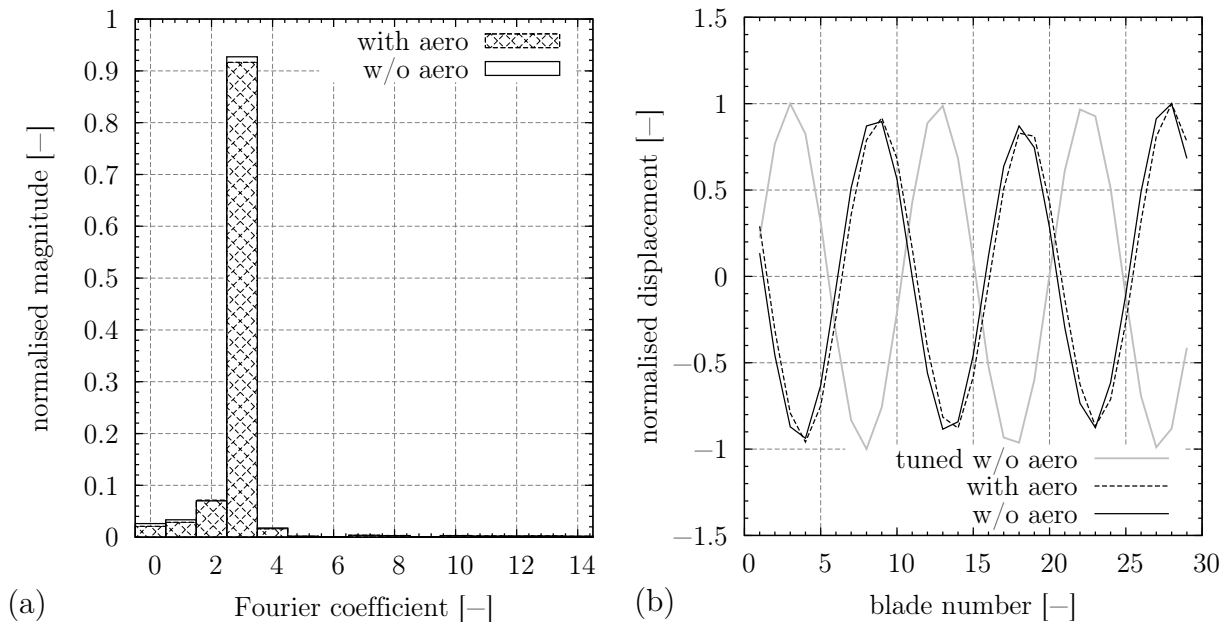


Figure C.9: Fourier coefficients (a) and mode shape (b) of mode 6, $DFT_{\max} = 3$

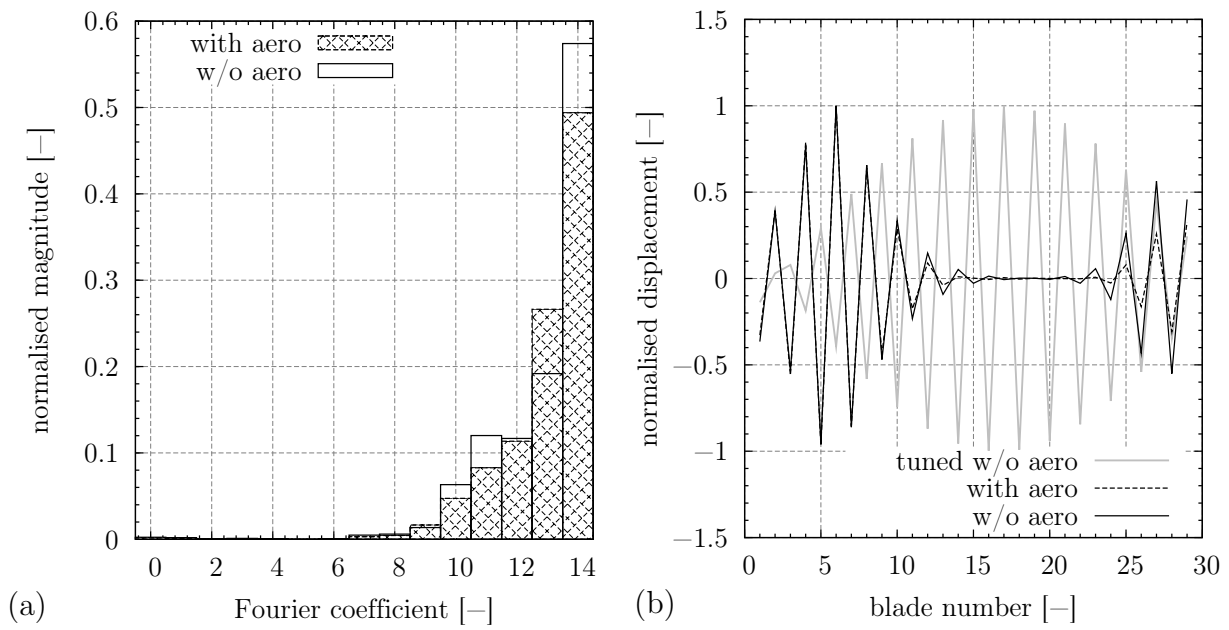


Figure C.10: Fourier coefficients (a) and mode shape (b) of mode 6, $DFT_{\max} = 14$

Appendix D

Forced Response of Measured Patterns

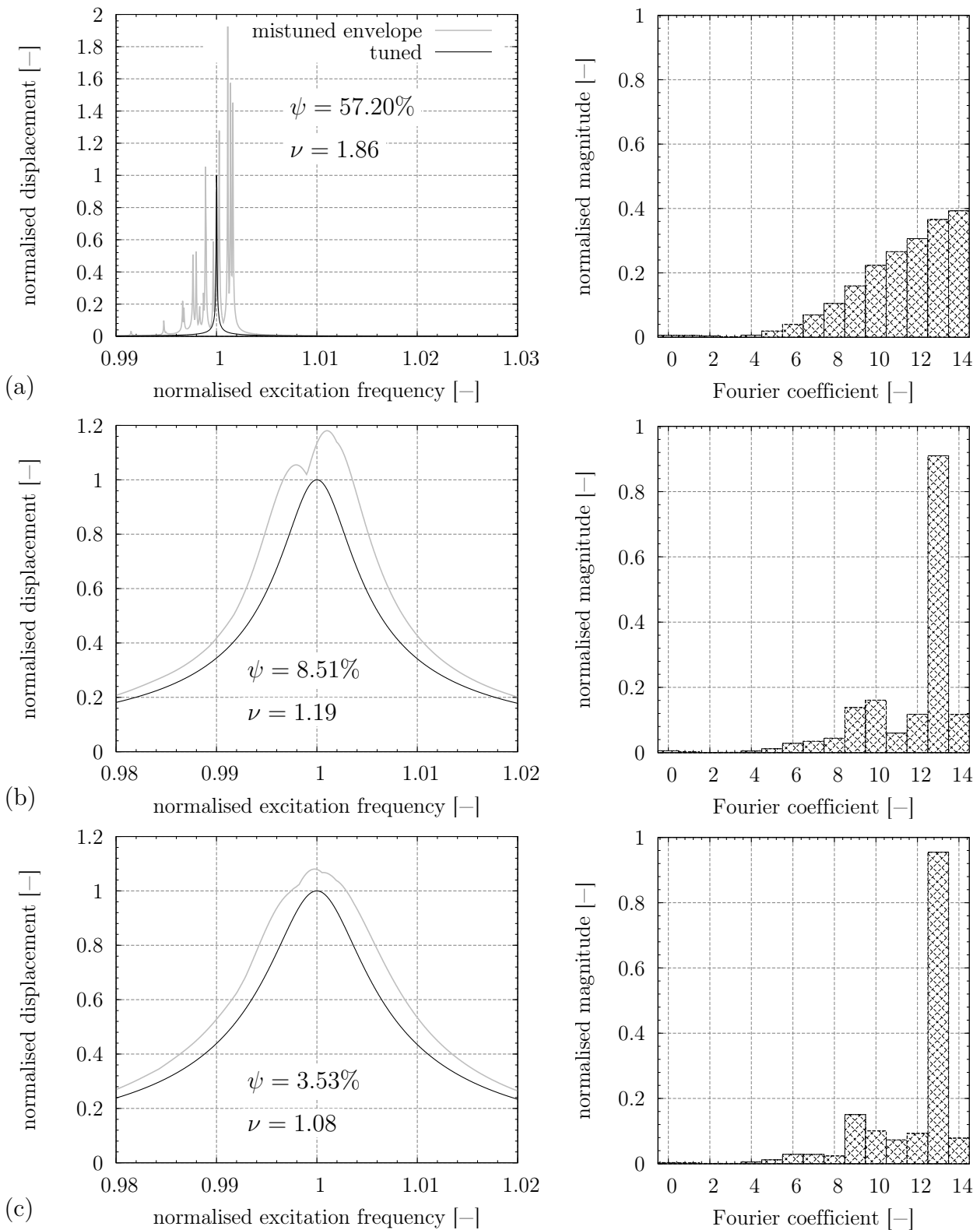


Figure D.1: Frequency response function and Fourier coefficients of mistuned ODS at resonance frequency without aerodynamic damping (a), with constant damping (b) and with blade individual damping (c) - mode 2, nd 13

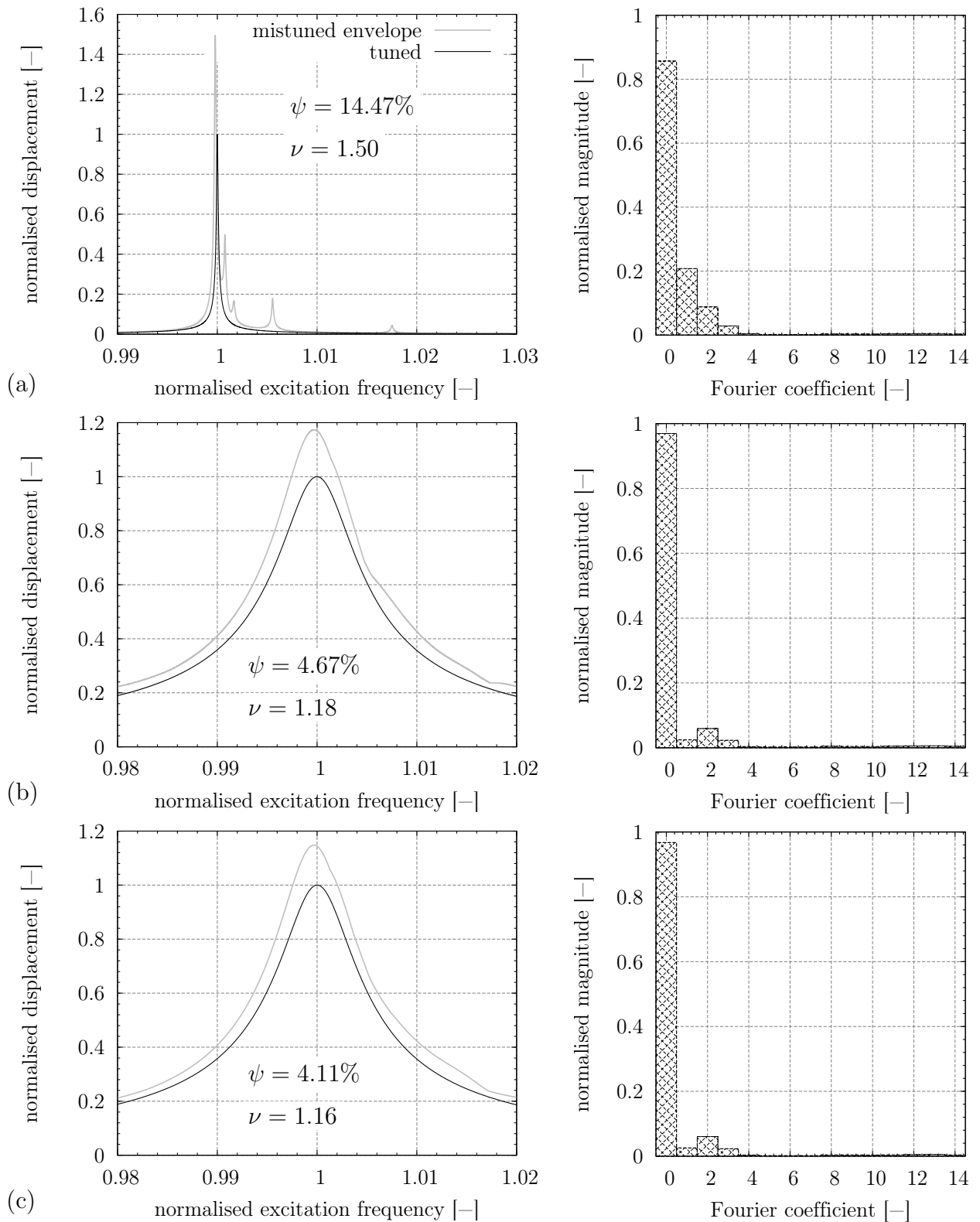


Figure D.2: Frequency response function and Fourier coefficients of mistuned ODS at resonance frequency without aerodynamic damping (a), with constant damping (b) and with blade individual damping (c) - mode 3, nd 0

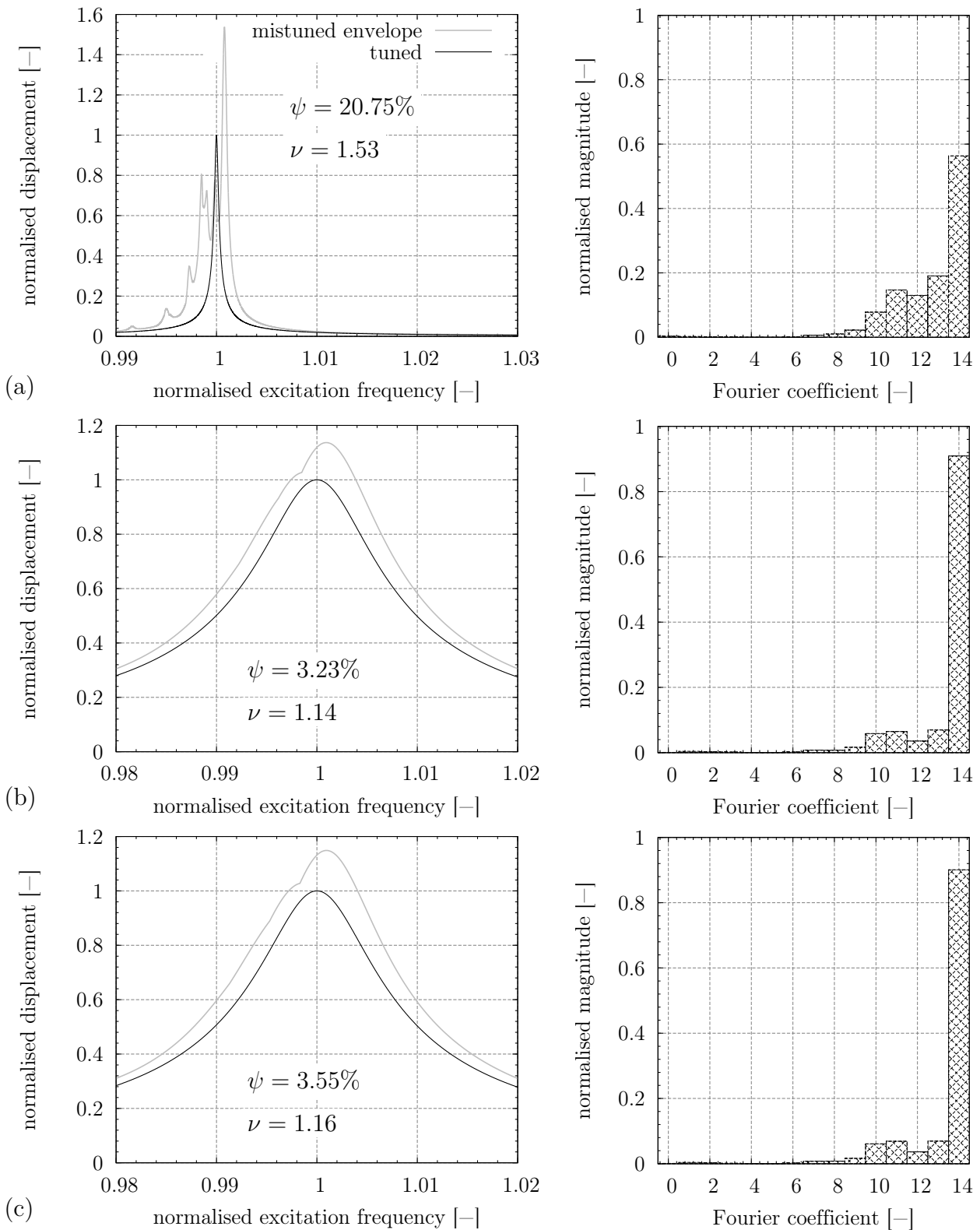


Figure D.3: Frequency response function and Fourier coefficients of mistuned ODS at resonance frequency without aerodynamic damping (a), with constant damping (b) and with blade individual damping (c) - mode 6, nd 14

Appendix E

Probability Density of Positive Nodal Diameters - Mode 1

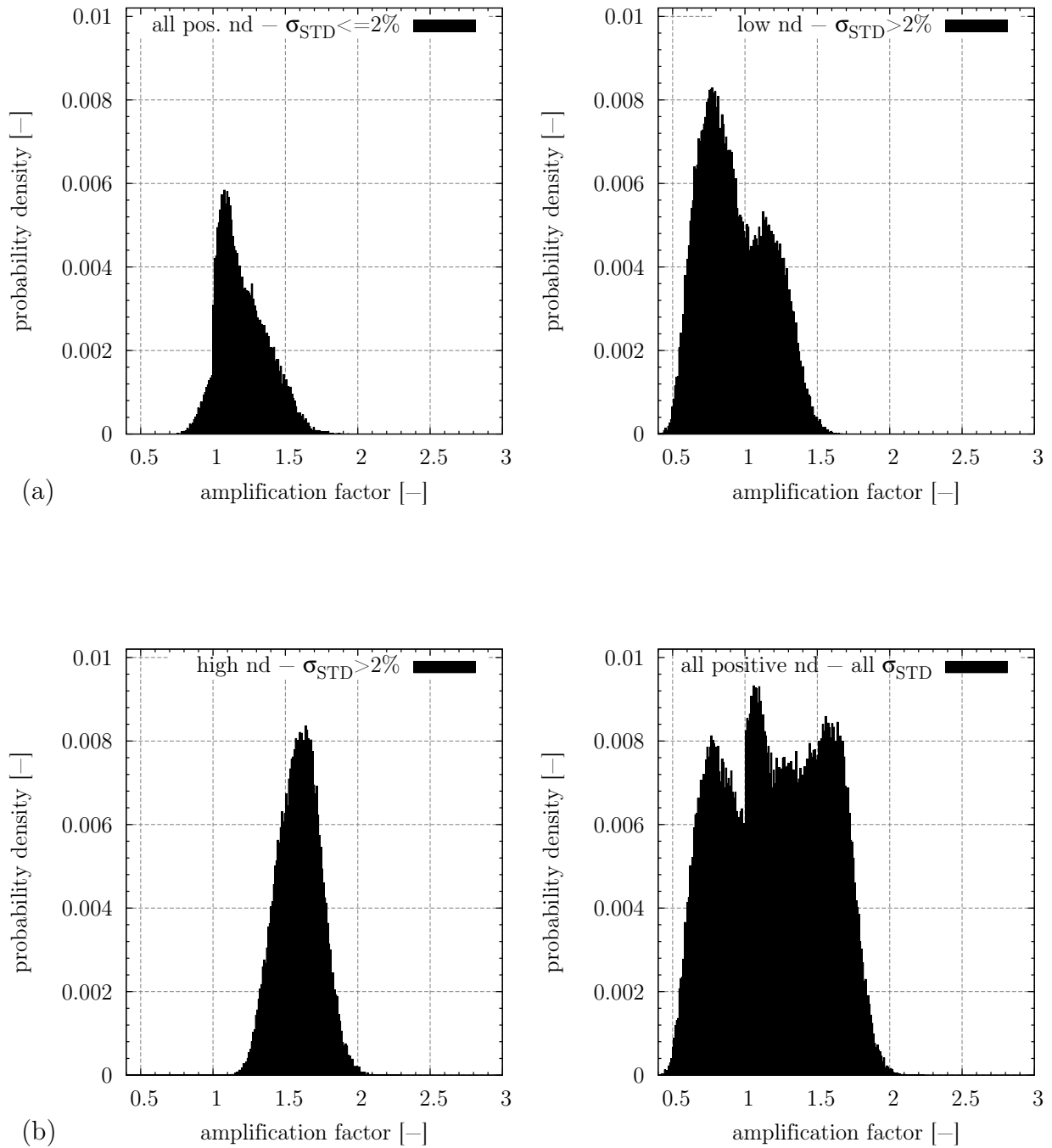


Figure E.1: Probability density of positive nodal diameters, mode 1

Bibliography

- [1] ACARE: *European Aeronautics: A Vision for 2020*. Technical report, Advisory Council for Aeronautics Research in Europe, Januar 2001.
- [2] Allemang, R.J.: *The Modal Assurance Criterion (MAC): Twenty Years of Use and Abuse*. Sound and Vibration Magazine, 37(8):14–23, August 2003.
- [3] Ayer, T.C. and Verdon, J.M.: *Validation of a Nonlinear Unsteady Aerodynamic Simulator for Vibrating Blade Rows*. Journal of Turbomachinery, 120:112 – 121, 1998.
- [4] Ayers, J.P.; Feiner, D.M. and Griffin, J.H.: *A Reduced-Order Model for Transient Analysis of Bladed Disk Forced Response*. Journal of Turbomachinery, 128(3):466–473, 2006.
- [5] Bardina, J.E.; Huang, P.G. and Coakley, T. J.: *Turbulence Modeling, Validation, Testing and Development*. Nasa technical memorandum 110446, National Aeronautics and Space Administration, Ames Research Center, April 1997.
- [6] Basu, P. and Griffin, J.H. : *The Effect of Limiting Aerodynamic and Structural Coupling in Models of Mistuned Bladed Disk Vibration*. Journal of Vibration Acoustics Stress and Reliability in Design, 108(2):132–139, 1986.
- [7] Beirow, B.: *Grundlegende Untersuchungen zum Schwingungsverhalten von Verdichterslaufrädern in Integralbauweise*. Shaker Verlag, 2009.
- [8] Beirow, B. and Kühhorn, A.: *A Method for determining blade mistuning on integrally manufactured rotor wheels*, 2008. patent, number EP1988391.
- [9] Beirow, B.; Kühhorn, A. and Schrape, S.: *Influence of Air Flow on Blisk Vibration Behaviour*. In *1st CEAS European Air and Space Conference, 10. - 13.09.2007, Berlin, CEAS-2007-058*, 2007. Paper CEAS-2007-058.
- [10] Belz, J. and Hennings, H.: *Experimental Flutter Investigations of an Annular Compressor Cascade: Influence of Reduced Frequency on Stability*. In Hall, K.C.; Kielb, R.E. and Thomas, J.P. (editor): *Unsteady Aerodynamics, Aeroacoustics and Aeroelasticity of Turbomachines*. Springer Verlag, 2006.

- [11] Belz, J.; Carstens, V. and Hennings, H.: *Seminar - Aeroelastik von Triebwerksbeschaufelungen*. Institute of Aeroelasticity, DLR Göttingen, 2008.
- [12] Bladh, R.; Castanier, M.P. and Pierre, C.: *Component-Mode-Based Reduced Order Modeling Techniques for Mistuned Bladed Disks—Part I: Theoretical Models*. Journal of Engineering for Gas Turbines and Power, 123(1):89–99, 2001.
- [13] Bladh, R.; Castanier, M.P. and Pierre, C.: *Component-Mode-Based Reduced Order Modeling Techniques for Mistuned Bladed Disks—Part II: Application*. Journal of Engineering for Gas Turbines and Power, 123(1):100–108, 2001.
- [14] Boeing: *Boeing Market Outlook 2008*. Technical report, Boeing, 2008.
- [15] Brown, J.M.: *Probabilistic Analysis of Geometric Uncertainty Effects on Blade Modal Response*. Technical report, Turbine Engine Division, Air Force Research Laboratory, Wright-Patterson Air Base, Ohio, U.S.A., 2003.
- [16] Campobasso, M.S. and Giles, M.B.: *Analysis Of The Effect Of Mistuning On Turbomachinery Aeroelasticity*. In *ISUAAAT 2000, Lyon, France*, 2000.
- [17] Carstens, V. and Belz, J.: *Numerical Investigation of Nonlinear Fluid-Structure Interaction in Vibrating Compressor Blades*. Journal of Turbomachinery, 123(2):402–408, 2001.
- [18] Carta, F.O.: *Coupled Blade-Disk-Shroud Flutter Instabilities in Turbojet Engine Rotors*. Journal of Engineering for Power, pages 419 – 426, 1967.
- [19] Castanier, M.P. and Pierre, C.: *Modeling and Analysis of Mistuned Bladed Disk Vibration: Status and Emerging Directions*. Journal of Propulsion and Power, 22(2):384–396, 2006.
- [20] Castanier, M.P.; Óttarsson, G. and Pierre, C.: *A Reduced Order Modeling Technique for Mistuned Bladed Disks*. Journal of Vibration and Acoustics, 119(3):439–447, 1997.
- [21] Craig, R.R. and Bampton, M.C.C.: *Coupling of Substructures for Dynamic Analyses*. AIAA Journal, 6(7):1313–1319, 1968.
- [22] Crawley, E.F.: *Aeroelastic Formulation for Tuned and Mistuned Rotors*. In M. F. Platzer, F. O. Carta (editor): *AGARD Manual on Aeroelasticity in Axial Flow Turbomachines (Vol2) - Structural Dynamics and Aeroelasticity*, pages 19–1 – 19–24. Specialised Printing Services Limited, Loughton, Essex, 1987.
- [23] Crawley, E.F. and Hall, K.C.: *Optimization and Mechanisms of Mistuning in Cascades*. Journal of Engineering for Gas Turbines and Power, 107(2):418–426, 1985.

- [24] Crawley, E.F.; Curtiss Jr., H.C.; Peters, D.A.; Scanlan, R.H. and Sisto, F.: *A Modern Course in Aeroelasticity*. Dowell, E.H. (editor), Kluwer Academic Publishers, 3rd edition, 1995.
- [25] Cumpsty, N.A.: *Compressor Aerodynamics*. Krieger Publishing Company, 2004.
- [26] Duta, M.C.; Campobasso, M.S.; Giles, M.B. and Lapworth, L.B.: *Adjoint Harmonic Sensitivities for Forced Response Minimization*. Journal of Engineering for Gas Turbines and Power, 128(1):183–189, 2006.
- [27] Erdos, J.I.; Alzner, E. and McNally, W.: *Numerical Solution of Periodic Transonic Flow through a Fan Stage*. AIAA Journal, 15(11):1559–1568, 1977.
- [28] Ewins, D.J.: *The Effects of Detuning Upon the Vibration of Bladed Discs*. PhD thesis, University of Cambridge, 1966.
- [29] Ewins, D.J.: *Modal Testing: Theory, Practice and Application*. Research Studies Press Ltd., 2nd edition, 2000.
- [30] Feiner, D.M.: *A Fundamental Model of Mistuning for System Identification and Forced Response Prediction*. PhD thesis, Carnegie Mellon University, Pittsburgh, Pennsylvania, 2003.
- [31] Feiner, D.M. and Griffin, J.H.: *A Fundamental Model of Mistuning for a Single Family of Modes*. Journal of Turbomachinery, 124(4):597–605, 2002.
- [32] Feiner, D.M. and Griffin, J.H.: *Mistuning Identification of Bladed Disks Using a Fundamental Mistuning Model—Part I: Theory*. Journal of Turbomachinery, 126(1):150–158, 2004.
- [33] Ferziger, J.H. and Peric, M.: *Computational Methods for Fluid Dynamics*. Springer Verlag, 3rd edition, 2002.
- [34] Fransson, T.H. and Verdon, J.M.: *Updated report on 'Standard Configurations for Unsteady Flow Through Vibrating Axial-Flow Turbomachine-Cascades'*. Technical report, KTH Stockholm Sweden, 1992.
- [35] Försching, H.W.: *Grundlagen der Aeroelastik*. Springer Verlag, 1st edition, 1974.
- [36] Försching, H.W.: *Aeroelastic Stability of Cascades in Turbomachinery*. Progress in Aerospace Sciences, 30(3):213 – 266, 1994, ISSN 0376-0421.
- [37] Gad-el-Hak, M.: *Frontiers of Flow Control*. In Hak, Mohamed Gad-el and Andrew Pollard (editors): *Flow Control*, volume 53 of *Lecture Notes in Physics monographs*, pages 109–153. Springer Berlin / Heidelberg, 1998.

- [38] Gad-el-Hak, M.: *Introduction to Flow Control*. In Hak, Mohamed Gad-el and Andrew Pollard (editors): *Flow Control*, volume 53 of *Lecture Notes in Physics monographs*, pages 1–107. Springer Berlin / Heidelberg, 1998.
- [39] Giersch, Th.: *Numerische Analyse des aeroelastischen Verhaltens einer transsonischen Hochdruckverdichterstufe*. Diploma thesis, Brandenburg University of Technology Cottbus, 2009.
- [40] Giles, M.B.: *Non-Reflecting Boundary Conditions for the Euler Equations*. AIAA Journal, 28(12):2050 – 2058, 1990.
- [41] Giles, M.B.: *UNSFLO: A Numerical Method for the Calculation of Unsteady Flow in Turbomachinery*. Technical Report GTL Report 205, MIT - Gas Turbine Laboratory, 1991.
- [42] Gümmer, V.: *Pfeilung und V-Stellung zur Beeinflussung der dreidimensionalen Strömung in Leiträdern transsonischer Axialverdichter*. PhD thesis, TU Berlin, 2000.
- [43] Grüber, B.: *Über den Einfluss der Viskosität auf das aerodynamische Dämpfungsverhalten bei schwingenden ebenen Verdichtergittern in transsonischer Strömung*. PhD thesis, Institute of Aeroelasticity, DLR Göttingen, Düsseldorf, 2002. Technical Report VDI No. 437.
- [44] Grieb, H.: *Verdichter für Turbo-Flugtriebwerke*. Springer Verlag, 2009.
- [45] Griffin, J.H.: *On Predicting the Resonant Response of Bladed Disk Assemblies*. Journal of Engineering for Gas Turbines and Power, 110(1):45–50, 1988.
- [46] Griffin, J.H. and Hoosac, T.M.: *Model Development and Statistical Investigation of Turbine Blade Mistuning*. Journal of Vibration Acoustics Stress and Reliability in Design, 106(2):204–210, 1984.
- [47] Hall, K.C. and Crawley, E.F.: *Calculation of Unsteady Flows in Turbomachinery Using the Linearized Euler Equations*. AIAA Journal, 27(6):777–787, 1989.
- [48] Hanamura, Y.; Tanaka, H. and Yamaguchi, K.: *A Simplified Method to Measure Unsteady Forces Acting on the Vibrating Blades in Cascade*. Bulletin of JSME, 23(180-12):880–887, 1980.
- [49] Happawana, G.S.; Nwokah, O.D.I.; Bajaj, A.K. and Azene, M.: *Free and Forced Response of Mistuned Linear Cyclic Systems: A Singular Perturbation Approach*. Journal of Sound and Vibration, 211(5):761 – 789, 1998, ISSN 0022-460X.
- [50] He, L.: *Method of Simulating Unsteady Turbomachinery Flows with Multiple Perturbations*. AIAA Journal, 30(11):2730–2735, 1992.

- [51] He, L.: *Handbook of Turbomachinery*, chapter 5, pages 257–308. Logan, E. Jr. and Roy, R. (editors), Marcel Dekker Inc., 2nd edition, 1995.
- [52] He, Z.; Epureanu, B.I. and Pierre, C.: *Effects of Unsteady Aerodynamics on the Dynamic Response of Mistuned Bladed Disks*. In Bathe, K.J. (editor): *Proceedings of 3rd MIT Conference on Computational Fluid and Solid Mechanics*, 2005.
- [53] Hennings, H.: *Windkanal-Flutteruntersuchungen an einem endlichen, geraden 2d-Verdichtergitter in inkompressibler Strömung*. PhD thesis, DLR, 1996.
- [54] Höhn, W.: *Unsteady Viscous Flow Around Cascaded Vibrating Blades at or near Stall*. Technical Report TRITA-KRV-1996-2, KTH Stockholm, 1996.
- [55] Hönisch, P. and Kühhorn, A.: *Mistuning und Dämpfung von Radialturbinenrädern*. In *Herbsttagung 2010, Forschungsvereinigung Verbrennungskraftmaschinen e. V. (FVV)*, number R552, 2010.
- [56] Huff, D.L.: *Unsteady Flow Field Predictions of Oscillating Cascades*. In Atassi, H. M. (editor): *Proceedings of the 6th International Symposium on Unsteady Aerodynamics, Aeroacoustics and Aeroelasticity of Turbomachines and Propellers*. Springer Verlag, 1991.
- [57] Hurty, W.C.: *Dynamic Analysis of Structural Systems using Component Modes*. AIAA Journal, 3(4):678–685, 1965.
- [58] Imregun, M.: *Structural and Aeroelastic Vibration Analysis of Bladed Systems*. PhD thesis, Imperial College London, 1983.
- [59] Irretier, H.: *Zum Einfluss des Schwingungsverhaltens eines scheibenförmigen Tragkörpers auf die Eigenfrequenzen der Schaufeln thermischer Turbomaschinen*. Engineering-Archive, 50:85–102, 1981.
- [60] Judge, J.; Pierre, C. and Mehmed, O.: *Experimental Investigation of Mode Localization and Forced Response Amplitude Magnification for a Mistuned Bladed Disk*. Journal of Engineering for Gas Turbines and Power, 123(4):940–950, 2001.
- [61] Kahl, G.: *Aeroelastic Effects of Mistuning and Coupling in Turbomachinery Bladings*. Thesis nr. 2629, EPFL Lausanne, 2002.
- [62] Kaza, K.R.V. and Kielb, R.E.: *Flutter and Response of a Mistuned Cascade in Incompressible Flow*. AIAA Journal, 20(8):1120–1127, 1982.
- [63] Kemme, R.: *Numerische Untersuchungen zum aeroelastischen Verhalten eines hochbelasteten Verdichterrotores*. Research report - Deutsches Zentrum für Luft- und Raumfahrt, number 28, Institute of Aeroelasticity, DLR Göttingen, 2004.

- [64] Kenyon, J.A. and Griffin, J.H.: *Forced Response of Turbine Engine Bladed Disks and Sensitivity to Harmonic Mistuning*. International Gas Turbine and Aeroengine Congress and Exhibition, 125(1):113–120, 2003.
- [65] Kenyon, J.A.; Griffin, J.H. and Feiner, D.M.: *Maximum Bladed Disk Forced Response From Distortion of a Structural Mode*. Journal of Turbomachinery, 125(2):352–363, 2003.
- [66] Kielb, R.E.; Feiner, D.M.; Griffin, J.H. and Miyakozawa, T.: *Flutter of Mistuned Bladed Disks with Aerodynamic and FMM Structural Coupling*. In *Proceedings of ASME TurboExpo 2004 Power for Land, Sea and Air, June 14-17, Vienna, Austria, 2004*.
- [67] Kielb, R.E.; Hall, K.C.; Hong, E. and Pai, S.S.: *Probabilistic Flutter Analysis of a Mistuned Bladed Disk*. In *ASME Turbo Expo 2006: Power for Land, Sea and Air, May 8-11, 2006, Barcelona, Spain, 2006*.
- [68] Klauke, Th.: *Schaufelschwingungen realer integraler Verdichterräder im Hinblick auf Verstimmung und Lokalisierung*. PhD thesis, Brandenburg University of Technology Cottbus, 2007. Der Andere Verlag, Tönning, Lübeck und Marburg.
- [69] Klauke, Th.; Kühhorn, A. and Strehlau, U.: *Frequency Crossing and Frequency Veering Effects of Mistuned Blade Integrated Disks (Blisks)*. Journal of Turbomachinery, submitted for publication.
- [70] Klinger, H.; Lazik, W. and Wunderlich, Th.: *The Engine 3E Core Engine*. In *Proceedings of ASME Turbo Expo 2008: Power for Land, Sea and Air, June 9-13, 2008, Berlin, Germany*, number GT2008-50679, 2008.
- [71] Kruse, M.J. and Pierre, C.: *An Experimental Investigation of Vibration Localization in Bladed Disks, Part I: Free Response*. In *Proc. of the 42nd ASME Gas Turbine & Aero Engine Congress, User's Symposium and Exposition, Orlando, Florida, 1997*.
- [72] Kruse, M.J. and Pierre, C.: *An Experimental Investigation of Vibration Localization in Bladed Disks, Part II: Forced Response*. In *Proc. of the 42nd ASME Gas Turbine & Aero Engine Congress, User's Symposium and Exposition, Orlando, Florida, 1997*.
- [73] Lane, F.: *System Mode Shapes in the Flutter of Compressor Blade Rows*. Journal of Aeronautical Sciences, 23:54–66, 1956.
- [74] Li, H.D. and He, L.: *Blade Aerodynamic Damping Variation with Rotor-Stator Gap – A Computational Study using Single-Passage Approach*. In *Proceedings of ASME Turbo Expo 2003 Power for Land, Sea, and Air, June 16–19, 2003, Atlanta, Georgia, USA, 2003*.

- [75] Li, H.D. and He, L.: *Toward Intra-Row Gap Optimization for One and Half Stage Transonic Compressor*. Journal of Turbomachinery, 127(3):589–598, 2005.
- [76] Lin, C.C. and Mignolet, M.P.: *Effects of Damping and Damping Mistuning on the Forced Vibration Response of Bladed Disks*. Journal of Sound and Vibration, 193(2):525 – 543, 1996, ISSN 0022-460X.
- [77] Marshall, J.G. and Imregun, M.: *A Review of Aeroelasticity Methods with Emphasis on Turbomachinery Applications*. Journal of Fluids and Structures, 10:237–267, 1996.
- [78] Martel, C.; Corral, R. and Llorens, J.M.: *Stability Increase of Aerodynamically Unstable Rotors Using Intentional Mistuning*. Journal of Turbomachinery, 130(1):011006, 2008.
- [79] Mata, S.; Di Mare, L.; Imregun, M. and Green, J.: *An Efficient Generalised Single-Passage Method for Turbomachinery Forced Response*. In *Proceedings of the 12th International Symposium on Unsteady Aerodynamics, Aeroacoustics & Aeroelasticity of Turbomachines ISUAAAT121-4 September 2009, Imperial College London, UK, 2009*.
- [80] Mignolet, M.P. and Lin, C.C.: *Identification of Structural Parameters in Mistuned Bladed Disks*. Journal of Vibration and Acoustics, 119(3):428–438, 1997.
- [81] Mignolet, M.P.; Rivas-Guerra, A.J. and Delor, J.P.: *Identification of Mistuning Characteristics of Bladed Disks From Free Response Data—Part I*. Journal of Engineering for Gas Turbines and Power, 123(2):395–403, 2001.
- [82] Miyakozawa, T.: *Flutter and Forced Response of Turbomachinery with Frequency Mistuning and Aerodynamic Asymmetry*. PhD thesis, Duke University, 2008.
- [83] Montgomery, M. D. and Verdon, J.M.: *A Three-Dimensional Linearized Unsteady Euler Analysis for Turbomachinery Blade Rows*. Technical report, NASA, United Technology Research Center, East Hartford, Connecticut, 1997.
- [84] Moyroud, F.; Fransson, T.H.; Jacquet-Richardet, G.: *A Comparison of Two Finite Element Reduction Techniques for Mistuned Bladed Disks*. Journal of Engineering for Gas Turbines and Power, 124(4):942–952, 2002.
- [85] Newmark, M.: *A Method of Computation for Structural Dynamics*. ASCE Journal of Engineering Mechanics Division 8, pages 67–94, 1959.
- [86] Nikolic, M.: *New Insights into the Blade Mistuning Problem*. PhD thesis, Imperial College London, August 2006.

- [87] Nipkau, J.: *Numerische Analyse des Einflusses aeroelastischer Vorgänge auf das Schwingungsverhalten von Axialverdichter-Blisk-Stufen*. Diploma thesis, Brandenburg University of Technology Cottbus, 2007.
- [88] Nowinski, M. and Panovsky, J.: *Flutter Mechanisms in Low Pressure Turbine Blades*. *Journal of Engineering for Gas Turbines and Power*, 122(1):82–88, 2000.
- [89] Petrie-Repar, P.J.: *Development of an Efficient and Robust Linearised Navier-Stokes Flow Solver*. In K.C. Hall et al. (editor): *Unsteady Aerodynamics, Aeroacoustics and Aeroelasticity of Turbomachines*, pages 437 – 448. Springer Verlag, 2006.
- [90] Petrie-Repar, P.J.: *Three-Dimensional Non-Reflecting Boundary Condition for Linearized Flow Solvers*. In *Proceedings of ASME Turbo Expo 2010: Power for Land, Sea and Air, June 14-18, 2010, Glasgow, UK*, number GT2010-23335, 2010.
- [91] Petrie-Repar, P.J.; McGhee, A. and Jacobs, P.A.: *Three-Dimensional Viscous Flutter Analysis of Standard Configuration 10*. In *ASME Turbo Expo 2007*, 2007. GT2007-27800.
- [92] Petrov, E.P.: *Vibrations of Mistuned Bladed Discs in Gas Flow: High-Fidelity Analysis and Amplitude Reduction by Mistuning*. In *Proceedings of the 12th ISUAAAT, 1-4 September 2009, Imperial Colleg London, UK*, 2009.
- [93] Petrov, E.P.: *A Method for Forced Response Analysis of Mistuned Bladed Disks With Aerodynamic Effects Included*. *Journal of Engineering for Gas Turbines and Power*, 132(6):062502, 2010.
- [94] Petrov, E.P.: *Reduction of Forced Response Levels for Bladed Discs by Mistuning: Overview of the Phenomenon*. In *Proceedings of ASME Turbo Expo 2010: Power for Land, Sea and Air, June 14-18, Glasgow*, number GT2010-23299. ASME, 2010.
- [95] Petrov, E.P.; Di Mare, L.; Hennings, H. and Elliott, R.: *Forced Response of Mistuned Bladed Disks in Gas Flow: A Comparative Study of Predictions and Full-Scale Experimental Results*. *Journal of Engineering for Gas Turbines and Power*, 132(5):052504, 2010.
- [96] Petrov, E.P.; Sanliturk, K.Y. and Ewins, D.J.: *A New Method for Dynamic Analysis of Mistuned Bladed Disks Based on the Exact Relationship Between Tuned and Mistuned Systems*. *Journal of Engineering for Gas Turbines and Power*, 124(3):586–597, 2002.
- [97] Reddy, T.S.R.; Bakhle, M.A. and Srivastava, R.: *A Review of Recent Aeroelastic Analysis Methods for Propulsion at NASA Lewis Research Center*. Nasa technical paper 3406, NASA Lewis Research Center, 1993.
- [98] Roache, P.J.: *Verification and Validation in Computational Science and Engineering*. Hermosa Publishers, 1998.

- [99] Sayma, A.I.; and Vahdati, M. and Imregun, M.: *An Integrated Nonlinear Approach for Turbomachinery Forced Response Prediction. Part I: Formulation.* Journal of Fluids and Structures, 14(1):87 – 101, 2000, ISSN 0889-9746.
- [100] Schmitt, S.: *Simulation of Flutter and Forced Response in Turbomachinery Blade Rows.* PhD thesis, Insitute of Propulsion Technology, DLR Köln, 2003. DLR-Research report 2003-22.
- [101] Schrape, S.; Kühhorn, A. and Golze, M.: *Simulation fluidgedämpfter Strukturschwingungen durch partitionierte Fluid-Struktur-Kopplung mittels MpCCI.* In: *Tagungsband des 3. NAFEMS CFD Seminar: Simulation gekoppelter Strömungsvorgänge (Multifield FSI)*, Wiesbaden, 2006. NAFEMS.
- [102] Schrape, S.; Nipkau, J.; Kühhorn, A. and Beirow, B.: *Application of Aeroelastic Methods in Compressor Cascade Configurations Using Commercial Code Coupling.* In *ASME 2008 Pressure Vessels and Piping Conference, July 27-31, 2008, Chicago, Illinois, USA, PVP2008-61274*, 2008.
- [103] Seinturier, E.; Lombard, J.P.; Berthillier, M. and Sgarzi, O.: *Turbine Mistuned Forced Response Prediction Comparison with Experimental Results.* In *ASME Turbo Expo 2002*, number GT2002-30424, June 3-6 2002.
- [104] Seinturier, E.; Lombard, J.P.; Dumas, M.; Dupont, C.; Sharma, V. and Jérôme, D.: *Forced Response Prediction Methodology for the Design of HP Compressors Bladed Disks.* In *ASME Turbo Expo 2004*, number GT2004-53372, June 14-17 2004.
- [105] Sinha, A. and Chen, S.: *A Higher Order Technique to Compute the Statistics of Forced Response of a Mistuned Bladed Disk Assembly.* Journal of Sound and Vibration, 130(2):207 – 221, 1989, ISSN 0022-460X.
- [106] Slater, J.C.; Minkiewicz, G.R. and Blair A.J.: *Forced Response of Bladed Disk Assemblies - A Survey.* The Shock and Vibration Digest, 31(1):17–24, 1999.
- [107] Spalart, P.R. and Allmaras, S.R.: *A One-Equation Turbulence Model for Aerodynamic Flows.* La Recherche Aérospatiale, 1:5–21, 1994.
- [108] Srinivasan, A.V.: *Flutter and Resonant Vibration Characteristics of Engine Blades.* Journal of Engineering for Gas Turbines and Power, 119:742–775, 1997.
- [109] Srinivasan, A.V. and Tavares, G.G.: *Direct Use of Unsteady Aerodynamic Pressures in the Flutter Analysis of Mistuned Blades.* Journal de Physique, 5(10):1587–1597, 1995.
- [110] Strehlau, U. and Kühhorn, A.: *Experimental and Numerical Investigations of HPC Blisks with a Focus on Travelling Waves.* In *ASME TurboExpo, June 14-18, Glasgow, Great Britain, GT2010-22463*, 2010.

- [111] Óttarsson, G. and Pierre, C.: *A Transfer Matrix Approach to Free Vibration Localization in Mistuned Blade Assemblies*. Journal of Sound and Vibration, 197(5):589 – 618, 1996, ISSN 0022-460X.
- [112] Vahdati, M.; Sayma, A.I. and Imregun, M.: *An Integrated Nonlinear Approach for Turbomachinery Forced Response Prediction. Part II: Case Studies*. Journal of Fluids and Structures, 14(1):103 – 125, 2000, ISSN 0889-9746.
- [113] Verdon, J.M.: *Linearized Unsteady Aerodynamic Theory*. In Platzer, M.F. and F.O. Carta (editors): *AGARD Manual on Aeroelasticity in Axial-Flow Turbomachines - AGARD-AG-298*, volume 1, chapter 2. Specialised Printing Services Limited, Loughton, Essex, März 1987.
- [114] Verdon, J.M.: *Review of Unsteady Aerodynamic Methods for Turbomachinery Aeroelastic and Aeroacoustic Applications*. AIAA Journal, 31:235–250, 1993.
- [115] Vogt, D.M.: *Experimental Research on Aeroelasticity*. In *Structural Design of Aircraft Engines: Key Objectives and Techniques*. von Karman Institute for Fluid Dynamics, 2008.
- [116] Wagner, J.T.: *Coupling of Turbomachine Blade Vibrations Through the Rotor*. ASME Journal of Engineering for Power, 89:502–512, 1967.
- [117] Wei, S.T. and Pierre, C.: *Localization Phenomena in Mistuned Assemblies with Cyclic Symmetry Part I: Free Vibrations*. Journal of Vibration Acoustics Stress and Reliability in Design, 110(4):429–438, 1988.
- [118] Wei, S.T. and Pierre, C.: *Localization Phenomena in Mistuned Assemblies with Cyclic Symmetry Part II: Forced Vibrations*. Journal of Vibration Acoustics Stress and Reliability in Design, 110(4):439–449, 1988.
- [119] Whitehead, D.S.: *Effect of Mistuning on the Vibration of Turbomachine Blades induced by Wakes*. Journal of Mechanical Engineering Science, 8(1):15–21, 1966.
- [120] Whitehead, D.S.: *Research Note: Effect of Mistuning on Forced Vibration of Blades with Mechanical Coupling*. Journal Mechanical Engineering Science, 18(6):306–307, 1976.
- [121] Whitehead, D.S.: *The Maximum Factor by Which Forced Vibration of Blades Can Increase Due to Mistuning*. Journal of Engineering for Gas Turbines and Power, 120(1):115–119, 1998.
- [122] Willcox, K. and Peraire, J.: *Application of Reduced-Order Aerodynamic Modeling to the analysis of Structural Uncertainty in Bladed Disks*. In *Proceedings of ASME TURBO EXPO 2002, June 3-6 2002, Amsterdam, Netherlands*, number GT-2002-30680, 2002.

-
- [123] Yang, M.T. and Griffin, J.H.: *A Normalized Modal Eigenvalue Approach for Resolving Modal Interaction*. Journal of Engineering for Gas Turbines and Power, 119(3):647–650, 1997.
- [124] Yang, M.T. and Griffin, J.H.: *A Reduced-Order Model of Mistuning Using a Subset of Nominal System Modes*. Journal of Engineering for Gas Turbines and Power, 123(4):893–900, 2001.